

Synthesis, characterization and physical/chemical properties of polyoxometalate-based materials

Zur Erlangung des akademischen Grades eines
DOKTORS DER NATURWISSENSCHAFTEN

(Dr. rer. nat.)

von der KIT-Fakultät für Chemie und Biowissenschaften
des Karlsruher Instituts für Technologie (KIT)



genehmigte

Dissertation

von

M.Sc. Marcel Patrick Merkel

aus

Mannheim-Neckarau, Deutschland

Karlsruhe, 2019

KIT-Dekan: Prof. Dr. Reinhard Fischer

Referent: Prof. Dr. Annie Powell

Korreferent: Prof. Dr. Peter Roesky

Tag der mündlichen Prüfung: 26. Juli 2019

Für meine Familie und meine Freundin Dr. Krisana Peewasan

Acknowledgements

This thesis was carried out from October 2015 to June 2019 at the Institute for Inorganic Chemistry at the Karlsruhe Institute of Technology (KIT) under supervision of Prof. Dr. Annie K. Powell.

First of all I would like to thank Prof. Dr. Annie K. Powell for giving me the opportunity to do my PhD study in a comfortable and very welcoming atmosphere in her working group. Additionally, I would like to thank her for a very kindness, excellent support and interesting topic.

In addition, I would like to thank deeply from my heart to all:

- Dr. Masooma Ibrahim: for the many tips and suggestions and the wonderful support that I was allowed to enjoy during the time of this study.
- Gertraud Amschlinger: for her kindness and cozy atmosphere and for every help I got.
- Dr. Christopher Anson: for solving and refining my single crystal X-ray structures and nice conversations.
- Dr. Olaf Fuhr and Prof. Dr. Dieter Fenske: for measuring single crystals and nice conversations.
- Dr. Andreas Eichhöfer: for the introductions to single crystal X-ray diffractometers, powder X-ray diffractometer and for every help I received from him.
- Sven Stahl: for introduction in NMR-spectrometer, for ordering all chemicals, measuring all the elemental analyses and for every help.
- My colleagues: Dr. Nicolas Leblanc, Dr. Sebastian Schmidt, Dr. Yan Peng, Dr. Markus Schroth, Lena Friedrich, Anthony Carter, Hagen Kämmerer, Thomas Ruppert, Rouven Pflieger and Umaira Shuaib: for every kind conversation, help with reactions and cozy atmosphere.

- Cooperation Partners: Dr. George E. Kostakis, Dr. Mbomekalle Israël, Prof. Dr. Pedro De Oliveira and Dr. Ying-Chu Chen..
- My lovely family and friends: Especially to my parents Christoph and Gabrielle Merkel, my brother Dr. Marcus Merkel, my aunt Renate Ott, my uncle Thomas Ott and my grandparents Anna and Joachim Prudlik and Josef and Elfriede Cebulla: for supporting me and being always there for me. My dear girlfriend: Dr. Krisana Peewasan: for every support and every help I got from her.

Annotation:

The ions shown in the figures are not to scale. Organic hydrogen atoms, as well as solvent molecules are often not shown for clarity. The numerical values such as bond lengths and angles are given in standard deviation. This is in parentheses after each value and refers to the last digit. The lengths are given in Angstroms, where $1 \text{ \AA} = 1.10 \cdot 10^{-10} \text{ m}$.

The abbreviation TM stands for transition metals in low oxidation state.

SUMMARY

Polyoxometalate based metal organic frameworks (POMOFs) can be regarded in general terms as frameworks containing Polyoxometalates (POMs). Here, we can identify three distinct categories: (a) POMs occupying the cavities of a metal organic framework (MOF) structure (POM@MOF), (b) POMs used as secondary building units (SBUs) in the network and (c) POMs as part of the linker of the framework. For this research presented in this thesis, it was decided to concentrate on the barely explored area (c). Furthermore, it seemed a useful strategy to compare combining metals from the d series (TM = Cu, Zn, Cd, Mn, Mo) with rare earth metal ions (RE = Y, La – Lu).

The first stage of the exploration was to develop suitable L – POM – L linkers, where L is a Tris-functionalized ((OHCH₂)₃CNH₂) unit and POM is the Anderson-Evans POM. This Polyanion was chosen because it provides three octahedrally arranged coordination sites above and below the central plane, which can be occupied by three hydroxyl groups of a Tris ligand. This Tris-ligand can be functionalized at the amine group using suitable N-R forming reagents, such as R'HC=O, R'HC-X (X = Cl, Br) and R'COCl. R was chosen such the terminus T_{func} provides a coordinating group for a TM or RE nodes. T_{func} can be for example N_{py}, O_{COO}, N_{C≡N}, etc. In this way L – POM – L linkers were formed. Two of these L – POM – Ls proved to be particularly successful for producing transition metal based POMOFs, where the functional group is pyridyl and RE based POMOFs, where the functional group is carboxylate. These could be characterized using single crystal X-ray diffraction, which is important in this field since we ultimately should be able to relate the functionality to topology. In this context optical properties such as bandgap, UV-vis and Fourier Transform Infrared (FT-IR) Spectroscopy were investigated. The highlight within the TM-based series was the activity of [N(*n*-C₄H₉)₄]₅[CuCl(DMF){MnMo₆O₁₈((OCH₂)₃CN=CH(4-C₅H₄N))₂}]₂·3DMF (**13**) for the A³-Coupling without the need for inert conditions. For the RE-series the Dy based compound [Dy(DMF)₄(H₂O)]₂[Dy₃

(DMF)₆][((MnMo₆O₁₈)((OCH₂)₃CNHCH₂(C₆H₄)COO)₂)]₃·5DMF (**12**)-Dy proved to be the most versatile. Finally, a completely new topology was discovered for compound [Zn(DMF)₄][Zn(DMF)₂MnMo₆O₁₈{(OCH₂)₃CN=CH(4-C₅H₄N)}₂]₂·10DMF (**14A**) and interestingly the synthesis for this compound has a bifurcation in terms of topology since the equally abundant component [(Zn(DMF)₃)₂(Zn(DMF)₄MnMo₆O₁₈{(OCH₂)₃CN=CH(4-C₅H₄N)}₂)]₂·9DMF (**14B**) of the reaction has a completely different topologically structure.

Zusammenfassung

Polyoxometallat-basierte Metall organische Netzwerke (POMOFs) können allgemein als Netzwerke angesehen werden, welche Polyoxometallate (POMs) beinhalten. Hier lassen sich drei Kategorien unterscheiden: (a) POMs, welche die Hohlräume einer Metal organic framework (MOF)-Struktur belegen (POM@MOF), (b) POMs, die als Secondary Building Units (SBUs) im Netzwerk verwendet werden und (c) POMs, die als Teil des Linkers des Frameworks genutzt werden. In der vorgestellten Arbeit wurden die POMOFs der Kategorie (c) untersucht. Darüber hinaus wurde die Kombination aus Metallen der d - Reihe (TM = Cu, Zn, Cd, Mn, Mo) mit Seltenerdmetallionen (RE = Y, La - Lu) verglichen.

Im ersten Teil der Forschungsarbeit wurden L-POM-L-Linker entwickelt, wobei L eine Tris-funktionalisierte ((OHCH₂)₃CNH₂) Einheit und POM das Anderson-Evans-Polyanion ist. Dieses Polyanion weist drei oktaedrisch angeordnete Koordinationsstellen oberhalb und unterhalb der zentralen Ebene auf, die von drei Hydroxylgruppen eines Tris - Liganden besetzt werden können. Dieser Tris-Ligand kann an der Aminogruppe unter Verwendung geeigneter N-R-bildender Reagenzien wie R'HC = O, R'HC-X (X = Cl, Br) und R'COCl funktionalisiert werden. R wurde so gewählt, dass der Terminus T_{func} eine koordinierende Gruppe für einen TM- oder RE-Knotenpunkt bereitstellt. T_{func} kann beispielsweise N_{py}, O_{COO}, N_{C=N} usw. sein. Auf diese Weise wurden L-POM-L-Linker gebildet. Zwei dieser L-POM-Ls erwiesen sich als besonders erfolgreich für die Herstellung von Übergangsmetallbasierten POMOFs, mit Pyridylgruppen als funktionelle Gruppen und RE-basierte POMOFs, bei denen die funktionelle Gruppen Carboxylate sind. Diese konnten mittels Einkristall-Röntgenstrukturanalyse charakterisiert werden, womit die Funktionalität mit der Topologie in Beziehung gesetzt werden konnte. In diesem Zusammenhang wurden optische Eigenschaften wie Bandlücken, UV-Vis- und Fourier-Transformierte-Infrarot- (FT-IR-) Spektroskopie untersucht. Das Highlight innerhalb der TM-basierten Reihe war die Aktivität von

$[N(n\text{-C}_4\text{H}_9)_4]_5[\text{CuCl}(\text{DMF})\{\text{MnMo}_6\text{O}_{18}((\text{OCH}_2)_3\text{CN}=\text{CH}(4\text{-C}_5\text{H}_4\text{N}))_2\}_2] \cdot 3\text{DMF}$
(13) für A³-Kupplungsreaktionen ohne Luftausschluss. Für die RE-Reihe erwies sich die auf Dy basierende Verbindung $[\text{Dy}(\text{DMF})_4(\text{H}_2\text{O})_2]_2[\text{Dy}_3(\text{DMF})_6][(\text{MnMo}_6\text{O}_{18})((\text{OCH}_2)_3\text{CNHCH}_2(\text{C}_6\text{H}_4)\text{COO})_2]_3 \cdot 5\text{DMF}$ **(12)**-Dy als die vielseitigste. Schließlich wurde für eine weitere Verbindung $[\text{Zn}(\text{DMF})_4][\text{Zn}(\text{DMF})_2\text{MnMo}_6\text{O}_{18}\{(\text{OCH}_2)_3\text{CN}=\text{CH}(4\text{-C}_5\text{H}_4\text{N})\}_2]_2 \cdot 10\text{DMF}$ **(14A)** eine völlig neue Topologie entdeckt. Interessanterweise weist die Synthese für diese Verbindung eine Bifurkation in Bezug auf die Topologie auf, da die ebenso häufig vorkommende Komponente $[(\text{Zn}(\text{DMF})_3)_2(\text{Zn}(\text{DMF})_4\text{MnMo}_6\text{O}_{18}\{(\text{OCH}_2)_3\text{CN}=\text{CH}(4\text{-C}_5\text{H}_4\text{N})\}_2)]_2 \cdot 9\text{DMF}$ **(14B)** der Reaktion eine völlig andere topologische Struktur aufweist.

Table of Contents

1	Historical Background	7
2	Motivation and Objective	9
3	Introduction	11
3.1	Polyoxometalates	11
3.1.1	Classification of POMs	13
3.1.2	Isomers of polyoxometalates.....	23
3.1.3	Lacunary derivatives of polyanions	25
3.2	Metal-Organic Frameworks (MOFs)	27
3.2.1	Primary Buildings Units (PBUs).....	28
3.2.2	Linkers for MOFs.....	28
3.2.3	Secondary Building Units (SBUs)	30
3.2.4	Topological consideration of MOFs	31
3.2.5	Crystal-to-crystal (CTC) (topotactic) transformation	33
3.3	Polyoxometalate-based Metal-Organic Frameworks (POMOFs) .	34
3.3.1	Properties of POMOFs	36
3.4	Catalysis	38
3.4.1	A ³ -coupling	38
3.4.2	Catalytic reaction for the implementation of furfural with amines.....	39
3.4.3	Electrocatalysis.....	41
3.4.4	Photo-electrocatalysis.....	45

4	Experimental Section	48
4.1	Instrumentation	48
4.1.1	Fourier Transform-Infrared (FT-IR) Spectroscopy	48
4.1.2	Elemental Analysis (EA).....	48
4.1.3	Single crystal X-ray diffraction (SCXRD).....	48
4.1.4	Powder X-ray diffraction (PXRD)	49
4.1.5	Nuclear Magnetic Resonance (NMR) Spectroscopy	49
4.1.6	Topology	50
4.1.7	Analysis of the coordination geometry of the metal centres	50
4.1.8	Solid state UV-vis spectroscopy	50
4.1.9	Electrochemistry.....	50
4.1.10	Photo-electrochemistry.....	51
4.2	Synthesis and synthetic strategies	51
4.3	Synthesis of previously reported precursors (Pre) and linkers (L)	53
4.3.1	$[N(n-C_4H_9)_4]_4[Mo_8O_{26}]$ (1).....	53
4.3.2	$Na_3[Al(OH)_6Mo_6O_{18}] \cdot 2nH_2O$ ($n = 2-10$) (2)	54
4.3.3	$[N(n-C_4H_9)_4]_3[MnMo_6O_{18}\{(OCH_2)_3CNH_2\}_2]$ (3)	54
4.3.4	$[N(n-C_4H_9)_4]_3[MnMo_6O_{18}\{(OCH_2)_3CN=CH(4-C_5H_4N)\}_2] \cdot 3DMF$ (4) .	55
4.3.5	4-HOOC(C ₆ H ₄)CH ₂ NHC(CH ₂ OH) ₃ (L1)	55
4.4	Synthesis of novel precursors (Pre) and potential linkers (L)	56
4.4.1	$[N(n-C_4H_9)_4]_4[(MnMo_6O_{18})((OCH_2)_3CNHCH_2(C_6H_4)COOH)((OCH_2)_3CNHCH_2(C_6H_4)COO)] \cdot 3DMF$ (5).....	56

4.4.2	[N(<i>n</i> -C ₄ H ₉) ₄] ₃ [(AlMo ₆ O ₁₈)((OCH ₂) ₃ CCH ₂ OCH ₂ C(CH ₂ OH) ₃) ₂]. 2H ₂ O (6)	57
4.4.3	4-N≡C(C ₆ H ₄)CH ₂ NHC(CH ₂ OH) ₃ (L2).....	58
4.4.4	[N(<i>n</i> -C ₄ H ₉) ₄] ₃ [(MnMo ₆ O ₁₈)((OCH ₂) ₃ CNH(C ₆ H ₄)C≡N) ₂]. 6MeCN (7)	58
4.4.5	4-NO ₂ (C ₆ H ₄)C=ONHC(HOCH ₂) ₃ (L3).....	59
4.4.6	[N(<i>n</i> -C ₄ H ₉) ₄] ₃ [MnMo ₆ O ₁₈ {(OCH ₂) ₃ CNHC=O(C ₆ H ₄)NO ₂ } ₂]. 6DMF (8)	60
4.4.7	(C ₆ H ₅)NHC(CH ₂ OH) ₃ (L4).....	60
4.4.8	[N(<i>n</i> -C ₄ H ₉) ₄] ₃ [(MnMo ₆ O ₁₈)((OCH ₂) ₃ CNHC ₆ H ₅) ₂]. MeCN·H ₂ O (9)	61
4.4.9	[N(<i>n</i> -C ₄ H ₉) ₄] ₂ [Mn ₂ Mo ₄ O ₁₄ ((OCH ₂ CH ₂) ₂ NCH ₂ CH ₂ OH) ₂] (10).....	62
4.5	Synthesis of extended structures.....	63
4.5.1	Synthesis of rare earth containing polyoxometalate-based metal organic frameworks (RE-POMOFs)	63
4.5.2	Synthesis of transition metal containing polyoxometalate-based metal organic frameworks (TM-POMOFs)	71
4.6	Catalytic studies.....	73
4.6.1	A ³ -Coupling	73
4.6.2	Catalytic reaction for the implementation of furfural with morpholine	75
4.6.3	Photo-electrocatalytic studies.....	75
4.6.4	Electrocatalytic studies.....	76
5	Results and Discussion	77
5.1	Previously reported precursors (Pre).....	77

5.1.1	$[N(n\text{-C}_4\text{H}_9)_4]_3[\text{MnMo}_6\text{O}_{18}\{(\text{OCH}_2)_3\text{CN}=\text{CH}(4\text{-C}_5\text{H}_4\text{N})\}_2] \cdot 3\text{DMF}$ (4)	77
5.2	Novel precursors (Pre)	82
5.2.1	$[N(n\text{-C}_4\text{H}_9)_4]_4[(\text{MnMo}_6\text{O}_{18})((\text{OCH}_2)_3\text{CNHCH}_2(\text{C}_6\text{H}_4)\text{COOH})((\text{OCH}_2)_3\text{CNHCH}_2(\text{C}_6\text{H}_4)\text{COO})] \cdot 3\text{DMF}$ (5)	82
5.2.2	$[N(n\text{-C}_4\text{H}_9)_4]_3[(\text{AlMo}_6\text{O}_{18})((\text{OCH}_2)_3\text{CCH}_2\text{OCH}_2\text{C}(\text{CH}_2\text{OH})_3)_2] \cdot 2\text{H}_2\text{O}$ (6)	90
5.2.3	$[N(n\text{-C}_4\text{H}_9)_4]_3[(\text{MnMo}_6\text{O}_{18})\{(\text{OCH}_2)_3\text{CNH}(\text{C}_6\text{H}_4)\text{C}\equiv\text{N}\}_2] \cdot 6\text{MeCN}$ (7)	96
5.2.4	$[N(n\text{-C}_4\text{H}_9)_4]_3[\text{MnMo}_6\text{O}_{18}\{(\text{OCH}_2)_3\text{CNHC}=\text{O}(\text{C}_6\text{H}_4\text{NO}_2)\}_2] \cdot 6\text{DMF}$ (8)	101
5.2.5	Steps towards developing the POM as linker strategy (c) to the synthesis of POMOFs	105
5.2.6	$[N(n\text{-C}_4\text{H}_9)_4]_2[\text{Mn}_2\text{Mo}_4\text{O}_{14}((\text{OCH}_2\text{CH}_2)_2\text{NCH}_2\text{CH}_2\text{OH})_2]$ (10).....	109
5.3	Extended structures	115
5.3.1	Rare earth containing polyoxometalate-based metal organic frameworks (RE-POMOFs)	118
5.3.2	Transition metal containing polyoxometalate-based metal organic frameworks (TM-POMOFs)	150
6	Conclusion and Outlook	185
7	References	188
8	Appendix	199
8.1	Crystallographic data	199

8.2	SHAPE analysis results for coordination polyhedra	212
8.2.1	SHAPE analysis for compound (10)	212
8.2.2	SHAPE analysis for compound (11)-Ce	217
8.2.3	SHAPE analysis for compound (12)-Dy	234
8.2.4	SHAPE analysis for compound (13)	238
8.2.5	SHAPE analysis for compound (14A)	240
8.2.6	SHAPE analysis for compound (14B)	242
8.2.7	SHAPE analysis for compound (15)	245
8.3	Publications	249
8.4	Conferences	249
8.5	Work shops	249
8.6	Stay Abroad	250
8.7	Collaborations	250
8.8	Teaching assistant	250
9	Eidesstattliche Erklärung	252

List of Abbreviations

1D	One-dimension
2D	Two-dimension
3D	Three-dimension
°	Degree
°C	Degree Celsius
4,4'-BPY	4,4'-bipyridine
Å	Ångstrom
acac	Acetylacetonate
A_{ox}	Activity of oxidized species
A_{red}	Activity of reduced species
a.u.	Arbitrary units
ADTP	1,3,5,7-tetrakis(4-phosphonophenyl)adamantine
ADTS	1,3,5,7-tetrakis(4-sulfonophenyl)adamantine
BDC	1,4-benzenedicarboxylate
BPCN	4,4'-biphenyldicarbonitrile
BPDC	Biphenyl-4,4'-dicarboxylate
BTC	1,3,5-benzenetricarboxylate
C	Coulomb
Cat.	Catalyst

List of Abbreviations

cm	Centimetre
CMOS	Complementary-Metal-Oxide-Semiconductor
CP	Coordination Polymers
CTC	Crystal-to-crystal
CV	Cyclic voltammetry
DABCO	1,4-diazabicyclo[2.2.2]octane
DCM	Dichloromethane
DMF	Dimethylformamid
DMSO	Dimethyl sulfoxide
E	Potential
EA	Elemental Analysis
e ⁻	Electron
E ₀	Standard potential
E _λ	Reversal potential
eq.	Equivalent
E _{start}	Initial potential
Et ₂ O	Diethyl ether
eV	Electronvolt
F	Faraday constant (= 96,487 A s/mol)
FT-IR	Fourier-Transform- Infrared
FTO	Fluorine-doped tin oxide

List of Abbreviations

g	Gram
h^+	Hole
h	Hour
HER	Hydrogen evolution reaction
HKUST	Hong Kong University of Science and Technology
HMT	Hexamethylenetetramine
HOMO	Highest occupied molecular orbital
HPA	Hybrid Pixel Array
HPC	Hybrid Photon Counting
HPOM	Heteropolyoxometalates
HSAB	Hard and Soft (Lewis) Acids and Bases
Hz	Hertz
IRMOF	Isorecticular Metal Organic Framework
IPOM	Isopolyoxometalates
i-PrOH	Isopropanol
J	Joule
K	Kelvin
L	Linker
l	Layering
LMCT	Ligand-Metal Charge Transfer
Ln	Lanthanide

List of Abbreviations

LSV	Linear sweep voltammetry
LUMO	Lowest unoccupied molecular orbital
mM	Millimolar
M	Molar
MB	Methylene blue
MeCN	Acetonitrile
MeOH	Methanol
MHz	Megahertz
MIL	Matériaux de l'Institut Lavoisier
min	Minute
mL	Millilitre
mmol	Millimol
MOF	Metal Organic Framework
NENU	Northeast Normal University
nm	Nanometre
NMR	Nuclear Magnetic resonance
OAc	Acetate
OER	Oxygen evolution reaction
o.n.	Overnight
O _t	Terminal oxygen
PBU	Primary building unit
POM	Polyoxometalate
ppm	Parts per million
Pre	Precursor
r.t.	Room temperature

List of Abbreviations

PXRD	Powder X-ray diffraction
py	Pyridine
R	Gas constant
R-BDC	R group (such as Br-, NH ₂ -, etc.) functionalised BDC
RE	Rare earth
RhB	Rhodamine B
s	stirring
SBU	Secondary building unit
SCXRD	Single crystal X-ray diffraction
simu	Simulated
T	Temperature
TBA	Tetrabutylammonium
TCO	Transparent conducting oxide
TEAH ₃	Triethanolamine
TM	Transition metal
TMS	Tetramethylsilane
Tris	Tris(hydroxymethyl)methane
UV	Ultraviolet
V	Volt
vis	Visible
XRD	X-ray diffraction
z	Number of electrons

List of Abbreviations

The nomenclature used in this thesis is based on the Chemical Abstracts^a and on the guidelines recommended by the IUPAC-IUB Commission^b. Technical terms are written in italics.

^a *Chemical Abstracts*, Index Guide, 77.

^b IUPAC Commission on Nomenclature of Organic Chemistry (CNOC) und IUPAC-IUB Commission on Biochemical Nomenclature (CBN), Tentative Rules for Carbohydrate Nomenclature, *Biochemistry* **1971**, 10, 3983-4004; *Eur. J. Biochem.* **1971**, 21, 455-477.

Conversion of energy units: $1 \text{ eV} = 1.602 \cdot 10^{-19} \text{ J} = 11604.52500617 \text{ K} = 1239.84193 \text{ nm} = 8065.54429 \text{ cm}^{-1} = 3.288465396(20) \cdot 10^{15} \text{ Hz}$

1 HISTORICAL BACKGROUND

In 1826, Berzelius reported the formation of a dark grey precipitate on mixing aqueous solutions of MoCl_5 and Na_2HPO_4 .¹ The resultant powder turned into a black solution on addition of aqueous ammonia. The molecular structure of this compound could not be determined since X-ray crystallography was first established in the early 1900's. In 1933, the crystal structure of the polyanion was formulated as $\text{H}_3[\text{PMo}_{12}\text{O}_{40}] \cdot 5\text{H}_2\text{O}$ by Keggin and was named after him.² The progression of single crystal X-ray diffraction plays a crucial role in the development of POM chemistry and since then many other structures based on V, Nb, Ta, Cr, Mo and W have been determined and reported.^{3,4} Applications for POMs include catalysis,⁵⁻⁸ medicine,⁹⁻¹¹ and battery materials.^{6,12}

In 1913, Werner was the first inorganic chemist receiving the Nobel Prize "in recognition of his work on the linkage of atoms in molecules by which he has thrown new light on earlier investigations and opened up new fields of research especially in inorganic chemistry."¹³ With his work, he paved the way for nowadays' coordination chemistry and thus of coordination polymers termed by Bailar in 1964.¹⁴ Such coordination polymers may be 1-, 2- or 3-dimensional materials constructed from coordination complexes featuring bridging ligands. Over the past few decades, this class of material has been termed Scaffolding-like materials, metal organic frameworks (MOFs), hybrid organic-inorganic materials and organic zeolite analogues with unavoidable overlap with experts on this field such as Yaghi, Robson, Long and Rowsell.^{15,16} These materials have potential applications in various fields such as gas storage,¹⁷⁻¹⁹ separation,^{18,20} (enantioselective) catalysis,^{17,18,21} magnetism,²² proton conduction,²³ drug delivery^{24,25} and nonlinear optical materials.^{17,18,20,22,25}

The combination of the aforementioned two classes of material results in the designation POMOF, firstly reported by Hasuhalter *et al* in 1997.²⁶ This new

1. Historical Background

material has the potential to combine the properties of POMs with those of porous frameworks.

2 MOTIVATION AND OBJECTIVE

Coordination Polymers (CPs), also called MOFs, consist of organic building blocks (so-called linkers) and inorganic building blocks (so-called secondary building units (SBUs)) forming 3D porous frameworks. Here, the linkers contain functional groups, such as carboxylate,^{21,27} amine²⁸, pyridyl,²¹ nitrile,²⁹ sulfonate²⁹ or phosphonate³⁰, coordinating to the SBUs, which may be based on Zn,^{27,28} Ni,³⁰ Cu,^{21,31} Na,²⁹ Ag,²⁹ Mg,²⁸ Fe,³² Cr¹⁷ or other metals ions and thus building up a network. Nowadays, many time honoured compounds, such as Prussian Blue and Hofmann clathrates are part of the class of coordination polymers.^{33,34} Due to the fact that Prussian Blue has pores, it has a much lower density compared to FeO.³⁵ Although in Prussian Blue the organic linker is relatively small, this is sufficient to consider this material as a MOF. This leads to the consideration of how the properties of the resulting 3D network can be influenced by modifying the building units. When examining the ligands in the two compounds Prussian Blue and FeO, it is noticeable that the cyanide ion is longer than an oxo ligand, which explains the porosity of Prussian Blue. This results in the assumption that the surface area of a framework can be adjusted by the length of the linker. Extending a linker in a coordination network decrease the density in two ways – organic moieties are lighter than most metal ions and the creation of larger spacers decrease the proportion of the heavier metal atoms.

Since it is already known that a large number of POMs are electrocatalytically active, they are potential candidates for electrode materials. However, there are some drawbacks linked to high solubilities and low surface areas of POMs. These kinds of issues can be solved by introducing suitable organic ligands, whereby the solubility of the frameworks in aqueous solutions decreases and by building up a framework also the surface area of the compound increases. A combination of POMs and MOFs result in polyoxometalate-based metal organic frameworks, so-

2. Motivation and Objective

called POMOFs.^{36,37,38} These compounds may combine and/or improve the properties of POMs and MOFs. Until now, as shown in Figure 2.1, three subgroups of POMOFs are known in literature: (a) POMs occupy the cavities of a MOF structure (POM@MOF),³⁹⁻⁴² (b) POMs used as SBUs in the network^{36,37,43,44,45} and (c) POMs as part of the linker of the framework.^{46,47}

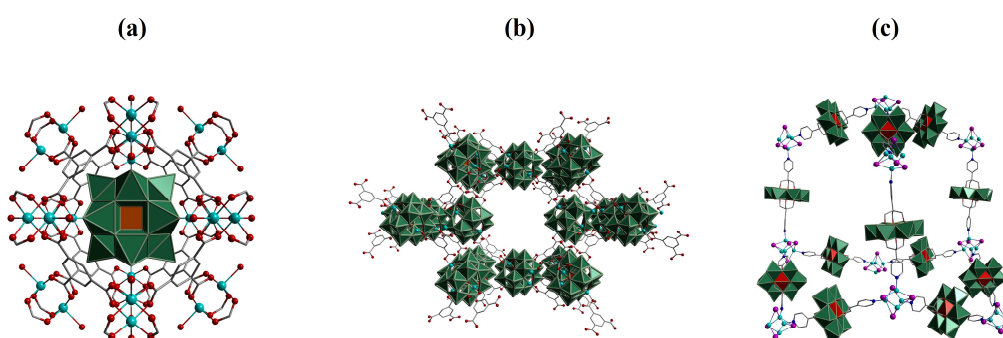


Figure 2.1: (a) POM@MOF structure published by Su et al.⁴⁸, colour code: Cu: light blue, O: red, C: grey wire/tick, Keggin polyanions: green polyanion with orange polyhedral model; (b) Keggin ions as SBUs in an organic-inorganic framework published by Dolbecq et al.³⁷, colour code: Zn: light blue, O: red, C: grey wire/stick, Keggin polyanions: green polyhedral models and (c) Anderson-Evans POMs as part of the linker of the framework published by Yang et al.⁴⁷, colour code: Cu: light blue, I: violet, O: red, C: grey wire/stick, N: blue, Anderson-Evans polyanions: green ring with red polyhedral models.

This field of research is still in its infancy but currently getting an increasing amount of attention due to emergent applications in many fields such as catalysis,^{42,47,49} proton conduction,^{50,51} sorption⁴¹ and electrode materials.³⁷

Since the POMs as linkers approach is the least explored area of POMOF chemistry and its formation of the product is predictable compared to the other approaches, this was chosen as the basis for the research presented in this thesis.

3 INTRODUCTION

3.1 Polyoxometalates

Polyoxometalates (POMs) are anionic metal oxide clusters composed of transition metals (so-called metal addenda atoms $M = W, Mo, Nb, V$ and Ta) in high oxidation states.^{4,37} Since the first report of a POM $[PMo_{12}O_{40}]^{3-}$ by Berzelius in 1826,¹ the application of polyoxometalates in different areas such as catalysis,⁵⁻⁸ medicine⁹⁻¹¹ and as electrode materials^{6,12} amongst many others have been developed. In an alkaline-aqueous medium, metal ions M^{n+} with oxidation states of 5+ and 6+ and an ionization energy of 50 to 80 eV form monomeric tetraoxoanions $[MO_4]^{3-}$ and $[MO_4]^{2-}$.⁴ Under acidic conditions, however, M^{n+} ions initially form mixed oxo-hydroxo species that later react by polycondensation to form polyoxometalates. Not only does the pH have an influence on the formation of POM structures, but also the concentration of the reactants, counterions and temperature are responsible for the shape of POMs.^{52,53} Generally, POMs are built from MO_6 octahedral units (so-called addenda octahedra) that are linked through edge-, corner- or face-sharing units, whereas the last case is rare due to the repulsion of the metal centres (see Figure 3.1).⁴ In the initial phase of the formation of MO_6 units ($M = V, Nb, Ta, Mo$ and W), the coordination state of the metal ions increase from four to six, whereby the metal atom is coordinated to six oxygen atoms.⁴ In the case of links via shared edges, the structure can be stabilised by avoiding the electrostatic repulsion between metal atoms due to the location of metal atoms far from one another.⁴

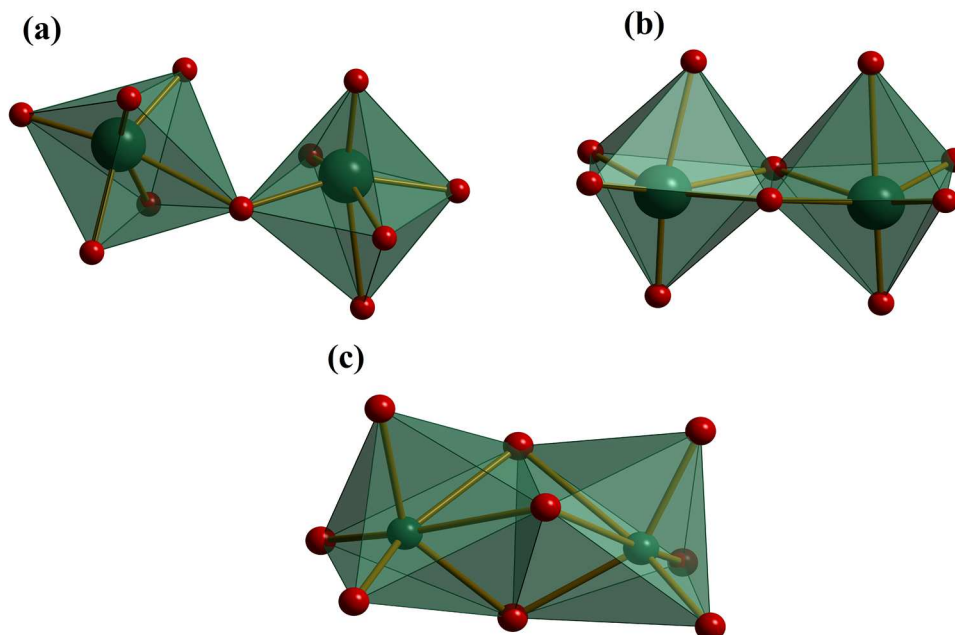


Figure 3.1: The three possible unions between two MO_6 octahedral units. (a): corner-sharing, (b): edge-sharing and (c): face-sharing. Each corner represents an oxygen position.

With increasing grade of condensation, it becomes progressively difficult for the metal ions to avoid electrostatic repulsion, whereby, the linking by edges ceases.⁵⁴ However, another explanation for this behaviour is that, i.e. for Mo^{6+} and W^{6+} the terminal oxygen atoms are strongly π -bound.⁴ Terminal oxygen atoms are not *trans* to each other regarding competition of the same t_{2g} -metal orbital.⁴ Thus, each terminal oxygen atom is opposite to a bridging oxygen atom, whereby, the metal atom is located to the terminal oxygen (*trans*-effect). Furthermore, the localization of two metal atoms is due to electric repulsion between these metal centres. Due to the π -bond to the terminal oxygen, the affinity to neighbouring metal ions is reduced. Additionally, Lipscomb and co-workers discovered that no MO_6 octahedron in POMs have more than two terminal oxygen atoms.⁴ Figure 3.2 shows the Lindqvist polyanion with its metal, terminal and bridging oxygen atoms.

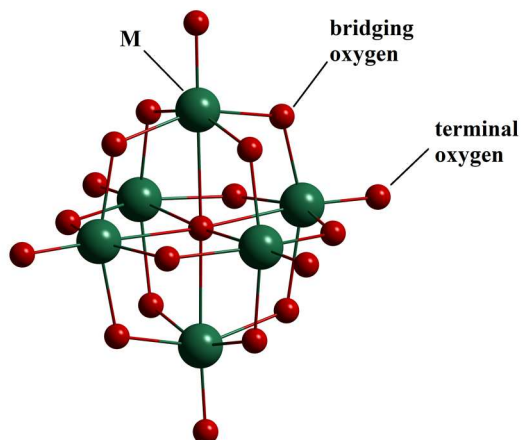


Figure 3.2: Ball-and-stick representation of the Lindqvist polyanion with its terminal and bridging oxygen atoms.

3.1.1 Classification of POMs

3.1.1.1 Iso- and heteropolyoxometalates

In general, polyoxometalates can be subdivided into two groups: isopolymetalate (IPOM) ($[M_mO_y]^{p-}$ with $M = Mo, W, V, Nb$ and Ta) and heteropolymetalate (HPOM) ($[X_xM_mO_y]^{q-}$ with $x \leq m$, in which X is a heteroatom, i.e. $Co, Al, Fe, Ga, Si, Ge, P, As, V$, and S).^{4,55,56} Amongst the IPOM metals, Mo^{6+} and W^{6+} are more easily studied since they form $d\pi-p\pi-M-O$ -bonds more readily than the other metals, such as their ionic radius and charge issues.⁵⁷

As aforementioned, in 1826, Berzelius reported the synthesis of the first POM formulated as $H_3[PMo_{12}O_{40}] \cdot 5H_2O$ by Keggin in 1933.^{1,2} This Polyoxometalate is in the subclass HPOM. To date, more than 70 elements (except the noble gases), which can function as heteroatoms, have been reported.⁵⁸ Here, the heteroatoms may be tetrahedral, octahedral, square-antiprismatic or icosahedral coordinated. A HPOM containing only one heteroatom is called a mononuclear complex. In the case of two heteroatoms, it is called a binuclear complex. The term "ternary HPOM"

3. Introduction

means that the complex contains one type of heteroatom and two different poly atoms (also called mixed HPOM).^{4,59} The following Table 3.1 shows examples for different classes of polyoxometalate based materials.

Table 3.1: Examples for different kinds of POMs.^{60,61}

Class of POM	Examples
Isopolyanions	$[V_4O_{12}]^{4-}$, $[Nb_6O_{19}]^{18-}$, $[Ta_6O_{19}]^{8-}$, $[Cr_4O_{13}]^{2-}$, $[Mo_7O_{24}]^{6-}$, $[Mo_8O_{26}]^{4-}$, $[Mo_{36}O_{112}(H_2O)_{16}]^{18-}$, $[W_6O_{19}]^{2-}$, $[W_7O_{24}]^{6-}$, $[H_2W_{12}O_{42}]^{10-}$
Heteropolyanions	$[PW_{12}O_{40}]^{3-}$, $[H_7P_8W_{48}O_{184}]^{33-}$, $[P_2W_{18}O_{62}]^{6-}$, $[PV_{14}O_{42}]^{9-}$, $[MnMo_9O_{32}]^{6-}$
Isopoly- and Heteropolyanions with mixed metal addenda atoms	$[Nb_2W_4O_9]^{4-}$, $[PV_2Mo_{10}O_{40}]^{5-}$

3.1.1.1.1 Lindqvist Anion $[M_6O_{19}]^{p-}$

An example for an IPOM is the Lindqvist $[M_6O_{19}]^{p-}$ anion ($M = Mo^{6+}$, W^{6+} , $p = 2$; $M = V^{5+}$, Nb^{5+} , Ta^{5+} , $p = 8$) made up of 6 edge-sharing octahedral units resulting in an expanded octahedron of O_h symmetry (see Figure 3.3).⁶²⁻⁶⁴ This compound can be further used as starting material for the synthesis of other POMs.⁶⁵

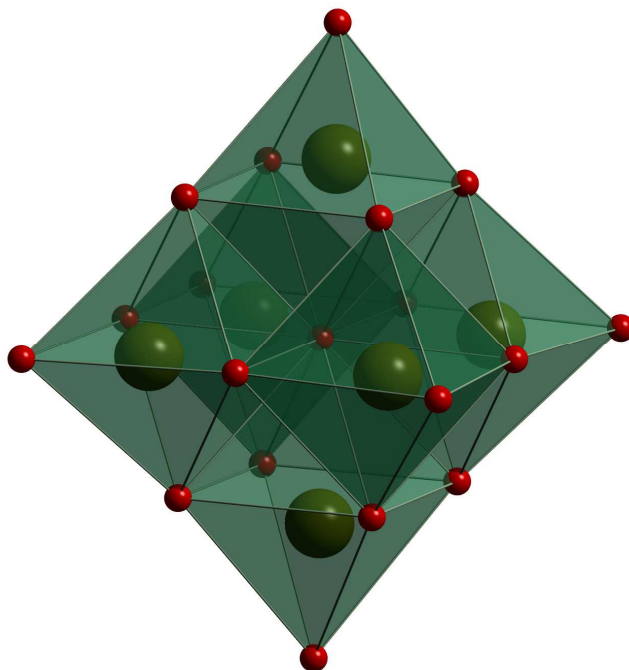


Figure 3.3: Lindqvist hexatungstate anion $[M_6O_{19}]^{2-}$.

3.1.1.1.2 Octamolybdate $[Mo_8O_{26}]^{4-}$

There are in total six isomers (α , β , γ , δ , ϵ , ξ) of octamolybdates known, whereby the most stable ones are the α - and β isomers.⁵² The case of the isomers of the octamolybdate demonstrates a good example for the effect of counterions on the shape of the polyanion. Since the α isomer is formed using large organic cations at pH = 3 - 4, the β isomer is mainly formed utilizing small counterions at pH = 2. In the following only the α isomer will be discussed. The α isomer, shown in Figure 3.4, consists of a ring of six MoO_6 edge shared octahedral bicapped MoO_4 tetrahedra resulting to a polyanion with symmetry close to D_{3d} . Amongst others, this compound is used as precursor for the synthesis of Mn^{3+} and Fe^{3+} based Anderson-Evans POMs (see section 3.1.1.2.1.1).⁶⁶

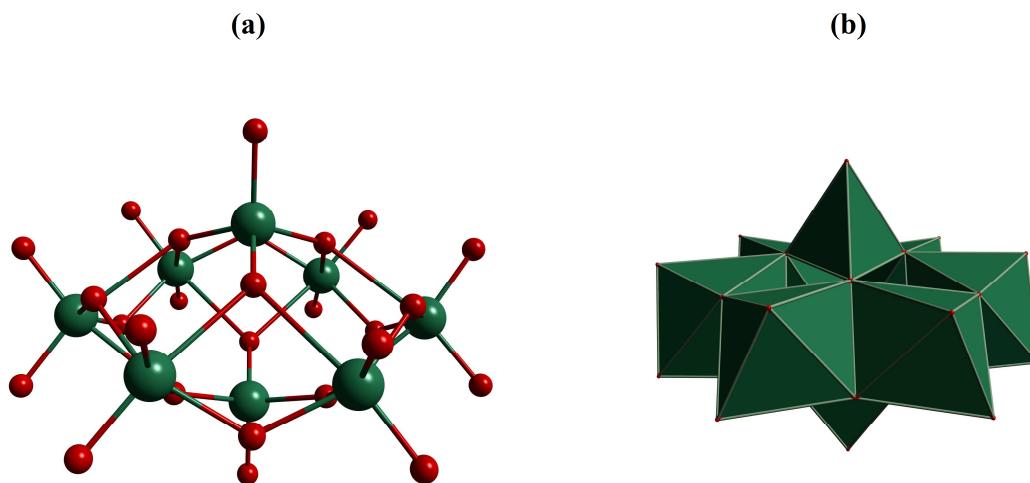


Figure 3.4: $[\alpha\text{-Mo}_8\text{O}_{26}]^{4-}$: (a): Ball-and-Stick and (b): polyhedral representation. Colour code: addenda atom Mo/octahedron: turquoise sphere/octahedron and O: red sphere.

3.1.1.2 Examples of heteropolyoxometalates

3.1.1.2.1 Anderson-Evans polyanion $[\text{X}(\text{OH})_6\text{M}_6\text{O}_{18}]^{n-}$

The Anderson-Evans polyoxometalate has a planar structure as shown in Figure 3.5. It is composed of six edge-shared addenda octahedra (MO_6) with a central octahedron heteroatom X. In this polyanion, X is connected to metal addenda atoms M via six triple-bridging $\mu_3\text{-O}$ atoms forming the central octahedron. Using $\mu_3\text{-}$ and double-bridging $\mu_2\text{-O}$ atoms, the metal addenda atoms are linked to each other. Including terminal O_t atoms, the octahedra of the metal addenda atoms are completed. In general, the Anderson-Evans structure can be divided into two subclasses: the non-protonated *A*-Type with the general formula $[\text{X}^{n+}\text{M}_6\text{O}_{24}]^{(12-n)-}$ which has the central heteroatom in high oxidation states (e.g. Te^{6+} ,⁶⁷ I^{7+} ,⁶⁸ $\text{M} = \text{Mo}^{6+}$ or W^{6+}) and the protonated *B*-Type with the general formula $[\text{X}^{n+}(\text{OH})_6\text{M}_6\text{O}_{18}]^{(6-n)-}$ with heteroatoms in low a oxidation state (such as Al^{3+} ,⁶⁹ Cr^{3+} ,⁷⁰ Fe^{3+} ,⁷¹ $\text{M} = \text{Mo}^{6+}$ or W^{6+}).⁷²

3. Introduction

In the *B*-Type, the six protons are located at the six μ_3 -O atoms at the heteroatom's octahedron, meaning that there are three μ_3 -OH groups triangularly above and three μ_3 -OH groups triangularly below the plane of the POM at the heteroatom X with the triangles in an antiprismatic (octahedral) arrangement (Figure 3.6).

The symmetry of the Anderson-Evans structure is D_{3d} . Numerous Anderson-Evans POMs containing heteroatoms with oxidation states from 2+ to 7+ are reported and summarised in Table 3.2.

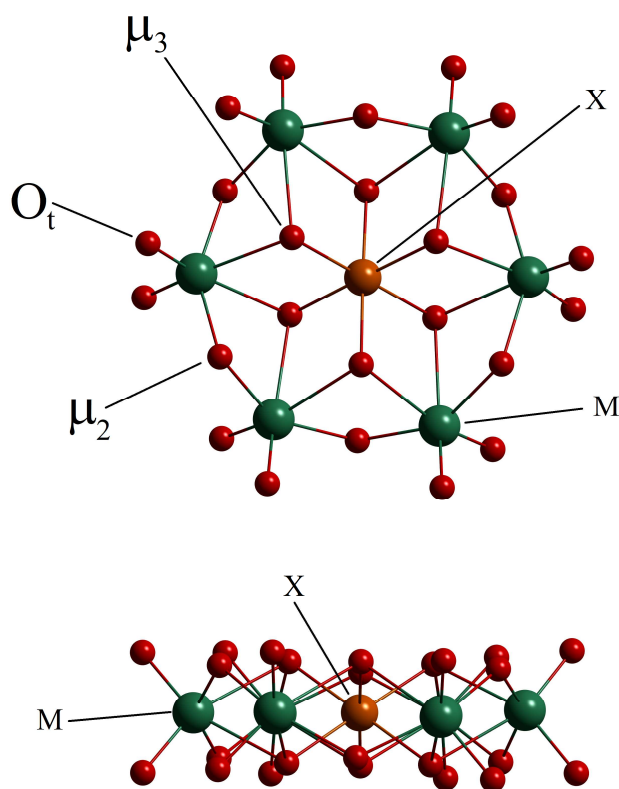


Figure 3.5: Anderson-Evans POM anion $[XM_6O_{24}]^{n-}$ seen from a top view (top) and a side view (bottom). Colour code: Heteroatom X: orange sphere/octahedron, addenda atom/octahedron: M turquoise sphere/octahedron and O: red sphere.

3. Introduction

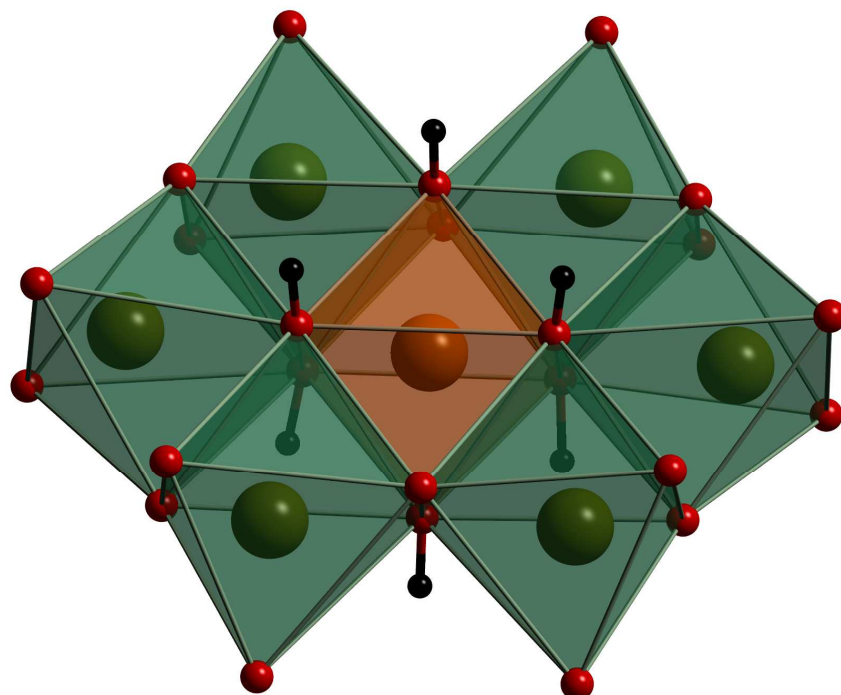


Figure 3.6: B-Type Anderson-Evans POM with six protons located at the six μ_3 -O atoms at the heteroatom's octahedron. Colour code: Heteroatom X: orange sphere/octahedron, addenda atom/octahedron: M turquoise sphere/octahedron, O: red sphere, H: black sphere.

Table 3.2: Examples for different Anderson-Evans POMs with oxidation states from 2+-7+ and associated references.

Heteroatom	Anderson-Evans POM	ref.
Te ⁶⁺	[TeW ₆ O ₂₄] ⁶⁻	67
I ⁷⁺	[IMo ₆ O ₂₄] ⁵⁻	68
Al ³⁺	[Al(OH) ₆ Mo ₆ O ₁₈] ³⁻	69
Cr ³⁺	[Cr(OH) ₆ Mo ₆ O ₁₈] ³⁻	70
Pt ⁴⁺	[Pt(OH) ₃ W ₆ O ₂₁] ⁵⁻	73
Mn ⁴⁺	[MnW ₆ O ₂₄] ⁸⁻	74
Sb ⁵⁺	[SbW ₆ O ₂₄] ⁷⁻	75
Zn ²⁺	[Zn(OH) ₆ Mo ₆ O ₁₈] ⁴⁻	76

Table 3.2 continue:

Heteroatom	Anderson-Evans POM	ref.
Cu ²⁺	[Cu(OH) ₆ Mo ₆ O ₁₈] ⁴⁻	77
Ni ²⁺	[Ni(OH) ₆ Mo ₆ O ₁₈] ⁴⁻	78
Pt ⁴⁺	[Pt(OH) ₆ Mo ₆ O ₁₈] ²⁻	79
Co ³⁺	[Co(OH) ₆ Mo ₆ O ₁₈] ³⁻	80
Rh ³⁺	[Rh(OH) ₆ Mo ₆ O ₁₈] ³⁻	81
Ga ³⁺	[Ga(OH) ₆ Mo ₆ O ₁₈] ³⁻	82
Te ⁶⁺	[TeMo ₆ O ₂₄] ⁶⁻	83

In the case of [IMo₆O₂₄]⁵⁻ and [TeMo₆O₂₄]⁶⁻, John Stuart Anderson attributed these structures to the [MoO₆Mo₆O₁₈]⁶⁻ type, but the shape of both types of structures differs.⁴ Aforementioned, [X(OH)₆M₆O₁₈]ⁿ⁻ has a planar structure, but in the case of [MO₆M₆O₁₈]ⁿ⁻ (M = Mo, W), it has a tub-shape structure (see Figure 3.7) because it does not contain a heteroatom, it belongs to the group of IPOMs.^{84,85}

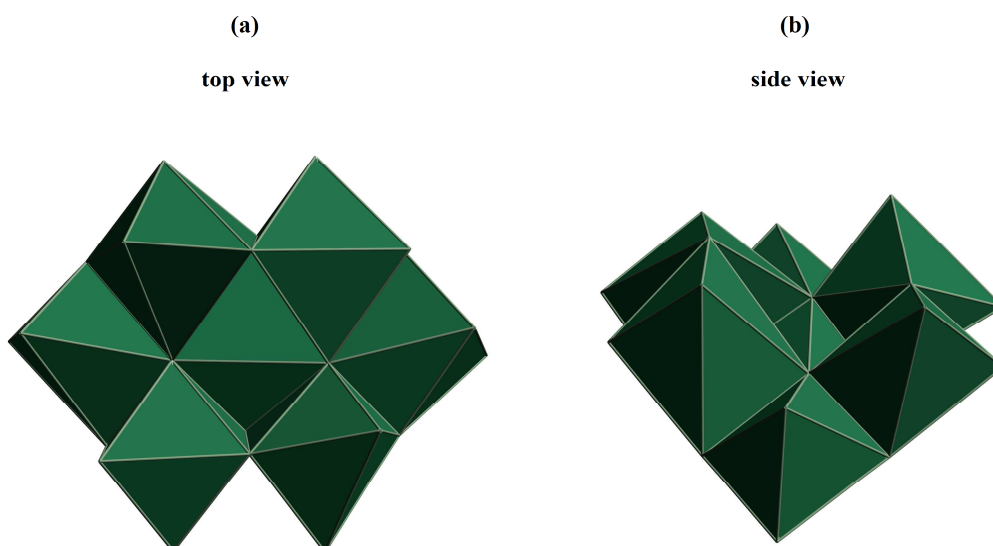


Figure 3.7: Tub-shaped structure of [MoO₆Mo₆O₁₈]⁶⁻, polyhedral representation seen from a top view (a) and a side view (b).

The motif of the Anderson-Evans structure is not only present in POM chemistry, but also occurs in other areas such as cationic clusters. An example is $[\text{Al}_7(\text{OH})_{12}(\text{H}_2\text{O})_{12}]^{9+}$, where a ring of six Al^{3+} is surrounding a central Al^{3+} ion.⁸⁶ The hydroxyl groups in this structure are both μ_2 and μ_3 oxygen atoms in this Anderson-Evans motif. The 12 H_2O molecules coordinate to the addenda atoms and replace the terminal oxygen atoms.

3.1.1.2.1.1 The inorganic-organic Anderson-Evans polyoxometalate hybrid

As previously mentioned, the protonated *B*-Type Anderson-Evans POM contains six protons situated at the six $\mu_3\text{-O}$ atoms at the heteroatom's octahedron. Introducing organic tris(hydroxymethyl)methane ligands $((\text{OHCH}_2)_3\text{CR})$ (Tris-R), each of the three protons above and below the plane of the POM can be substituted by the organic ligand (see Figure 3.8).⁷² In principle, the group R can be any imaginable group such as $-\text{NH}_2$, $-\text{OH}$, $-\text{CH}_2\text{OH}$, $-\text{Aryl}$ and further derivatives of imines and amides. So far, three approaches to achieve modified Anderson-Evans POMs have been reported: (I) The Tris-ligands are synthesized first, followed by a condensation reaction in order to attach them to the POM (*pre*-functionalization), (II) the Tris-ligands, $[\alpha\text{-Mo}_8\text{O}_{26}]^{4-}$ and a metal salt (such as $\text{Mn}(\text{OAc})_3$ or $\text{Fe}(\text{acac})_3$) are used as starting materials and form the POM hybrid and (III) the Tris-ligands, which are already grafted onto the POM can be further modified by organic reactions such as amidation and Schiff base reaction (*post*-functionalization).^{72,87} The $[\alpha\text{-Mo}_8\text{O}_{26}]^{4-}$ precursor (section 3.1.1.1.2) in approach (II) already contains the ring of six MoO_6 edge shared octahedra. The bicapping MoO_4 tetrahedra can be replaced by Mn^{3+} or Fe^{3+} ions by introducing them in the plane of the ring, thus forming the Anderson-Evans structure.

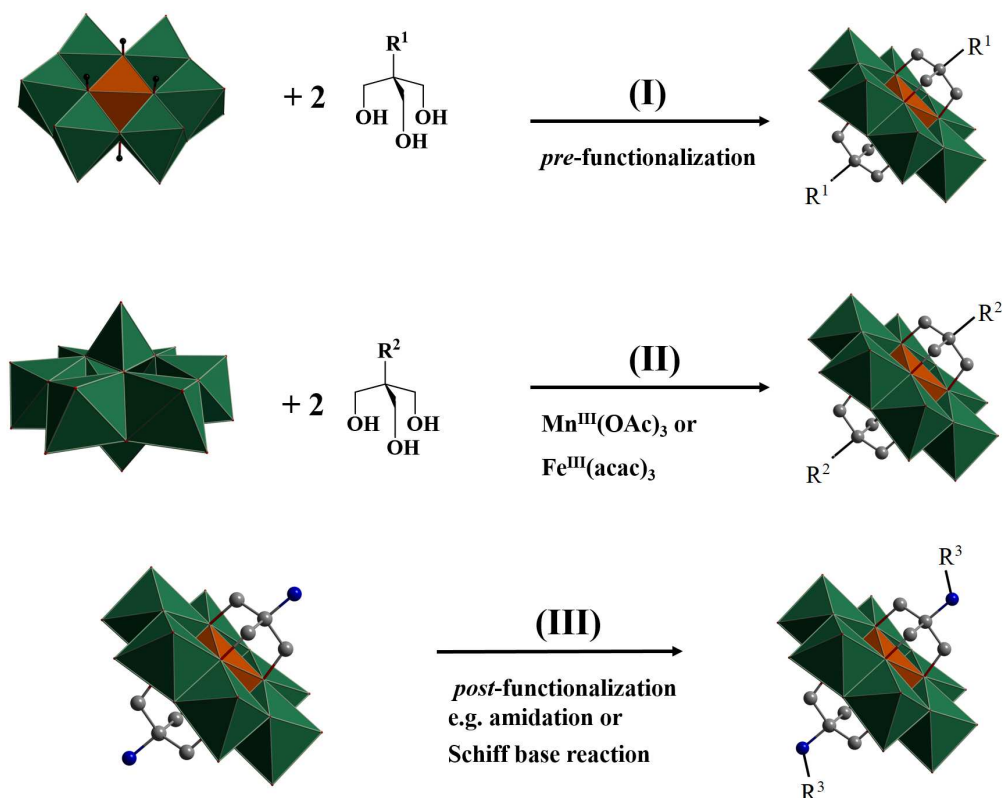


Figure 3.8: The three approaches to synthesizing Anderson Evans-hybrids: (I) pre-functionalization; (II) reaction of $[\alpha\text{-Mo}_8\text{O}_{26}]^{4-}$, metal salt and ligand; (III) post-functionalization. Colour code: Heteroatom-octahedron XO_6 : orange octahedron, addenda octahedron MO_6 : turquoise octahedron, C: grey, H: black, N: blue, R: = $-\text{NH}_2$, $-\text{OH}$, $-\text{CH}_2\text{OH}$, $-\text{Aryl}$ and further derivatives of imines and amides. (H atoms are omitted for clarity, except in the case of (I) for protonated Anderson-Evans anion.)

3.1.1.2.2 Keggin polyanion $[\text{XM}_{12}\text{O}_{40}]^n-$

The Keggin polyanion is in the subclass HPOM and consists of twelve MO_6 octahedra, surrounding a tetrahedrally coordinated heteroatom $[\text{XO}_4]$.⁵³ In other words, this $[\text{XO}_4]$ unit is encapsulated by four $[\text{M}_3\text{O}_{13}]$ units (“triads”) which are linked by corner sharing to each other and to the central $[\text{XO}_4]$ tetrahedron.⁴ The metal addenda atoms for most of the Keggin polyanions are molybdenum and tungsten. There is a number of reports of possible heteroatoms known, including 3d transition metals and main group elements (B^{3+} , C, As^{5+} , Fe^{3+} , Co^{2+} , Co^{3+} and Cu^{2+}),

but the most commonly used are P^{5+} , Si^{4+} and Ge^{4+} .^{4,53} This type of POM has an overall symmetry of T_d (see Figure 3.9).²

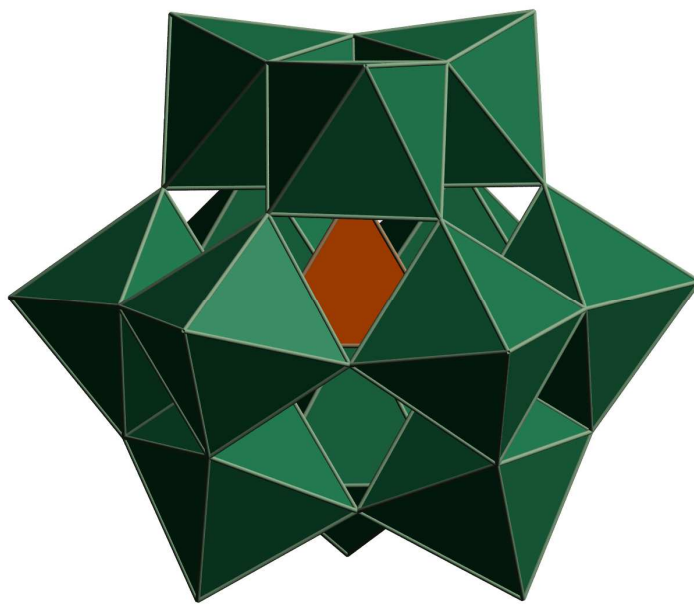


Figure 3.9: Keggin structure with tetrahedron centre surrounded by four corner shared $[M_3O_{13}]$ triads.

Depending on the metal addenda atoms molybdenum or tungsten, the T_d symmetry of the Keggin structure may differ and become i.e. D_{2d} . Furthermore, it is known that in the case of molybdenum there is a displacement in the Mo-O-Mo bonds from “short” to “long”. This difference in bond lengths reduces the symmetry based on the mirror planes of M_2 triplets.⁵⁶

3.1.1.2.3 The Wells-Dawson polyanion $[X_2W_{18}O_{62}]^{6-}$ ($X = P^V, As^V$)

In the case of the Wells-Dawson polyanions the most common heteroatoms are P^{5+} and As^{5+} .⁸⁸ The structure of the Wells-Dawson POM is formed from the direct union of two $[A-\alpha-XW_9O_{34}]^{n-}$ or two $[A-\beta-XW_9O_{34}]^{n-}$ trilacunary Keggin units (see

3. Introduction

section 3.1.3.1) through the six upper crown oxygens (see Figure 3.10). The $[\alpha\text{-X}_2\text{W}_{18}\text{O}_{62}]^{6-}$ ($X = \text{P}^{5+}, \text{As}^{5+}$) Wells-Dawson α isomer results from two $[\text{A-}\alpha\text{-XW}_9\text{O}_{34}]$ units, whereas the β isomer is obtained by the union of $[\text{A-}\alpha\text{-XW}_9\text{O}_{34}]$ and $[\text{A-}\beta\text{-XW}_9\text{O}_{34}]$ fragments. By combining two $[\text{A-}\beta\text{-XW}_9\text{O}_{34}]$ isomeric units, the γ isomer is formed. The different isomerisation of POMs will be discussed in section 3.1.2.⁸⁸

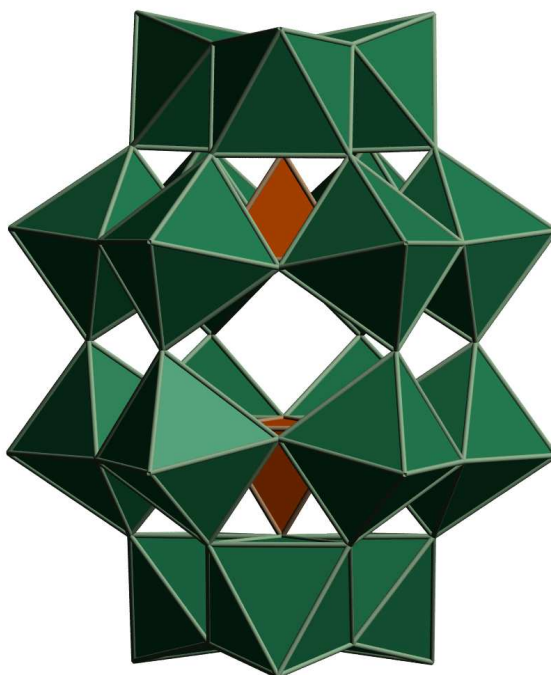


Figure 3.10: Wells-Dawson $[\alpha\text{-X}_2\text{W}_{18}\text{O}_{62}]^{6-}$ ($X = \text{P}^{5+}, \text{As}^{5+}$) polyanion.

3.1.2 Isomers of polyoxometalates

3.1.2.1 Isomers of Keggin- and Wells-Dawson-type polyoxometalate

According to the structural studies on POMs by Baker and Figgis in 1970, there are five structural isomers of Keggin polyanions (α , β , γ , δ and ϵ isomer) (see Figure 3.11).^{89,90} The α isomer represents the parent anion, whereas the β , γ , δ and ϵ isomers

3. Introduction

are generated by rotation of 1, 2, 3 and 4 $[M_3O_{13}]$ triads through 60° . The parent anion and their resulting isomers have symmetries of T_d , C_{3v} , C_{2v} , C_{3v} and T_d , respectively.⁹¹ Amongst them, the α isomer shows the highest stability, due to an increase of rotated triads reducing the stability of the structure.⁹¹ This observation results from the increase of Coulomb repulsion which hinders the $p\pi$ - $d\pi$ orbital overlapping.⁴ These isomers can be obtained by slight changes in reaction conditions, which underline the flexible nature of POMs.

Similar to the Keggin-type structures, the Wells-Dawson POM can have three structural isomers. The α isomer is the parent anion, whereas the β and γ isomers can be obtained by rotation of 1 and 2 triads through 60° , respectively.⁸⁸

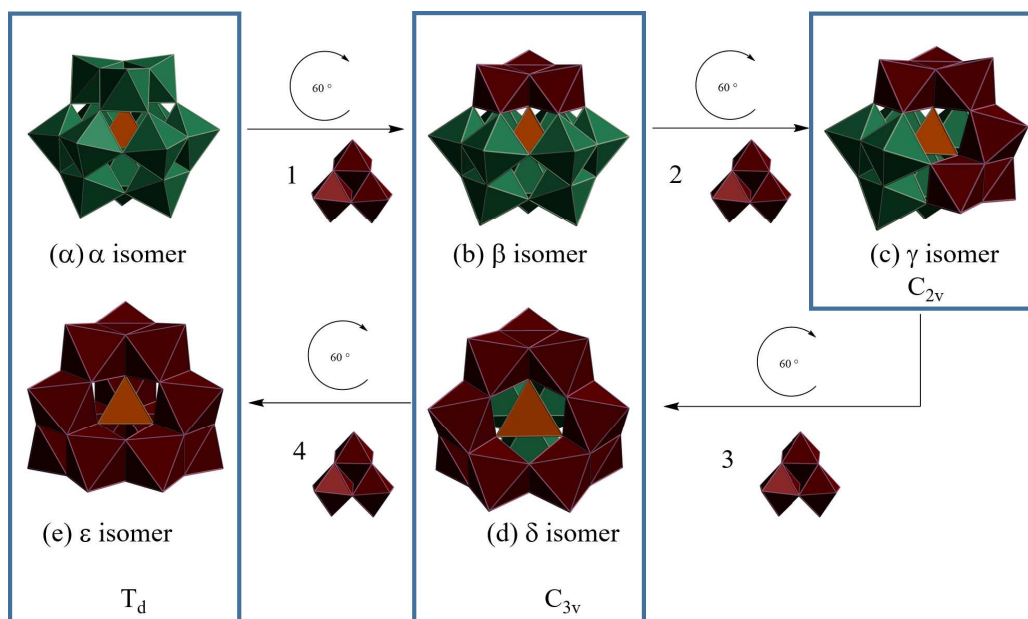


Figure 3.11: The five Baker-Figgis isomers of Keggin polyanion. Rotated $[M_3O_{13}]$ triads are represented in the dark red polyhedra.

As for the Anderson-Evans structure, there is also a famous Al based analogous cation to the ϵ -Keggin structure $[\epsilon\text{-AlO}_4\text{Al}_{12}(\text{OH})_{24}(\text{H}_2\text{O})_{12}]^{7+}$ (“Al₁₃”) discovered by Johansson *et al.*⁴ The central AlO_4 tetrahedron is connected to twelve

surrounding AlO_6 octahedra via edge-shared hydroxyl groups and the octahedral corners are occupied by H_2O molecules.

3.1.3 Lacunary derivatives of polyanions

Lacunary derivatives of parent anions can be achieved by removing a various number of octahedra under different reaction conditions. Lacunary species can be obtained from α , β and γ isomers.⁹¹⁻⁹³ In this thesis, only the α isomer based lacunary polyanions will be discussed.

3.1.3.1 Lacunary derivatives based on the Keggin ion $[\alpha\text{-XM}_{12}\text{O}_{40}]^n$

Three possible lacunary species can be derived from a plenary $[\alpha\text{-XM}_{12}\text{O}_{40}]^n$ Keggin structure, are shown in Figure 3.12. By elimination of one octahedron, the mono-lacunary species $[\alpha\text{-XM}_{11}\text{O}_{40}]^p$ can be formed. On the other hand, the A-Type species $[A\text{-}\alpha\text{-XM}_9\text{O}_{40}]^q$ is obtained by removing a corner shared-triad. Likewise, the B-Type fragment $[B\text{-}\alpha\text{-XM}_9\text{O}_{40}]^m$ results from the removal of edge-shared triads.^{92,93}

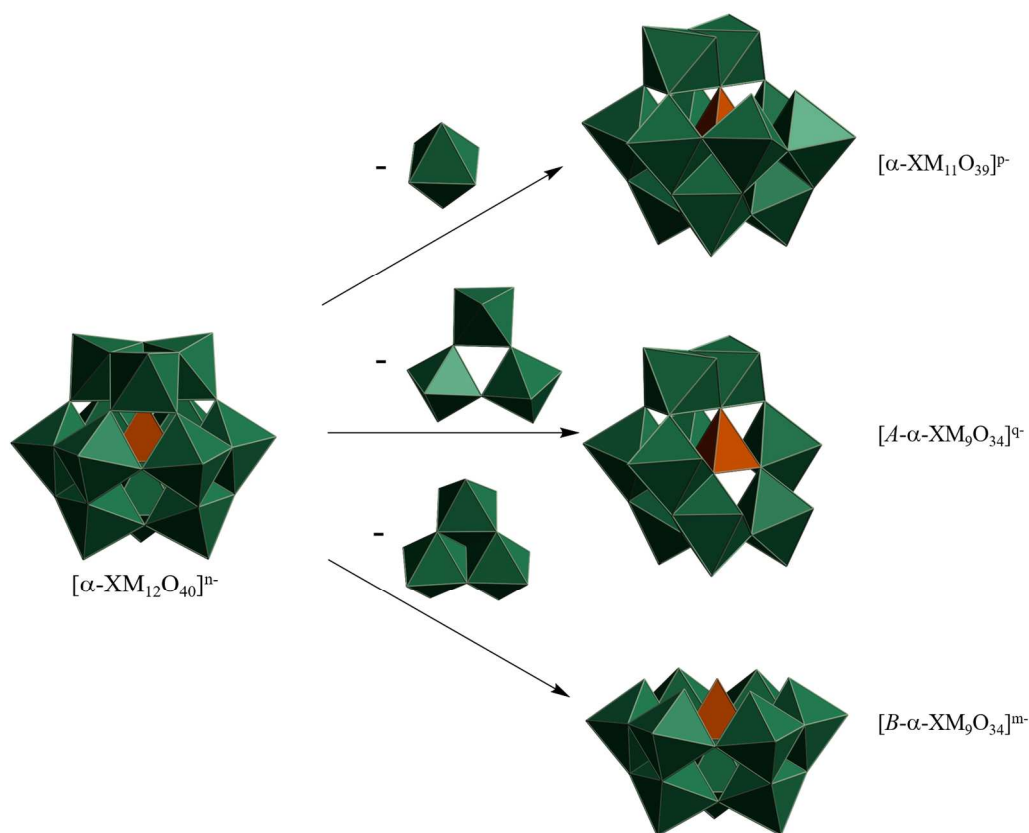


Figure 3.12: Mono- and trilacunary species derived from $[\alpha\text{-XM}_{12}\text{O}_{40}]^{n-}$ Keggin polyanion.

3.1.3.2 Lacunary derivatives based on the Wells-Dawson ion $[\alpha\text{-X}_2\text{W}_{18}\text{O}_{62}]^{6-}$

For the α -Wells-Dawson polyanion, four possible lacunary species are known. The monolacunary α_1 - and α_2 -type derivatives are formed by removing one octahedron from the belt or from the cap, respectively. The latter trilacunary species $[\text{P}_2\text{W}_{15}\text{O}_{56}]^{12-}$ (see Figure 3.13 (a)) is obtained by the removal of one $[\text{M}_3\text{O}_{13}]$ triad corresponding to a cap, whereas the hexalacunary $[\text{H}_2\text{P}_2\text{W}_{12}\text{O}_{48}]^{12-}$ (see Figure 3.13 (b)) is formed when two triads from the belt portion of the parent anion are removed.⁹⁴

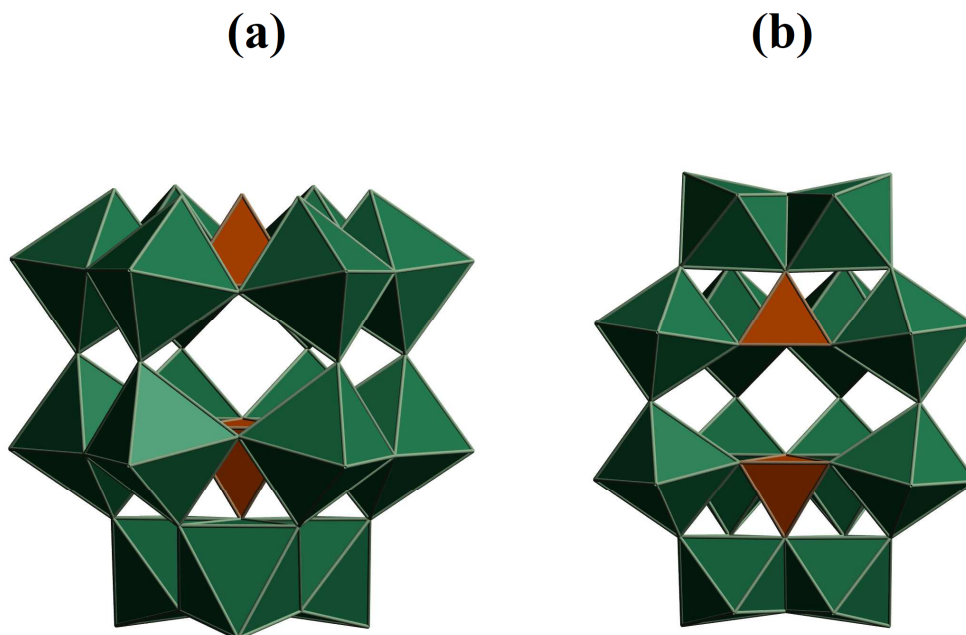


Figure 3.13: Tri- and Hexalacunary species of the α -Wells-Dawson heteropolyanions
 (a) $[P_2W_{15}O_{56}]^{12-}$, (b) $[H_2P_2W_{12}O_{48}]^{12-}$.

3.2 Metal-Organic Frameworks (MOFs)

Recently, there is a growing interest in the field of metal-organic frameworks (MOFs), resulting in an increasing number of reported structures. These materials have potential applications in various fields such as gas storage,¹⁷⁻¹⁹ separation,^{18,20} (enantioselective) catalysis,^{17,18,21} magnetism,²² proton conduction,²³ drug delivery^{24,25} and nonlinear optical materials.^{17,18,20,22,25} Metal-organic-frameworks are constructed of inorganic building blocks, so-called secondary building units (SBUs) and organic ligands (also called linkers) which generate a 3D network.

3.2.1 Primary Buildings Units (PBUs)

The term “Primary Building Units” (PBUs) comprises the organic ligands and metal atoms or polyatomic clusters, respectively.⁹⁵ The latter can be based on Zn,^{27,28} Ni,³⁰ Cu,^{21,31} Na,²⁹ Ag,²⁹ Mg,²⁸ Fe,³² Cr¹⁷ and other metals ions, whereas the linkers have essential functional groups (see section 3.2.2), in order to coordinate to the SBUs (see section 3.2.3) resulting from the metal ions.

3.2.2 Linkers for MOFs

As shown in Figure 3.14, organic ligands, which are used in MOF structures, contain coordinating functional groups such as carboxylate,^{21,27} amine²⁸, pyridyl,²¹ nitrile,²⁹ sulfonate²⁹ or phosphonate³⁰. However, there are also some ligands, which contain more than one type of functional group.

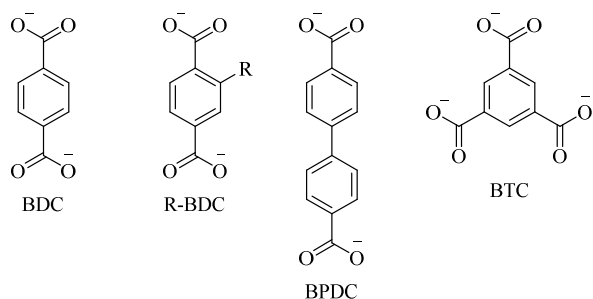
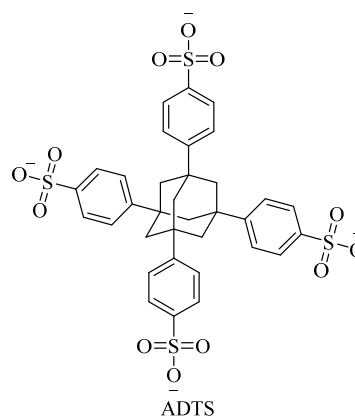
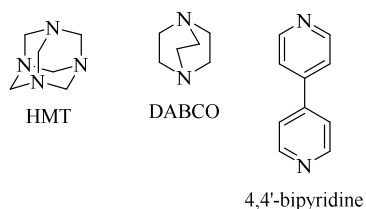
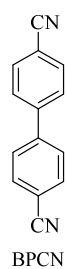
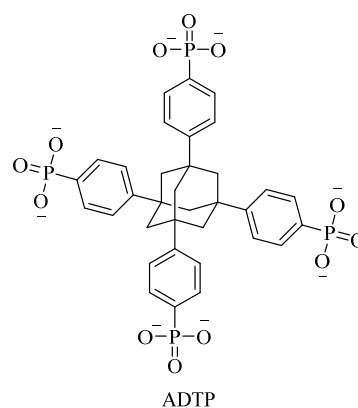
Carboxylate**Sulfonate****Amine****Nitrile****Phosphate**

Figure 3.14: Examples of organic ligands used for MOF constructions.

One representative is R-BDC, where besides the carboxylate functional groups in BDC, a Br- or NH₂-group is present in ortho position. Every linker has a given geometry of linking point, ranging from linear up to tetrahedral geometry. The abbreviation codes and the geometry of the linkers are listed in Table 3.3.

Table 3.3: Names of ligands, their abbreviation codes and associated references.

Abbreviations	Name	geometry	ref.
BDC	1,4-benzenedicarboxylate	linear	17
R-BDC	R group (such as Br-, NH ₂ -, etc.) functionalised BDC	linear	17,19
BPDC	biphenyl-4,4'-dicarboxylate	linear	17
BTC	1,3,5-benzenetricarboxylate	trigonal	17
ADTS	1,3,5,7-tetrakis(4-sulfonophenyl)adamantine	tetrahedral	96
HMT	hexamethylenetetramine	tetrahedral	97
DABCO	1,4-diazabicyclo[2.2.2]octane	linear	98
4,4'-BPY	4,4'-bipyridine	linear	99
BPCN	4,4'-biphenyldicarbonitrile	linear	97
ADTP	1,3,5,7-tetrakis(4-phosphonophenyl)adamantine	tetrahedral	96

3.2.3 Secondary Building Units (SBUs)

The metal atoms or polyatomic clusters mentioned in the notion of PBUs, form so-called Secondary Building Units (SBUs) in solution. These SBUs can be seen as junctions between linkers with a certain geometry. Figure 3.15 shows three examples for carboxylate based SBUs. The SBU, used in the isorecticular MOFs (IRMOFs)-series,¹⁷ is the Zn₄O cluster, in which a central oxygen atom is tetrahedrally coordinated by four Zn²⁺ ions. Furthermore, each Zn atom is coordinated by one O atom of three carboxylate ligands. The first report of the use

3. Introduction

of Zn_4O as SBU was established by Yaghi *et al.* in 1999.¹⁰⁰ Another example for a junction is the Cu_2 core utilized in HKUST-1, which was first reported in 1999 by Williams *et al.* where two Cu^{2+} ions are coordinated by four carboxylate ligands and two water molecules forming a paddle wheel shape node.¹⁰¹ Moreover, these two H_2O molecules can be replaced by a neutral N-donor ligand (e.g. DABCO, 4,4'-BPY) in order to expand the framework.^{98,99,102} Similar to the Zn_4O cluster in the IRMOF-series, the SBU in MIL-101 which was first reported by Margiolaki *et al.* in 2005, contains a central oxygen atom.¹⁰³ In this case, however, this central O atom is triply bridging three Cr^{3+} ions establishing a trigonal SBU. In addition, each Cr atom is further coordinated by one O atom of four carboxylate and one H_2O ligand.

However, it is not necessary that a SBU is built from multicore clusters, even single metal atoms such as Na, Ni and Ag can function as a junction.²⁹

3.2.4 Topological consideration of MOFs

The combination of the building blocks SBU and linker leads to a framework. The topology is influenced by both the structure of the SBU and of the linker. Figure 3.15 shows three examples of SBUs and the corresponding MOF structure obtained by using the associated linker.

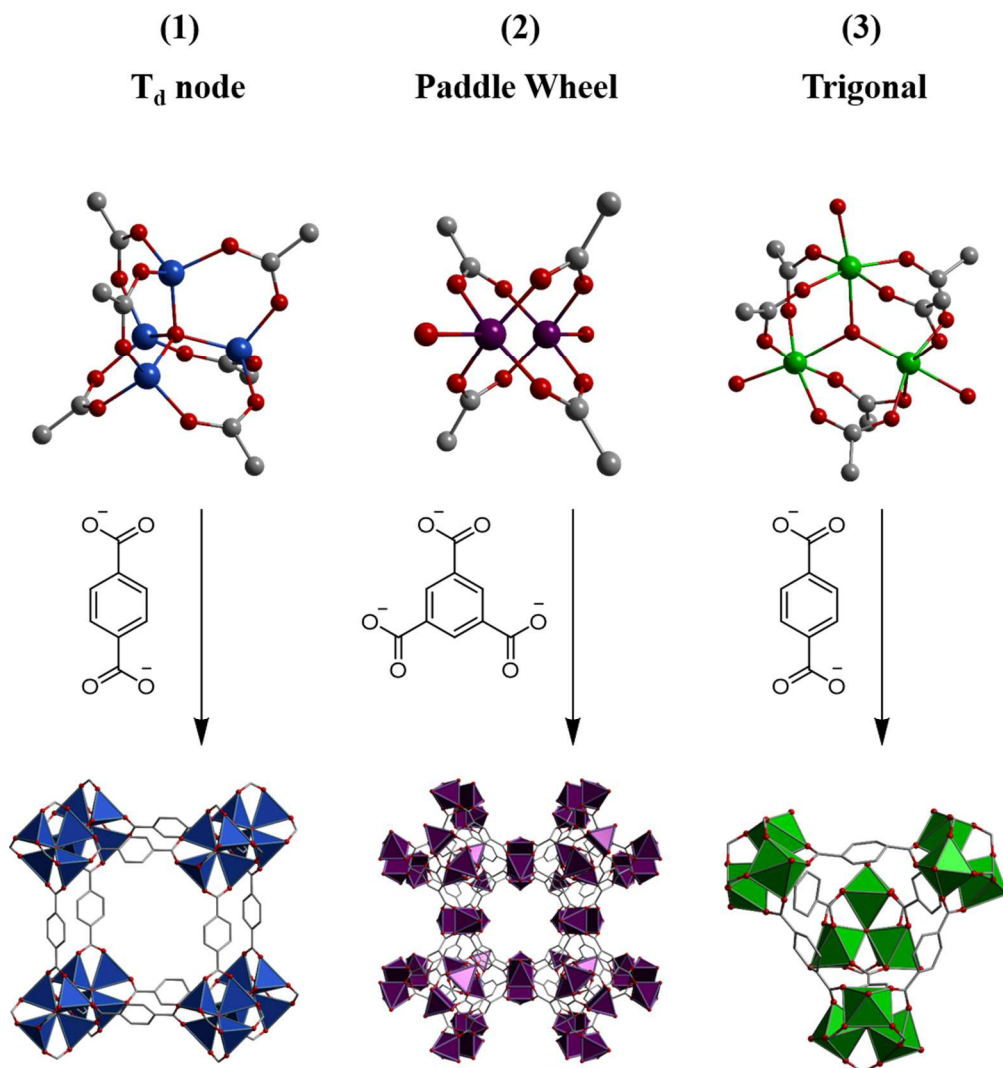


Figure 3.15: Three possible secondary building units (SBUs) and the associated linkers forming three different frameworks: (1) Zn₄O (Colour code: Zn: light blue, O: red, C: grey) and BDC forming MOF-5; (2) Cu₂(H₂O)₂ (Colour code: Cu: violet, O: red, C: grey) and BTC forming HKUST-1; (3) Cr₃O (Colour code: Cr: green, O: red, C: grey) and BDC forming MIL-101. In order to see the coordination sites, the metal cores of the SBU units are already coordinated by carboxylate groups. H atoms are omitted for clarity.

In the cases of MOF-5 and MIL-101 the utilized linker is BDC, however, the resulting topology of the two structures is different. This indicates that the choice of the SBU is essential for the topology of the framework.

By replacing BTC with BDC in HKUST-1, the resulting compound forms 2D sheets of Cu(BDC), which evidence further that the choice of the linker influences the topology of the framework.¹⁰⁴ In this case, the H₂O molecules which coordinate via the O to the Cu atom, are replaced by DMF molecules. In order to achieve a 3D structure these DMF molecules can be substituted by 4,4'-BPY or DABCO, thus providing connections between the 2D layers.

Changing the geometry of the linker within a coordination polymer is not the only option to achieve a novel structure, also extending the organic backbone of the rigid linker results in a new framework. Replacing BDC by BPDC in MOF-5 for example results in an elongated network with an isorecticular structure (so-called IR-MOF), which reveals that both structures have the same topology.¹⁰⁵ However, if the chosen organic ligand is too long, the stability of the network is reduced.¹⁰⁶ This results in catenation of frameworks, which stabilizes the overall material. There are two types of catenation: interpenetration and interweaving.^{106,107} In the case of interpenetration the networks are maximally displaced from each other by shifting the second framework exactly one half of the pore size in the *a*, *b* and *c* directions. This reduces the pore size of the material without a blockage of adsorptive sites. In interwoven frameworks, the distance between two networks is minimized without atomic overlapping, thus blocking potential adsorptive sites. This results that the topology of the resultant material can not longer be described by a single network, but how the individual frameworks are related to each other.¹⁰⁸

3.2.5 Crystal-to-crystal (CTC) (topotactic) transformation

The crystal-to-crystal (CTC) transformation of coordination polymers is an interesting topic having an effect of the dimensionality and the physical properties of the material. The crystal structure transformation can be influenced by the expansion of coordination numbers, the removal/exchange of solvent molecules

3. Introduction

and the rearrangement of bonds.¹⁰⁹ To date, a CTC transformation can be done by the change of the temperature of the MOF structure, via reactions of the framework with small molecules or by photochemical reactions.¹¹⁰

Englert *et al.* demonstrated the change of the dimensions of an 1D chain of $[\text{ZnCl}_2(\mu\text{-bipy})]_\infty$ to a 2D structure $[\text{Zn}(\mu\text{-Cl})_2(\mu\text{-bipy})]_\infty$ by cooling down the crystals below 130 K.¹¹¹ This process is reversible by warming up the compound to 360 K. Heat treating of MOF structures can cause the loss of solvent molecules, which might result in the distortion and sliding of networks, change in conformation, coordination environment or space groups.^{112–120} The removal of the solvent molecules in the pores of the network also affect the properties of the structure, such as magnetism and luminescence properties.^{121,122} Furthermore, the solvent molecules can be also reversible replaced by guest molecules or other solvent molecules.¹¹⁸

An example for the reaction of CPs with small molecules is the oxidation of Ni^{2+} to Ni^{3+} with I_2 in $[\text{Ni}_2\text{L}]_3(\text{BTC})_4 \cdot 6\text{py} \cdot 36\text{H}_2\text{O}$ (L = bismacrocylic ligand ($\text{C}_{26}\text{H}_{52}\text{N}_{10}$)) to form $[\text{Ni}_2\text{L}]_3(\text{BTC})_4(\text{I}_3)_4 \cdot n\text{I}_2 \cdot 17\text{H}_2\text{O}$, whereas the channels of the new formed networks contain I_3^- ions and I_2 molecules.¹¹⁵

The CTC transformation via photocatalytic reaction requires olefins as part of the linker in the MOF system. Under irradiation these olefins can react intermolecular in a [2 + 2] cycloaddition, resulting in a change of the network.¹²³

3.3 Polyoxometalate-based Metal-Organic Frameworks (POMOFs)

A combination of the aforementioned materials namely POMs and MOFs result in polyoxometalate-based metal organic frameworks, so-called POMOFs.^{36,37,38} These generated compounds may combine and/or improve or even have new properties

3. Introduction

which the individual components POMs and MOFs do not have. To date, three subgroups of POMOFs are known in the literature: (a) POMs occupying the cavities of a MOF structure (POM@MOF),³⁹⁻⁴² (b) POMs used as SBUs in the network^{36,37,43,44,45} and (c) POMs as part of the linker of the framework.^{46,47} Figure 3.16 illustrates these three examples of POMOFs. (a) POM@MOF system, Keggin anions occupy the hollow space in a HKUST-1 network, the so-called NENU-series, published by Su *et al.*⁴⁸ (b) Keggin ions can also be part of SBUs in a 3D-framework, as reported by Dolbecq *et al.*³⁷. (c) In order to achieve a structure where POMs are part of the linker, the Anderson-Evans anion is a good candidate, published by Yang *et al.*⁴⁷ Table 3.4 contains information of the three subgroups of POMOF systems with associated examples of POMs and references.

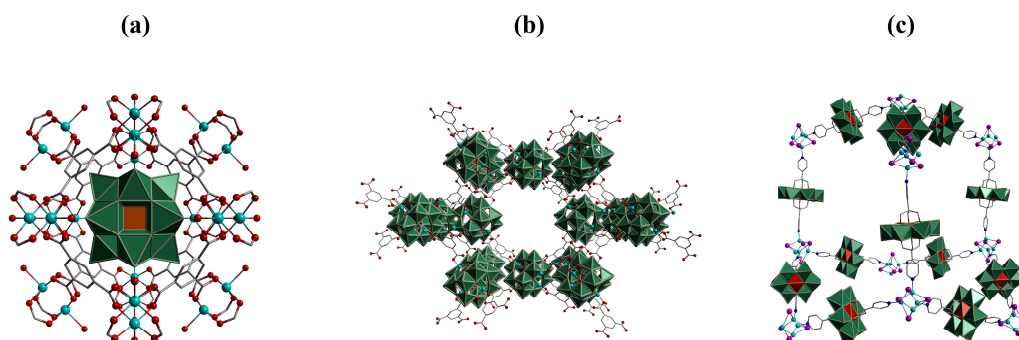


Figure 3.16:(a) POM@MOF structure published by Su *et al.*⁴⁸, colour code: Cu: light blue, O: red, C: black, Keggin polyanions green polyhedral model; (b) Keggin ions as SBUs in an organic-inorganic framework published by Dolbecq *et al.*³⁷, colour code: Zn: light blue, O: red, C: black, Keggin polyanions green polyhedral models and (c) Anderson-Evans POMs as part of the linker of the framework published by Yang *et al.*⁴⁷, colour code: Cu: light blue, I: violet, O: red, C: black, N: blue, Anderson-Evans polyanions (green ring with red polyhedral models).

Table 3.4: Table of different POMOF systems and associated references.

POM building unit	POM@MOF	POM as SBU	POM as Linker	ref.
TMS-POM(lacunary Keggin ion)	X			42
Keggin ion	X			40
Keggin ion	X			41
Lindqvist ion	X			39
Keggin ion		X		36
Keggin ion		X		37
Keggin ion		X		43
Keggin ion		X		44
Keggin ion		X		50
Keggin ion		X		124
Keggin ion		X		125
Anderson-Evans ion		X		49
TMS-POM(lacunary Keggin ion)		X		38
Wells-Dawson ion		X		45
Anderson-Evans ion			X	46
Anderson-Evans ion			X	47
Lindqvist ion			X	126

3.3.1 Properties of POMOFs

POMOF materials may have properties, which the individual components POMs and MOFs do not have. In the following, some examples of the three subgroups of POMOFs and their properties will be discussed.

3. Introduction

(a): In the case of POM@MOF, Craig *et al.* reported aerobic H₂S and thiol oxidation by taking advantage of the catalytic properties of the POM and the large surface area of the MOF in [Cu₃(C₉H₃O₆)₂]₄[{(CH₃)₄N}₄CuPW₁₁O₃₉H].⁴²

(b): In order to use POMs as SBUs in a 3D network, a bridging atom such as Ni,^{38,51,127} Zn,^{36,37,44} Cu,^{49,50,128} or Ag^{125,40,129} between the terminal oxygen atoms of the POM and the functional group of an organic linker (usually a carboxylate or an N-donor ligand) is needed. These compounds were investigated as a catalyst for the Hydrogen Evolution Reaction (HER),^{37,44} electro-catalyst for the reduction of bromate,³⁶ proton conductor⁵⁰ and photocatalyst for the reduction of rhodamine-B (RhB)¹²⁸ and methylene blue (MB),⁴⁹ respectively. Nohra *et al.* synthesised a compound with the formula (TBA)₃[PMo^V₈Mo^{VI}₄O₃₆(OH)₄Zn₄][C₆H₃(COO)₃]_{4/3}·6H₂O also called (ε(trim)_{4/3}) that shows the onset for the hydrogen evolution reaction (HER) in an (1 M LiCl and HCl (pH = 1)) medium at +20 mV.³⁷ Compared to platinum as an electrode which has an onset for HER at -242 mV, (ε(trim)_{4/3}) shows an anodic shift which means that this material is more active than Pt.³⁷

Regarding the field of hydrogen technology, Wei *et al.* reported three POMOF composites {[X(HbpdC)(H₂O)₂]₂[PM₁₂O₄₀]}ⁿ⁻ (X = Cu²⁺, Ni²⁺; M = Mo, W), which could be potential candidates for proton exchange membranes in fuel cells.^{50,51} However, compared to Nafion[®] (standard proton exchange membrane), which has an activation energy E_a of ca. 0.15 eV (when it is fully humidified), these POMOF systems exhibit a much higher activation energy of about 1 eV.^{51,50} That means, in the case of POMOFs, further investigation is needed in order to apply them as an alternative candidate to Nafion[®].

(c): The third approach is based on the use of organic-inorganic-POM hybrids, which already contain organic ligands with suitable coordination groups, thus the candidates for this purpose are Lindqvist- and Anderson-Evans-based POM hybrids. In 2008, Hasenknopf *et al.* published amongst others the hybrids [V₆O₁₃{(OCH₂)₃CCH₂OC(O)(4-C₅H₄N)}₂]²⁻ and [MnMo₆O₁₈{(OCH₂)₃CNHCO

$(4\text{-C}_5\text{H}_4\text{N})_2\text{]}^{3-}$, where these were used in a second step to coordinate to a Ru-porphyrin-derivative via the pyridyl groups.⁸⁷ Ross *et al.* also used the previously mentioned Mn-Anderson-Evans-hybrid in order to form 2D- and 3D-structures with Cu^{2+} and Zn^{2+} , respectively.⁴⁶ Furthermore, $[\text{MnMo}_6\text{O}_{18}\{(\text{OCH}_2)_3\text{C}(\text{C}_5\text{H}_4\text{N})_2\}]^{3-}$ was also used for the coordination to Cu^{2+} and Zn^{2+} .⁴⁶ In 2016, Yang *et al.* employed the aforementioned hybrid with CuI under various conditions and demonstrated coordination polymers linked by Cu_xI_x moieties (where $x = 2, 4$) building up 2D- and 3D-structures.⁴⁷ In this study, the 3D structure $(\text{TBA})_6[\text{Cu}_4\text{I}_4][\text{MnMo}_6\text{O}_{18}((\text{OH}_2\text{C})_3\text{C}(\text{C}_5\text{H}_4\text{N}))_2]_2$ was also investigated as a catalyst for click reactions between azide- and alkyne-derivatives.

3.4 Catalysis

3.4.1 A³-coupling

A three-component coupling of an aldehyde, an amine and an alkyne (A³-Coupling) using $\text{Cu}^{1+/2+}$ or Ag^{1+} as catalyst, has proved to be a powerful method in order to synthesize propargylic amines in one-pot reactions as a versatile building block for biological active compounds.^{130,131} Figure 3.17 shows an example of A³-Coupling using R^1 to R^4 for imaginary residue. In the first step the aldehyde and the secondary amine form an iminium cation.¹³² Theoretically, it is also possible to use primary amines instead of secondary amines, whereby an imine is formed as the product of the first step (also termed Schiff base).¹³² Via tautomerism, the positive charge at the nitrogen atom can be transferred to the carbon atom of the former aldehyde group. In parallel, a Cu based catalyst coordinates to an alkyne, followed by an insertion of the Cu ion between the triple bond and the terminal hydrogen atom. This activated form of alkyne couples with the corresponding iminium ion to form the desired product.

In previous reports, this kind of reaction required harsh and inert conditions. We were therefore interested in developing novel catalysts, which can work under mild and aerobic conditions.¹³¹

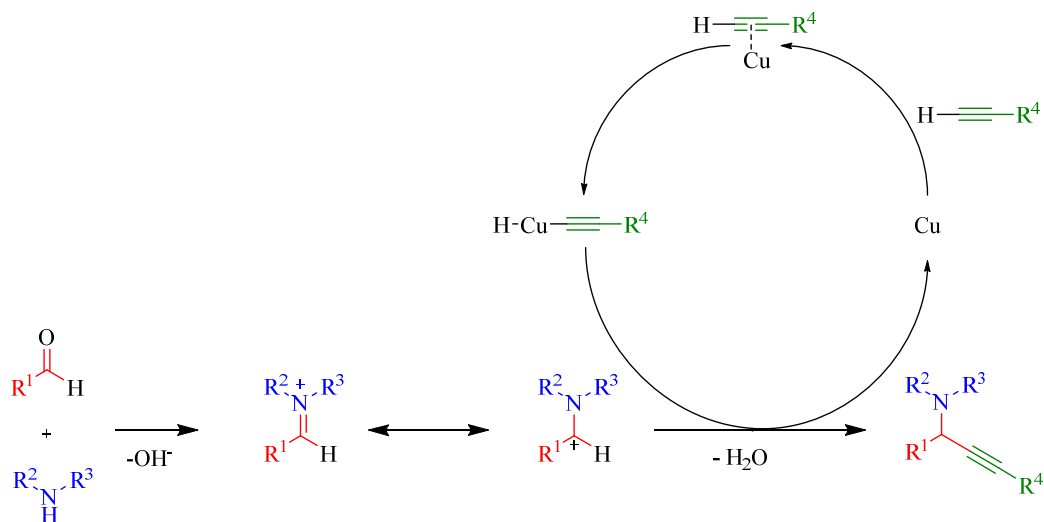


Figure 3.17: A^3 -Coupling of an aldehyde, an amine and an alkyne in order to form propargylic amines.

3.4.2 Catalytic reaction for the implementation of furfural with amines

Rare earth metal ($RE^{3+} = Dy, Eu, La$) containing compounds are well known as catalysts for the reaction of furfural and amines, to form *trans*-4,5-diaminocyclopentenones. These structural motifs are versatile building blocks for the retrosynthetic pathway of (-)-agelastatin A.¹³³ This architecturally unique cytotoxic tetracyclic alkaloid was first isolated from the axinellid sponge *Agelas dendromorpha*.^{134,135} Over decade, the conversion of the commercially available biomass furfural to diastereoselective cyclopentenones have been intensively established and explored. Figure 3.18 shows the reaction of furfural with morpholine to form *trans*-4,5-dimorpholinocyclopent-2-en-1-one.^{136,137}

3. Introduction

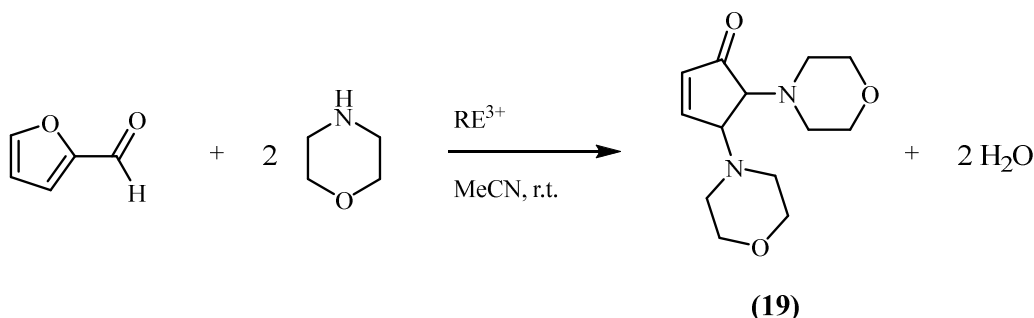


Figure 3.18: Synthesis of *trans*-4,5-dimorpholinocyclopent-2-en-1-one from furfural and morpholine.

Figure 3.19 illustrates the proposed mechanism of this reaction.¹³⁶ In the first step, a RE^{3+} ion coordinates to the formyl group of furfural, thus increasing the electrophilicity on the carbon of the aldehyde. The activated formyl group reacts with the amino group of the secondary amine forming an iminium cation and releasing an OH^- anion. In the next step, a RE^{3+} ion coordinates to the oxygen of the furan ring, which results in an increased electrophilicity on C5 of the furan ring. A nucleophile (e.g. R_2NH) can react with this carbon atom, releasing H^+ , which forms H_2O with the previously released OH^- ion. The RE^{3+} then detaches from the oxygen of the furan ring which is followed by a ring-opening step, causing a charge separation (oxygen atom is negatively charged, nitrogen atom is positively charged). A ring closing step follows (shown with red arrows), connecting the C5 and C1 atoms of the aforementioned intermediate, resulting in a neutral *trans*-4,5-diaminocyclopent-2-enone derivative.

3. Introduction

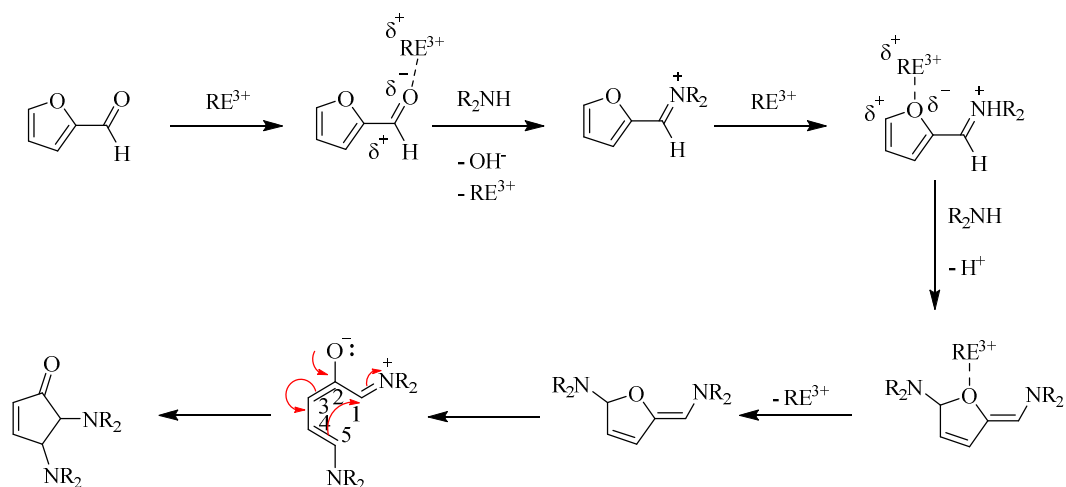


Figure 3.19: Proposed overview of the general mechanism of the reaction of furfural and a secondary amine using a rare earth metal in oxidation state 3+ as Lewis acid, which acts as a catalyst.

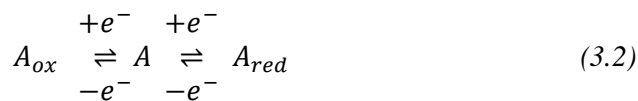
3.4.3 Electrocatalysis

Another interesting field of catalysis is electrocatalysis, where a catalyst can be utilized as an electrode material (heterogeneous electrocatalysis)⁴⁴ or in solution (homogeneous electrocatalysis).¹³⁸ One interesting area in this field is the splitting of water into its components (equation (3.1)).³⁷



Amongst many other methods, linear sweep voltammetry (LSV) and cyclic voltammetry (CV) are the most common methods used in electrochemistry. Here, the three-electrode setup is used, where the potential is measured between the reference and the working electrode and the current is detected between the working and the counter-electrode.^{139,140} During an electrochemical process a reactant can be oxidized or reduced, respectively:

3. Introduction



As shown in Figure 3.20, a **linear sweep voltammogram** starts at an initial potential E_{start} (1), at which no electrode process takes place. Subsequently, the potential will be altered by a constant rate (so-called scan rate) v , until the reversal potential E_λ (2) is reached, indicated by the arrow in the direction of the sweep scan.

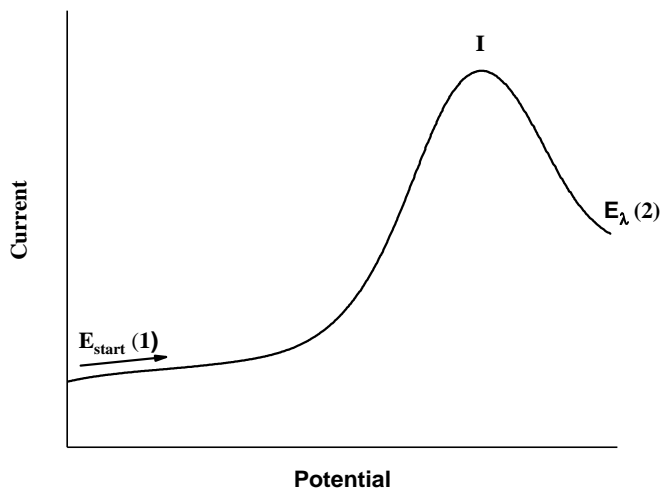


Figure 3.20: Linear sweep voltammetry.

Before describing and explaining the shape of a cyclic voltammogram, it should be noted that in this work the convention according to IUPAC is used for the evaluation of cyclic voltammogram, which is: “The international, or IUPAC convention displays negative (reducing) potentials to the left of 0.00, and positive (oxidizing) potentials to the right. Cathodic (reduction) currents are displayed as negative (down) values along the ordinate, while anodic (oxidation) currents are displayed as positive (up).”¹⁴¹

As shown in Figure 3.20, the linear sweep voltammogram begins at E_{start} (1) on the left hand side of the current/voltage plot where no current flows. As the voltage is

3. Introduction

increased by a constant scan rate to the right (oxidative values), a potential is reached at which the reactant A is being electrochemically oxidized. At this stage two parallel processes take place:¹⁴²

By increasing the potential E, the oxidation of species A takes place, which causes a concentration gradient at the electrode and an increase of the current.

According to the Nernst equation:

$$E = E_0 + \frac{RT}{zF} \ln \frac{A_{ox}}{A_{red}} \quad (3.3)$$

Inserting the constants R and F, transforming from natural logarithm to decadal logarithm and choosing the temperature 25 °C, the equation is:

$$E = E_0 + \frac{0.059 V}{z} \log \frac{A_{ox}}{A_{red}} \quad (3.4)$$

E: potential

E₀: standard potential

R: gas constant (8.314510 J/(mol·K))¹⁴³

T: temperature in Kelvin

z: number of electrons involved in the electrochemical reaction

F: Faraday constant (= 9.6485309 · 10⁴ C/mol)¹⁴³

A_{ox}: activity of oxidized species

A_{red}: activity of reduced species

the concentration of the reduced species A decreases. However, a diffusion layer δ is gradually formed, surrounding the surface of the electrode, which counteracts the

3. Introduction

concentration gradient and thus reduces the number of electrochemical reactions. The resulting current sinks again, an oxidation peak (I) is observed and the potential reaches E_λ , where the voltammogram ends.

In the case of **cyclic voltammetry** (a cyclic voltammogram is shown in Figure 3.21) the electrochemical processes are the same as in linear sweep voltammetry. However, a cyclic voltammogram does not stop at E_λ , rather, this value is fixed as a turning point and the sign of the scan rate will be changed.

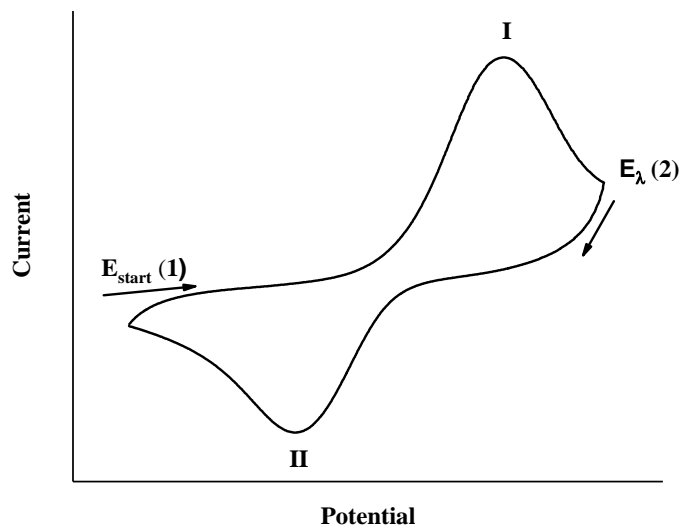


Figure 3.21: Cyclic voltammogram.

At this point, the resulting product A_{ox} is partly distributed due to diffusion processes into the electrolyte; however, the environment of the electrode is still surrounded by it. This means the concentration of the initial species A around the electrode approaches zero. This can be also seen in the cyclic voltammogram, as with the change of the sign of the scan rate the current continues to decrease. At this stage the oxidized species gets reduced again, whereas with further continuing scan rate the concentration of A increases around the electrode surface. At a certain

potential, species A, which surrounds the electrode, becomes reduced to A_{red} . This is accompanied by a strong increase of negative current, where the processes mentioned for the anodic current are also taking place for the cathodic one, but for the reduction of A to A_{red} . This results in a reduction peak (II) and the cyclic voltammogram ends at the initial potential E_{start} .

3.4.4 Photo-electrocatalysis

Photocatalysts can facilitate chemical reactions with the help of irradiation. This type of material must fulfill certain properties in order to be called a photocatalyst. As before, the catalyst can be present in homogenous or heterogeneous media. In this work, only heterogeneous catalysis will be discussed, but firstly, the differences between conductors, semi-conductors and insulators are described. As shown in Figure 3.22, all three types of materials have a valence and conduction band, and in the case of semi-conductors and insulators, a bandgap is added. The valence (HOMO) band contains electrons, whereas the conduction (LUMO) band is empty by definition. Furthermore, a bandgap is an area separating the valence band from the conduction band. In the case of a conductor, the valence band and the conduction band overlap. By applying an electric voltage, movement of the valence electrons takes place because these have enough unoccupied energy states in the conduction band to move.¹⁴⁴ If the valence band and the conduction band are energetically separated from each other, first a small bandgap is created, as is the case for the semi-conductor (Figure 3.22 (b)). In order to bring the electrons from the valence band into the conduction band, a certain amount of energy is needed. For semi-conductors such as ZnO and TiO₂ the value is about 3.2 eV, which corresponds to 388 nm or 25810 cm⁻¹.^{145,146} By increasing the bandgap, the energy which is needed to bring electrons from the valence to the conduction band is increased, until this barrier is too large for any electron transfer. This kind of

3. Introduction

material is called an insulator. The bandgap can be calculated by using the absorbance of the solid state UV-vis spectrum for the Tauc method.

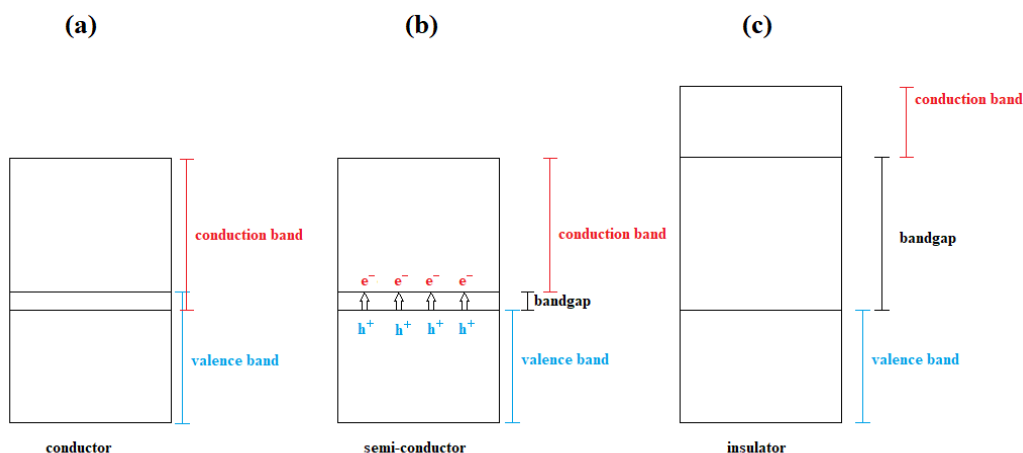


Figure 3.22: Schematic drawing of a conductor (a), semi-conductor (b) and insulator (c).

For a photocatalyst, the material class of a semiconductor is required because the electrons in the valence band can be transported to the conduction band by irradiation (heat or light).¹⁴⁴ By a transition of an electron from HOMO to LUMO, a hole (h^+) is created in the valence band. This results in a charge separation, whereby the negatively charged electrons can be used for a reduction and the positively charged holes for an oxidation of one or more reactants.¹⁴⁷ In principle, this charge separation is easier to achieve when the bandgap is small, but would increase the probability of a recombination of e^- and h^+ , reducing the efficiency of the system.¹⁴⁸ On the other hand, a charge separation in a semi-conductor with a large bandgap requires more energy.

The combination of photo- and electrocatalysis creates the field of photo-electrocatalysis. Here, the photocatalyst serves as a working electrode. Linear sweep voltammetry (explained in section 3.4.3) is the method used and a Xe lamp (300 W, $\lambda = 185 - 2000$ nm) is utilized with a frequency chop light scan of for

3. Introduction

example 0.33 Hz. Figure 3.23 shows an example for a photocatalytic study. At the moment when the light is switched on the current increases dramatically. When the light is switched off, however, it drops again. This behavior indicates a photocatalytically active material.

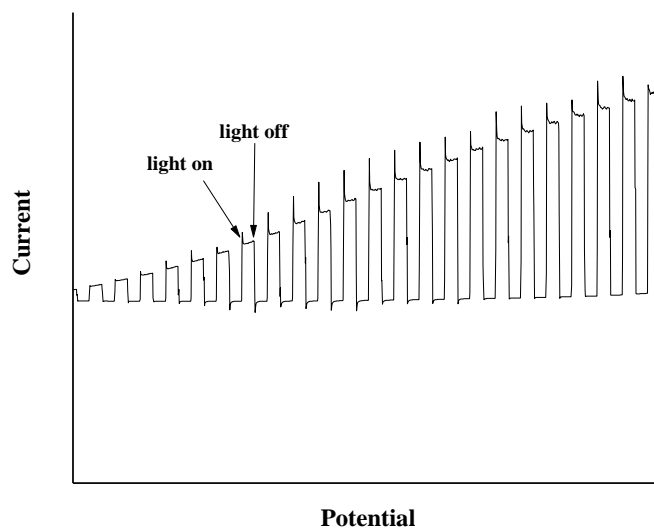


Figure 3.23: Linear sweep voltammetry with a certain frequency chop light scan shining on the catalyst.

4 EXPERIMENTAL SECTION

4.1 Instrumentation

4.1.1 Fourier Transform-Infrared (FT-IR) Spectroscopy

Infrared spectra were recorded on a Perkin Elmer Spectrum GX FT-IR spectrometer as KBr pellets in the range 400 cm^{-1} to 4000 cm^{-1} with a resolution of 8 cm^{-1} . The following abbreviations were used to describe the peak characteristics: br = broad, sh = shoulder, s = strong, m = medium and w = weak.

4.1.2 Elemental Analysis (EA)

To determine the carbon, hydrogen, nitrogen and sulfur fractions of the samples, elemental analysis was carried out using a "Vario Micro Cube" device from Perkin Elmer.

4.1.3 Single crystal X-ray diffraction (SCXRD)

The structures in this thesis were measured using single crystal X-ray diffraction (SCXRD) on area detector diffractometers: IPDS II (Mo-K α , $\lambda = 0.71073\text{ \AA}$, detector: image plate), STADIVARI (Mo-K α , $\lambda = 0.71073\text{ \AA}$; Cu-K α , $\lambda = 1.5405\text{ \AA}$, detector: Dectris Pilatus 300K (detector: CMOS)) and STADIVARI (Ga-K α , $\lambda = 1.34143\text{ \AA}$, detector: Dectris Eiger2 R 4M (detector type: HPC)) (STOE) and Supernova (Mo-K α , $\lambda = 0.71073\text{ \AA}$; Cu-K α , $\lambda = 1.5405\text{ \AA}$, detector: Dectris Pilatus R 200K (detector: HPA)) (Rigaku). The measurements were taken

at temperatures of 150 K and 180 K. The crystals were attached to the goniometer head with perfluoroether oil. In order to determine the unit cell, first some frames were recorded at different angles of rotation. Then a complete measurement based on the orientation matrix and the lattice constant was performed, the data integrated and corrected for Lorentz and polarization factors. The structure determination and refinement were performed using SHELXTL¹⁴⁹ or OLEX2.¹⁵⁰ Figures were produced using the program Diamond 4.1.¹⁵¹

4.1.4 Powder X-ray diffraction (PXRD)

To check the purity of crystalline compounds, diffractograms of the samples were recorded using a STOE STADI-P diffractometer with Cu-K α radiation ($\lambda = 1.5405 \text{ \AA}$) at room temperature and processed using the WinXPow software.¹⁵² The simulated PXRD patterns of the crystal structures were generated using PowderCell 2.3.¹⁵³

4.1.5 Nuclear Magnetic Resonance (NMR) Spectroscopy

NMR spectra of the compounds were measured using a Bruker Ultrashield plus 500 (500 MHz) and Varian 500 MHz spectrometer. ¹H- and ¹³C-measurements were recorded using deuterated solvents and referenced to tetramethylsilane (TMS) as an internal standard ($\delta = 0 \text{ ppm}$).

4.1.6 Topology

The topologies of some of the obtained crystal structures were assigned using the program ToposPro 5.3.3.4 and the figures were produced using the program Mercury 3.10.1.^{154,155}

4.1.7 Analysis of the coordination geometry of the metal centres

The coordination geometries of selected metal centres within the crystal structures were determined using the program SHAPE.¹⁵⁶

4.1.8 Solid state UV-vis spectroscopy

Solid state UV-vis spectra were recorded on a VARIAN CARY 500 Scan UV-vis - NIR spectrophotometer in the range 200 nm to 800 nm at a scan rate of 600 nm/min. Samples were dispersed in a drop of mineral oil for spectroscopy (Nujol mulls) and sandwiched between two quartz glass plates.

4.1.9 Electrochemistry

Electrocatalytic studies were performed using an EG & G 273 A. Potentials are quoted against a saturated calomel electrode (SCE). The counter electrode was a platinum gauze of large surface area. All experiments were performed at room temperature.

4.1.10 Photo-electrochemistry

Photo-electrocatalytic studies were performed utilizing a Xe lamp (300 W, $\lambda = 185 - 2000$ nm) with a 0.33Hz chop light scan and a potentiometer CS350 single channel potentiostat of the company CorrTest[®]Instruments with a linear sweep voltammetry scan mode over the range -0.8 V to 1.4 V at a scan rate of 0.01 V/s. A 3-electrode system with Ag/AgCl as a reference electrode and a platinum wire as a counter electrode was used. The sample to be examined was spin-coated onto a ZnO-coated fluorine-doped tin oxide (FTO) substrate and used as working electrode.

4.2 Synthesis and synthetic strategies

All reactions were carried out in both in air, under inert atmosphere and solvothermal conditions (Figure 4.1). Crystals were obtained either by diethyl ether vapour diffusion into the mother liquor (Figure 4.2) or using layering method (Figure 4.3). Crystalline powder of these compounds and ligands were obtained by stirring of the reactants. The methods of *pre*- and *post*-functionalization are described in section 3.1.1.2.1.1. Chemicals were purchased from Alfa Aesar, Sigma Aldrich, VWR Chemicals, ROTH, Merck, TCI or Honeywell and were used without further purification.

4. Experimental Section

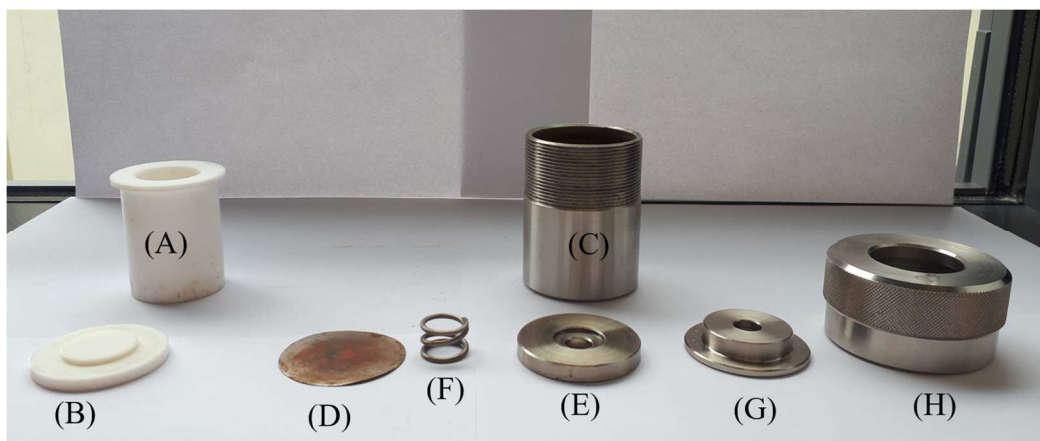


Figure 4.1: Setup for solvothermal reaction (autoclave), Reaction mixture is placed in teflon container (A) and closed with teflon lid (B). This container will be placed in the stainless steel container (C), covered with metal plate (D) and (E), the spring is put on top of (E), followed by (G) and sealed with (H). Then the autoclave can be transferred in an oven and the reaction can be started.

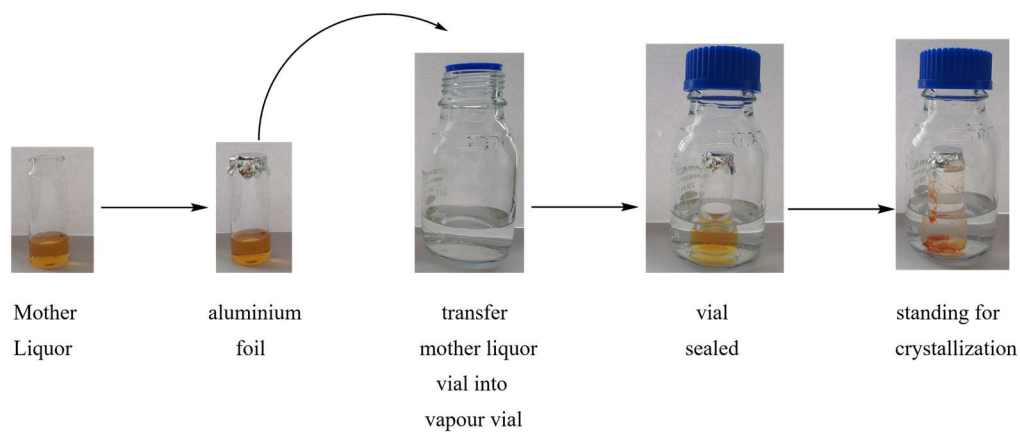


Figure 4.2: Diethyl ether vapour diffusion. The vial containing the mother liquor is covered with an aluminium foil. This vial is then transferred into a bigger vial containing diethyl ether. The bigger vial will be sealed and kept for crystallization.

4. Experimental Section

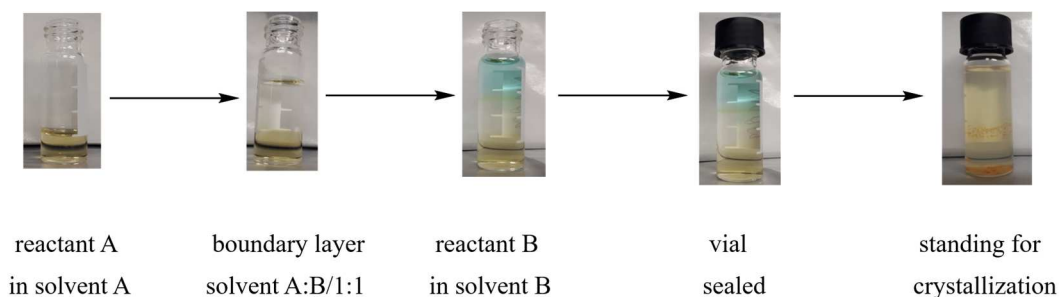


Figure 4.3: Layering method. Reactant A in solvent A is put into the vial, followed by the buffer layer consisting of solvent A and B in ration 1:1. Then reactant B in solvent B will be layered on top of the buffer layer. The vial will be sealed and kept for crystallization.

4.3 Synthesis of previously reported precursors (Pre) and linkers (L)

4.3.1 $[N(n\text{-C}_4\text{H}_9)_4]_4[\text{Mo}_8\text{O}_{26}]$ (1)

$[N(n\text{-C}_4\text{H}_9)_4]_4[\alpha\text{-Mo}_8\text{O}_{26}]$ (1) was synthesized according to the literature method.⁶⁵ A solution of $\text{Na}_2\text{MoO}_4 \cdot 2\text{H}_2\text{O}$ (5.00 g, 20.70 mmol) dissolved in 12 mL H_2O was acidified with 5.17 mL of 6.0 M aqueous HCl (31.00 mmol) with vigorous stirring over a period of 2 min at room temperature. Then a solution of tetrabutylammonium bromide (3.34 g, 10.40 mmol) dissolved in 10 mL H_2O was added and the resulting suspension stirred for 10 min. The resulting white precipitate was isolated by filtration and was washed with 20 mL of H_2O , 20 mL of ethanol, 50 mL acetone and 20 mL diethyl ether, The solid was air dried to yield 4.85 g (2.30 mmol, 89 % based on Mo). The product was characterized using FT-IR spectroscopy (KBr, cm^{-1}): 3473 (br, w), 2968 (s), 2938 (sh), 2878 (s), 2742 (w), 1883 (br, w), 1702 (w), 1484 (s), 1386 (m), 1348 (sh), 1288 (w), 1138 (w), 954 (sh), 918 (s), 857 (s), 812 (s), 664 (s), 559 (m), 522 (m), 501 (m), 417 (w).

4.3.2 $\text{Na}_3[\text{Al}(\text{OH})_6\text{Mo}_6\text{O}_{18}] \cdot 2n\text{H}_2\text{O}$ ($n = 2-10$) (2)

$\text{Na}_3[\text{Al}(\text{OH})_6\text{Mo}_6\text{O}_{18}]$ (2) was synthesized according to the literature method.¹⁵⁷ To a solution of 25 mL of H_2O and 10 mL of acetic acid $\text{AlCl}_3 \cdot 6\text{H}_2\text{O}$ (1.5 g, 6.21 mmol) and $\text{Na}_2\text{MoO}_4 \cdot 2\text{H}_2\text{O}$ (3.5 g, 14.50 mmol) were added under stirring. The pH value was adjusted to 1.8 by addition of 35 % hydrochloric acid. The resulting reaction mixture was kept at room temperature in an open 100 mL flask and after one week white crystals were isolated by filtration and dried in air to yield 2.0 g (1.76 mmol, 73 % based on Mo). The product was characterized using FT-IR spectroscopy (KBr, cm^{-1}): 3299 (br, s), 1619 (m), 957 (sh), 919 (s), 798 (w), 648 (s), 576 (sh), 525 (sh), 451 (m), 388 (s).

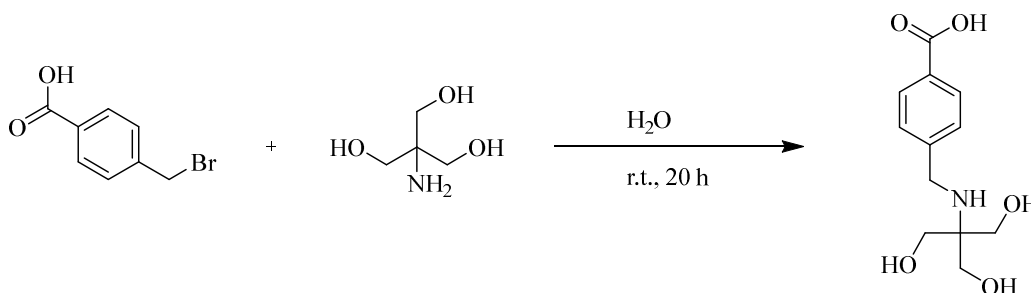
4.3.3 $[\text{N}(n\text{-C}_4\text{H}_9)_4]_3[\text{MnMo}_6\text{O}_{18}\{(\text{OCH}_2)_3\text{CNH}_2\}_2]$ (3)

$[\text{N}(n\text{-C}_4\text{H}_9)_4]_3[\text{MnMo}_6\text{O}_{18}\{(\text{OCH}_2)_3\text{CNH}_2\}_2]$ (3) was synthesized according to the literature method.⁶⁶ A mixture of $[\text{N}(n\text{-C}_4\text{H}_9)_4]_4[\alpha\text{-Mo}_8\text{O}_{26}]$ (1) (8.00 g, 3.70 mmol), $\text{Mn}(\text{CH}_3\text{COO})_3 \cdot 2\text{H}_2\text{O}$ (1.49 g, 5.60 mmol) and tris(hydroxymethyl)amino methane (1.56 g, 12.80 mmol) in 150 mL acetonitrile was refluxed for 20 h. Then the orange suspension was cooled to room temperature and the brown precipitate was filtered off and discarded. The filtrate was placed in a diethyl ether atmosphere and after 2 h the resulting white precipitate was filtered off and discarded. Then the filtrate was again exposed to diethyl ether vapour. After one day, orange crystals had formed. For a higher yield, the diethyl ether diffusion was continued for another 10 days. The crystals were collected by filtration and air-dried to yield 7.45 g (3.94 mmol, 80 % based on Mn). The product was characterized using FT-IR spectroscopy (KBr, cm^{-1}): 3442 (br, m), 2961 (m), 2938 (sh), 2878 (m), 1650 (w), 1484 (m), 1386 (w), 1230 (w), 1047 (s), 941 (sh), 920 (s), 902 (sh), 830 (w), 799 (w), 662 (br, s), 562 (w), 459 (w), 414 (w).

4.3.4 $[N(n\text{-C}_4\text{H}_9)_4]_3[\text{MnMo}_6\text{O}_{18}\{(\text{OCH}_2)_3\text{CN}=\text{CH}(4\text{-C}_5\text{H}_4\text{N})\}_2]\cdot 3\text{DMF}$ (**4**)

For the synthesis of $[N(n\text{-C}_4\text{H}_9)_4]_3[\text{MnMo}_6\text{O}_{18}\{(\text{OCH}_2)_3\text{CN}=\text{CH}(4\text{-C}_5\text{H}_4\text{N})\}_2]\cdot 3\text{DMF}$ (**4**) reported in the literature,⁶⁶ an alternative procedure was developed. A mixture of $[N(n\text{-C}_4\text{H}_9)_4]_3[\text{MnMo}_6\text{O}_{18}\{(\text{OCH}_2)_3\text{CNH}_2\}_2]$ (**3**) (100 mg, 0.053 mmol) and 4-pyridinecarboxaldehyde (0.1 mL, 114 mg, 1.06 mmol) were dissolved in 2 mL DMF by heating gently. The reaction mixture was placed in a diethyl ether atmosphere and after 1 day, orange crystals had formed. A quantitative yield of 107 mg was achieved by continuing the diethyl ether diffusion for further 7 days. Elemental analysis (%) calc. for $\text{MnMo}_6\text{O}_{24.5}\text{C}_{69.5}\text{N}_{7.5}\text{H}_{133.5}$ (2096.918 g/mol) $[N(n\text{-C}_4\text{H}_9)_4]_3[\text{MnMo}_6\text{O}_{18}\{(\text{OCH}_2)_3\text{CN}=\text{CH}(4\text{-C}_5\text{H}_4\text{N})\}_2]\cdot 0.5\text{DMF}$: C: 39.81; N: 5.01; H: 6.42. Found: C: 39.40; N: 5.22; H: 6.57. FT-IR (KBr, cm^{-1}): 3571 (br), 3433 (br), 2972 (s), 2925 (sh), 2866 (s), 1674 (s), 1641 (sh), 1599 (m), 1563 (w), 1487 (m), 1461 (sh), 1408 (sh), 1385 (m), 1326 (w), 1260 (w), 1230 (w), 1174 (sh), 1155 (w), 1095 (s), 1026 (s), 941 (s), 921 (s), 905 (sh), 822 (w), 803 (w), 740 (sh), 668 (s), 566 (m), 520 (sh), 464 (w).

4.3.5 $4\text{-HOOC}(\text{C}_6\text{H}_4)\text{CH}_2\text{NHC}(\text{CH}_2\text{OH})_3$ (**L1**)



4-HOOC(C₆H₄)CH₂NHC(CH₂OH)₃ (L1) was synthesized according to the literature method.¹²⁶ 4-(chloromethyl)benzoic acid (10.0 g, 58.6 mol) was added over a period of 2 min to a solution of tris(hydroxymethyl)amino methane (35.6 g, 294 mmol) in 300 mL H₂O. The reaction mixture was stirred for 20 h at room

temperature, whereas the solid 4-(chloromethyl)benzoic acid was completely dissolved after 30 min and a white precipitate occurred after 7 h of addition. The white precipitate was filtered off and washed with H₂O (2 x 20 mL) and acetone (2 x 15 mL), followed by drying under vacuum to yield 10.2 g (68 %). The product was characterized using ¹H NMR (DMSO-d₆): δ = 3.21 (s, 6H), 3.82 (s, 2H), 7.43 (d, 2H), 7.81 (d, 2H).

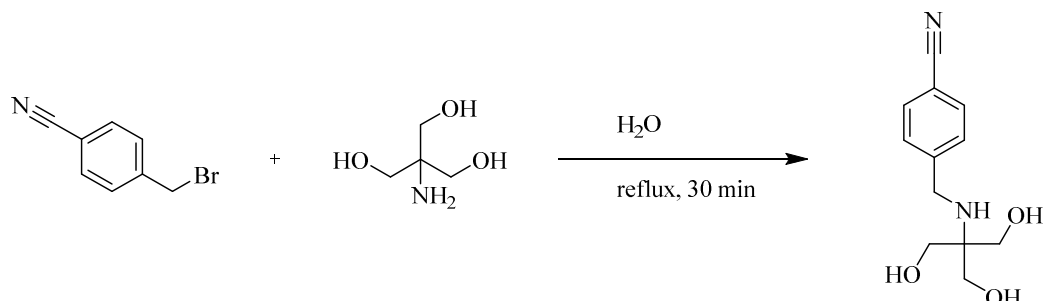
4.4 Synthesis of novel precursors (Pre) and potential linkers (L)

4.4.1 [N(*n*-C₄H₉)₄]₄[(MnMo₆O₁₈)((OCH₂)₃CNHCH₂(C₆H₄)COOH)((OCH₂)₃CNHCH₂(C₆H₄)COO)]·3DMF (**5**)

A mixture of [N(*n*-C₄H₉)₄]₄[α-Mo₈O₂₆] (**1**) (1.100 g, 0.50 mmol), Mn(OAc)₃·2H₂O (0.201 g, 0.75 mmol), 4-HOOC(C₆H₄)CH₂NHC(CH₂OH)₃ (**L1**) (0.438 g, 1.71 mmol), tetrabutylammonium bromide (0.215 g, 0.67 mmol) and 20 mL DMF was stirred for 22 h at 85 °C. The resulting suspension was centrifuged and the orange supernatant was placed in a diethyl ether atmosphere and after 2 days orange crystals had formed. For a higher yield, the diethyl ether diffusion was continued for another 13 days and the crystals were air dried to yield 1.012 g (57 % based on Mn; 64 % based on Mo). Elemental analysis (%) calc. for MnMo₆O₂₈C₈₈N₆H₁₇₁ (2391.901 g/mol) ([N(*n*-C₄H₉)₄]₄[(MnMo₆O₁₈)((OCH₂)₃CNHCH₂(C₆H₄)COOH)((OCH₂)₃CNHCH₂(C₆H₄)COO)]): C: 44.19; N: 3.51; H: 7.21. Found: C: 44.26; N: 3.58; H: 7.28. FT-IR (KBr, cm⁻¹): 3470 (br, m), 2964 (s), 2932 (sh), 2875 (s), 1713 (sh), 1675 (s), 1611 (sh, w), 1479 (s), 1390 (m), 1258 (w), 1156 (w), 1087 (m), 1043 (m), 942 (sh), 922(s), 904 (sh), 771 (sh), 670 (s), 569 (w), 505 (w), 455 (w).

4.4.2 $[\text{N}(n\text{-C}_4\text{H}_9)_4]_3[(\text{AlMo}_6\text{O}_{18})((\text{OCH}_2)_3\text{CCH}_2\text{OCH}_2\text{C}(\text{CH}_2\text{OH})_3)_2] \cdot 2\text{H}_2\text{O}$
(6)

A mixture of $\text{Na}_3[\text{Al}(\text{OH})_6\text{Mo}_6\text{O}_{18}] \cdot 2n\text{H}_2\text{O}$ ($n = 2\text{--}10$) (**2**) (0.354 g, 0.33 mmol) and dipentaerythritol (0.170 g, 0.66 mmol) was dissolved in 10 mL H_2O under stirring. The resultant white turbid solution was then stirred for 30 min. After addition of tetrabutylammonium bromide (0.333 g, 1.03 mmol), the mixture was stirred for 20 more min (pH = 5). Then the reaction mixture was transferred in a 25 mL Teflon container, which was sealed in a stainless steel reactor. The reaction mixture was heated to 120 °C over 1 h and then kept at that temperature for 96 hours, followed by cooling to room temperature with a cooling rate of 3.96 K/h. White crystals were obtained and air dried to yield 0.398 g (0.18 mmol, 54 % based on Mo). Elemental analysis (%) calc. for $\text{C}_{68}\text{H}_{160}\text{AlMo}_6\text{N}_3\text{O}_{39}$ (2191.48 g/mol) ($[\text{N}(n\text{-C}_4\text{H}_9)_4]_3[(\text{AlMo}_6\text{O}_{18})((\text{OCH}_2)_3\text{CH}_2\text{COCH}_2\text{C}(\text{CH}_2\text{OH})_3)_2] \cdot 7\text{H}_2\text{O}$): C: 36.35; N: 1.87; H: 7.17. Found: C: 36.59; N: 2.10; H: 6.97. FT-IR (KBr, cm^{-1}): 3438 (br, m), 2961 (s), 2937 (sh), 2878 (s), 1648 (w), 1480 (m), 1375 (w), 1313 (w), 1197 (w), 1135 (m), 1109 (sh), 1020 (m), 944 (sh), 921 (s), 898 (sh), 826 (w), 743 (sh), 665 (s), 569 (w), 523 (w), 477 (sh), 450 (w).

4.4.3 4-N≡C(C₆H₄)CH₂NHC(CH₂OH)₃ (**L2**)

4-(bromomethyl)benzotrile (5.0 g, 0.03 mol) was added over a period of 2 min to a solution of tris(hydroxymethyl)aminomethane (15.5 g, 0.13 mol) in 150 mL H₂O. The suspension was stirred for 1 h, followed by refluxing for 30 min. During this time, the suspension turned to a colourless, clear solution. The solution volume was reduced to 50 mL on a rotary evaporator. This solution was extracted with ethyl acetate (6x100 mL) and the organic phase dried over Na₂SO₄. The solvent was removed under vacuum and the residue washed with diethyl ether (3x50 mL). The solid was dried under vacuum to yield 4.43 g of product (74 %). Elemental analysis (%) calc. for C₁₂H₁₆N₂O₃ (236.27 g/mol): C: 61.00; N: 11.86; H: 6.83. Found: C: 61.07; N: 11.55; H: 6.84. ¹H NMR (500 MHz, DMSO): δ 7.75 (d, *J* = 8.2 Hz, 2H), 7.57 (d, *J* = 8.1 Hz, 2H), 4.31 (t, *J* = 5.4 Hz, 3H), 3.84 (s, 2H), 3.39 (d, *J* = 5.3 Hz, 6H). ¹³C NMR (126 MHz, DMSO): 148 (p-C_{Bz}CH₂), 132 (o-C_{Bz}), 129 (m-C_{Bz}), 119 (C≡N), 109 (C_{Bz}-C≡N), 61 (HOCH₂), 61 (CNH), 45 (CH₂NH).

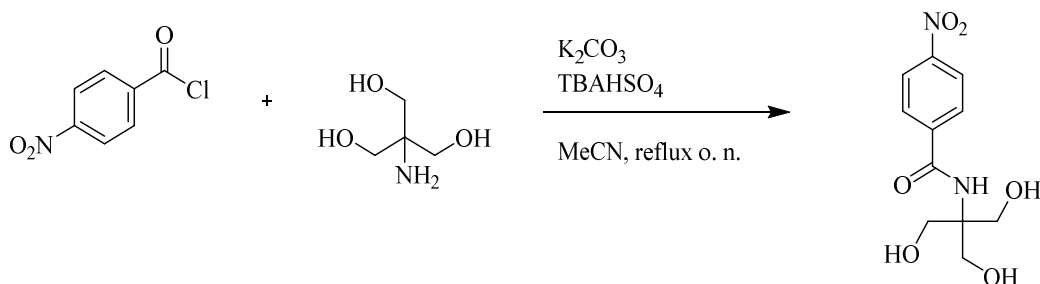
4.4.4 [N(*n*-C₄H₉)₄]₃[(MnMo₆O₁₈)((OCH₂)₃CNH(C₆H₄)C≡N)₂]·6MeCN (**7**)

A mixture of [N(*n*-C₄H₉)₄]₄[α-Mo₈O₂₆] (**1**) (0.822 g, 0.38 mmol), Mn(OAc)₃·2H₂O (0.155 g, 0.58 mmol), 4-N≡C(C₆H₄)CH₂NHC(CH₂OH)₃ (**L2**) (0.312 g, 1.32 mmol) and 15 mL MeCN was refluxed for 21 h. The resulting suspension was centrifuged and the orange supernatant was placed in a diethyl ether atmosphere and after 6

4. Experimental Section

days orange crystals had formed. For a higher yield, the diethyl ether diffusion was continued for another 8 days and the crystals were air dried to yield 0.44 g (36 % based on Mn, 41.3 % based on Mo). Elemental analysis (%) calc. for $\text{MnMo}_6\text{O}_{24}\text{C}_{72}\text{N}_7\text{H}_{130}$ (2086.41 g/mol) ($[\text{N}(n\text{-C}_4\text{H}_9)_4]_3[(\text{MnMo}_6\text{O}_{18})((\text{OCH}_2)_3\text{CNH}(\text{C}_6\text{H}_4)\text{C}\equiv\text{N})_2]$): C: 40.34; N: 4.70; H: 6.29. Found: C: 39.97; N: 4.67; H: 6.36. FT-IR (KBr, cm^{-1}): 3450 (br, m), 2964 (s), 2938 (sh), 2875 (s), 2231 (m), 1675 (m), 1611 (m), 1485 (s), 1384 (m), 1156 (w), 1081 (s), 1043 (s), 941 (sh), 920 (s), 902 (sh), 828 (w), 670 (s), 569 (m), 468 (m).

4.4.5 4- $\text{NO}_2(\text{C}_6\text{H}_4)\text{C}=\text{ONHC}(\text{HOCH}_2)_3$ (L3)



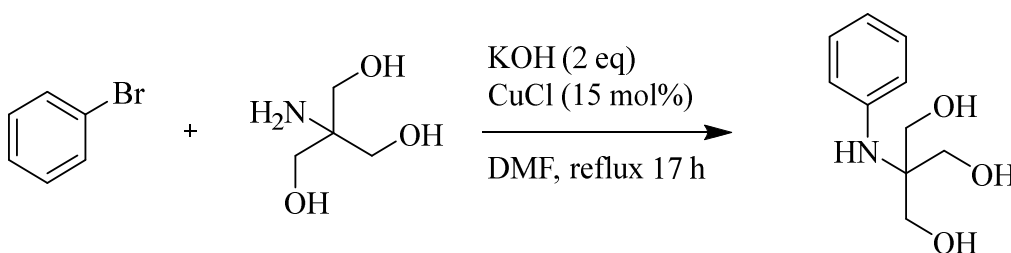
K_2CO_3 (17.27 g, 125 mmol), tris(hydroxymethyl)aminomethane (15.14 g, 125 mmol) and tetrabutylammonium hydrogensulfate (TBAHSO₄) (0.17 g, 0.01 mmol, 0.0002 mol%) were added to a solution of 4-nitrobenzoyl chloride (9.278 g, 50.00 mmol) in 150 ml acetonitrile. The resulting mixture was refluxed overnight. The resulting mixture was filtered off and the solvent of the filtrate was removed under vacuum to yield 11.08 g of a white solid (yield: 82 %). Elemental analysis (%) calc. for $\text{C}_{11}\text{H}_{14}\text{N}_2\text{O}_6$ (270.241 g/mol): C: 48.89; N: 10.37; H: 5.22. Found: C: 49.24; N: 10.52; H: 5.16. ^1H NMR (500 MHz, DMSO) δ (ppm) = 8.26 - 8.28 (m, 2 H), 8.02 - 8.04 (m, 2 H), 4.75 (t, $J=5.95$ Hz, 3 H), 3.74 (d, $J=5.95$ Hz, 6 H). ^{13}C NMR (126 MHz, DMSO): δ (ppm) = 166.0 (C), 149.1 (C), 144.4 (C), 129.3 (2 \times CH), 123.6 (2 \times CH), 63.5 (C), 60.3 (CH₂).

4. Experimental Section

4.4.6 $[N(n\text{-C}_4\text{H}_9)_4]_3[\text{MnMo}_6\text{O}_{18}\{(\text{OCH}_2)_3\text{CNHC}=\text{O}(\text{C}_6\text{H}_4\text{NO}_2)_2\}_2]\cdot 6\text{DMF}$ (**8**)

A mixture of $[N(n\text{-C}_4\text{H}_9)_4]_4[\alpha\text{-Mo}_8\text{O}_{26}]$ (**1**) (0.822 g, 0.382 mmol), $\text{Mn}(\text{OAc})_3\cdot 2\text{H}_2\text{O}$ (0.155 g, 0.578 mmol), 4- $\text{NO}_2(\text{C}_6\text{H}_4)\text{C}=\text{ONHC}(\text{HOCH}_2)_3$ (**L3**) (0.357 g, 1.32 mmol) and 15 mL DMF was stirred for 24 h at 85°C. The resulting suspension was centrifuged and the orange supernatant was placed in a diethyl ether atmosphere and after 3 days orange crystals had formed. For a higher yield, the diethyl ether diffusion was continued for another 4 days and the crystals were air dried to yield 0.214 g (15 % based on Mn, 17.5 % based on Mo). Elemental analysis (%) calc. for $\text{MnMo}_6\text{O}_{33}\text{C}_{79}\text{N}_{10}\text{H}_{151}$ (2399.669 g/mol) ($[N(n\text{-C}_4\text{H}_9)_4]_3 [\text{MnMo}_6\text{O}_{18}\{(\text{OCH}_2)_3\text{CNHC}=\text{O}(\text{C}_6\text{H}_4\text{NO}_2)_2\}_2]\cdot 3\text{DMF}$): C: 39.54; N: 5.84; H: 6.34. Found: C: 39.24; N: 5.91; H: 6.27. FT-IR (KBr, cm^{-1}): 3299 (br, m), 3058 (w), 2961 (s), 2930 (sh), 2870 (s), 1657 (s), 1605 (m), 1552 (sh, m), 1529 (m), 1492 (m), 1378 (w), 1341 (m), 1288 (w), 1154 (w), 1102 (m), 1028 (m), 941 (s), 922 (s), 906 (sh, s), 871 (w), 848 (w), 811 (w), 719 (sh, w), 670 (br, s), 560 (w), 512 (w), 460 (w).

4.4.7 $(\text{C}_6\text{H}_5)\text{NHC}(\text{CH}_2\text{OH})_3$ (**L4**)



KOH (5.61 g, 0.1 mol) and tris(hydroxymethyl)aminomethane (18.17 g, 150 mol) were placed in a Schlenk flask followed by its evacuation. Then under N_2 flow CuCl (0.74 g, 15 mol%), bromobenzene (5.2237 mL, 7.851 g, 0.05 mol) and 50 mL dry DMF were added. Oxygen was removed using a freeze-pump-thaw process. The

4. Experimental Section

reaction mixture was refluxed for 17 h, followed by cooling to room temperature and quenching by adding 50 mL H₂O under ice bath cooling. The resulting precipitate was filtered off and washed with 50 mL DCM. The aqueous phase was extracted with DCM (4 x 50 mL). The combined organic phases were dried over dry Na₂SO₄ and the solvent was removed under reduced pressure. The crude product was dissolved in a minimum amount of DCM and purified by column chromatography (gradient: 0 – 10 %, MeOH - DCM) to yield 1.288 g (13 %). Elemental analysis (%) calc. for C₁₀H₁₅NO₃ (197.23 g/mol): C: 60.90; N: 7.10; H: 7.67. Found: C: 60.59; N: 6.96; H: 7.42. ¹H NMR (500 MHz, DMSO): δ (ppm) = 7.79 (d, *J* = 7.8 Hz, 2H), 7.03 (t, *J* = 7.4 Hz, 2H), 6.57 (t, *J* = 7.4 Hz, 1H), 4.48 (t, *J* = 5.3 Hz, 3H (OH)), 1H (NH)), 3.55(d, *J* = 5.3 Hz, 6H). ¹³C NMR (126 MHz, DMSO): δ(ppm) = 147 (C), 129 (CH), 117 (CH), 116 (CH), 61 (CH₂), 61 (CH).

4.4.8 [N(*n*-C₄H₉)₄]₃[(MnMo₆O₁₈)((OCH₂)₃CNHC₆H₅)₂]·MeCN·H₂O (9)

A mixture of [N(*n*-C₄H₉)₄]₄[α-Mo₈O₂₆] (1) (0.822 g, 0.38156 mmol), Mn(OAc)₃·2H₂O (0.155 g, 0.5775 mmol), (C₆H₅)NHC(CH₂OH)₃ (L4) (0.260 g, 1.32 mmol) and 10 mL MeCN was refluxed for 19 h. Then the orange suspension was cooled to room temperature and the brown precipitate was filtered off and discarded. The filtrate was placed in a diethyl ether atmosphere and after 7 days, a dark brown oily phase had formed on the bottom of the vial. Another 3 days later, brown-orange crystals had formed on top of the oily phase. For a higher yield, the diethyl ether diffusion was continued for another 8 days. The crystals were collected by filtration and air-dried to yield 0.40 g (34 % based on Mn, 39.0 % based on Mo). Elemental analysis (%) calc. for MnMo₆O₂₄C₇₀N₆H₁₃₅ (2075.424 g/mol) ([N(*n*-C₄H₉)₄]₃[(MnMo₆O₁₈)((OCH₂)₃CNHC₆H₅)₂]·1MeCN·1H₂O): C: 40.16; N: 4.01; H: 6.59. Found: C: 40.49; N: 3.98; H: 6.79. FT-IR (KBr, cm⁻¹): 3417 (w), 3337 (w), 3191 (w), 3059 (w), 2964 (s), 2932 (sh), 2875 (s), 1675 (m), 1605 (s),

4. Experimental Section

1504 (sh), 1479 (s), 1384 (m), 1321 (w), 1295 (w), 1251 (w), 1194 (w), 1156 (w), 1099 (sh), 1087 (sh), 1055 (s), 1024 (sh), 941 (s), 920 (s), 903 (sh), 849 (w), 813 (br, w), 756 (w), 666 (br, s), 565 (w), 503 (w), 458 (w), 444 (w), 420 (w), 418 (w).

4.4.9 $[N(n\text{-C}_4\text{H}_9)_4]_2[\text{Mn}_2\text{Mo}_4\text{O}_{14}((\text{OCH}_2\text{CH}_2)_2\text{NCH}_2\text{CH}_2\text{OH})_2]$ (10)

A mixture of $[N(n\text{-C}_4\text{H}_9)_4]_4[\alpha\text{-Mo}_8\text{O}_{26}]$ (**1**) (0.82 g, 0.38 mmol), $\text{Mn}(\text{OAc})_3 \cdot 2\text{H}_2\text{O}$ (0.16 g, 0.58 mmol) and triethanolamine (TEAH_3) (0.51 g, 3.40 mmol) in 20 mL acetonitrile was refluxed for 20 h. Then the violet suspension was cooled to room temperature and the brown precipitate was filtered off and discarded. The resulting violet filtrate was placed in a diethyl ether atmosphere and after 2 days white crystals had formed, followed by violet crystals another 4 days later. The diethyl ether diffusion was continued for another 16 days until the solution became colourless. The mixture of white and violet crystals was filtered off, stirred in 4 mL acetonitrile for a few minutes and the left over white crystals were filtered off and discarded. These transparent crystals were analysed as $[\text{MoO}_2\{(\text{HOC}_2\text{H}_4\text{N}(\text{C}_2\text{H}_4\text{O})_2)\}]$.¹⁵⁸ The pure phase of violet crystals was obtained after a diethyl ether diffusion into the violet filtrate for 18 days to yield 0.22 g (19 % based on Mo, 50 % based on Mn). Elemental analysis (%) calc. for $\text{Mn}_2\text{Mo}_4\text{O}_{20}\text{C}_{44}\text{N}_4\text{H}_{96}$ (1496.90 g/mol) ($[N(n\text{-C}_4\text{H}_9)_4]_2[\text{Mn}_2\text{Mo}_4(\text{O})_{14}((\text{OCH}_2\text{CH}_2)_2\text{NCH}_2\text{CH}_2\text{OH})_2]$): C: 35.30; N: 3.74; H: 6.60. Found: C: 35.21; N: 3.77; H: 6.49. FT-IR (KBr, cm^{-1}): 3419 (br, m), 2964 (s), 2938 (sh), 2875 (s), 1744 (w), 1637 (w), 1485 (s), 1384 (m), 1295 (w), 1251 (w), 1175 (w), 1156 (w), 1074 (s), 1049 (sh), 992 (w), 930 (s), 907 (s), 782 (s), 717 (s), 665 (s), 602 (w), 580 (w), 534 (w), 464 (w).

4.5 Synthesis of extended structures

4.5.1 Synthesis of rare earth containing polyoxometalate-based metal organic frameworks (RE-POMOFs)

4.5.1.1 RE(DMF)₆RE(DMF)₅RE₃(DMF)₁₀[(MnMo₆O₁₈)((OCH₂)₃CNHCH₂(C₆H₄)COO)₂]₃·xDMF (RE = La - Nd) (**11**)

A boundary layer of a mixture of DMF/MeOH (1:1/v:v, 2 mL) was rapidly pipetted over a solution of [N(*n*-C₄H₉)₄]₄[(MnMo₆O₁₈)((OCH₂)₃CNHCH₂(C₆H₄)COOH)((OCH₂)₃CNHCH₂(C₆H₄)COO)]·3DMF (**5**) (10 mg, 0.0042 mmol) dissolved in 1 mL DMF. A solution of RE(NO₃)₃·5/6H₂O (RE = La - Nd) (10 mg, 0.0231 mmol) dissolved in 1 mL MeOH was rapidly pipetted on top to give a three layered system. Yellow crystals of (**11**) were obtained from the lower layer after five days and were dried under vacuum.

The following compounds were synthesized according to the aforementioned layering method:

Compound (**11**)-La layering: Yield: 4.5 mg (47 % based on (**5**)). Elemental analysis (%) calc. for C₁₄₇H₂₅₃La₅Mn₃Mo₁₈N₃₁O₁₀₉(6784.987 g/mol) (La(DMF)₆La(DMF)₅La₃(DMF)₁₀[(MnMo₆O₁₈)((OCH₂)₃CNHCH₂(C₆H₄)COO)₂]₃·4DMF): C: 26.02, N: 6.40, H: 3.76. Found: C: 26.15, N: 6.52, H: 3.91. FT-IR (KBr, cm⁻¹): 4312 (br, sh), 3315 (br, w), 2930 (m), 2855 (sh), 2817 (sh), 1650 (s), 1612 (sh), 1552 (w), 1499 (w), 1424 (m, sh), 1386 (m), 1303 (w), 1251 (m), 1175 (w), 1115 (m), 1070 (m), 1040 (m), 949 (s), 912 (s), 776 (w), 663 (br, s), 565 (sh), 460 (w), 414 (w).

Compound (**11**)-Ce layering: Yield: 3.9 mg (42 % based on (**5**)). Elemental analysis (%) calc. for C₁₄₄H₂₄₆N₃₀O₁₀₈Mn₃Mo₁₈Ce₅ (6717.945 g/mol) (Ce(DMF)₆Ce(DMF)₅Ce₃(DMF)₁₀[(MnMo₆O₁₈)((OCH₂)₃CNHCH₂(C₆H₄)COO)₂]₃·3DMF): C: 25.75, N: 6.25, H: 3.69. Found: C: 25.64, N: 6.35, H: 3.44. FT-IR (KBr, cm⁻¹):

4. Experimental Section

4315 (br, sh), 3317 (br, w), 2932 (m), 2857 (sh), 2820 (sh), 1655 (s), 1613 (sh), 1549 (w), 1501 (w), 1427 (m, sh), 1387 (m), 1300 (w), 1253 (m), 1178 (w), 1118 (m), 1073 (m), 1043 (m), 951 (s), 915 (s), 777 (w), 665 (br, s), 566 (sh), 461 (w), 415 (w).

Compound **(11)**-Pr layering: Yield: 3.2 mg (35 % based on **(5)**). Elemental analysis (%) calc. for $C_{135}H_{225}N_{27}O_{105}Mn_3Mo_{18}Pr_5$ (6502.622 g/mol) $(Pr(DMF)_6Pr(DMF)_5Pr_3(DMF)_{10}[(MnMo_6O_{18})((OCH_2)_3CNHCH_2(C_6H_4)COO)_2]_3)$: C: 24.94, N: 5.82, H: 3.47. Found: C: 25.18, N: 5.44, H: 3.47. FT-IR (KBr, cm^{-1}): 4315 (br, sh), 3316 (br, w), 2933 (m), 2858 (sh), 2821 (sh), 1653 (s), 1612 (sh), 1550 (w), 1500 (w), 1428 (m, sh), 1389 (m), 1300 (w), 1251 (m), 1176 (w), 1114 (m), 1071 (m), 1042 (m), 950 (s), 913 (s), 775 (w), 664 (br, s), 563 (sh), 460 (w), 413 (w).

Compound **(11)**-Nd layering: Yield: 3.7 mg (41 % based on **(5)**). Elemental analysis (%) calc. for $C_{135}H_{225}N_{27}O_{105}Mn_3Mo_{18}Nd_5$ (6519.294 g/mol) $(Nd(DMF)_6Nd(DMF)_5Nd_3(DMF)_{10}[(MnMo_6O_{18})((OCH_2)_3CNHCH_2(C_6H_4)COO)_2]_3)$: C: 24.87, N: 5.80, H: 3.48. Found: C: 24.52, N: 5.73, H: 3.46. FT-IR (KBr, cm^{-1}): 4310 (br, sh), 3313 (br, w), 2932 (m), 2857 (sh), 2818 (sh), 1651 (s), 1613 (sh), 1553 (w), 1498 (w), 1425 (m, sh), 1387 (m), 1305 (w), 1252 (m), 1176 (w), 1117 (m), 1071 (m), 1041 (m), 948 (s), 913 (s), 777 (w), 664 (br, s), 567 (sh), 461 (w), 415 (w).

In order to obtain larger amounts in microcrystalline powder form of **(11)** $[N(n-C_4H_9)_4]_4[(MnMo_6O_{18})((OCH_2)_3CNHCH_2(C_6H_4)COOH)((OCH_2)_3CNHCH_2(C_6H_4)COO)] \cdot 3DMF$ **(5)** (200 mg, 0.084 mmol) was dissolved in 20 mL DMF and a solution of $RE(NO_3)_3 \cdot 5/6H_2O$ (RE = La - Nd) (200 mg, 0.462 mmol) dissolved in 20 mL MeOH was added under stirring over a period of 1 minute at room temperature. The solution turned turbid within 30 seconds and was stirred for a further 1.5 h. The resulting powder was dried under vacuum.

4. Experimental Section

The La - Nd containing compounds (**11**) could best be obtained using a stirring method:

Compound (**11**)-La stirring: Yield: 76 mg (41 % based on (**5**)). Elemental analysis (%) calc. for $C_{141}H_{239}N_{29}O_{107}Mn_3Mo_{18}La_5$ (6638.799 g/mol) $(La(DMF)_6La(DMF)_5La_3(DMF)_{10}[(MnMo_6O_{18})((OCH_2)_3CNHCH_2(C_6H_4)COO)_2]_3 \cdot 2DMF)$: C: 25.51, N: 6.12, H: 3.63. Found: C: 25.33, N: 6.37, H: 3.97. FT-IR (KBr, cm^{-1}): 4311 (br, sh), 3317 (br, w), 2931 (m), 2856 (sh), 2815 (sh), 1651 (s), 1613 (sh), 1553 (w), 1498 (w), 1425 (m, sh), 1388 (m), 1304 (w), 1252 (m), 1176 (w), 1116 (m), 1073 (m), 1041 (m), 951 (s), 913 (s), 778 (w), 660 (br, s), 567 (sh), 461 (w), 415 (w).

Compound (**11**)-Ce stirring: Yield: 77 mg (40 % based on (**5**)). Elemental analysis (%) calc. for $C_{150}H_{260}N_{32}O_{110}Mn_3Mo_{18}Ce_5$ (6864.133 g/mol) $(Ce(DMF)_6Ce(DMF)_5Ce_3(DMF)_{10}[(MnMo_6O_{18})((OCH_2)_3CNHCH_2(C_6H_4)COO)_2]_3 \cdot 5DMF)$: C: 26.25, N: 6.53, H: 3.82. Found: C: 26.02, N: 6.74, H: 3.93. FT-IR (KBr, cm^{-1}): 4310 (br, sh), 3317 (br, w), 2931 (m), 2856 (sh), 2818 (sh), 1651 (s), 1613 (sh), 1555 (w), 1497 (w), 1423 (m, sh), 1384 (m), 1301 (w), 1254 (m), 1178 (w), 1119 (m), 1073 (m), 1042 (m), 952 (s), 913 (s), 778 (w), 662 (br, s), 567 (sh), 461 (w), 415 (w).

Compound (**11**)-Pr stirring: Yield: 82 mg (45 % based on (**5**)). Elemental analysis (%) calc. for $C_{135}H_{225}N_{27}O_{105}Mn_3Mo_{18}Pr_5$ (6502.622 g/mol) $(Pr(DMF)_6Pr(DMF)_5Pr_3(DMF)_{10}[(MnMo_6O_{18})((OCH_2)_3CNHCH_2(C_6H_4)COO)_2]_3)$: C: 24.94, N: 5.82, H: 3.47. Found: C: 25.13, N: 5.47, H: 3.48. FT-IR (KBr, cm^{-1}): 4312 (br, sh), 3315 (br, w), 2931 (m), 2852 (sh), 2817 (sh), 1653 (s), 1612 (sh), 1552 (w), 1489 (w), 1424 (m, sh), 1387 (m), 1305 (w), 1253 (m), 1178 (w), 1117 (m), 1072 (m), 1042 (m), 950 (s), 913 (s), 777 (w), 662 (br, s), 566 (sh), 460 (w), 415 (w).

4. Experimental Section

Compound **(11)**-Nd stirring: Yield: 79 mg (43 % based on **(5)**). Elemental analysis (%) calc. for $C_{135}H_{225}N_{27}O_{105}Mn_3Mo_{18}Nd_5$ (6519.294 g/mol)(Nd(DMF)₆Nd(DMF)₅Nd₃(DMF)₁₀[(MnMo₆O₁₈)((OCH₂)₃CNHCH₂(C₆H₄)COO)₂]₃): C: 24.87, N: 5.80, H: 3.48. Found: C: 24.62, N: 5.63, H: 3.56. FT-IR (KBr, cm⁻¹): 4312 (br, sh), 3315 (br, w), 2932 (m), 2855 (sh), 2819 (sh), 1650 (s), 1613 (sh), 1552 (w), 1497 (w), 1424 (m, sh), 1386 (m), 1306 (w), 1251 (m), 1175 (w), 1116 (m), 1070 (m), 1042 (m), 949 (s), 914 (s), 776 (w), 663 (br, s), 566 (sh), 460 (w), 414 (w).

The purity of the microcrystalline compounds resulting from the stirring method was confirmed by PXRD (section 5.3.1.1.3).

4.5.1.2 [RE(DMF)₄(H₂O)]₂[RE₃(DMF)₆][(MnMo₆O₁₈)((OCH₂)₃CNHCH₂(C₆H₄)COO)₂]₃·xDMF (RE = Y, Sm - Lu) (**12**)

A boundary layer of a mixture of DMF/MeOH (1:1/v:v, 2 mL) was rapidly pipetted over a solution of [N(*n*-C₄H₉)₄]₄[(MnMo₆O₁₈)((OCH₂)₃CNHCH₂(C₆H₄)COOH)((OCH₂)₃CNHCH₂(C₆H₄)COO)]·3DMF (**5**) (10 mg, 0.0042 mmol) dissolved in 1 mL DMF. A solution of RE(NO₃)₃·5/6H₂O (RE = Y, Sm - Lu) (10 mg, 0.0231 mmol) dissolved in 1 mL MeOH was rapidly pipetted on top to give a three layered system. Yellow crystals of **(12)** were obtained from the lower layer after five days and were dried under vacuum.

The following compounds were synthesized according to the aforementioned layering method:

Compound **(12)**-Y layering: Yield: 3.2 mg (35 % based on **(5)**). Elemental analysis (%) calc. for $C_{138}H_{236}N_{28}O_{108}Mn_3Y_5Mo_{18}$ (6351.738 g/mol) ([Y(DMF)₄(H₂O)]₂[Y₃(DMF)₆[(MnMo₆O₁₈)((OCH₂)₃CNHCH₂(C₆H₄)COO)₂]₃·8DMF): C: 26.09, N:

4. Experimental Section

6.18, H: 3.75. Found: C: 25.76, N: 6.44, H: 4.11. FT-IR (KBr, cm^{-1}): 4314 (br, sh), 3315 (br, w), 2930 (m), 28556(sh), 2817 (sh), 1650 (s), 1613 (sh), 1552 (w), 1450 (w), 1424 (m, sh), 1386 (m), 1304 (w), 1251 (m), 1175 (w), 1165 (m), 1070 (m), 1040 (m), 952 (s), 912 (s), 776 (w), 665 (br, s), 565 (sh), 460 (w), 412 (w).

Compound **(12)**-Sm layering: Yield: 4.5 mg (52 % based on **(5)**). Elemental analysis (%) calc. for $\text{C}_{120}\text{H}_{194}\text{N}_{22}\text{O}_{102}\text{Mn}_3\text{Mo}_{18}\text{Sm}_5$ (6220.446 g/mol) ($[\text{Sm}(\text{DMF})_4(\text{H}_2\text{O})]_2[\text{Sm}_3(\text{DMF})_6[(\text{MnMo}_6\text{O}_{18})((\text{OCH}_2)_3\text{CNHCH}_2(\text{C}_6\text{H}_4)\text{COO})_2]_3 \cdot 2\text{DMF}]$): C: 23.17, N: 4.95, H: 3.14. Found: C: 23.01, N: 5.20, H: 3.45. FT-IR (KBr, cm^{-1}): 4313 (br, sh), 3313 (br, w), 2930 (m), 2855 (sh), 2819 (sh), 1650 (s), 1613 (sh), 1554 (w), 1499 (w), 1425 (m, sh), 1386 (m), 1305 (w), 1251 (m), 1177 (w), 1117 (m), 1071 (m), 1041 (m), 949 (s), 912 (s), 776 (w), 665 (br, s), 565 (sh), 462 (w), 414 (w).

Compound **(12)**-Eu layering: Yield: 5.6 mg (62 % based on **(5)**). Elemental analysis (%) calc. for $\text{C}_{129}\text{H}_{215}\text{N}_{25}\text{O}_{105}\text{Mn}_3\text{Mo}_{18}\text{Eu}_5$ (6447.747 g/mol) ($[\text{Eu}(\text{DMF})_4(\text{H}_2\text{O})]_2[\text{Eu}_3(\text{DMF})_6[(\text{MnMo}_6\text{O}_{18})((\text{OCH}_2)_3\text{CNHCH}_2(\text{C}_6\text{H}_4)\text{COO})_2]_3 \cdot 5\text{DMF}]$): C: 24.03, N: 5.43, H: 3.36. Found: C: 23.95, N: 5.71, H: 3.60. FT-IR (KBr, cm^{-1}): 4313 (br, sh), 3315 (br, w), 2930 (m), 2856 (sh), 2817 (sh), 1650 (s), 1612 (sh), 1553 (w), 1499 (w), 1424 (m, sh), 1386 (m), 1305 (w), 1251 (m), 1175 (w), 1114 (m), 1070 (m), 1042 (m), 949 (s), 912 (s), 778 (w), 665 (br, s), 565 (sh), 460 (w), 414 (w).

Compound **(12)**-Gd layering: Yield: 3.6 mg (42 % based on **(5)**). Elemental analysis (%) calc. for $\text{C}_{117}\text{H}_{187}\text{N}_{21}\text{O}_{101}\text{Mn}_3\text{Mo}_{18}\text{Gd}_5$ (6181.802 g/mol) ($[\text{Gd}(\text{DMF})_4(\text{H}_2\text{O})]_2[\text{Gd}_3(\text{DMF})_6[(\text{MnMo}_6\text{O}_{18})((\text{OCH}_2)_3\text{CNHCH}_2(\text{C}_6\text{H}_4)\text{COO})_2]_3 \cdot 1\text{DMF}]$): C: 22.73, N: 4.76, H: 3.05. Found: C: 22.37, N: 4.95, H: 3.35. FT-IR (KBr, cm^{-1}): 4312 (br, sh), 3317 (br, w), 2930 (m), 2855 (sh), 2819 (sh), 1650 (s), 1613 (sh), 1552 (w),

4. Experimental Section

1499 (w), 1424 (m, sh), 1388 (m), 1303 (w), 1251 (m), 1175 (w), 1118 (m), 1070 (m), 1040 (m), 949 (s), 913 (s), 776 (w), 663 (br, s), 565 (sh), 462 (w), 414 (w).

Compound **(12)**-Tb layering: Yield: 4.1 mg (45 % based on **(5)**). Elemental analysis (%) calc. for $C_{129}H_{215}N_{25}O_{105}Mn_3Mo_{18}Tb_5$ (6482.554 g/mol) ($[Tb(DMF)_4(H_2O)]_2 [Tb_3(DMF)_6] [(MnMo_6O_{18})((OCH_2)_3CNHCH_2(C_6H_4)COO)_2]_3 \cdot 5DMF$): C: 23.90, N: 5.40, H: 3.42. Found: C: 23.75, N: 5.56, H: 3.58. FT-IR (KBr, cm^{-1}): 4312 (br, sh), 3315 (br, w), 2930 (m), 2855 (sh), 2818 (sh), 1650 (s), 1612 (sh), 1556 (w), 1498 (w), 1424 (m, sh), 1387 (m), 1303 (w), 1251 (m), 1176 (w), 1115 (m), 1071 (m), 1040 (m), 948 (s), 912 (s), 776 (w), 663 (br, s), 566 (sh), 460 (w), 415 (w).

Compound **(12)**-Dy layering: Yield: 4.2 mg (48 % based on **(5)**). Elemental analysis (%) calc. for $C_{117}H_{187}Dy_5Mn_3Mo_{18}N_{21}O_{101}$ (6208.411 g/mol) ($[Dy(DMF)_4(H_2O)]_2 [Dy_3(DMF)_6] [(MnMo_6O_{18})((OCH_2)_3CNHCH_2(C_6H_4)COO)_2]_3 \cdot 1DMF$): C: 22.63, N: 4.74, H: 3.04. Found: C: 22.51, N: 5.06, H: 3.38. FT-IR (KBr, cm^{-1}): 4312 (br, sh), 3315 (br, w), 2931 (m), 2855 (sh), 2817 (sh), 1651 (s), 1612 (sh), 1552 (w), 1499 (w), 1425 (m, sh), 1386 (m), 1304 (w), 1251 (m), 1175 (w), 1115 (m), 1071 (m), 1040 (m), 949 (s), 912 (s), 775 (w), 663 (br, s), 565 (sh), 461 (w), 414 (w).

Compound **(12)**-Ho layering: Yield: 4.0 mg (43 % based on **(5)**). Elemental analysis (%) calc. for $C_{126}H_{208}N_{24}O_{104}Mn_3Mo_{18}Ho_5$ (6439.485 g/mol) ($[Ho(DMF)_4(H_2O)]_2 [Ho_3(DMF)_6] [(MnMo_6O_{18})((OCH_2)_3CNHCH_2(C_6H_4)COO)_2]_3 \cdot 4DMF$): C: 23.50, N: 5.22, H: 3.26. Found: C: 23.26, N: 5.44, H: 3.58. FT-IR (KBr, cm^{-1}): 4312 (br, sh), 3316 (br, w), 2930 (m), 2855 (sh), 2817 (sh), 1651 (s), 1612 (sh), 1552 (w), 1499 (w), 1426 (m, sh), 1386 (m), 1305 (w), 1251 (m), 1175 (w), 1116 (m), 1070 (m), 1041 (m), 949 (s), 912 (s), 776 (w), 665 (br, s), 565 (sh), 461 (w), 414 (w).

4. Experimental Section

Compound **(12)**-Er layering: Yield: 3.8 mg (39 % based on **(5)**). Elemental analysis (%) calc. for $C_{147}H_{257}N_{31}O_{111}Mn_3Mo_{18}Er_5$ (6962.785 g/mol) $([Er(DMF)_4(H_2O)]_2[Er_3(DMF)_6][(MnMo_6O_{18})((OCH_2)_3CNHCH_2(C_6H_4)COO)_2]_3 \cdot 11DMF)$: C: 25.36, N: 6.24, H: 3.72. Found: C: 24.98, N: 6.45, H: 3.93. FT-IR (KBr, cm^{-1}): 4312 (br, sh), 3316 (br, w), 2930 (m), 2856 (sh), 2817 (sh), 1650 (s), 1613 (sh), 1552 (w), 1499 (w), 14254 (m, sh), 1386 (m), 1305 (w), 1251 (m), 1175 (w), 1115 (m), 1071 (m), 1040 (m), 949 (s), 913 (s), 776 (w), 663 (br, s), 566 (sh), 460 (w), 414 (w).

Compound **(12)**-Tm layering: Yield: 3.4 mg (35 % based on **(5)**). Elemental analysis (%) calc. for $C_{147}H_{257}N_{31}O_{111}Mn_3Mo_{18}Tm_5$ (6971.161 g/mol) $([Tm(DMF)_4(H_2O)]_2[Tm_3(DMF)_6][(MnMo_6O_{18})((OCH_2)_3CNHCH_2(C_6H_4)COO)_2]_3 \cdot 11DMF)$: C: 25.33, N: 6.23, H: 3.72. Found: C: 25.22, N: 6.46, H: 3.89. FT-IR (KBr, cm^{-1}): 4313 (br, sh), 3315 (br, w), 2931 (m), 2855 (sh), 2817 (sh), 1651 (s), 1612 (sh), 1552 (w), 1499 (w), 1422 (m, sh), 1386 (m), 1303 (w), 1252 (m), 1175 (w), 1115 (m), 1071 (m), 1040 (m), 949 (s), 912 (s), 778 (w), 663 (br, s), 565 (sh), 461 (w), 414 (w).

Compound **(12)**-Yb layering: Yield: 3.8 mg (44 % based on **(5)**). Elemental analysis (%) calc. for $C_{129}H_{215}N_{25}O_{105}Mn_3Mo_{18}Yb_5$ (6553.127 g/mol) $([Yb(DMF)_4(H_2O)]_2[Yb_3(DMF)_6][(MnMo_6O_{18})((OCH_2)_3CNHCH_2(C_6H_4)COO)_2]_3 \cdot 5DMF)$: C: 23.64, N: 5.34, H: 3.31. Found: C: 23.93, N: 5.71, H: 3.38. FT-IR (KBr, cm^{-1}): 4312 (br, sh), 3315 (br, w), 2932 (m), 2855 (sh), 2817 (sh), 1652 (s), 1612 (sh), 1552 (w), 1499 (w), 1426 (m, sh), 1386 (m), 1303 (w), 1253 (m), 1175 (w), 1117 (m), 1070 (m), 1041 (m), 949 (s), 912 (s), 775 (w), 663 (br, s), 566 (sh), 460 (w), 415 (w).

Compound **(12)**-Lu layering: Yield: 3.1 mg (34 % based on **(5)**). Elemental analysis (%) calc. for $C_{129}H_{215}N_{25}O_{105}Mn_3Mo_{18}Lu_5$ (6562.762 g/mol) $([Lu(DMF)_4(H_2O)]_2$

4. Experimental Section

[Lu₃(DMF)₆[(MnMo₆O₁₈)((OCH₂)₃CNHCH₂(C₆H₄)COO)₂]₃·5DMF): C: 23.61, N: 5.34, H: 3.30. Found: C: 23.24, N: 5.66, H: 3.65. FT-IR (KBr, cm⁻¹): 4313 (br, sh), 3315 (br, w), 2932 (m), 2855 (sh), 2817 (sh), 1651 (s), 1612 (sh), 1553 (w), 1499 (w), 1425 (m, sh), 1386 (m), 1305 (w), 1251 (m), 1175 (w), 1116 (m), 1070 (m), 1040 (m), 949 (s), 913 (s), 776 (w), 663 (br, s), 565 (sh), 461 (w), 414 (w).

In order to obtain larger amounts in microcrystalline powder form of Dy containing **(12)** [N(*n*-C₄H₉)₄]₄[(MnMo₆O₁₈)((OCH₂)₃CNHCH₂(C₆H₄)COOH)((OCH₂)₃CNH(C₆H₄)COO)]·3DMF **(5)** (200 mg, 0.084 mmol) was dissolved in 20 mL DMF and a solution of Dy(NO₃)₃·6H₂O (200 mg, 0.462 mmol) dissolved in 20 mL MeOH was added under stirring over a period of 1 minute at room temperature. The solution turned turbid within 30 seconds and was stirred for a further 1.5 h. The resulting powder was dried under vacuum to yield 78 mg (40% based on **(5)**). Elemental analysis (%) calc. for C₁₅₀H₂₆₄Dy₅Mn₃Mo₁₈N₃₂O₁₁₂ (7012.443 g/mol) ([Dy(DMF)₄(H₂O)]₂[Dy₃(DMF)₆][(MnMo₆O₁₈)((OCH₂)₃CNHCH₂(C₆H₄)COO)₂]₃·12DMF): C: 25.69, N: 6.39, H: 3.79. Found: C: 25.42, N: 6.12, H: 3.96. FT-IR (KBr, cm⁻¹): 4313 (br, sh), 3315 (br, w), 2931 (m), 2855 (sh), 2817 (sh), 1651 (s), 1613 (sh), 1552 (w), 1499 (w), 1425 (m, sh), 1386 (m), 1305 (w), 1251 (m), 1176 (w), 1115 (m), 1071 (m), 1040 (m), 949 (s), 913 (s), 776 (w), 663 (br, s), 566 (sh), 460 (w), 415 (w).

The purity of this microcrystalline compound resulting from the stirring method was confirmed by PXRD (section 5.3.1.2.3).

4.5.2 Synthesis of transition metal containing polyoxometalate-based metal organic frameworks (TM-POMOFs)

4.5.2.1 $[N(n\text{-C}_4\text{H}_9)_4]_5[\text{CuCl}(\text{DMF})\{\text{MnMo}_6\text{O}_{18}((\text{OCH}_2)_3\text{CN}=\text{CH}(4\text{-C}_5\text{H}_4\text{N}))_2\}_2] \cdot 3\text{DMF}$ (**13**)

4-pyridinecarboxaldehyde (0.4 mL, 456 mg, 4.24 mmol) was added to a solution of $[N(n\text{-C}_4\text{H}_9)_4]_3[\text{MnMo}_6\text{O}_{18}\{(\text{OCH}_2)_3\text{CNH}_2\}_2]$ (**3**) (200 mg, 0.11 mmol) and $\text{CuCl}_2 \cdot 2\text{H}_2\text{O}$ (9 mg, 0.05 mmol) dissolved in 4 mL DMF. This reaction mixture was sealed and stirred at 85 °C for 20 h. The reaction was cooled to room temperature and the suspension was centrifuged. Then the supernatant was placed in a diethyl ether atmosphere and after 1 day, dark green crystals had formed. For a higher yield, the diethyl ether diffusion was continued for another 14 days. The crystals were collected by filtration and air-dried to yield 170 mg (80% based on Cu). Elemental analysis (%) calc. for $\text{C}_{123}\text{H}_{231}\text{N}_{14}\text{O}_{49}\text{ClMn}_2\text{CuMo}_{12}$ $[N(n\text{-C}_4\text{H}_9)_4]_5[\text{CuCl}(\text{DMF})\{\text{MnMo}_6\text{O}_{18}((\text{OCH}_2)_3\text{CN}=\text{CH}(4\text{-C}_5\text{H}_4\text{N}))_2\}_2]$ (4050.36999 g/mol): C: 36.47; N: 4.84; H: 5.75. Found: C: 36.21; N: 4.63; H: 5.82. FT-IR (KBr, cm^{-1}): 3482 (br, m), 2964 (s), 2932 (sh), 2875 (s), 1675 (s), 1561 (w), 1485 (m), 1384 (m), 1321 (w), 1251 (w), 1156 (w), 1093 (s), 1030 (s), 943 (s), 923 (s), 904 (sh), 830 (w), 803 (w), 665 (br, s), 563 (w), 518 (w), 462 (w).

4.5.2.2 $[\text{Zn}(\text{DMF})_4][\text{Zn}(\text{DMF})_2\text{MnMo}_6\text{O}_{18}\{(\text{OCH}_2)_3\text{CN}=\text{CH}(4\text{-C}_5\text{H}_4\text{N}))_2\}_2] \cdot 10\text{DMF}$ (**14A**) and $[(\text{Zn}(\text{DMF})_3)_2(\text{Zn}(\text{DMF})_4\text{MnMo}_6\text{O}_{18}\{(\text{OCH}_2)_3\text{CN}=\text{CH}(4\text{-C}_5\text{H}_4\text{N}))_2\}_2] \cdot 9\text{DMF}$ (**14B**)

Compounds (**14A**) and (**14B**) were obtained as a mixture of crystals using a layering method. A boundary layer of a mixture of DMF/acetonitrile (1:1/v:v, 2 mL) was rapidly pipetted over a solution of $[N(n\text{-C}_4\text{H}_9)_4]_3[\text{MnMo}_6\text{O}_{18}\{(\text{OCH}_2)_3\text{CN}=\text{CH}(4\text{-C}_5\text{H}_4\text{N}))_2\}_2] \cdot 3\text{DMF}$ (**4**) (10 mg, 0.005 mmol) dissolved in 1 mL DMF. A solution of

4. Experimental Section

ZnCl₂ (9 mg, 0.051 mmol) dissolved in 1 mL acetonitrile was rapidly pipetted on top to give a three layered system. Crystals of **(14A)** and **(14B)** were obtained from the buffer layer after one day. FT-IR (KBr, cm⁻¹) **(14A)+(14B)**: 3418 (br), 2972 (s), 2925 (sh), 2866 (s), 1648 (s), 1612 (sh), 1563 (w), 1490 (w), 1434 (m), 1375 (m), 1326 (w), 1247 (m), 1174 (w), 1148 (w), 1115 (sh), 1089 (m), 1063 (sh), 1023 (s), 947 (s), 922 (sh), 912 (sh), 888 (sh), 866 (sh), 839 (w), 802 (w), 671 (s), 655 (s), 592 (sh), 566 (sh), 543 (sh), 520 (sh), 461 (w), 421 (w).

4.5.2.3 [Cd(DMF)₂][Cd][N(*n*-C₄H₉)₄]₂[MnMo₆O₁₈{(OCH₂)₃CN=CH(4-C₅H₄N)}₂]₂·2DMF (**15**)

A boundary layer of a mixture of DMF/acetonitrile (1:1/v:v, 2 mL) was rapidly pipetted over a solution of [N(*n*-C₄H₉)₄]₃[MnMo₆O₁₈{(OCH₂)₃CN=CH(4-C₅H₄N)}₂]₂·3DMF (**4**) (10 mg, 0.005 mmol) dissolved in 1 mL DMF. A solution of Cd(NO₃)₂·4H₂O (15 mg, 0.049 mmol) dissolved in 1 mL acetonitrile was rapidly pipetted on top to give a three layered system. Crystals of **(15)** were obtained from the buffer layer after one day and were dried under vacuum to yield 8.8 mg (quantitative yield). Elemental analysis (%) calc. for C₈₄H₁₄₄N₁₄O₅₂Mn₂Mo₁₂Cd₂ (3668.083 g/mol) [Cd·2DMF][Cd][N(*n*-C₄H₉)₄]₂[MnMo₆O₁₈{(OCH₂)₃CN=CH(4-C₅H₄N)}₂]₂·2DMF: C: 27.50; N: 5.35; H: 3.96. Found: C: 27.55; N: 5.52; H: 3.74. FT-IR (KBr, cm⁻¹): 3405 (br, m), 3224 (sh), 3156 (sh), 2960 (sh), 2936 (m), 2870 (m), 1646 (s), 1560 (sh, w), 1492 (sh, w), 1461 (sh, w), 1436 (m), 1382 (m), 1323 (w), 1294 (sh), 1249 (w), 1116 (sh), 1091 (m), 1060 (sh), 1026 (s), 950 (s), 922 (s), 907 (sh), 879 (sh, s), 825 (w), 803 (w), 662 (br, s), 566 (m), 518 (sh), 461 (w), 413 (w).

In order to obtain larger amounts in microcrystalline powder form of **(15)** [N(*n*-C₄H₉)₄]₃[MnMo₆O₁₈{(OCH₂)₃CN=CH(4-C₅H₄N)}₂]₂·3DMF (**4**) (100 mg, 0.048 mmol) was dissolved in 20 mL DMF and a solution of Cd(NO₃)₂·4H₂O

4. Experimental Section

(150 mg, 0.486 mmol) dissolved in 20 mL acetonitrile was added under stirring over a period of 1 minute at room temperature. The solution turned turbid within 30 seconds and was stirred for a further 1.5 h. The resulting powder was dried under vacuum to yield 88 mg (quantitative yield). Elemental analysis (%) calc. for $C_{84}H_{144}N_{14}O_{52}Mn_2Mo_{12}Cd_2$ (3668.083 g/mol) $[Cd(DMF)_2][Cd][N(n-C_4H_9)_4]_2[MnMo_6O_{18}\{(OCH_2)_3CN=CH(4-C_5H_4N)\}_2] \cdot 2DMF$: C: 27.50; N: 5.35; H: 3.96. Found: C: 27.61; N: 5.65; H: 3.61. FT-IR (KBr, cm^{-1}): 3405 (br, m), 3224 (sh), 3156 (sh), 2960 (sh), 2936 (m), 2870 (m), 1646 (s), 1560 (sh, w), 1492 (sh, w), 1461 (sh, w), 1436 (m), 1382 (m), 1323 (w), 1294 (sh), 1249 (w), 1116 (sh), 1091 (m), 1060 (sh), 1026 (s), 950 (s), 922 (s), 907 (sh), 879 (sh, s), 825 (w), 803 (w), 662 (br, s), 566 (m), 518 (sh), 461 (w), 413 (w). The purity of this microcrystalline compound resulting from the stirring method was determined by PXRD (section 5.3.2.4.3).

4.6 Catalytic studies

4.6.1 A^3 -Coupling

The basis of A^3 -Coupling is described in section 3.4.1.

General reaction procedure: 250 mg of 4 Å molecular sieves were placed into a vial. In the course of the reaction, 1 eq. of water is produced as a side product, which is excluded by the use of the molecular sieves. Then 5 mol% of compound (**13**) and 5 mL of isopropanol were added. Subsequently, alkyne (3.6 mmol, 1.2 eq.), aldehyde (3.0 mmol, 1.0 eq.) and amine (3.3 mmol, 1.1 eq.) were added. The reaction mixture was refluxed overnight. After completion of the reaction (TLC monitoring) the reaction mixture was cooled to room temperature and filtered over Celite®. The residue was washed with 15 mL isopropanol, then the solvent was removed under reduced pressure. The resulting crude product (yellow oil) was

4. Experimental Section

dissolved in minimum amount of ethylacetate and purified by column chromatography (gradient: 0 – 5 %, ethylacetate – hexane).

Compound (16): **1-(1,3-diphenylprop-2-ynyl)piperidine**

Pale yellow oil, 430 mg, 52 %; ^1H NMR (CDCl_3 , 500 MHz) δ (ppm) = 7.67 (d, J = 7.5 Hz, 2H), 7.58-7.52 (m, 2H), 7.42-7.29 (m, 6H), 4.83 (s, 1H), 2.62-2.57 (m, 4H), 1.62 (dp, J = 12.9, 7.5 Hz, 4H), 1.48 (dd, J = 11.8, 5.8 Hz, 1H); ^{13}C NMR (CDCl_3 , 126 MHz) δ (ppm) = 138.5 (C), 131.7 (2 \times CH), 128.4 (2 \times CH), 128.1 (2 \times CH), 127.9 (2 \times CH), 127.3 (2 \times CH), 123.2 (C), 87.7 (C), 85.9 (C), 62.3 (2 \times CH₂), 50.6 (CH), 26.1 (2 \times CH₂), 224.3(2 \times CH₂).

Compound (17): **1-(3-(4-fluorophenyl)-1-(4-phenylprop-2-ynyl) pyrrolidine**

Pale yellow oil, 437 mg, 49 %; ^1H NMR (CDCl_3 , 500 MHz) δ (ppm) = 7.63-7.52 (m, 2H), 7.50-7.42 (m, 2H), 7.11-6.93 (m, 3H), 4.85 (s, 1H), 2.72-6.60 (m, 4H), 1.87-1.72 (m, 4H); ^{13}C NMR (CDCl_3 , 126 MHz) δ (ppm) = 163.5 (C), 161.6 (C), 135.4 (C), 133.7 (2 \times CH), 129.9 (2 \times CH), 119.2 (C), 115.7 (2 \times CH), 115.2 (2 \times CH), 86.2 (C), 86.1 (C), 58.4 (CH), 50.2 (CH₂), 23.6 (CH₂).

Compound (18): **1-(1-cyclopentyl-3-phenylprop-2-ynyl)piperidine**

Pale yellow oil, 746 mg, 93 %; ^1H NMR (CDCl_3 , 500 MHz) δ (ppm) = 7.49-7.43 (m, 2H), 7.34-7.25 (m, 3H), 3.24 (d, J = 9.4 Hz, 1H), 2.69 (s, 2H), 2.47 (s, 2H), 2.32-2.17 (m, 1H), 1.97-1.86 (m, 1H), 1.84-1.74 (m, 1H), 1.71-1.41 (m, 12H); ^{13}C NMR (CDCl_3 , 126 MHz) δ (ppm) = 131.6 (2 \times CH), 128.0 (2 \times CH), 127.5 (CH), 123.7 (C), 88.0 (C), 85.6 (C), 63.6 (CH), 50.8 (C), 42.3 (CH₂), 30.7 (CH₂), 30.2 (CH₂), 26.2 (CH₂), 25.3 (CH₂), 25.1 (CH₂), 24.6 (CH₂).

4.6.2 Catalytic reaction for the implementation of furfural with morpholine

The basis of catalytic reaction for the implementation of furfural with a secondary amine is described in section 3.4.2.

General reaction procedure: In air, 4 Å molecular sieves (250 mg) were weighed into a vial. The use of molecular sieves is necessary, since 1 eq. of water is produced as a side product during the reaction. Then 4 mL of MeCN, the appropriate amount of (**11**)-Ce or (**12**)-Dy (0.5 % and 1 %), furfural (41 µL, 0.048 g, 0.5 mmol, 1 eq.) and morpholine (87 µL, 0.087 g, 1 mmol, 2 eq.) were subsequently added. The reaction was stirred at room temperature and the conversion of the reaction was monitored by sampling and determined by NMR measurements. Therefore, the samples was filtered over Celite[®], washed with DCM and the filtrate was concentrated under reduced pressure.

Compound (**19**): *trans*-4,5-dimorpholinocyclopent-2-en-1-one:

yellow oil, which solidified on standing, ¹H NMR (500MHz, CDCl₃) δ 7.61 (1H, dd, *J* = 6.2, 2.2 Hz), 6.24 (1H, dd, *J* = 6.2, 1.8 Hz), 3.82, (1H, s), 3.73 (4H, t, *J* = 4.5 Hz), 3.69 (4H, t, *J* = 4.7 Hz), 3.29 (1H, d, *J* = 3.0 Hz), 2.87-2.80 (2H, m), 2.70-2.56 (6H, m).

4.6.3 Photo-electrocatalytic studies

The basis of photo-electrocatalytic studies is described in section 3.4.4.

Samples for photo-electrocatalytic studies were prepared by spin coating. 10 mg of the respective compound was suspended in 1 mL methanol and 50 µL of this suspension were spin coated (1000 rpm) onto a ZnO based coated fluorine-doped tin oxide (FTO) substrate and heat treated with an infrared lamp for 1 min. This process was repeated ten times for every sample.

4. Experimental Section

Then the sample and a gold electrode were sandwiched between plastic plates, thus they are connected and can be utilized as working electrode. A Xe lamp (300 W) with a 0.33Hz chop light scan and a potentiometer with linear sweep voltammetry over the range -0.8 V to 1.4 V at a scan rate of 0.01 V/s as method were used for the studies.

4.6.4 Electrocatalytic studies

A one-compartment cell with a standard three-electrode configuration was used for cyclic voltammetry experiments. The reference electrode was a saturated calomel electrode (SCE) and the counter electrode a platinum gauze of large surface area; both electrodes were separated from the bulk electrolyte solution via fritted compartments filled with the same electrolyte. The working electrode was a 3 mm outer diameter GC. Prior to each experiment, solutions were thoroughly de-aerated for at least 30 min with pure argon. A positive pressure of this gas was maintained during subsequent work. The concentration of compound (**12**)-Dy in aqueous media was 0.4 mM. The composition of the various media in which the experiments were performed was as follows: for pH = 3.0, 0.2 M Na₂SO₄ + H₂SO₄; for pH = 5.0, 0.4 M NaCH₃COO + CH₃COOH; for pH = 7.0, 0.4 M 0.4 M NaH₂PO₄ + NaOH. The stability of the different compounds in solution was assessed by cyclic voltammetry. All experiments were performed at room temperature, which is controlled and fixed for the laboratory at 20°C. Results were very reproducible from one experiment to the other and slight variations observed over successive runs are rather attributed to the uncertainty associated with the detection limit of the equipment and not to the working electrode pre-treatment nor to possible fluctuations in temperature.

5 RESULTS AND DISCUSSION

The core of compounds **(4)** to **(9)** contain an Anderson-Evans POM $\{M^{3+}Mo_6O_{18}\}$ ($M^{3+} = Al^{3+}$ or Mn^{3+}) fragment. In all cases, two triply deprotonated tris(hydroxymethyl)methane-based ligands are attached to this moiety at the M^{3+} centre via the deprotonated hydroxyl groups, above and below the plane, thus completing the core structure of the Anderson-Evans POM $\{M^{3+}Mo_6O_{24}\}$. The resulting general formula is $\{L - (M^{3+}Mo_6O_{24}) - L\}^{n-}$ ($n = 3$ or 4), so-called L – POM – L or POM hybrid. The six Mo metal addenda atoms and the central heteroatom M^{3+} have octahedral coordination geometry and the coordination sites of M^{3+} are filled by six oxo ligands, which are further shared with the organic ligand and Mo centres of the surrounding octahedra. In order to define the length of the potential L – POM – L linker, the distance between the terminating atoms of the organic unit is given in terms of T_{func} , where T is the terminal atom and func is the functional group it belongs to.

5.1 Previously reported precursors (Pre)

5.1.1 $[N(n-C_4H_9)_4]_3[MnMo_6O_{18}\{(OCH_2)_3CN=CH(4-C_5H_4N)\}_2] \cdot 3DMF$ (**4**)

The reaction was carried out via a *post*-functionalization (section 3.1.1.2.1.1) by dissolving a mixture of $[N(n-C_4H_9)_4]_3[MnMo_6O_{18}\{(OCH_2)_3CNH_2\}_2]$ (**3**) and 4-Pyridinecarboxaldehyde in DMF, followed by exposure to ether vapour in order to isolate compound **(4)** in the form of crystals.

5.1.1.1 Single crystal structure

The crystallographic data of compound (**4**) are given in Table 8.1.

The single crystal X-ray diffraction analysis reveals that compound (**4**) crystallizes in the triclinic space group $P-1$ with the unit cell parameters $a = 16.346(3) \text{ \AA}$, $b = 17.020(3) \text{ \AA}$, $c = 20.078(4) \text{ \AA}$, $\alpha = 83.67(3)^\circ$, $\beta = 71.79(3)^\circ$, $\gamma = 67.63(3)^\circ$ and $V = 4907(2) \text{ \AA}^3$. The structure of the polyanion in (**4**), which is shown in Figure 5.1, is composed of an Anderson-Evans POM $\{\text{MnMo}_6\text{O}_{18}\}$ fragment and two triply deprotonated ligands $\{(\text{OCH}_2)_3\text{CN}=\text{CH}(4\text{-C}_5\text{H}_4\text{N})\}^3$. The general description of this kind of compound was explained at the beginning of this chapter.

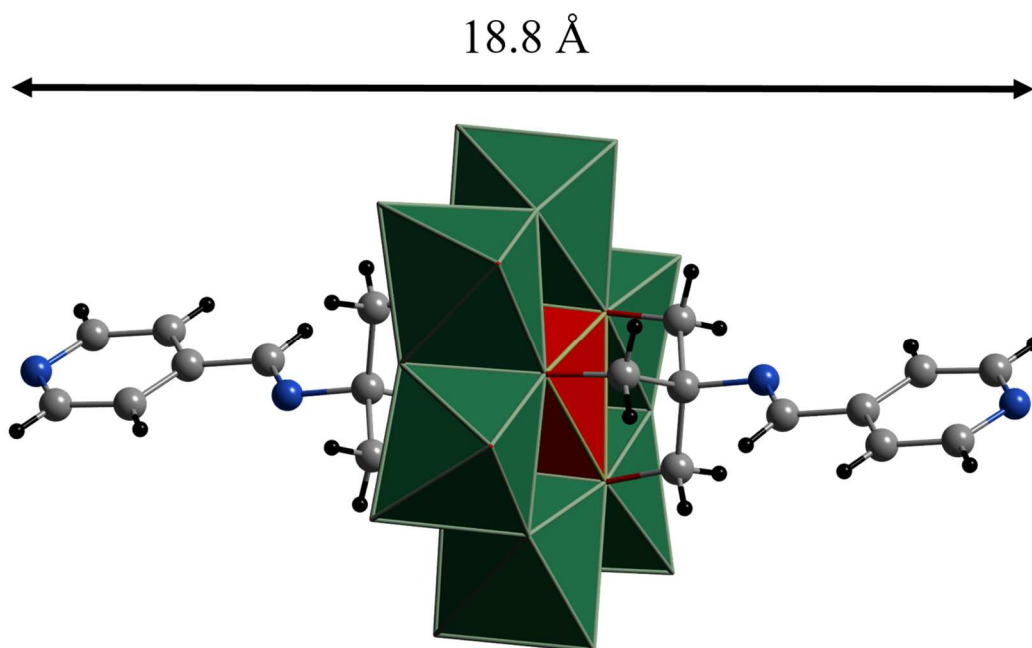


Figure 5.1: L – POM – L moiety in (**4**). Colour code: Anderson-Evans polyanions: green ring with red polyhedral models, H: black, O: red, C: grey, N: blue. TBA counterions and DMF molecules are omitted for clarity.

The $N_{py} - N_{py}$ distance of the ligands attached to the Anderson-Evans POM within one L – POM - L is 18.8 Å. As previously mentioned, the synthesis of **(4)** has already been reported, but so far without any crystal structure. For this reason, there is no possibility to compare the $N_{py} - N_{py}$ distance of compound **(4)** of this work with the previously published one.⁶⁶ Instead, the $N_{py} - N_{py}$ distance can be compared to that of $[MnMo_6O_{18}\{(OCH_2)_3C(4-C_5H_4N)\}_2]^{3-}$ and $[MnMo_6O_{18}\{(OCH_2)_3CNHCO(4-C_5H_4N)\}_2]^{3-}$, which have distances of 14.7 Å and 19 Å, respectively.^{46,47}

The POM hybrid has a total charge of 3-, which is balanced by three tetrabutylammonium ($[N(n-C_4H_9)_4]^+$) cations. Furthermore, there are three DMF molecules per asymmetric unit, whereas one of these was identified in the lattice via the SQUEEZE function within PLATON.¹⁵⁹

5.1.1.2 Powder X-ray diffraction

Figure 5.2 shows the simulated (simu) and experimental (exp) PXRD-patterns of **(4)**. It is clearly seen that the experimental result shows a good accordance to **(4)**-simu. Merely, the ratio of the intensities of the respective reflections differ. This deviation can be explained due to the fact that the simulated pattern was generated from a single crystal measurement made at 180 K, whereas, in contrast, the experimental PXRD was performed at room temperature.

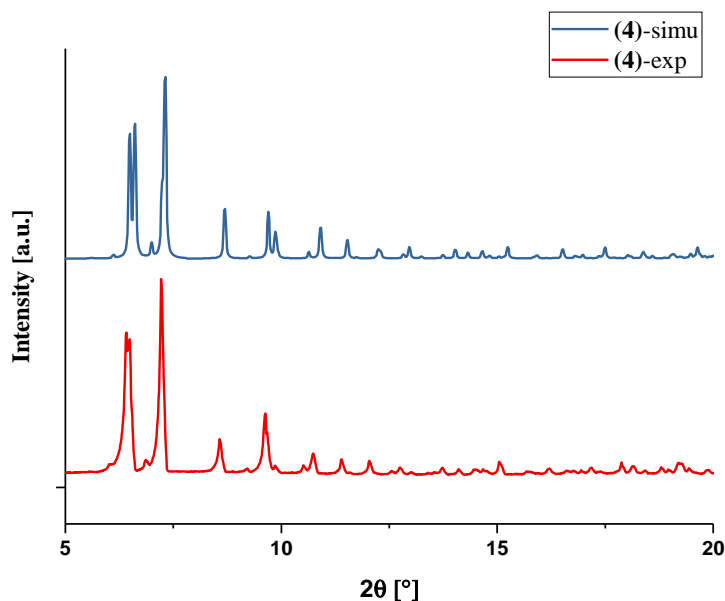


Figure 5.2: Simulated (*simu*) and experimental (*exp*) PXRD-patterns of (4).

5.1.1.3 Solid state UV-vis studies

Figure 5.3 shows the solid state UV-vis spectrum of compound (4). The spectrum reveals one absorption band at $\lambda = 525$ nm, which can be allocated to a d-d electron transfer from the t_{2g} orbital to the e_g^* orbital within one Mn^{3+} ion. Additionally, the maximum absorption at $\lambda = 280$ nm can be assigned to electron transfers from highest occupied molecule orbitals (HOMOs) of oxygen atoms (ligand = e^- -donors) to lowest unoccupied molecular orbitals (LUMOs) of metal atoms (= e^- -acceptors), so-called ligand to metal charge transfer (LMCT). The change of absorbance at $\lambda = 350$ nm was caused by the change of the lamp during the record of the spectrum. The bandgap of 2.85 eV was found using the Tauc method.

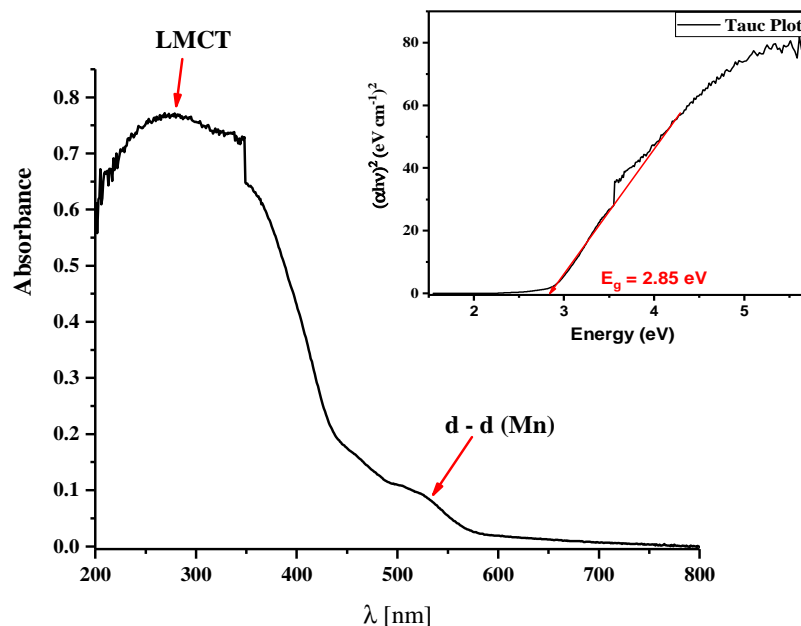


Figure 5.3: Solid state UV-vis spectrum of compound (4).

5.1.1.4 Conclusion

Compound (4) was obtained via a *post*-functionalization by dissolving a mixture of $[N(n\text{-C}_4\text{H}_9)_4]_3[\text{MnMo}_6\text{O}_{18}\{(\text{OCH}_2)_3\text{CNH}_2\}_2]$ (3) and 4-pyridinecarboxaldehyde in DMF, followed by exposure to ether vapour in order to isolate compound (4) in the form of crystals. This is an alternative synthetic route, which simplifies the isolation of the desired product and also gives a higher yield compared to the reported synthesis strategy.⁶⁶ Furthermore, isolation in the form of single crystals allowed for a SCXRD to be performed. The compound was also characterized by PXRD, EA, UV-vis and FT-IR spectroscopy.

5.2 Novel precursors (Pre)

5.2.1 $[N(n\text{-C}_4\text{H}_9)_4]_4[(\text{MnMo}_6\text{O}_{18})((\text{OCH}_2)_3\text{CNHCH}_2(\text{C}_6\text{H}_4)\text{COOH})((\text{OCH}_2)_3\text{CNHCH}_2(\text{C}_6\text{H}_4)\text{COO})]\cdot 3\text{DMF}$ (**5**)

The reaction was carried out by stirring a mixture of $[N(n\text{-C}_4\text{H}_9)_4]_4[\text{Mo}_8\text{O}_{26}]$ (**1**), 4- $\text{HOOC}(\text{C}_6\text{H}_4)\text{CH}_2\text{NHC}(\text{CH}_2\text{OH})_3$ (**L1**), $\text{Mn}(\text{OAc})_3\cdot 2\text{H}_2\text{O}$ and DMF for 22 h at 85 °C. Afterwards, compound (**5**) was isolated as crystalline material by exposure to ether vapour.

5.2.1.1 Single crystal structure

The crystallographic data of compound (**5**) are given in Table 8.2.

The single crystal X-ray diffraction analysis shows that compound (**5**) crystallizes in the monoclinic space group $P2_1/c$ with the unit cell parameters: $a = 22.3589(8)$ Å, $b = 17.1768(9)$ Å, $c = 32.5454(12)$ Å, $\beta = 100.346(3)^\circ$ and $V = 12296.0(9)$ Å³. The structure of the polyanion in (**5**), which is shown in Figure 5.4 (a), is composed of an Anderson-Evans POM $\{\text{MnMo}_6\text{O}_{18}\}$ fragment, one triply deprotonated ligand (**L1**) $\{(\text{OCH}_2)_3\text{CNHCH}_2(\text{C}_6\text{H}_4)\text{COOH}\}^{3-}$ and one fourfold deprotonated ligand (**L1**) $\{(\text{OCH}_2)_3\text{CNHCH}_2(\text{C}_6\text{H}_4)\text{COO}\}^{4-}$.

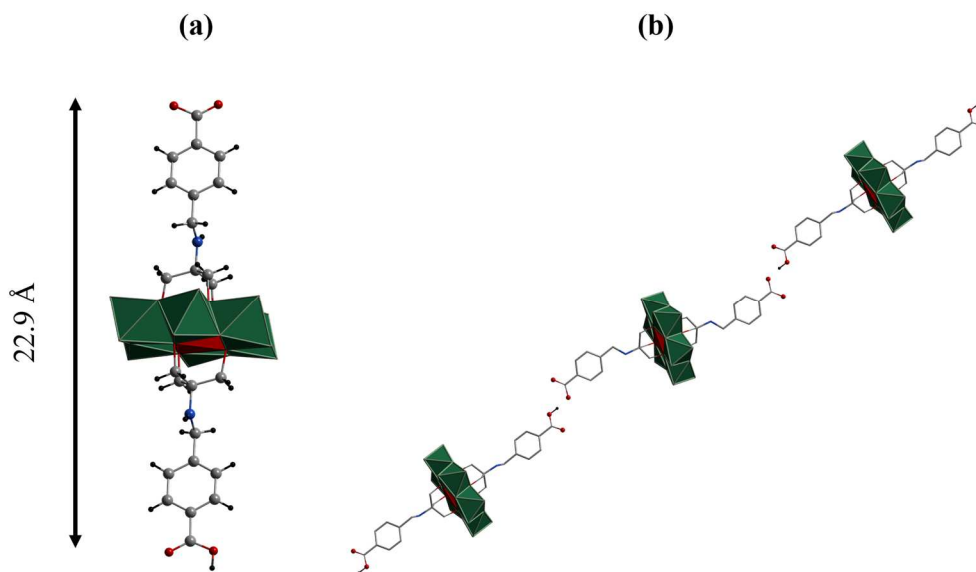


Figure 5.4: *L* – POM – *L* moiety in **(5)**: Single hybrid (a) and 1D “zigzag” chains (b). Colour code: Anderson-Evans polyanions: green ring with red polyhedral models, O: red, C: grey, N: blue, H: black. TBA counterions and DMF molecules are omitted for clarity. For (b): C and N atoms: wire/stick design and only H atoms of carboxylate groups are shown.

The general description of this kind of compound was explained at the beginning of this chapter.

The $O_{\text{COO}} - O_{\text{COO}}$ distance of the ligands attached to the Anderson-Evans POM within one POM hybrid ranges from 22.3 Å to 22.9 Å. In comparison to compound **(4)**, precursor **(5)** is on average 4.3 Å longer.

The POM hybrid has a total charge of 4-, which is balanced by four tetrabutylammonium ($[N(n\text{-C}_4\text{H}_9)_4]^+$) cations. Furthermore, there are three DMF molecules per asymmetric unit, whereas one of these could be identified in the lattice via the SQUEEZE function within PLATON.¹⁵⁹

The single hybrids of **(5)** form 1D zigzag chains via hydrogen bonds between two carboxylate groups of the organic ligands of two different hybrid units. Here, the $\text{H}\cdots\text{O}$ distance between two hybrids is 1.4939(36) Å and the $\text{O-H}\cdots\text{O}$ angle

amounts to 163.6° . According to Legon and Millen, these suggest moderate hydrogen bonds.¹⁶⁰ Figure 5.4 (b) shows one of these “zigzag” chains, where it is also seen that the carboxylate groups of the hybrid in the middle are both deprotonated. On the other hand, the other two hybrids contain protonated carboxylate groups, which means that the hybrid in the middle should have a charge of -5 and the other two polyanions a charge of -3. Due to the fact that the hybrids are in principle identical it can be assumed that statistically each hybrid contains one protonated and one deprotonated ligand and has a charge of -4.

Figure 5.5 shows an extract of the chains formed by the POM hybrids in perspectives along *a*, *b* and *c*-axis, respectively. In the structure, two types of L – POM – L units form the chains resulting in two types of chains with an A-B alternation. For a better understanding, these two types of links within the chains are coloured in green and red. The view along the *b*-axis (see Figure 5.5 (b)) shows that each chain is formed by an A-B alternation of green and red hybrids. It also reveals that in the *a*-*c* plane, the chains lie parallel to each other and the shortest distance between two terminal oxygen atoms of two neighbouring polyanions is 8.7 Å. In the *b*-*c* plane (Figure 5.5 (a)) and the *a*-*b* plane (Figure 5.5 (c)) the chains have a tilted angle of 107.5° and 96.3° , respectively.

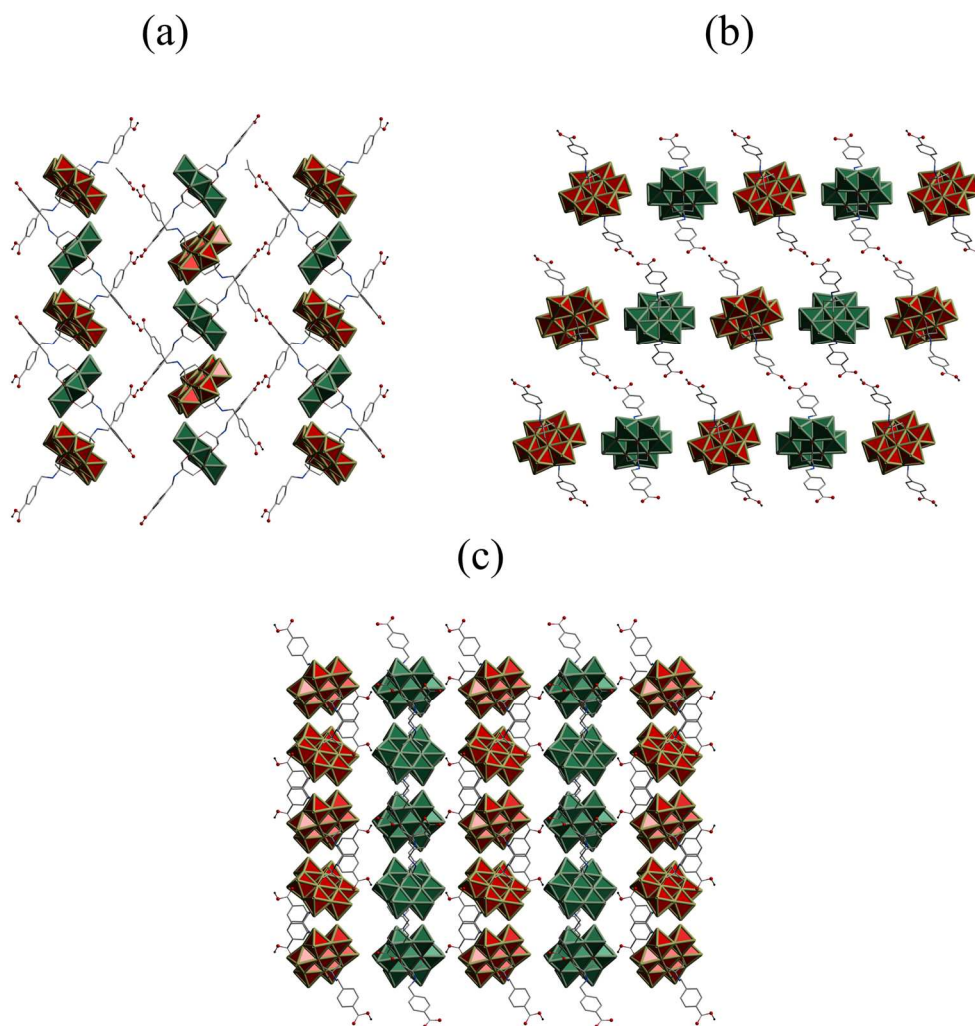


Figure 5.5: View along the *a*-axis (a), *b*-axis (b) and *c*-axis (c). Colour code: Anderson-Evans polyanions: green, red, polyhedral models, O: red, H (only of carboxylate groups): black, C: grey wire/stick, N: blue wire stick. TBA counterions and DMF molecules are omitted for clarity.

5.2.1.2 Powder X-ray diffraction

Figure 5.6 shows the simulated (simu) and experimental (exp) PXRD-patterns of (5). The 2θ values of the reflections of (5)-exp shows a good agreement to (5)-simu.

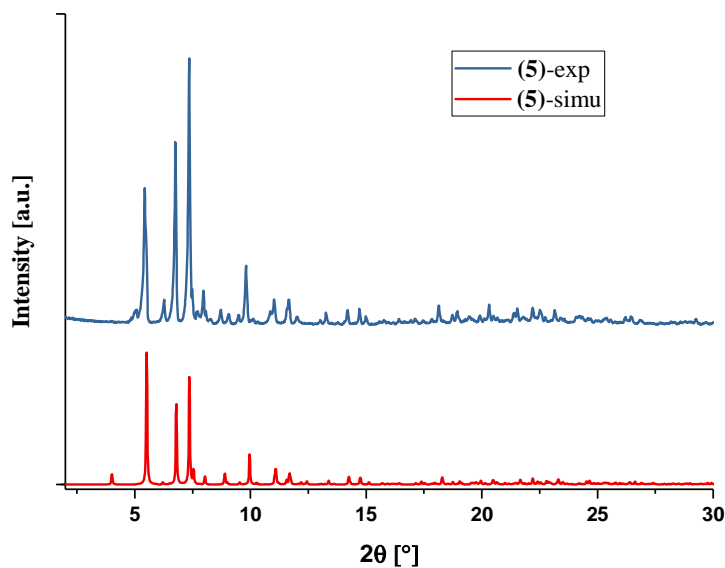


Figure 5.6: Simulated (simu) and experimental (exp) PXRD-patterns of (5).

5.2.1.3 Solid state UV-vis studies

Figure 5.7 shows the solid state UV-vis spectrum of compound (5). The spectrum reveals one absorption band at $\lambda = 524$ nm, which can be allocated to a d-d electron transfer from the t_{2g} orbital to the e_g^* orbital within one Mn^{3+} ion. Furthermore, the maximum absorption at $\lambda = 300$ nm can be allocated to a LMCT. The change of absorbance at $\lambda = 350$ nm was caused by the change of the lamp during the record of the spectrum. The bandgap of 3.12 eV was found using the Tauc method.

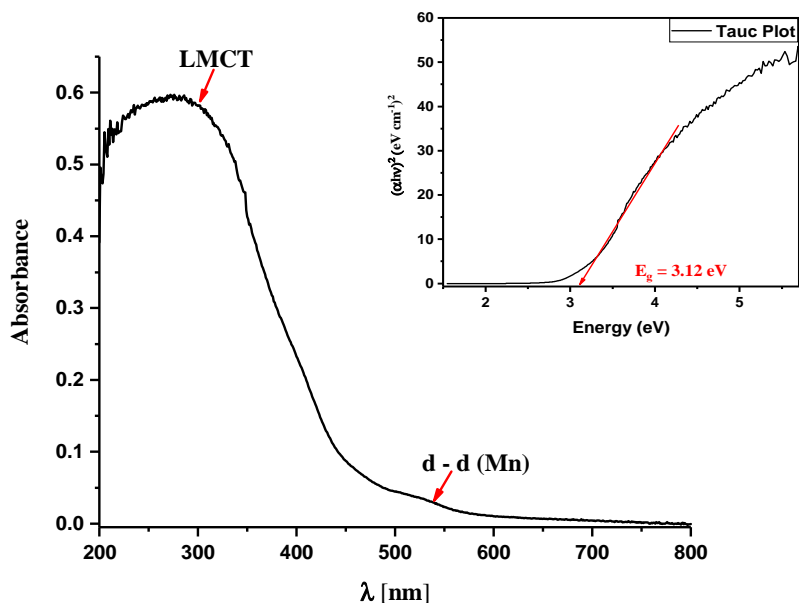


Figure 5.7: Solid state UV-vis spectrum of compound (5).

5.2.1.4 Catalytic studies

Photo-electrocatalytic studies

Photo-electrocatalytic studies of compound (5) were performed with a Xe lamp (300 W) with a 0.33 Hz chop light scan and a potentiometer with linear sweep voltammetry over the range -0.8 V to 1.4 V at a scan rate of 0.01 V/s in 0.5 M Na₂SO₄ (pH = 8.6) solution. A 3-electrode system with Ag/AgCl as a reference electrode and a platinum wire as a counter electrode were used. Compound (5) was taken up in methanol and spin-coated on a ZnO-coated Fluorine-doped Tin Oxide (FTO) substrate and used as working electrode.

The results of the photo-electrocatalytic studies, shown in Figure 5.8, demonstrate that compound (5) is a potential catalyst for water splitting.

By the use of linear sweep voltammetry under irradiation of artificial sunlight (see Figure 5.8 (a)), the current starts to develop at a potential of -0.2 V vs. Ag/AgCl

and shows the highest value of $5.81 \cdot 10^{-1} \text{ mA/cm}^2$ at 1.4 V vs. Ag/AgCl. Due to the fact that these values do not significant change after repeating the measurement another two times, the stability of compound (5) can be confirmed under these conditions.

Since compound (5) was applied onto a ZnO-based substrate and ZnO absorbs light in the UV region, which also has photo-electrocatalytic properties for water splitting, the measurement was repeated with UV-cutoff filter ($< 420 \text{ nm}$) in order to exclude the catalytic effect of the ZnO based substrate (see Figure 5.8 (b)). In addition, three measurements of linear sweep voltammetry were recorded in order to confirm the stability of compound (5) under these conditions.

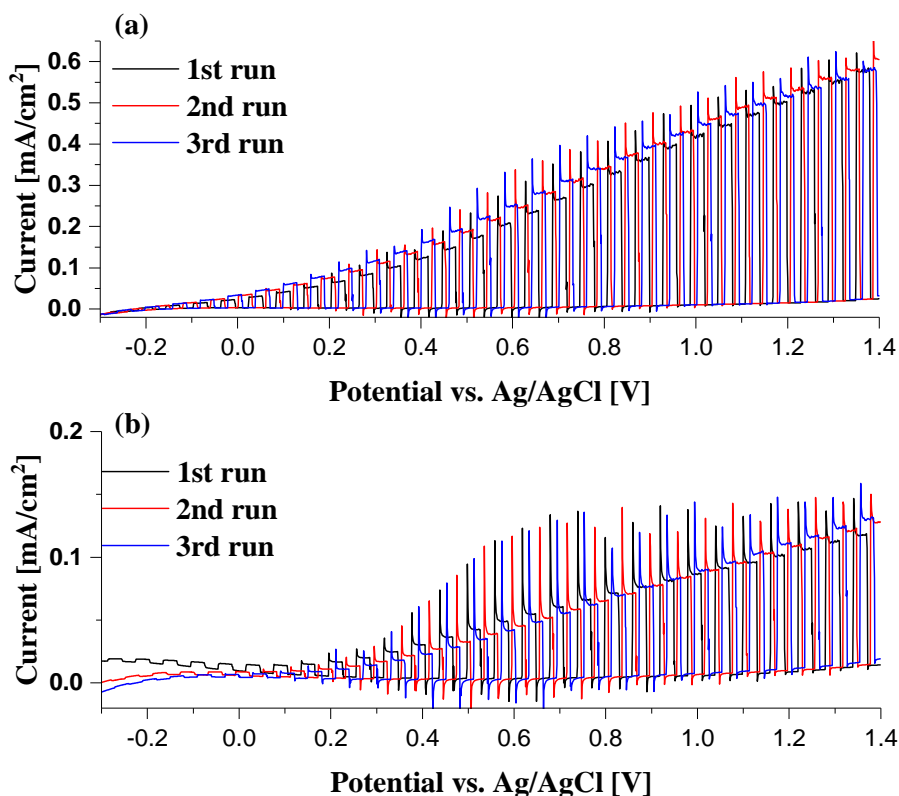


Figure 5.8: Photo-electrocatalytic results of compound (5) recorded in 0.5 M Na₂SO₄ (pH = 8.6) over the range -0.3 V to 1.4 V at a scan rate of 0.01 V/s and sunlight simulation without any filter (a) and with a filter filtering the radiation below 420 nm (b).

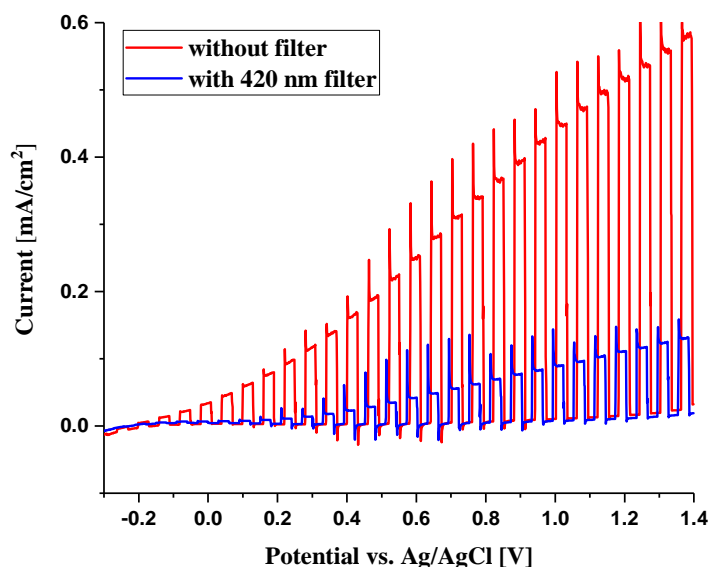


Figure 5.9: Comparison of photocatalytic studies of compound (5) in 0.5 M Na₂SO₄ (pH = 8.6) over the range -0.3 V to 1.4 V at a scan rate of 0.01 V/s: Studies with and without filter (< 420 nm), for comparison in each case the final 3rd cycle was chosen.

Figure 5.9 shows the direct comparison of catalytic studies with and without filter. It is clearly seen that a development of a current with the filter occurs at a potential of 0 V vs. Ag/AgCl, which corresponds to a shift of +0.2 V compared to measurement without any filter. On alternation of the scan rate the current increases to a maximum of $1.31 \cdot 10^{-1}$ mA/cm² at 1.4 V vs. Ag/AgCl. This shows that filtering radiation below 420 nm reduces the catalytic activity of the system by 77 %.

5.2.1.5 Conclusion

Compound (5) was successfully synthesized by stirring a mixture of [N(*n*-C₄H₉)₄][Mo₈O₂₆] (1), (4-C₆H₄COOH)CH₂NHC(CH₂OH)₃ (L1), Mn(OAc)₃·2H₂O and DMF for 22 h at 85 °C and was isolated in the form of crystals, whereby a crystal structure could be determined. Furthermore, this

compound was also characterized by PXRD, EA, UV-vis and FT-IR spectroscopy. Preliminary photo-electrocatalytic studies reveal that compound **(5)** shows catalytic properties applicable to water splitting. These studies require further investigation including optimizing the coating of **(5)** onto the substrate.

5.2.2 $[N(n-C_4H_9)_4]_3[(AlMo_6O_{18})((OCH_2)_3CCH_2OCH_2C(CH_2OH)_3)_2] \cdot 2H_2O$ **(6)**

The reaction was carried out via a *pre*-functionalization (section 3.1.1.2.1.1) under solvothermal conditions. A mixture of $Na_3[Al(OH)_6Mo_6O_{18}] \cdot 2nH_2O$ ($n = 2-10$), dipentaerythritol, tetrabutylammonium bromide and H_2O was stirred for 30 min in a Teflon container, which was then sealed in a stainless steel reactor. The reaction mixture was heated to 120 °C within 1 h period and then kept at that temperature for 96 hours, followed by cooling to room temperature with a cooling rate of 3.96 K/h, resulting in white crystalline material.

5.2.2.1 Single crystal structure

The crystallographic data of compound **(6)** are given in Table 8.3.

The single crystal X-ray diffraction analysis reveals that compound **(6)** crystallizes in the monoclinic space group $P2_1/n$ with the unit cell parameters: $a = 13.9305(11) \text{ \AA}$, $b = 23.8385(13) \text{ \AA}$, $c = 15.3355(12) \text{ \AA}$, $\beta = 113.593(7)^\circ$, $V = 4667.0(6) \text{ \AA}^3$. The structure of the polyanion in **(6)**, which is shown in Figure 5.10, is composed of an Anderson-Evans POM $\{AlMo_6O_{18}\}$ fragment and two triply deprotonated dipentaerythritol $\{(OCH_2)_3CCH_2OCH_2C(CH_2OH)_3\}^{3-}$ ligands. The general description of this kind of compound was explained at the beginning of this chapter. The non-coordinating methoxy groups of the organic ligands

attached to the POM unit are disordered and the longest $O_{\text{methoxy}} - O_{\text{methoxy}}$ distance within one L – POM – L is 18.9 Å.

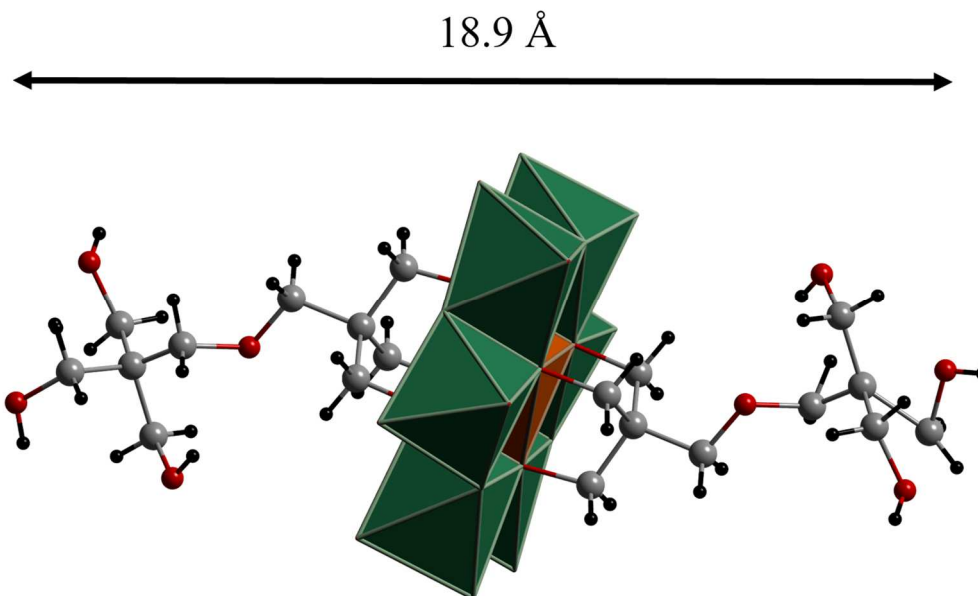


Figure 5.10: L – POM – L unit in **(6)**. One part of disorder is omitted for clarity. Colour code: Anderson-Evans polyanions: green ring with orange polyhedral models, O: red, C: grey, H: black. TBA counterions and water molecules are omitted for clarity.

The POM hybrid has a total charge of 3-, which is balanced by three tetrabutylammonium ($[N(n-C_4H_9)_4]^+$) cations. The *n*-butyl groups of the TBA ions are highly disordered with one disordered over a special position of an inversion centre. The central-N atoms is disordered either side of the inversion centre and could not be refined satisfactorily. The electron density of this TBA ion was calculated using the SQUEEZE function within PLATON.¹⁵⁹ In addition, two lattice water molecules were identified.

The single L – POM – Ls of **(6)** form 1D zigzag chains via hydrogen bonds between a hydroxyl group of the end of a ligand and a terminal oxygen of the $\{AlMo_6O_{18}\}$ unit (see Figure 5.11 and Figure 5.12). Here, the $H \cdots O$ distance between two hybrids is 1.93 Å and the $O-H \cdots O$ angle is in the range 163.3 ° to 133.4 ° due to the

disorder of the ligand. According to Legon and Millen, these suggest moderate hydrogen bonds.¹⁶⁰

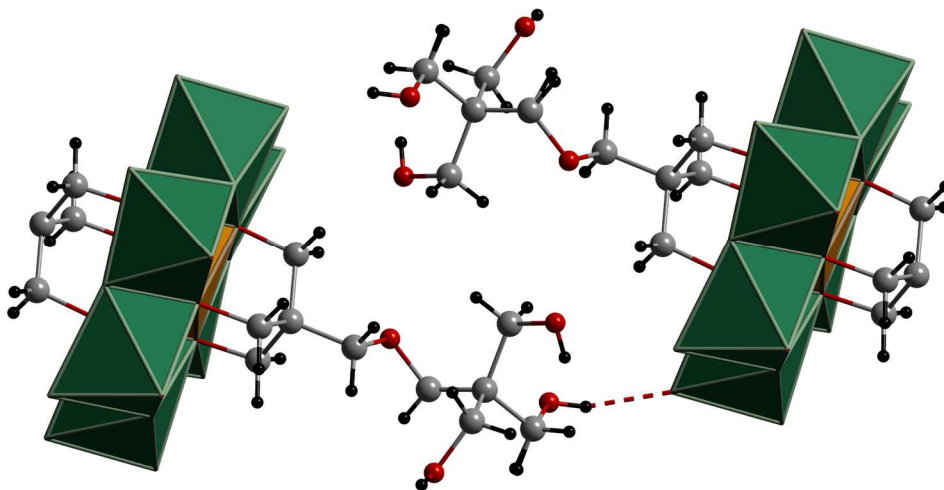


Figure 5.11: H-bond between a hydroxyl group of the end of a ligand and a terminal oxygen of the $\{AlMo_6O_{18}\}$ unit. Only H atoms of hydroxyl groups are shown. Colour code: Anderson-Evans polyanions: green ring with orange polyhedral models, O: red, C: grey, H: black. TBA counterions and water molecules are omitted for clarity.

Figure 5.12 shows an extract of the chains formed by the POM hybrids along a , b and c -axis, respectively, whereas the view long the c -axis shows the side view of the chains. In the crystal structure, two different types of chains with an A-B alternation are present. The tilted angle between two of these chains amounts to $162.472(542)^\circ$. Furthermore, the chains might be held together by electrostatic interaction of H_2O molecules and TBA cations.

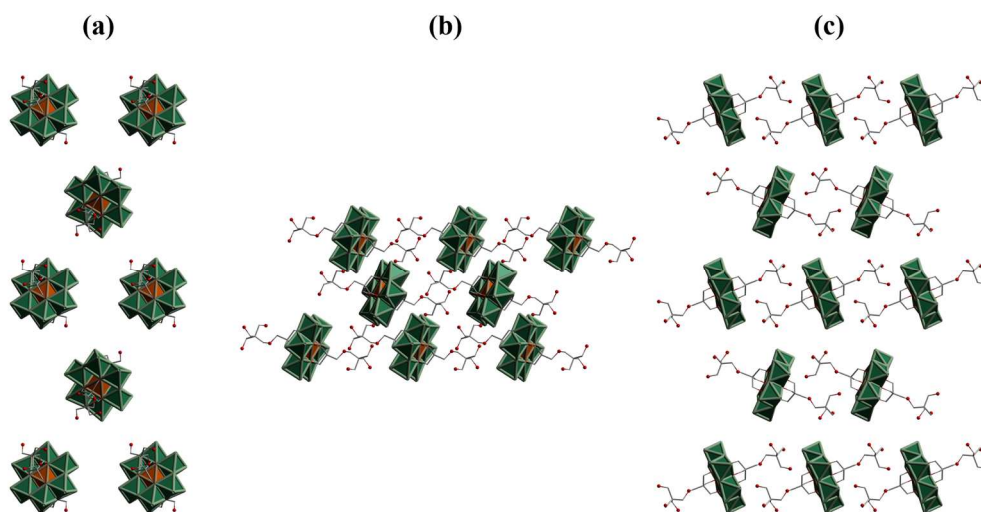


Figure 5.12: View along the *a*-axis (a), *b*-axis (b) and *c*-axis (c). Colour code: Anderson-Evans polyanions: green ring with orange polyhedral models, O: red, C: grey wire/stick. TBA counterions, water molecules and H atoms are omitted for clarity.

5.2.2.2 Powder X-ray diffraction

Figure 5.13 shows the simulated (simu) and experimental (exp) PXRD-patterns of (6). The comparison of both patterns show that the ratio of intensities of reflections and their shifts along the 2θ axis are not in good accordance. This deviation can be explained due to the fact that the simulated pattern was generated from a single crystal measurement made at 180 K, whereas, in contrast, the experimental PXRD was performed at room temperature and it is impossible to account for a solvent loss.

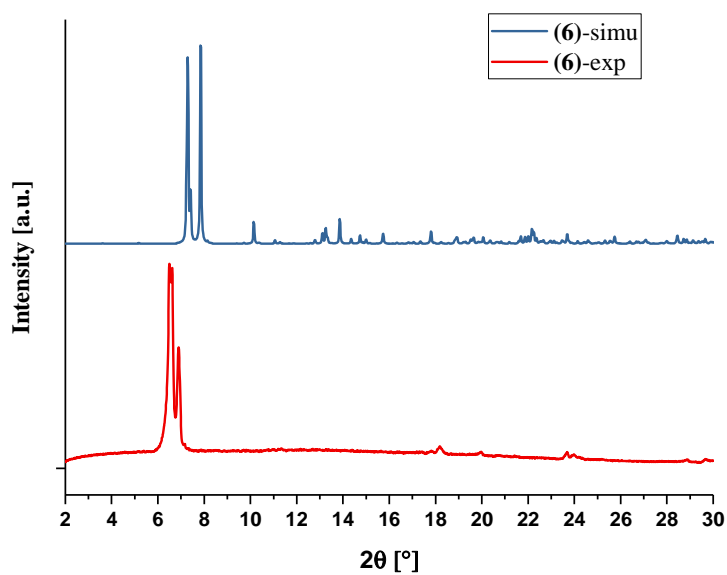


Figure 5.13: Simulated (*simu*) and experimental (*exp*) PXRD-patterns of (6).

5.2.2.3 Solid state UV-vis studies

Figure 5.14 shows the solid state UV-vis spectrum of compound (6). The spectrum reveals one maximum absorption at $\lambda = 258$ nm, which can be assigned as LMCT. No d-d transitions are observed in line with the lack of d electrons. The bandgap of 3.77 eV was found using the Tauc method.

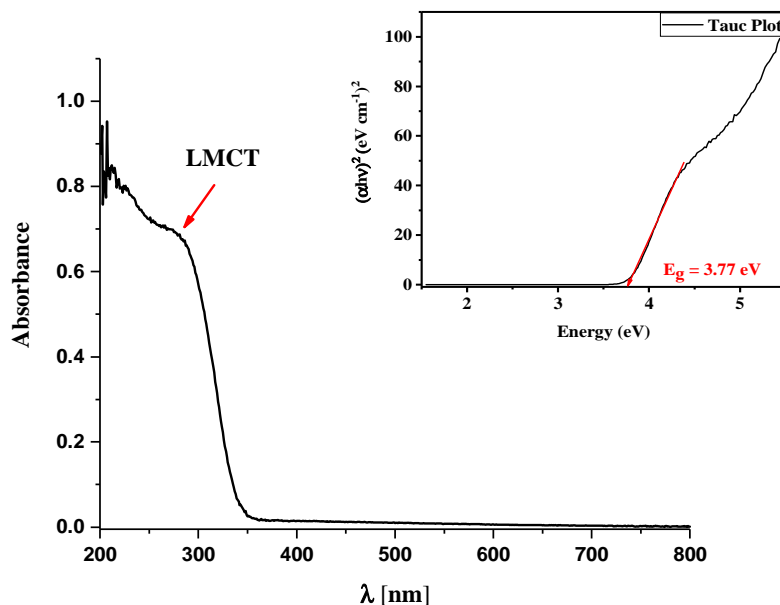


Figure 5.14: Solid state UV-vis spectrum of compound (6).

5.2.2.4 Conclusion

Compound (6) was successfully synthesized via a *pre*-functionalization under solvothermal conditions and isolated in the form of crystals. The crystal structure reveals that the hybrids form 1D zigzag chains via hydrogen bonds between an methoxy group of one hybrid and a terminal oxygen of a neighbouring hybrid. Furthermore, (6) was also characterized by PXRD, EA, UV-vis and FT-IR spectroscopy. This compound, with its terminal oxygen atoms and the organic ligands, is a potential linker for the construction of POMOFs. However, a synthesis of such a framework based on this POM hybrid has not been developed yet.

5.2.3 $[N(n\text{-C}_4\text{H}_9)_4]_3[(\text{MnMo}_6\text{O}_{18})\{(\text{OCH}_2)_3\text{CNH}(\text{C}_6\text{H}_4)\text{C}\equiv\text{N}\}_2]\cdot 6\text{MeCN}$ (**7**)

The reaction was carried out by refluxing a mixture of $[N(n\text{-C}_4\text{H}_9)_4]_4[\text{Mo}_8\text{O}_{26}]$ (**1**), 4- $\text{N}\equiv\text{C}(\text{C}_6\text{H}_4)\text{CH}_2\text{NHC}(\text{CH}_2\text{OH})_3$ (**L2**), $\text{Mn}(\text{OAc})_3\cdot 2\text{H}_2\text{O}$ in MeCN for 21 h. The desired compound (**7**) was isolated as crystalline material by exposure to ether vapour.

5.2.3.1 Single crystal structure

The crystallographic data of compound (**7**) are given in Table 8.4.

The single crystal X-ray diffraction analysis reveals that compound (**7**) crystallizes in the triclinic space group $P\bar{1}$ with the unit cell parameters $a = 20.3358(3) \text{ \AA}$, $b = 28.4667(5) \text{ \AA}$, $c = 30.2411(5) \text{ \AA}$, $\alpha = 67.3340(10)^\circ$, $\beta = 70.1380(10)^\circ$, $\gamma = 76.5140(10)^\circ$ and $V = 15087.5(5) \text{ \AA}^3$. The structure of the polyanion in (**7**), which is shown in Figure 5.15, is composed of an Anderson-Evans POM $\{\text{MnMo}_6\text{O}_{18}\}$ fragment and two triply deprotonated ligands (**L2**) $\{4\text{-N}\equiv\text{C}(\text{C}_6\text{H}_4)\text{CH}_2\text{NHC}(\text{CH}_2\text{O})_3\}^{3-}$.

The general description of this kind of compound was explained at the beginning of this chapter.

The $\text{N}_{\text{C}\equiv\text{N}} - \text{N}_{\text{C}\equiv\text{N}}$ distance of the ligands attached to the Anderson-Evans POM within one POM hybrid ranges from 22.1 \AA to 23.7 \AA .

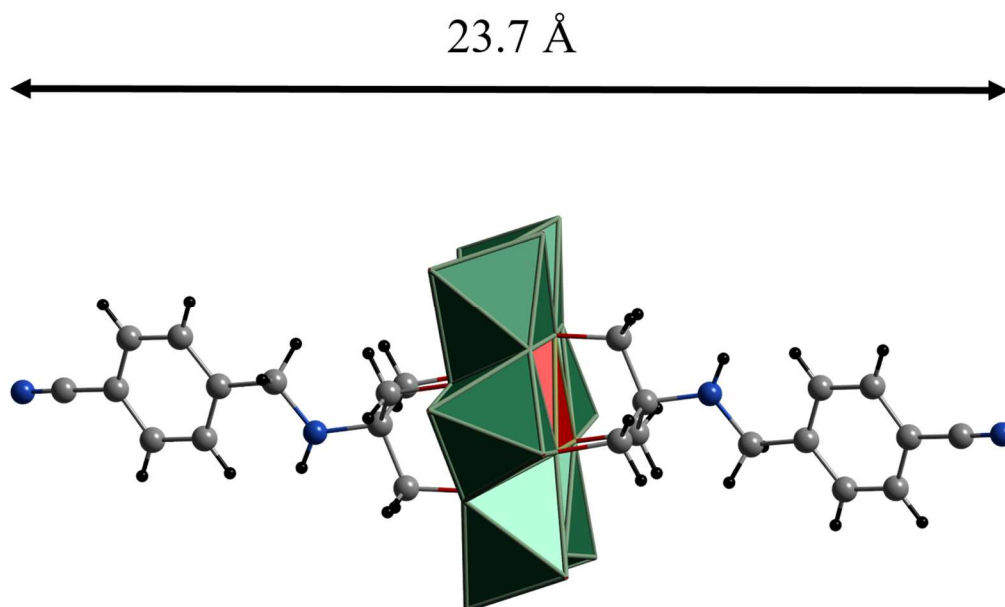


Figure 5.15: L – POM – L moiety in (7). Colour code: Anderson-Evans polyanions: green ring with red polyhedral models, O: red, C: grey, N: blue, H: black. TBA counterions and MeCN molecules are omitted for clarity.

Figure 5.16 shows an extract of (7) with a disordered organic ligand. This disorder can be explained by the inversion of the nitrogen in the amine, which connects the Tris unit with the organic residue.¹⁶¹ Furthermore, most of the structures of this work contain this kind of disorder caused by the kink at N atoms (kink at N disorder). Not only amines but also Schiff bases are affected by this effect.

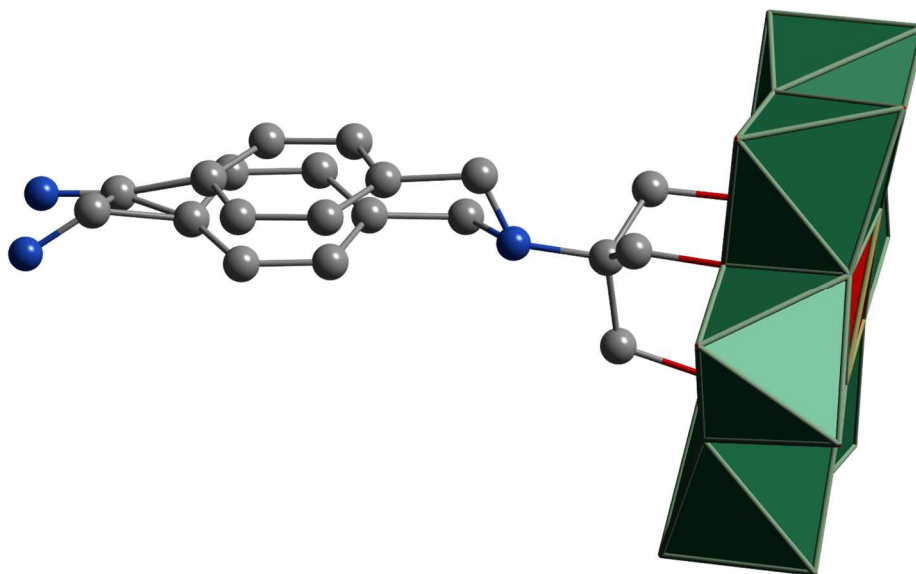


Figure 5.16: *L* – POM moiety in (7) with disordered organic ligand. Colour code: Anderson-Evans polyanions: green ring with red polyhedral models, O: red, C: grey, N: blue. TBA counterions, MeCN molecules and H atoms are omitted for clarity.

The POM hybrid has a total charge of 3-, which is balanced by three tetrabutylammonium ($[N(n-C_4H_9)_4]^+$) cations. Furthermore, there are eighteen MeCN molecules per asymmetric unit, whereas eleven of these could be identified in the lattice via the SQUEEZE function within PLATON.¹⁵⁹

5.2.3.2 Powder X-ray diffraction

Figure 5.17 shows the simulated (simu) and experimental (exp) PXRD-patterns of (7). It is clearly seen that the experimental result shows a good accordance to (7)-simu. The five weak low angle reflections in the simulated pattern are not observable in the measured one as a result of the signal to noise ratio at low diffractions angles.

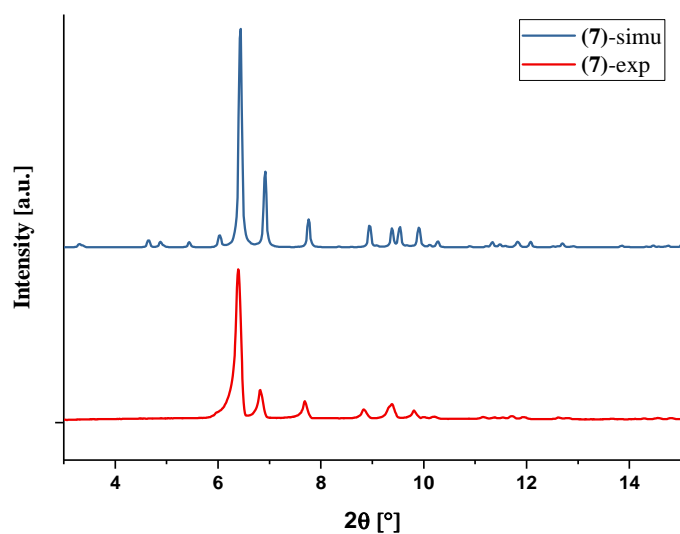


Figure 5.17: Simulated (*simu*) and experimental (*exp*) PXRD-patterns of (7).

5.2.3.3 Solid state UV-vis studies

Figure 5.18 shows the solid state UV-vis spectrum of compound (7). The spectrum reveals one absorption band at $\lambda = 527$ nm, which can be assigned to a d-d electron transfer from the t_{2g} orbital to the e_g^* orbital within one Mn^{3+} ion. The maximum absorption at $\lambda = 271$ nm can be allocated to a LMCT. The change of absorbance at $\lambda = 350$ nm was caused by the change of the lamp during the record of the spectrum. The bandgap of 3.12 eV was found using the Tauc method.

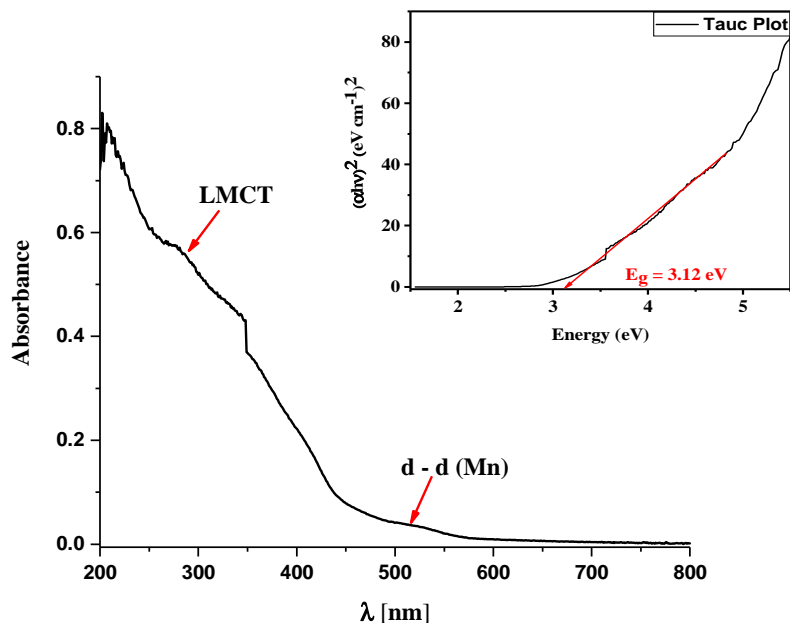


Figure 5.18: Solid state UV-vis spectrum of compound (7).

5.2.3.4 Conclusion

Compound (7) was successfully synthesized by refluxing a mixture of $[N(n\text{-C}_4\text{H}_9)_4]_4[\text{Mo}_8\text{O}_{26}]$ (**1**), $4\text{-N}\equiv\text{C}(\text{C}_6\text{H}_4)\text{CH}_2\text{NHC}(\text{CH}_2\text{OH})_3$ (**L2**), $\text{Mn}(\text{OAc})_3 \cdot 2\text{H}_2\text{O}$ and MeCN for 21 h and was isolated in the form of crystals, whereby a crystal structure could be determined. Furthermore, this compound was also characterized by PXRD, EA, UV-vis and FT-IR spectroscopy. This compound, with its terminal oxygen atoms and the organic ligands, is a potential linker for the construction of POMOFs. However, a synthesis of such a framework based on this L – POM - L has not been developed yet. Although amorphous material results from reactions aimed at creating frameworks no single crystals have been obtained to date.

5.2.4 $[N(n\text{-C}_4\text{H}_9)_4]_3[\text{MnMo}_6\text{O}_{18}\{(\text{OCH}_2)_3\text{CNHC}=\text{O}(\text{C}_6\text{H}_4\text{NO}_2)\}_2]\cdot 6\text{DMF}$ (**8**)

The reaction was carried out by stirring a mixture of $[N(n\text{-C}_4\text{H}_9)_4]_4[\text{Mo}_8\text{O}_{26}]$ (**1**), 4- $\text{NO}_2(\text{C}_6\text{H}_4)\text{C}=\text{ONHC}(\text{HOCH}_2)_3$ (**L3**), $\text{Mn}(\text{OAc})_3\cdot 2\text{H}_2\text{O}$ and DMF for 24 h at 85 °C. Afterwards, compound (**8**) was isolated as crystalline material by exposure to ether vapour.

5.2.4.1 Single crystal structure

The crystallographic data of compound (**8**) are given in Table 8.5.

The single crystal X-ray diffraction analysis reveals that compound (**8**) crystallizes in the orthorhombic space group *Pbcn* with the unit cell parameters: $a = 63.585(4)$ Å, $b = 18.1926(12)$ Å, $c = 26.6998(12)$ Å, $V = 30886(3)$ Å³. The structure of the polyanion in (**8**), which is shown in Figure 5.19, is composed of an Anderson-Evans POM $\{\text{MnMo}_6\text{O}_{18}\}$ fragment and two triply deprotonated ligands (**L3**) $\{(\text{OCH}_2)_3\text{CNHC}=\text{O}(\text{C}_6\text{H}_4\text{NO}_2)\}^{3-}$.

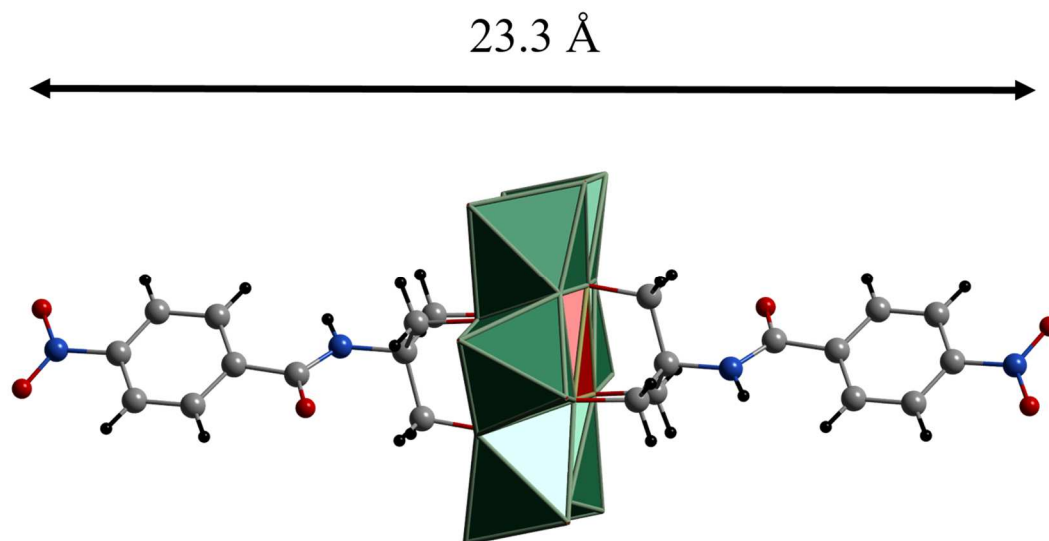


Figure 5.19: L – POM – L unit in (8). Colour code: Anderson-Evans polyanions: green ring with red polyhedral models, O: red, C: grey, N: blue, H: black. TBA counterions, DMF molecules and H atoms are omitted for clarity.

The general description of this kind of compound was explained at the beginning of this chapter.

The $O_{\text{NOO}} - O_{\text{NOO}}$ distance of the ligands attached to the Anderson-Evans POM within one L – POM - L ranges from 22.8 Å to 23.3 Å.

The POM hybrid has a total charge of 3-, which is balanced by three tetrabutylammonium ($[N(n\text{-C}_4\text{H}_9)_4]^+$) cations.

The asymmetric unit contains one complete $[\text{MnMo}_6\text{O}_{18}\{(\text{OCH}_2)_3\text{CNHC}=\text{O}(\text{C}_6\text{H}_4\text{NO}_2)\}_2]^{3-}$ polyanion, one half of the hybrid $[\text{MnMo}_6\text{O}_{18}\{(\text{OCH}_2)_3\text{CNHC}=\text{O}(\text{C}_6\text{H}_4\text{NO}_2)\}_2]^{3-}$, 4.5 tetrabutylammonium cations and 6 DMF molecules, whereas four of the cations and four DMF molecules could be refined, the N atom and one *n*-butyl group of the remaining half of a TBA cation are disordered about the twofold axis. The remaining *n*-butyl groups are disordered, thus the cation could not be refined satisfactorily. Electron density apparently resulting from two further DMF molecules was also observed, but could not be

modelled. The contribution of the half cation and two DMF molecules were therefore modelled using the SQUEEZE function within PLATON.¹⁵⁹

5.2.4.2 Powder X-ray diffraction

Figure 5.20 shows the simulated (simu) and experimental (exp) PXRD-patterns of **(8)**. It is clearly seen that the experimental result shows a good accordance to **(8)**-simu.

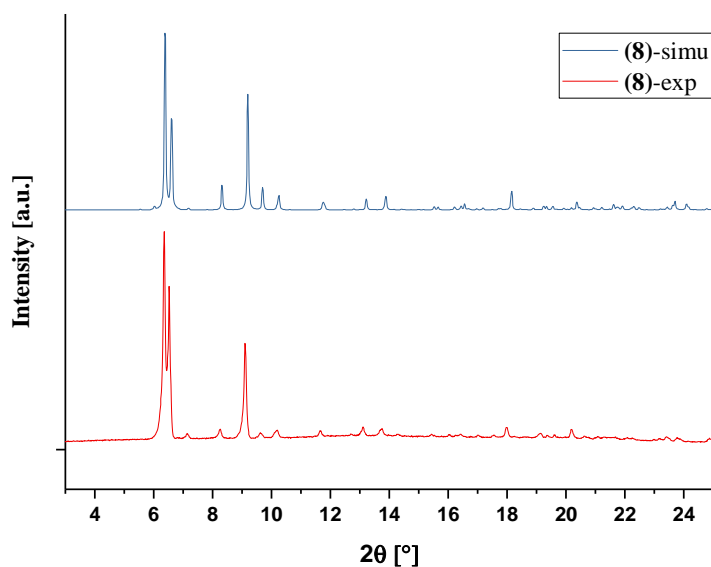


Figure 5.20: Simulated (simu) and experimental (exp) PXRD-patterns of **(8)**.

5.2.4.3 Solid state UV-vis studies

Figure 5.21 reveals the solid state UV-vis spectrum of compound **(8)**. The spectrum shows one absorption band at $\lambda = 526$ nm, which can be allocated to a d-d electron transfer from the t_{2g} orbital to the e_g^* orbital within one Mn^{3+} ion. The maximum absorption at $\lambda = 291$ nm can be allocated to a LMCT. The change of absorbance

at $\lambda = 350$ nm was caused by the change of the lamp during the record of the spectrum. The bandgap of 2.92 eV was found using the Tauc method.

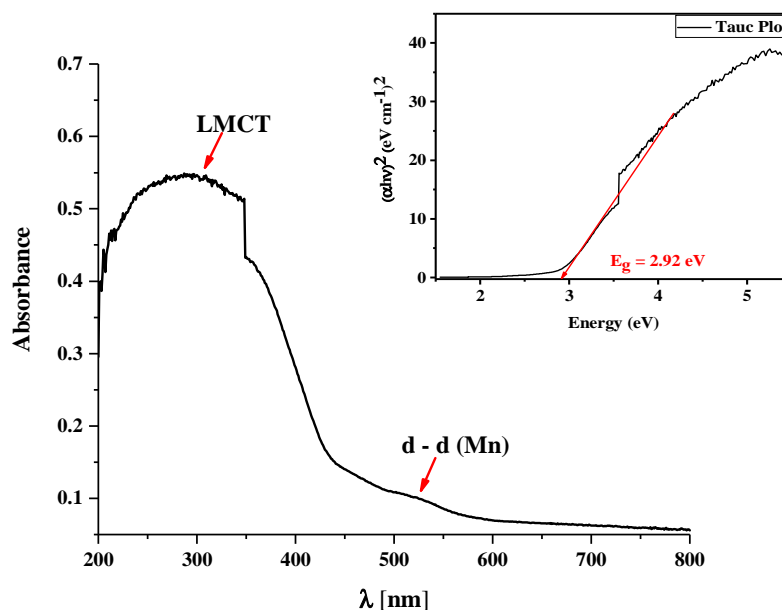


Figure 5.21: Solid state UV-vis spectrum of compound (8).

5.2.4.4 Conclusion

Compound (8) was successfully synthesized by stirring a mixture of $[N(n-C_4H_9)_4]_4[Mo_8O_{26}]$ (1), 4-NO₂(C₆H₄)C=ONHC(HOCH₂)₃ (L3), Mn(OAc)₃·2H₂O and DMF for 24 h at 85 °C and was isolated in the form of crystals, whereby a crystal structure could be determined. Furthermore, this compound was also characterized by PXRD, EA, UV-vis and FT-IR spectroscopy. This compound, with its terminal oxygen atoms and the organic ligands, is a potential linker for the construction of POMOFs. The nitro group can be converted into an amine group and thus become a suitable functional group for building up

networks. However, a synthesis of such a framework based on this POM hybrid has not been developed yet.

5.2.5 Steps towards developing the POM as linker strategy (c) to the synthesis of POMOFs

5.2.5.1 $[N(n\text{-C}_4\text{H}_9)_4]_3[(\text{MnMo}_6\text{O}_{18})((\text{OCH}_2)_3\text{CNH}(\text{C}_6\text{H}_5)_2)]\cdot\text{MeCN}\cdot\text{H}_2\text{O}$ (**9**)

The first strategy was to synthesize (**9**) as a “proof of principle” if the “inverse” POMOF methodology might prove fruitful. This approach inverts the nature of the node to be organic rather than inorganic. For reasons of wanting to establish a robust and simple approach this line of inquiry was abandoned. The reaction was carried out by refluxing a mixture of $[N(n\text{-C}_4\text{H}_9)_4]_4[\text{Mo}_8\text{O}_{26}]$ (**1**), $(\text{C}_6\text{H}_5)\text{NHC}(\text{CH}_2\text{OH})_3$ (**L4**), $\text{Mn}(\text{OAc})_3\cdot 2\text{H}_2\text{O}$ and MeCN for 19 h. Afterwards, compound (**9**) was isolated as crystalline material by exposure to ether vapour.

5.2.5.2 Single crystal structure

The crystallographic data of compound (**9**) are given in Table 8.6.

The single crystal X-ray diffraction analysis reveals that compound (**9**) crystallizes in the triclinic space group $P\bar{1}$ with the unit cell parameters $a = 13.9550(10)$ Å, $b = 17.1438(14)$ Å, $c = 19.1438(16)$ Å, $\alpha = 81.478(7)^\circ$, $\beta = 78.320(6)^\circ$, $\gamma = 83.957(6)^\circ$ and $V = 4422.2(6)$ Å³. The structure of the polyanion in (**9**), which is shown in Figure 5.22, is composed of an Anderson-Evans POM $\{\text{MnMo}_6\text{O}_{18}\}$ fragment and two triply deprotonated ligands (**L4**) $\{(\text{OCH}_2)_3\text{CNHC}_6\text{H}_5\}^{3-}$.

The general description of this kind of compound was explained at the beginning of this chapter.

The $C_{\text{para}}-C_{\text{para}}$ distance of the ligands attached to the Anderson-Evans POM within one L – POM - L amounts to 15.7 Å.

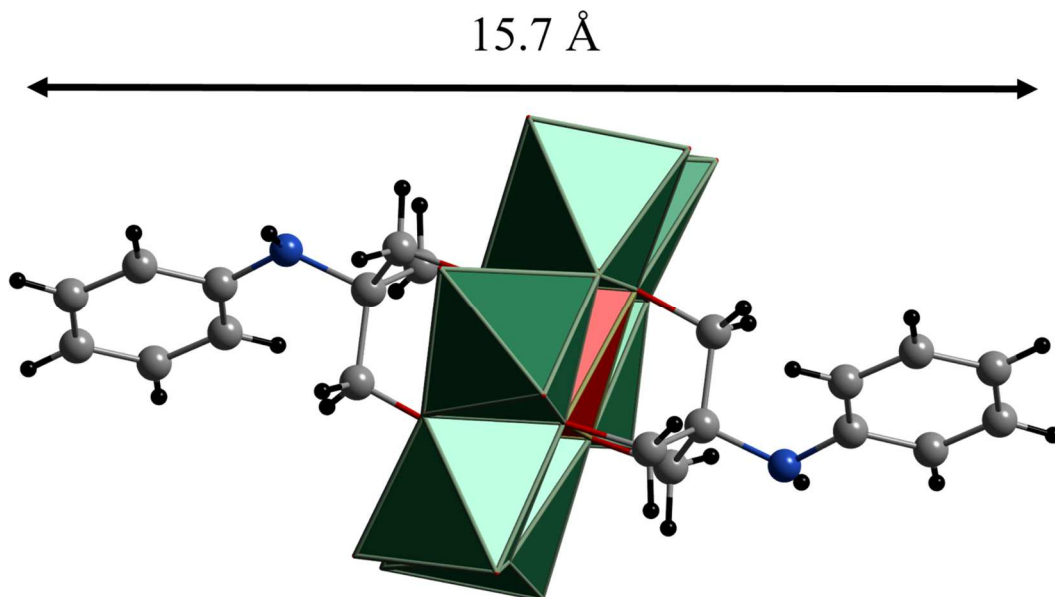


Figure 5.22: L – POM – L unit in (9). Colour code: Anderson-Evans polyanions: green ring with red polyhedral models, O: red, C: grey, N: blue, H: black.

The POM hybrid has a total charge of 3-, which is balanced by three tetrabutylammonium ($[N(n-C_4H_9)_4]^+$) cations. Additionally, there are one MeCN and one water molecules per POM hybrid.

5.2.5.3 Powder X-ray diffraction

Figure 5.23 shows the simulated (simu) and experimental (exp) PXRD-patterns of (9). The comparison of both patterns shows that the simulated pattern is shifted by $+0.3^\circ$ in 2θ . This can be explained, considering the fact that the simulated pattern

was generated from a single crystal measurement made at 180 K, whereas, in contrast, the experimental PXRD pattern was obtained at room temperature.

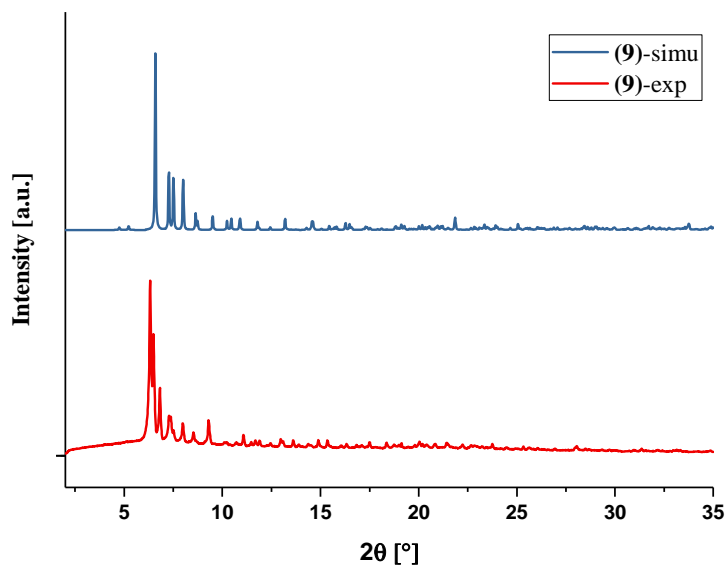


Figure 5.23: Simulated (*simu*) and experimental (*exp*) PXRD-patterns of **(9)**.

5.2.5.4 Solid state UV-vis studies

Figure 5.24 shows the solid state UV-vis spectrum of compound **(9)**. The spectrum reveals one absorption band at $\lambda = 527$ nm, which can be allocated to a d-d electron transfer from the t_{2g} orbital to the e_g^* orbital within one Mn^{3+} ion. Furthermore, the maximum absorption at $\lambda = 278$ nm can be allocated to a LMCT. The change of absorbance at $\lambda = 350$ nm was caused by the change of the lamp during the record of the spectrum. The bandgap of 2.83 eV was found using the Tauc method.

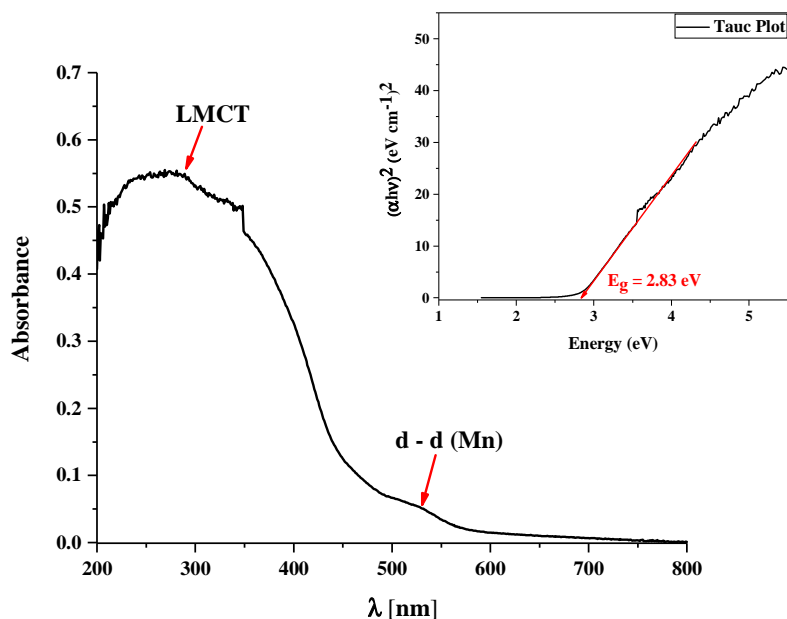


Figure 5.24: Solid state UV-vis spectrum of compound (9).

5.2.5.5 Conclusion

Compound (9), which was designed to test an inversive approach, was successfully synthesized by refluxing a mixture of $[N(n\text{-C}_4\text{H}_9)_4]_4[\text{Mo}_8\text{O}_{26}]$ (1), $(\text{C}_6\text{H}_5)\text{NHC}(\text{CH}_2\text{OH})_3$ (L4), $\text{Mn}(\text{OAc})_3 \cdot 2\text{H}_2\text{O}$ and MeCN for 19 h and was isolated in the form of crystals, whereby a crystal structure could be determined. Furthermore, this compound was also characterized by PXRD, EA, UV-vis and FT-IR spectroscopy. The L – POM - L can be further modified by e.g. Friedel-Crafts acylation/alkylation. This compound is a potential linker for the construction of POMOFs. However, this synthetic approach demands too many steps creating the desired POMOFs.

5.2.6 $[N(n\text{-C}_4\text{H}_9)_4]_2[\text{Mn}_2\text{Mo}_4\text{O}_{14}((\text{OCH}_2\text{CH}_2)_2\text{NCH}_2\text{CH}_2\text{OH})_2]$ (**10**)

In order to see if trialcohol ligands could be used to occupy the μ_3 -OR sited of the Anderson-Evans POM, the use of triethanolamine was explored. Under the conditions used two crystalline products could be isolated. One is the previously reported $[\text{MoO}_2\{(\text{HOC}_2\text{H}_4\text{N}(\text{C}_2\text{H}_4\text{O})_2)\}]^{158}$ (see Figure 5.25) and the second is (**10**). As already described in section 4.4.9 compound (**10**) can be isolated using fractional crystallization. Neither compound involves the Anderson-Evans POM but compound (**10**) does have a heterometallic POM core. The reaction was carried out by refluxing a mixture of $[N(n\text{-C}_4\text{H}_9)_4]_4[\text{Mo}_8\text{O}_{26}]$ (**1**), triethanolamine (TEAH_3), $\text{Mn}(\text{OAc})_3 \cdot 2\text{H}_2\text{O}$ and MeCN for 20 h. Afterwards, compound (**10**) was isolated as crystalline material by exposure to ether vapour.

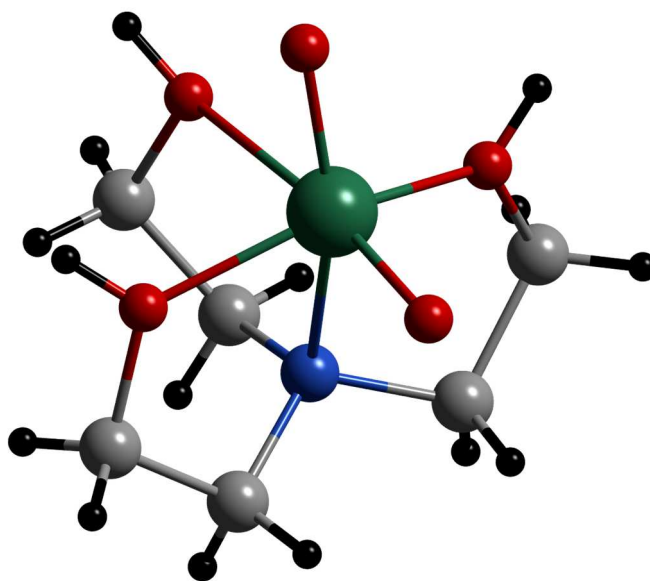


Figure 5.25: Structure of $[\text{MoO}_2\{(\text{HOC}_2\text{H}_4\text{N}(\text{C}_2\text{H}_4\text{O})_2)\}]$. Colour code: Mo: green, O: red, C: grey, N: blue, H: black.

5.2.6.1 Single crystal structure

The crystallographic data of compound **(10)** are given in Table 8.7.

Compound $[\text{Mn}_2\text{Mo}_4(\mu_2\text{-O})_6(\text{O}_t)_8((\mu_3\text{-O})\text{CH}_2\text{CH}_2)_2\text{NCH}_2\text{CH}_2\text{OH}]_2^{2-}$ **(10)** crystallizes in the monoclinic space group $P2_1/n$ with the unit cell parameters: $a = 9.9770(11) \text{ \AA}$, $b = 16.1440(18) \text{ \AA}$, $c = 18.730(2) \text{ \AA}$, $\beta = 95.186(9)^\circ$ and $V = 3004.5(6) \text{ \AA}^3$. The structure of the polyanion in **(10)**, which is shown in Figure 5.26, is composed of the centrosymmetric dianionic heteropolymolybdate $\{\text{Mn}_2\text{Mo}_4\text{O}_{16}\}$ and two twofold deprotonated triethanolamine ligands, whereas the charge of the polyanion is balanced by two tetrabutylammonium cations.

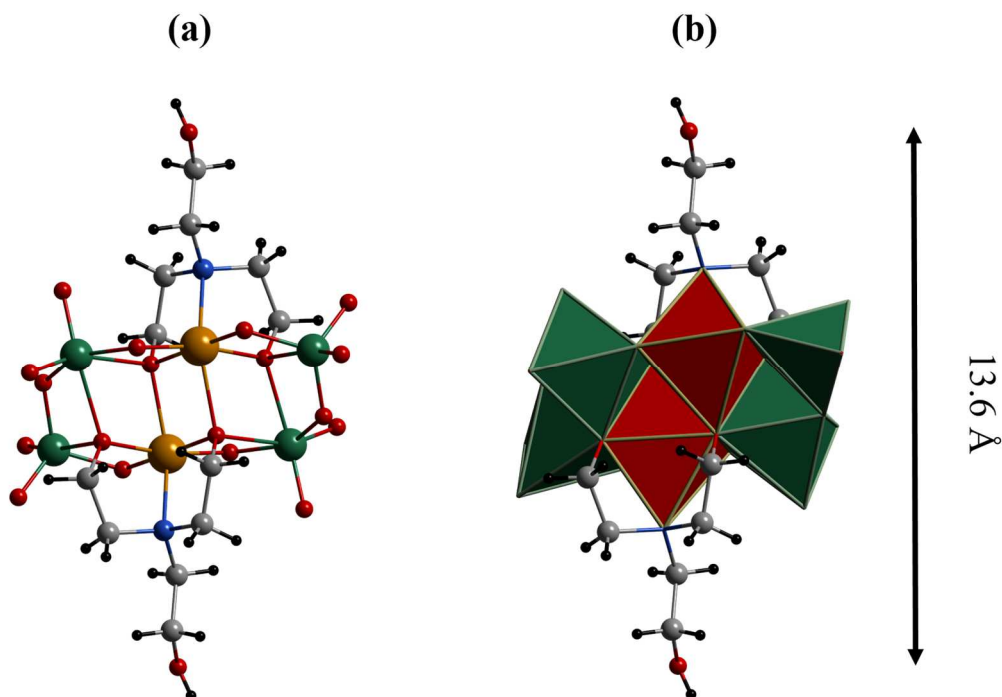


Figure 5.26: L – POM – L moiety in **(10)** without (a) and with (b) polyhedral model. Colour code: MoO₆/ MoO₅: green polyhedra, MnO₅N: red polyhedra, Mn: orange, Mo: green, O: red, C: grey, N: blue, H: black. TBA counterions are omitted for clarity.

The inorganic core structure is built from two $\{\text{Mo}^{6+}\text{O}_6\}$, two $\{\text{Mo}^{6+}\text{O}_5\}$ and two $\{\text{Mn}^{3+}\text{O}_5\text{N}\}$ moieties. The oxidation states of the metal centres were calculated by valance sum calculator. As shown in Figure 5.26 the Mn atoms are opposite to each other and each Mn atom is between two Mo atoms. This means that each $\{\text{MnO}_5\text{N}\}$ octahedron is edge sharing with a $\{\text{MoO}_6\}$ octahedron and a $\{\text{MoO}_5\}$ pentahedron, whereas a $\{\text{MoO}_6\}$ and a $\{\text{MoO}_5\}$ unit, which are opposite to each other, are sharing an edge.

The analysis with the computer program SHAPE¹⁵⁶ reveals that the geometries of the five-coordinated Mo atom in the $\{\text{MoO}_5\}$ unit, the six-coordinated Mo atom in the $\{\text{MoO}_6\}$ moiety and the six-coordinated Mn atom in the $\{\text{MnO}_5\text{N}\}$ part (shown in Figure 5.27) are distorted from the ideal shape. The deviation value of Mo from the idealized Johnson trigonal bipyramid (JTBPY) geometry is 1.903. In the case of the $\{\text{MoO}_6\}$ moiety, the deviation value of Mo from the idealized pentagonal pyramid (PPY) geometry is 30.345. For Mn in the $\{\text{MnO}_5\text{N}\}$ part, the deviation value from the idealized octahedron (OC) geometry is 2.977. The continuous shape measurements (CShM's) are listed in Table 8.14 in section 8.2.1.

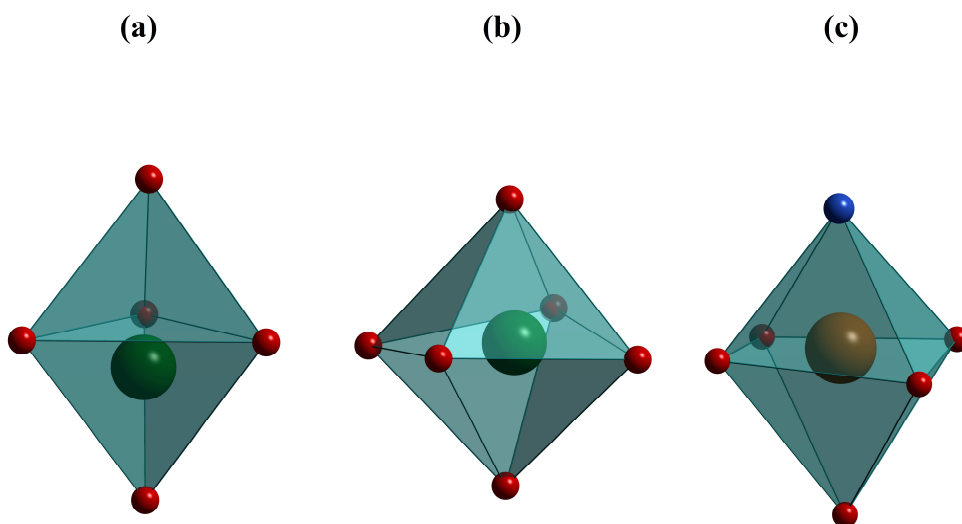


Figure 5.27: Coordination polyhedra of Mo in $\{\text{MoO}_5\}$ (a), Mo in $\{\text{MoO}_6\}$ (b) and Mn in $\{\text{MnO}_5\text{N}\}$ (c).

In the {MoO₆} units the Mo-O bond lengths display large variation ranging from 1.700(2) - 2.3228(19) Å (shortest: Mo-terminal O atom (O_t); longest: Mo-O_{TEA/μ₃-O}), while the O-Mo-O angles are between 68.55(7) - 162.20(10) °.

In the case of the {MoO₅} group the Mo-O bond lengths reach from 1.706(3) - 2.517(2) Å. Also in this case, the largest distance is attributed to a Mo-O_{TEA} and the shortest to a Mo-O_t bond. The O-Mo-O angles extent from 70.70(8) - 170.87(11) °.

In the {MnO₅N} part, the Mn-O distances are between 1.865(2) and 2.315(2) Å, while the O-Mn-O angles are in the region of 74.34(8) - 176.79(10) °. The Mn-N bond length is 2.286(3) Å, whereas the N-Mn-O angles fall in the range 79.32(9) - 148.74(8) °. At the same time, the angle of 148.74(8) ° corresponds to the elongated Jahn-Teller axis of Mn³⁺, which is defined by the N_{TEA} atom of a triethanolamine ligand and an O_{TEA} of a deprotonated ethoxy group of another triethanolamine ligand, lying opposite to each other.

The triethanolamine ligands are connected to the inorganic core via two deprotonated ethoxy groups forming an O_{μ₃} coordination site binding to one Mn and two Mo centres. The third ethoxy group is still protonated and not coordinating to any metal. The O_{ethoxy}-O_{ethoxy} distance between two ends of the ligands within one POM hybrid is 13.6 Å.

5.2.6.2 Powder X-ray diffraction

Figure 5.28 shows the simulated (simu) and experimental (exp) PXRD-patterns of **(10)**. It is clearly seen that the experimental result shows a good accordance to **(10)**-simu.

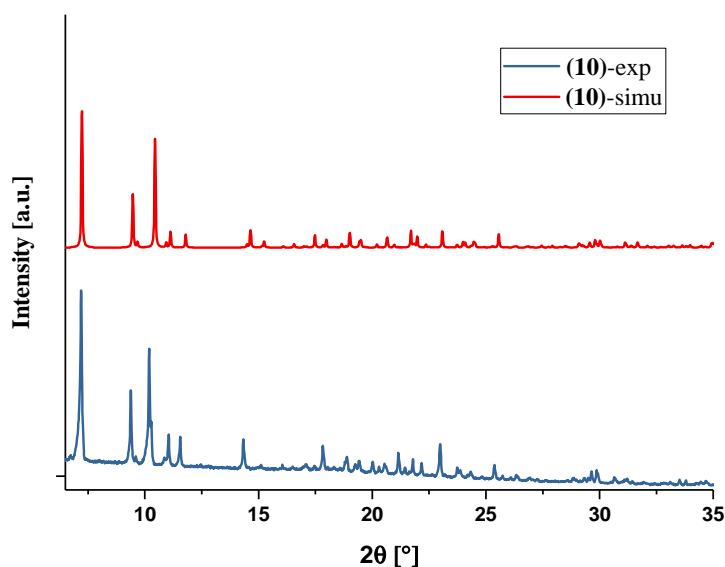


Figure 5.28: Simulated (*simu*) and experimental (*exp*) PXRD-patterns of **(10)**.

5.2.6.3 Solid state UV-vis studies

Figure 5.29 shows the solid state UV-vis spectrum of compound **(10)**. The spectrum reveals three absorption bands at $\lambda = 751$ nm, 534 nm and 479 nm, which can be allocated to d-d electron transfers from the t_{2g} orbital to the e_g^* orbital within one Mn^{3+} ion. The maximum absorption at $\lambda = 290$ nm can be allocated to a LMCT. The change of absorbance at $\lambda = 350$ nm was caused by the change of the lamp during the record of the spectrum. The bandgap of 3.31 eV was found using the Tauc method.

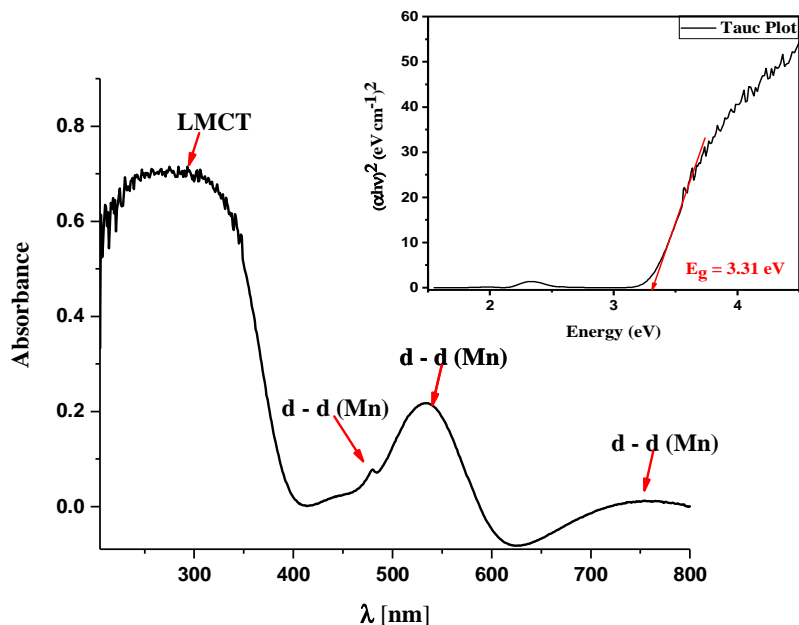


Figure 5.29: Solid state UV-vis spectrum of compound (10).

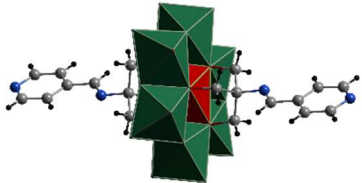
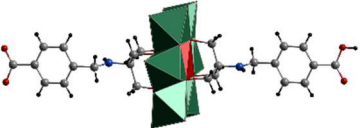
5.2.6.4 Conclusion

Compound (10) was successfully synthesized by refluxing a mixture of $[N(n-C_4H_9)_4]_4[Mo_8O_{26}]$ (1), triethanolamine ($TEAH_3$), $Mn(OAc)_3 \cdot 2H_2O$ and MeCN for 20 h and was isolated in the form of crystals, whereby a crystal structure could be determined. Furthermore, this compound was also characterized by PXRD, EA, UV-vis and FT-IR spectroscopy. This compound, with its terminal oxygen atoms and the organic ligands, is a potential linker for the construction of POMOFs. Furthermore, the hydroxyl groups can be transformed to an azide using NaN_3 and used as a reactive group for click reaction to form a triazole-based network. Though, a synthesis of such a framework based on this POM hybrid has not been developed yet. As a strategy for Anderson-Evans POM-based POMOFs, this clearly needs much more study.

5.3 Extended structures

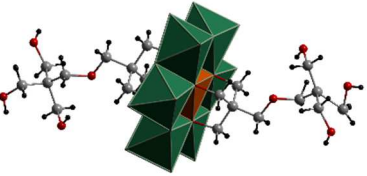
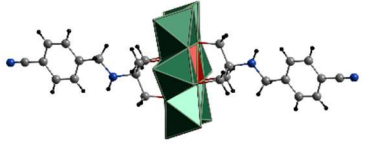
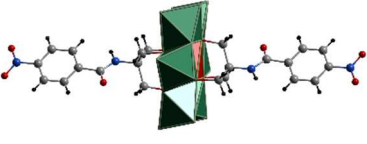
Table 5.1 summarizes the previously reported and novel L – POM – L hybrids.

Table 5.1: Summary of the previously reported and novel L – POM – L hybrids.

L – POM - L	Abbreviation for Linker	Hetero / central atom of POM	Length	Extended structures	functional group	Additional remarks
	no (post-functionalization)	Mn ³⁺	18.8 Å	(13), (14A), (114B), (15)	pyridyl	POMOFs with Cu, Zn and Cd
	L1	Mn ³⁺	22.9 Å	(11), (12)	carboxylate	POMOFs with RE (RE=Y, La – Lu)

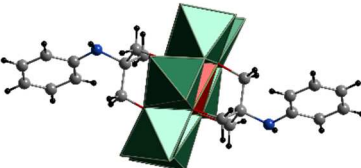
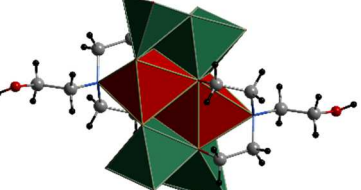
5. Results and Discussion

Table 5.1 continue:

L – POM - L	Abbreviation for Linker	Hetero / central atom of POM	Length	Extended structures	functional group	Additional remarks
	no (commercially available)	Al^{3+}	18.9 Å	no	hydroxyl	no
	L2	Mn^{3+}	23.7 Å	no	nitrile	no
	L3	Mn^{3+}	23.3 Å	no	nitro	no

5. Results and Discussion

Table 5.1 continue:

L – POM - L	Abbreviation for Linker	Hetero / central atom of POM	Length	Extended structures	functional group	Additional remarks
	L4	Mn^{3+}	15.7 Å	no	phenyl	no
	no (commercially available)	Mn^{3+}	13.6 Å	no	hydroxyl	Disruption strategy

5.3.1 Rare earth containing polyoxometalate-based metal organic frameworks (RE-POMOFs)

5.3.1.1 RE(DMF)₆RE(DMF)₅RE₃(DMF)₁₀[(MnMo₆O₁₈)((OCH₂)₃CNHCH₂(C₆H₄)COO)₂]₃·xDMF (RE = La - Nd) (11)

The series of compound comprising the family (11) could be obtained both by layering method and by stirring of the reactants [N(*n*-C₄H₉)₄]₄[(MnMo₆O₁₈)((OCH₂)₃CNHCH₂(C₆H₄)COOH)((OCH₂)₃CNHCH₂(C₆H₄)COO)]·3DMF (5) with the respective RE(NO₃)₃ salt.

5.3.1.1.1 Single crystal structure

For the description of the structure of the series of (11), Ce was chosen as a representative for RE.

The crystallographic data of compound (11)-Ce are given in Table 8.8.

The single crystal X-ray diffraction analysis reveals that compound (11)-Ce crystallizes in the monoclinic space group $P2_1$ with the unit cell parameters: $a = 19.2936(2) \text{ \AA}$, $b = 25.6462(2) \text{ \AA}$, $c = 26.1388(3) \text{ \AA}$, $\beta = 90.1440(10)^\circ$ and $V = 12933.6(2) \text{ \AA}^3$. The network structure of compound (11)-Ce is shown in Figure 5.30 and consists of three $\{(\text{MnMo}_6\text{O}_{18})((\text{OCH}_2)_3\text{CNHCH}_2(\text{C}_6\text{H}_4)\text{COO})_2\}^{5-}$, one $\{\text{Ce}(\text{DMF})_6\}^{3+}$, one $\{\text{Ce}(\text{DMF})_5\}^{3+}$ and one $\{\text{Ce}_3(\text{DMF})_{10}\}^{9+}$ units.

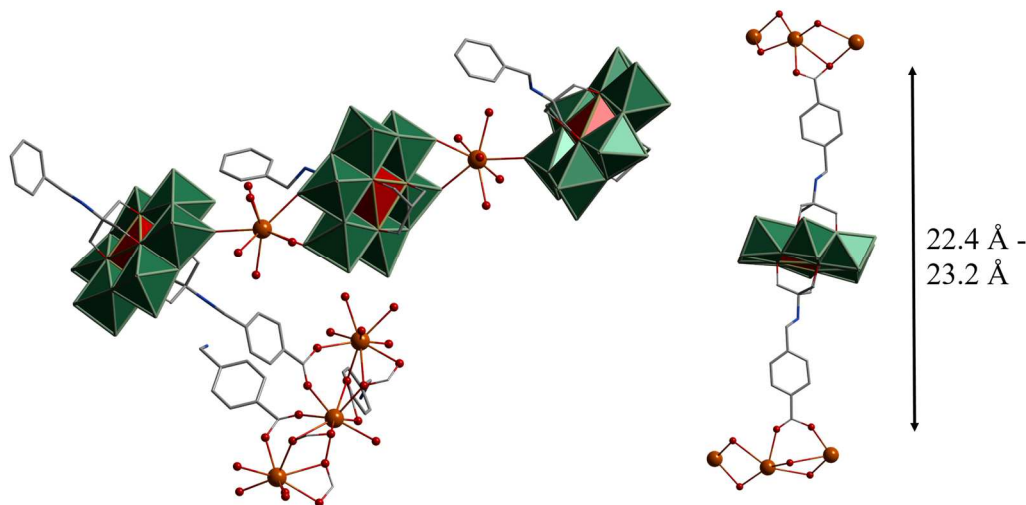


Figure 5.30: Structure of (II)-Ce. Colour code: Anderson-Evans polyanions: green ring with red polyhedral models, Ce: orange, O: red, C: grey wire/stick, N: blue wire/stick. Lattice DMF molecules and H atoms are omitted for clarity. DMF molecules coordinating to Ce atoms are represented by their O atoms.

For a simple description of the structure, Anderson-Evans POMs with different connection modes are marked in different colours. As shown in Figure 5.31 (a) an Anderson-Evans hybrid (shown in green) coordinates to one $\{\text{Ce}(\text{DMF})_5\}^{3+}$ unit (with Ce2 as central atom) via one terminal oxygen (O_t) atom. Furthermore, another Anderson-Evans hybrid (coloured in red) binds to this $\{\text{Ce}(\text{DMF})_5\}^{3+}$ moiety via two O_t atoms opposite to the green Anderson-Evans POM. This red marked Anderson-Evans hybrid is also attached to one $\{\text{Ce}(\text{DMF})_6\}^{3+}$ (with Ce1 as centre) unit through two O_t atoms, which lie across from the two O_t atoms coordinating to the first $\{\text{Ce}(\text{DMF})_5\}^{3+}$ moiety. A third Anderson-Evans hybrid (marked in blue) is connected to the $\{\text{Ce}(\text{DMF})_6\}^{3+}$ unit via one O_t atom opposite to the ones of the red Anderson-Evans polyanion. This blue coloured Anderson-Evans hybrid also links via a carboxylate group, which is part of the organic linker, to one $\{\text{Ce}_3(\text{DMF})_{10}\}^{9+}$ unit. As shown in Figure 5.31 (b), five additional Anderson-Evans POMs coordinate to this $\{\text{Ce}_3(\text{DMF})_{10}\}^{9+}$ unit via carboxylate groups coming from two green, two blue and two red Anderson-Evans hybrids.

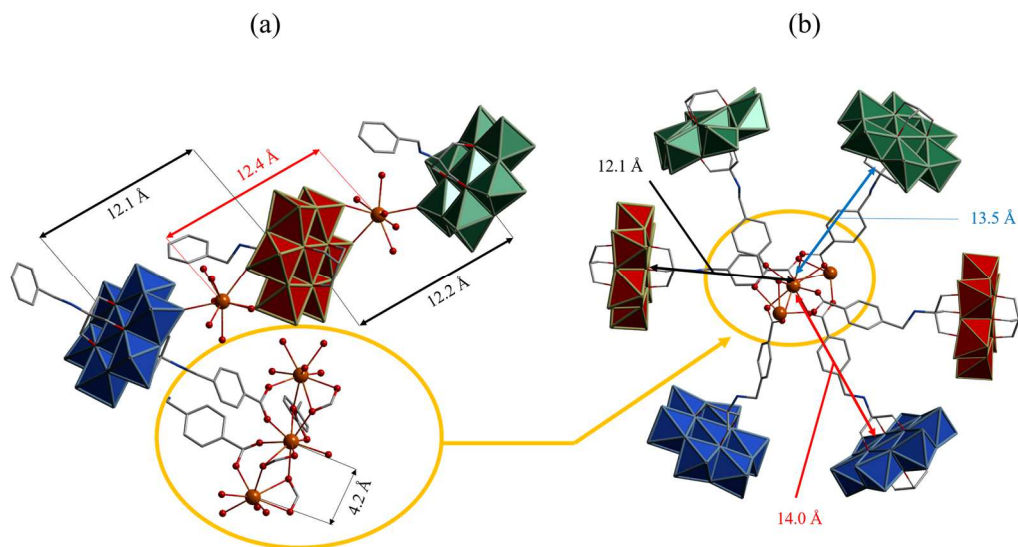


Figure 5.31: (a): Structure of **(11)**-Ce. DMF molecules and H atoms are omitted for clarity. (b): six Anderson-Evans polyanion coordinating to $\{\text{Ce}_3(\text{DMF})_{10}\}^{9+}$ unit via carboxylate groups. Colour code: Anderson-Evans polyanions: green, red, blue polyhedral models, Ce: orange, O: red, C: grey wire/stick, N: blue wire/stick. Lattice DMF molecules and H atoms are omitted for clarity. DMF molecules coordinating to Ce atoms are represented by their O atoms.

The distance between the Ce^{3+} centres in the $\{\text{Ce}(\text{DMF})_5\}^{3+}$ and the $\{\text{Ce}(\text{DMF})_6\}^{3+}$ units is 12.4 Å, whereas the distances between two Mn atoms of the POM moieties are about 12.2 Å. The Mn-Ce distance between a core of a hybrid and a Ce ion of the $\{\text{Ce}(\text{DMF})_5\}^{3+}$ and the $\{\text{Ce}(\text{DMF})_6\}^{3+}$ parts, respectively, ranges from 6.1 Å to 6.9 Å. The Ce-Ce distances within the $\{\text{Ce}_3(\text{DMF})_{10}\}^{9+}$ unit are 4.2 Å, whereas the Ce-Mn distance between the Ce_3 unit and a hybrid is in the range 12.1 Å to 14.0 Å. The $\text{O}_{\text{COO}}\text{-O}_{\text{COO}}$ distance within one POM hybrid ranges from 22.4 Å to 23.2 Å. In comparison to compound **(5)**, the hybrids in **(11)**-Ce are on average compressed by 0.3 Å.

In **(11)**-Ce several DMF molecules, which coordinate to the Ce centres, are disordered. For this reason, only the O atoms of two DMF molecules of the $\{\text{Ce}(\text{DMF})_6\}^{3+}$ unit, one DMF molecule of the $\{\text{Ce}(\text{DMF})_5\}^{3+}$ moiety and six DMF molecules of the $\{\text{Ce}_3(\text{DMF})_{10}\}^{9+}$ part could be refined. Furthermore, there are two

DMF molecules in the lattice, whereas 15 additional DMF molecules can be identified in the lattice via the SQUEEZE function within PLATON.¹⁵⁹

The green coloured Anderson-Evans polyanion is disordered. During the refinement process it was not possible to model this disorder with partial occupancy atoms, but only as single components with highly-anisotropic thermal ellipsoids with significant residual electron density surrounding this polyanion. Considering the Anderson-Evans POM as a wheel the organic parts $\{(OCH_2)_3CNHCH_2(C_6H_4)COO\}$ corresponds to its axle. The POM can rotate around this axis and is bonded to just one Ce atom, so that the POM can undergo a high amplitude of vibration. The amplitude of the vibration of the atoms within the POM increases as we move further from the central Mn atom. Due to the fact that the organic ligands are not linear, with the C-N bond forming a kink, this organic part is also twofold disordered about the direction of rotation (kink at N disorder, see section 5.2.3.1). For some of these ligands this disorder could be modelled, for others it was necessary to use one set of highly-anisotropic atoms.

The analysis with the computer program SHAPE¹⁵⁶ reveals that the geometries of the eight-coordinated Ce atom in the $\{Ce(DMF)_5(O_t)_3\}$ unit (with Ce2 as centre), the nine-coordinated Ce atom in the $\{Ce(DMF)_6(O_t)_3\}$ moiety (with Ce1 as core), the eight coordinated Ce atom in the $\{Ce(DMF)_4(O_{2,Coo})(O_{Coo})_2\}$ part (with Ce3 as centre), the nine-coordinated Ce atom in $\{Ce(DMF)(O_{2,Coo})_2(O_{Coo})_4\}$ unit (with Ce4 as central atom) and the nine-coordinated Ce atom in the $\{Ce(DMF)(O_{2,Coo})(O_{Coo})_6\}$ moiety (with Ce5 as core) (shown in Figure 5.32) are distorted from their ideal shapes.

The deviation values of Ce2 and Ce3 from the idealized square antiprism (SAPR) geometry are 0.517 and 0.307, respectively. The deviation value for Ce1, Ce4 and Ce5 from the idealized spherical capped square antiprism (CSAPR) geometry are 1.538, 2.542 and 1.289, respectively. The continuous shape measurements (CShM's) are listed in Table 8.15 in section 8.2.2.

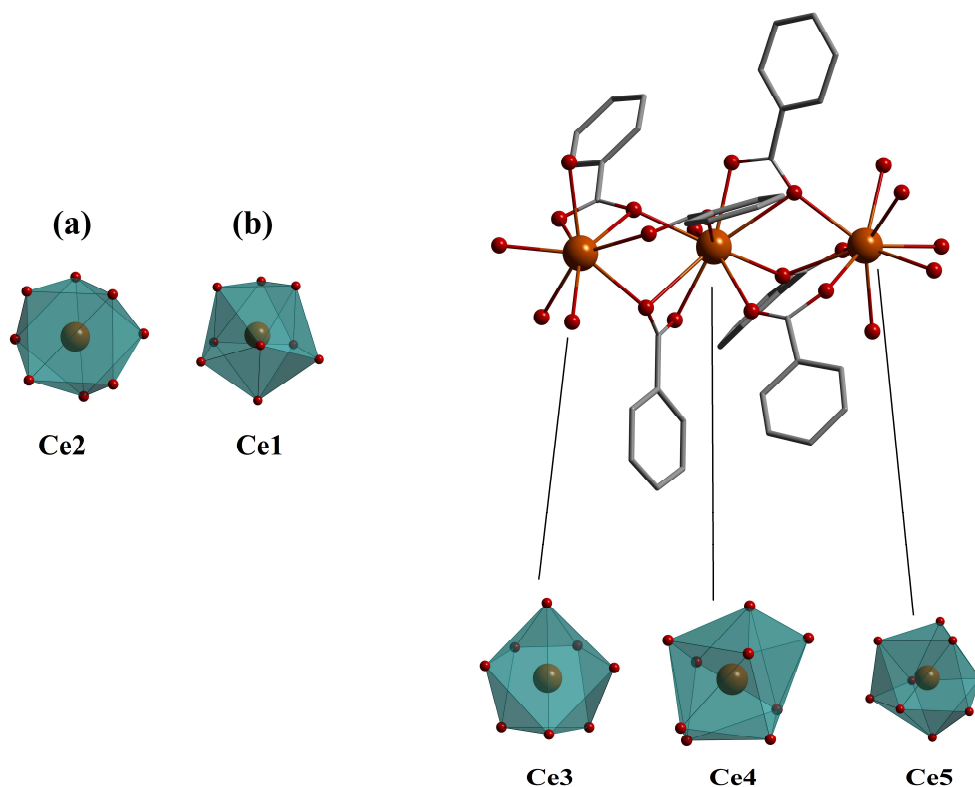


Figure 5.32: Environment of the $\{Ce(DMF)_5(O_t)_3\}$ (a), $\{Ce(DMF)_6(O_t)_3\}$ (b) and $\{Ce_3(DMF)_{10}(OOC(C_6H_4)_6)\}$ (c) units. Colour code: Ce: orange, O: red, C: grey wire/stick. DMF molecules coordinating to Ce atoms are represented by their O atoms.

5.3.1.1.2 Topological analysis

Compound **(11)**-Ce forms a 3D network and therefore its topological analysis requires the identification of the appropriate “bricks and building units”. The topological analysis reveals that the structure of compound **(11)**-Ce includes four different topological relevant units. Amongst others it contains two Mn cores resulting from two independent $\{(MnMo_6O_{18})((OCH_2)_3CNHCH_2(C_6H_4)COO)_2\}$ units (green and blue spheres), representing triply coordinating linker hybrids. Furthermore, it comprises one MnCe₂ unit, which is based on one $\{(MnMo_6O_{18})((OCH_2)_3CNHCH_2(C_6H_4)COO)_2\}$, one $\{Ce^{3+}(DMF)_6\}$ and one $\{Ce^{3+}(DMF)_5\}$ units (red spheres), whereas the POM coordinates to the Ce ions via each two terminal atoms, which means that this hybrid was originally a sixfold

linker, but became extended by the Ce cations and thus reduced to a fourfold linker. The blue and green spheres are connected to these red spheres, which represent the coordination of the blue and green labelled Anderson-Evans POM moieties of the hybrids to the $\{\text{Ce}^{3+}(\text{DMF})_6\}$ and $\{\text{Ce}^{3+}(\text{DMF})_5\}$ units, respectively, via terminal oxygen atoms of the POMs. The fourth component of the topology are the Ce_3 centres originating from one $\{\text{Ce}_3^{9+}(\text{DMF})_{10}\}$ unit (purple sphere). As shown in Figure 5.33 it is clearly seen that each purple sphere is hexagonally connected to each two green, blue and red spheres. This represents the coordination of the POM-hybrids to the $\{\text{Ce}_3^{9+}(\text{DMF})_{10}\}$ moiety via the carboxylate groups. Furthermore, each blue and green sphere binds to each two purple and one red sphere. Additionally, every red sphere links to two purple, one green and one blue sphere.

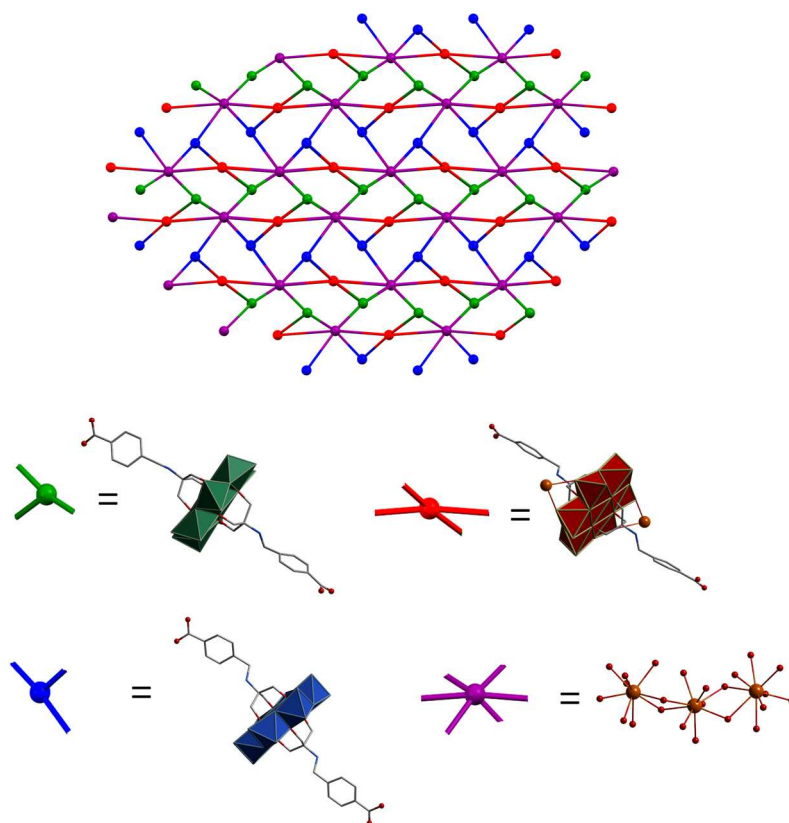


Figure 5.33: Topological net of (II)-Ce along the *a*-axis created from the *L*-POM-*L* 3-connecting, which is green and blue, from the 4-connecting, which is red and 6-connecting, which is the Ce_3 unit.

The topology can be identified as a 3,4,6-coordinated 3-nodal net with point symbol $\{6^{10}.8^3.10^2\}\{6^3\}2\{6^5.10\}$ and labeled as **3,4,6T281**.

5.3.1.1.3 Powder X-ray diffraction

Figure 5.34 shows the PXRD patterns of series **(11)**-RE with RE = La - Nd. The simulated pattern (**(11)**-Ce simu) serves as reference. From all PXRD patterns of **(11)**-RE, it is clearly seen that the samples contain the desired products. However, the patterns with the labelling “l” (= synthesized via layering method) show some extra reflections at e.g. 6.2° in 2θ and 24.1° in 2θ , respectively. This reveals that during the crystallization process at least one other unknown compound crystallizes. It was found that the formation of this by-product could be avoided using stirring method (labelled in Figure 5.34 with “s”).

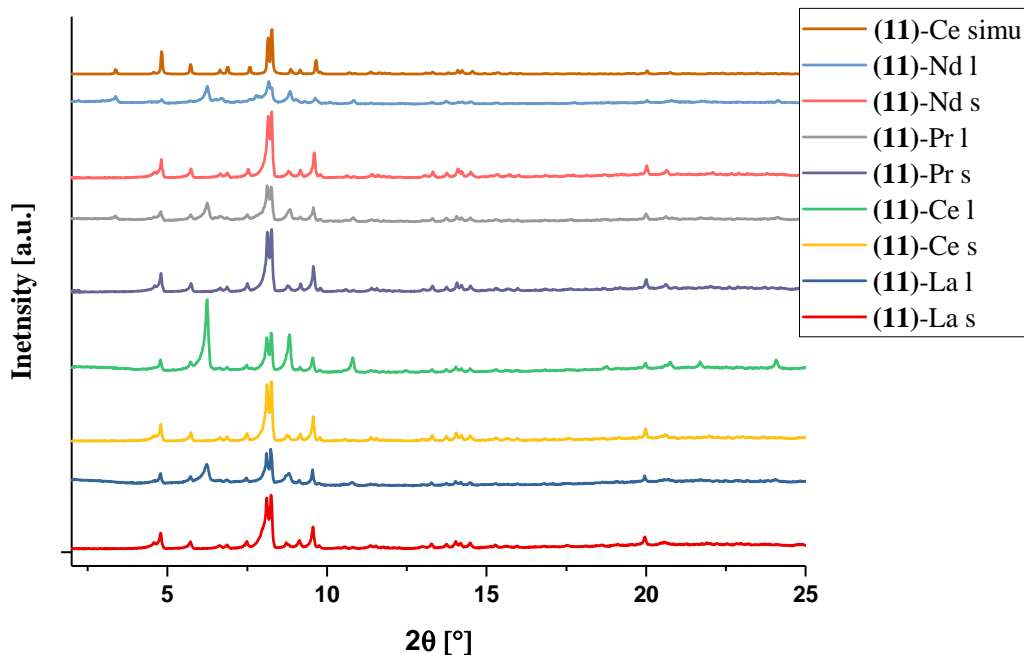


Figure 5.34: PXRD-patterns of the **(11)**-RE series (with RE = La - Nd), simu is abbreviation for simulation, “s” is abbreviation for stirring method, “l” is abbreviation for layering method.

For further characterization and properties compound **(11)**-Ce was chosen as a representative for this RE-series.

5.3.1.1.4 Solid state UV-vis studies

Figure 5.35 shows the solid state UV-vis spectrum of compound **(11)**-Ce. The spectrum demonstrate one absorption band at $\lambda = 526$ nm, which can be assigned to a d-d electron transfer from the t_{2g} orbital to the e_g^* orbital within one Mn^{3+} ion atom. The maximum absorption at $\lambda = 300$ nm can be allocated to a LMCT. The change of absorbance at $\lambda = 350$ nm was caused by the change of the lamp during the record of the spectrum. The bandgap of 2.76 eV was found using the Tauc method.

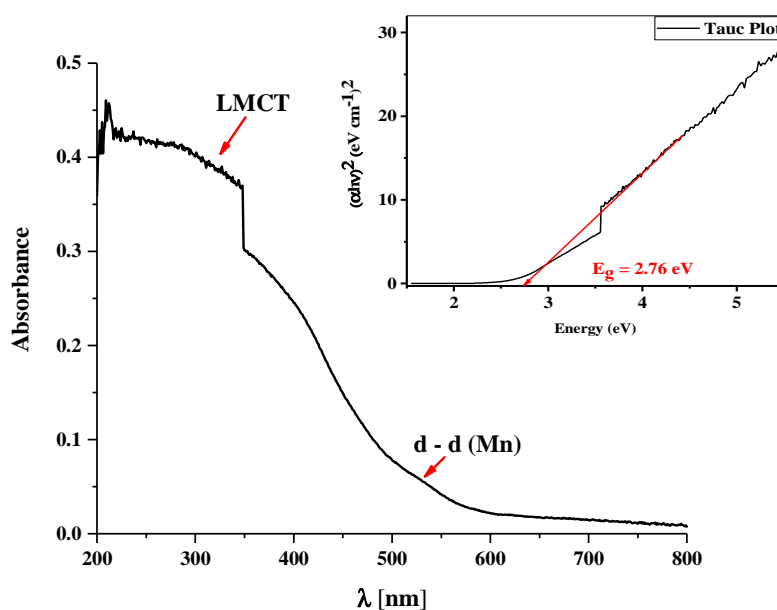


Figure 5.35: Solid state UV-vis spectrum of compound **(11)**-Ce.

5.3.1.1.5 Catalytic studies

Catalysis of the reaction of furfural with morpholine

Rare earth metal containing compounds are well known as catalysts for the reaction of furfural and morpholine, to form *trans*-4,5-dimorpholinocyclopent-2-en-1-one (**19**).¹³⁷ Therefore, the catalytic performance of compound (**11**)-Ce was investigated for this reaction (see Figure 5.36).

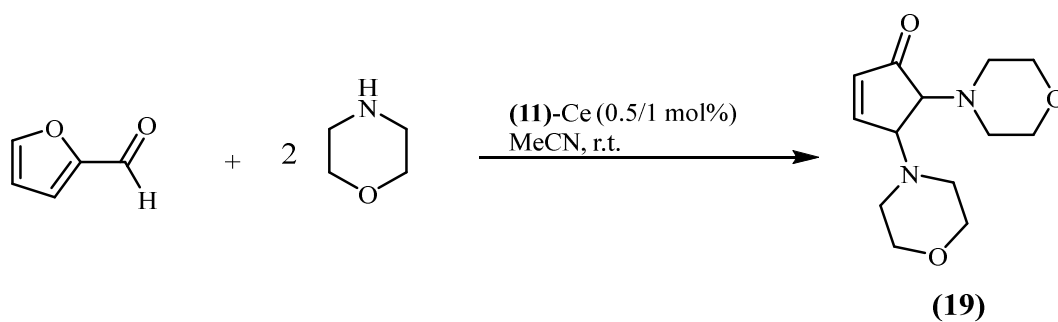


Figure 5.36: Synthesis of *trans*-4,5-dimorpholinocyclopent-2-en-1-one from furfural and morpholine.

Figure 5.37 and Figure 5.38 show the time-dependent studies of the conversion of furfural to (**19**) using ¹H-NMR for loadings of 0.5 and 1 mol%, respectively.

5. Results and Discussion

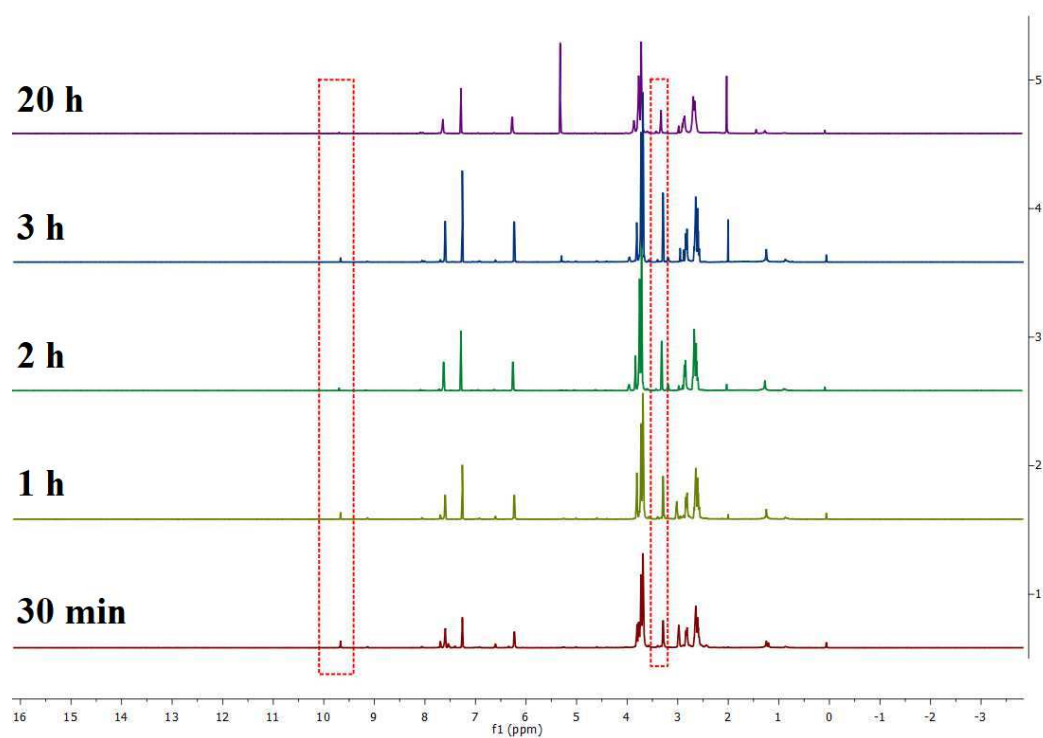


Figure 5.37: Time-dependent studies of conversion using ^1H -NMR for loading of 0.5 mol%.

In order to follow the progress of the conversion, the integral of the proton in the ^1H spectra of the aldehyde group of furfural at 9.67 ppm was compared to the desired *trans*-product's coupling constant of H4 and H5 at 3.29 ppm, which has the $J = 3.0$ Hz.

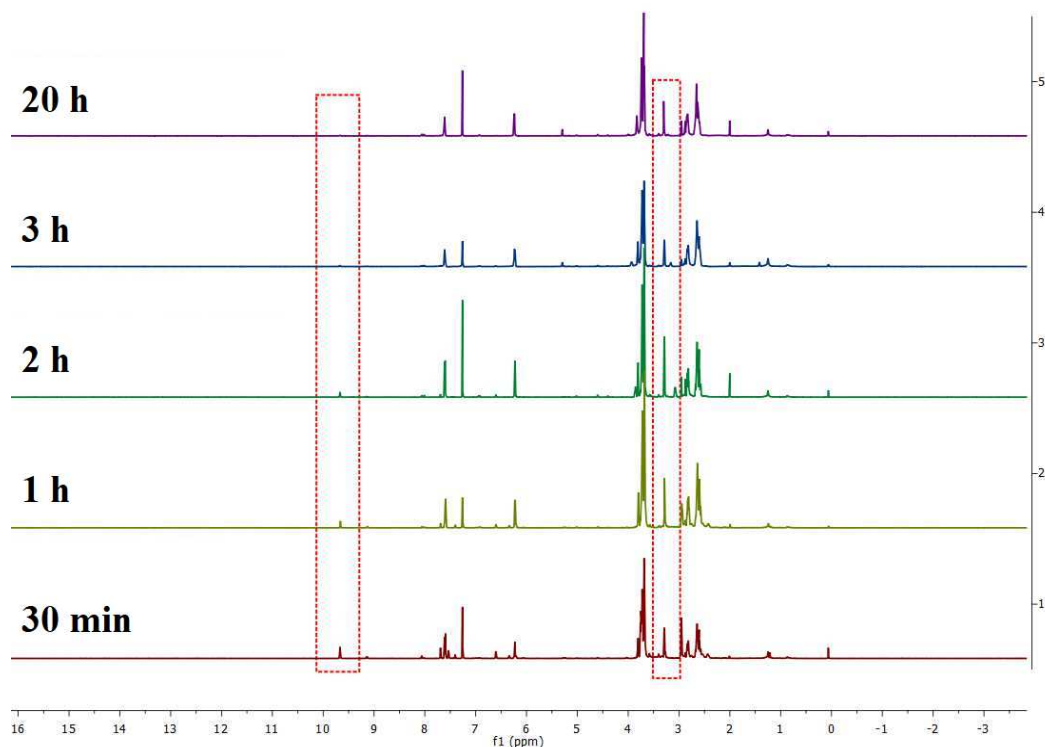


Figure 5.38: Time-dependent studies of conversion using $^1\text{H-NMR}$ for loading of 1 mol%.

Additionally, Figure 5.39 shows the summary of the results from the $^1\text{H-NMR}$ studies shown in Figure 5.37 and Figure 5.38. The results reveals that the catalyst (**11**)-Ce is highly efficient for the reaction of furfural with morpholine to form *trans*-4,5-dimorpholinocyclopent-2-en-1-one. It was found that after 30 min the conversion for the reaction with the loading of 0.5 mol% achieved a value of 86 %, whereas a plateau was reached with the completion of the conversion after three hours (red line). In comparison, the reaction with 1 mol% loading of the catalyst provided a conversion of 76 %, but the plateau, indicating the completion of the conversion (blue line), was also reached after three hours. The study demonstrates that the efficiency of the catalyst (**11**)-Ce found to be similar although the amount of catalyst was decreased to 0.5 mol%, resulting in the insignificant decrease in conversion of the desired product.

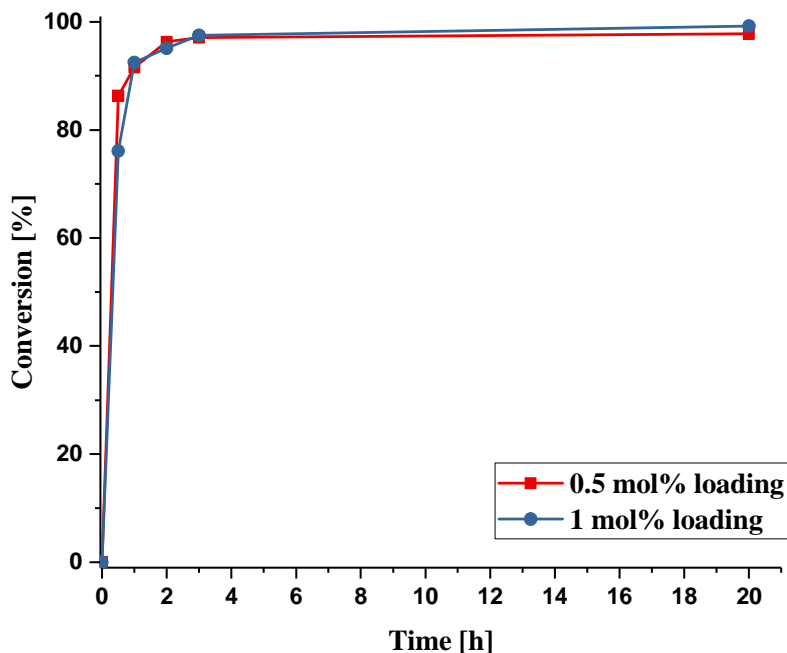


Figure 5.39: Conversion of furfural as a function of time in the reaction of furfural with morpholine with 0.5 mol% and 1 mol% loadings of the catalyst (**11**)-Ce, respectively. The conversion was determined by ^1H NMR spectroscopy.

Photo-electrocatalytic studies

The preparation of the working electrode and photo-electrocatalytic studies of compound (**11**)-Ce were performed under the same conditions of (**5**) (see section 5.2.1.4).

Figure 5.40 shows the results of the photo-electrocatalytic studies of (**11**)-Ce and thus its potential application for water splitting.

Utilizing artificial sunlight during linear sweep voltammetry (see Figure 5.40 (a)), an onset of the current appears at a potential of -0.3 V vs. Ag/AgCl with a maximum value of $3.47 \cdot 10^{-1} \text{ mA/cm}^2$ at 1.4 V vs. Ag/AgCl. The stability of compound (**11**)-

Ce under these conditions was confirmed by recording three measurements of linear sweep voltammetry where the values did not change considerably.

Likewise, in the case of utilizing the filter with a UV-cutoff, three runs of linear sweep voltammetry were recorded, in order to confirm the stability of compound (11)-Ce under these conditions. (see Figure 5.40 (b)). The direct comparison of catalytic studies with and without filter are shown in Figure 5.41.

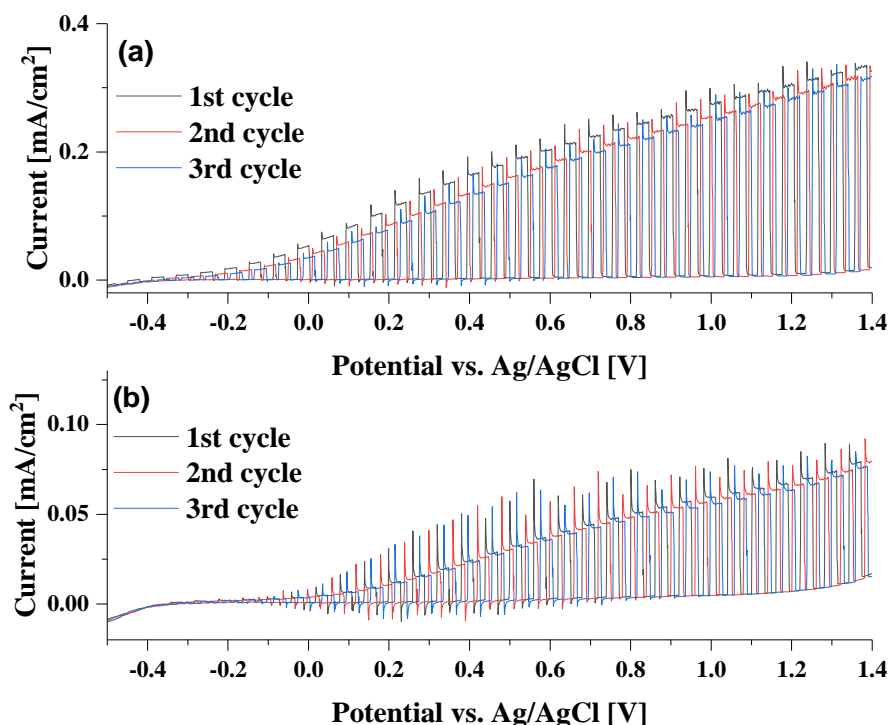


Figure 5.40: Photo-electrocatalytic results of compound (11)-Ce recorded in 0.5 M Na_2SO_4 ($\text{pH} = 8.6$) in the range -0.5 V to 1.4 V and a scan rate of 0.01 V/s and sunlight simulation without any filter (a) and with filtering the radiation below 420 nm (b).

For the filtered sample the onset of current begins at a potential of -0.2 V vs. Ag/AgCl, which corresponds to a shift of +0.1 V (anodic shift) compared to measurement without filter. Over the course of the scan the current increases to reach a maximum of $7.66 \cdot 10^{-2} \text{ mA/cm}^2$ 1.4 V vs. Ag/AgCl. This reveals that

filtering radiation below 420 nm reduces the catalytic activity of the system by 75 %.

Additionally, starting at a potential of +1.2 V the current slightly increases at phases even when the light of the Xe lamp is switched off. Since this process is light independent, this behavior occurs both under filtered and unfiltered light conditions, indicating a mere electrochemical process.

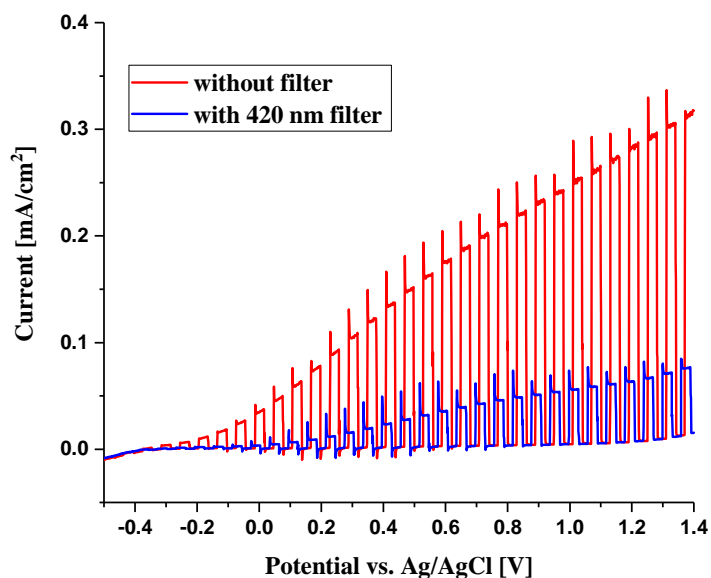


Figure 5.41: Comparison of photocatalytic studies of compound (11)-Ce in 0.5 M Na₂SO₄ (pH = 8.6) in the range -0.5 V to 1.4 V and a scan rate of 0.01 V/s: Studies with and without filter (< 420 nm), for comparison in each case the final 3rd run was chosen.

5.3.1.1.6 Conclusion

The family of (11) was successfully synthesized and isolated in the form of crystals and powder. This series contains the rare earth metals from La to Nd, whereas the Ce containing compound was chosen as a representative for characterizations such

as SCXRD, UV-vis spectroscopy and additionally, catalytic properties of this series.

The PXRD patterns of the whole series reveal that by changing the reaction conditions from the layering method to stirring conditions of the reactants the desired POMOFs could be obtained in the form of pure powders and an unknown impurity, which appears during the crystallization process of the layering method, could be avoided. Furthermore, the whole series was characterized by FT-IR spectroscopy.

Compound **(11)**-Ce shows interesting catalytic properties for the reaction of furfural and morpholine to form *trans*-4,5-dimorpholinocyclopent-2-en-1-one. In the absence of a catalyst, under similar conditions the reaction takes longer (≈ 80 days) and the thermodynamically stable product 2,4-diaminocyclopentene-2-enone is formed instead of the desired product *trans*-4,5-dimorpholinocyclopent-2-en-1-one.¹⁶² In respect of the successful transformation of furfural to the desired product in high conversion requires further investigation of **(11)**-Ce with alternative amine derivatives using primary and secondary amines, in particular aniline derivatives, piperidine, pyridine etc.

Preliminary photo-electrocatalytic studies reveal that compound **(11)**-Ce shows catalytic water splitting properties. However, these studies need further investigation and the process of coating of **(11)**-Ce onto the substrate has to be optimized.

5.3.1.2 $[\text{RE}(\text{DMF})_4(\text{H}_2\text{O})]_2[\text{RE}_3(\text{DMF})_6][(\text{MnMo}_6\text{O}_{18})((\text{OCH}_2)_3\text{CNHCH}_2(\text{C}_6\text{H}_4)\text{COO})_2]_3 \cdot x\text{DMF}$ (RE = Y, Sm - Lu) **(12)**

The series of compound **(12)**-RE (RE = Y, Sm – Lu) was obtained by over-layering a buffer solution of DMF/MeOH (1:1/v:v) on top of a solution of $[\text{N}(n\text{-C}_4\text{H}_9)_4]_4[(\text{MnMo}_6\text{O}_{18})((\text{OCH}_2)_3\text{CNHCH}_2(\text{C}_6\text{H}_4)\text{COOH})((\text{OCH}_2)_3\text{CNHCH}_2$

(C₆H₄COO)]·3DMF (**5**) in DMF. Afterwards, a solution of the respective RE(NO₃)₃ salt in MeOH was layered on top of the buffer layer. Due to the diffusion of the reactants through the layers, crystals formed, whereby a series of (**12**) could be obtained. Furthermore, it was possible to obtain the Dy-based POMOF of (**12**) in the form of powder by mixing the reactant (**5**) dissolved in DMF with Dy(NO₃)₃·6H₂O dissolved in MeOH.

5.3.1.2.1 Single crystal structure

For the description of the structure of the series of (**12**), Dy was chosen as a representative for RE.

The crystallographic data of compound (**12**)-Dy are given in Table 8.9.

The single crystal X-ray diffraction analysis shows that compound (**12**)-Dy crystallizes in the monoclinic space group $P2_1/c$ with the unit cell parameters: $a = 19.5819(7) \text{ \AA}$, $b = 25.2560(10) \text{ \AA}$, $c = 25.3233(9) \text{ \AA}$, $\beta = 90.306(3)^\circ$ and $V = 12523.7(8) \text{ \AA}^3$. The unit cell is very similar to the one of compound (**11**)-Ce and is closely isostructural, but the smaller ionic radius of Dy³⁺ seems to have resulted in a change of the space group from $P2_1$ to the centrosymmetric space group $P2_1/c$. The framework structure of compound (**12**)-Dy is shown in Figure 5.42 and consists of three $\{(\text{MnMo}_6\text{O}_{18})((\text{OCH}_2)_3\text{CNHCH}_2(\text{C}_6\text{H}_4)\text{COO})_2\}^{5-}$, two $\{\text{Dy}(\text{DMF})_4(\text{H}_2\text{O})\}^{3+}$ and one $\{\text{Dy}_3(\text{DMF})_6\}^{9+}$ moieties. Furthermore, five DMF molecules can be determined in the lattice by using the Olex2 solvent mask.¹⁶³

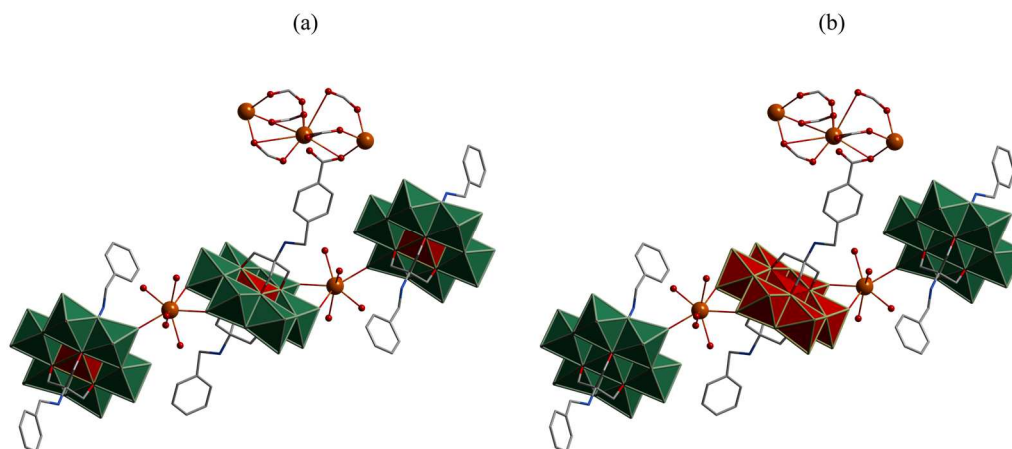


Figure 5.42: Structure of compound (12)-Dy. Colour code: Anderson-Evans polyanions: green ring with red polyhedral models (a), Anderson-Evans polyanions: green, red polyhedral models (b), Dy: orange, O: red, C: grey wire/stick, N: blue wire/stick. Lattice DMF molecules and H atoms are omitted for clarity. DMF and H₂O molecules of the {Dy(DMF)₄(H₂O)}³⁺ units are represented by their o atoms. DMF molecules of the {Dy₃(DMF)₆}⁹⁺ moiety are omitted for clarity.

For a simple description of the structure, Anderson-Evans POMs with different coordination modes are marked in different colours. As shown in Figure 5.42 (b) the red coloured Anderson-Evans POM coordinates to two {Dy(DMF)₄(H₂O)}³⁺ units via two terminal oxygen atoms. Additionally, these Dy³⁺ moieties are further linked to green marked hybrids by one terminal oxygen atom resulting in a coordination number of eight. Within this part of the structure (Figure 5.43) the Dy-Mn distances are 6.1 Å and 6.8 Å and the Mn-Mn distance between one green and one red hybrid is 12.1 Å. The Mn-Mn distance between one to another green POM amounts to 23.6 Å. The Dy-Dy distance is 12.1 Å. The length of one O_{COO} functional group to the other one within one hybrid ranges from 22.7 Å to 22.9 Å, which is in comparison to the free hybrid (5) compressed on average by 0.3 Å.

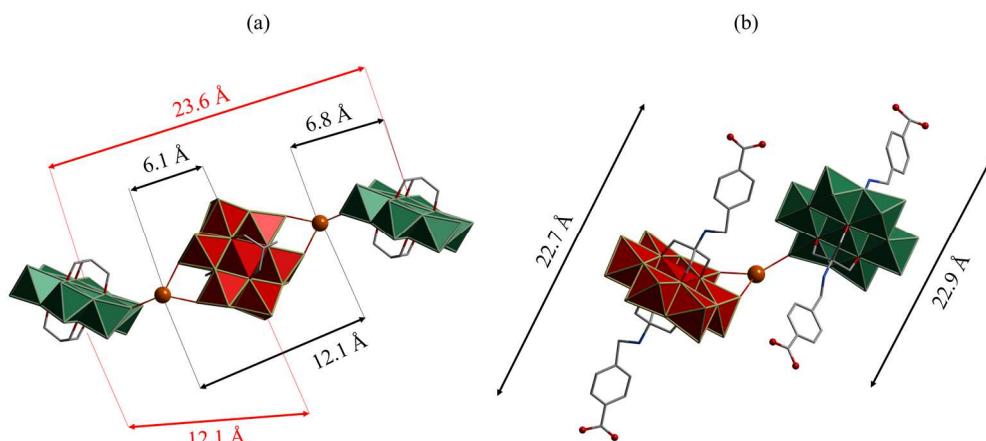


Figure 5.43: Extracts of the structure of (12)-Dy. Colour code: Anderson-Evans polyanions: green, red, polyhedral models, Dy: orange, O: red, C: grey wire/stick, N: blue wire/stick. DMF, water molecules and H atoms are omitted for clarity.

The analysis with the computer program SHAPE¹⁵⁶ reveals that the geometry of the eight-coordinated Dy atom in the $\{\text{Dy}(\text{DMF})_4(\text{H}_2\text{O})(\text{O}_t)_3\}$ unit (Figure 5.44) is distorted from the ideal shape.

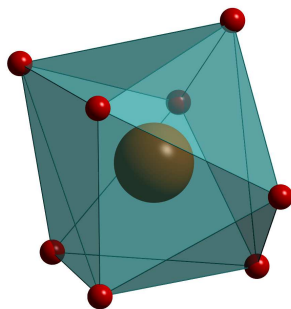


Figure 5.44: The environment of the $\{\text{Dy}(\text{DMF})_4(\text{H}_2\text{O})(\text{O}_t)_3\}$. Colour code: Dy: orange, O: red.

The deviation value of this Dy^{3+} core from the idealized square antiprism (SAPR) geometry is 0.646. The continuous shape measurements (CShM's) are listed in Table 8.16 in section 8.2.3.

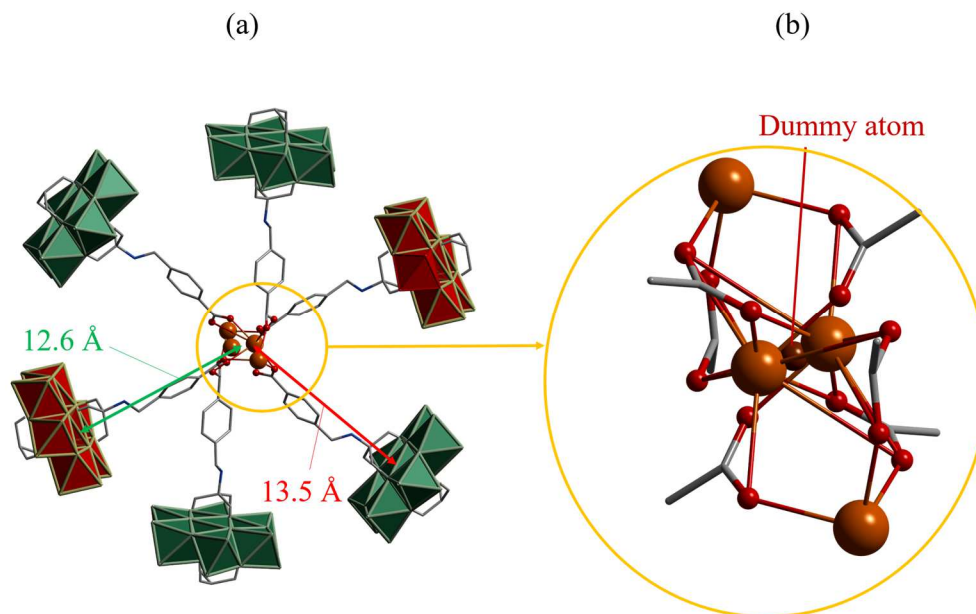


Figure 5.45: (a) Six Anderson-Evans polyanion coordinating to the $\{\text{Dy}_3(\text{DMF})_6\}^{9+}$ unit via carboxylate groups, (b) extract of the disordered $\{\text{Dy}_3(\text{DMF})_6\}^{9+}$ unit. Colour code: Anderson-Evans polyanions: green, red, polyhedral models, Dy: orange, O: red, C: grey wire/stick, N: blue wire/stick, dummy atom: brown. DMF, water molecules and H atoms are omitted for clarity.

In addition, the carboxylate groups of the hybrids coordinate to the $\{\text{Dy}_3(\text{DMF})_6\}^{9+}$ moiety, where the ratio of red to green polyanions coordinating to this core is 4:2 (see Figure 5.45 (a)).

The inversion centre of the centrosymmetric space group $P2_1/c$ in the crystal structure of (12)-Dy is between Dy3 and its inversion equivalent Dy3A (see Figure 5.45 (b)) within the $\{\text{Dy}_3(\text{DMF})_6\}^{9+}$ moiety. Due to this inversion center the middle Dy atom of the $\{\text{Dy}_3(\text{DMF})_6\}^{9+}$ unit is disordered. Furthermore, the coordinating carboxylate groups and the phenyl groups bound to these carboxylate groups are also disordered (kink at N disorder, see section 5.2.3.1). Nevertheless, the twofold disorder could be modelled for all of the organic ligands.

Due to the high degree of disorder, it was not possible to determine the geometries of the Dy atoms within the $\{\text{Dy}_3(\text{DMF})_6\}^{9+}$ unit.

Placing a dummy atom (Figure 5.45 (b)) between the twofold disordered Dy₃ atom (Dy₃A and Dy₃B) approximate distances of 12.6 Å to 13.7 Å between the Dy atoms of the {Dy₃(DMF)₆}⁹⁺ moiety to the Mn atoms of the L – POM - L units could be estimated.

5.3.1.2.2 Topological analysis

The topological analysis of (12)-Dy reveals that the structure has the same topology as for the closely isostructural compound (11)-Ce (see section 5.3.1.1.2) In Figure 5.33, in this case the blue and the green L – POM – Ls are equivalent.

5.3.1.2.3 Powder X-ray diffraction

Figure 5.46 shows the PXRD patterns of series (12)-RE with RE = Y, Sm - Lu. The simulated pattern ((12)-Dy simu) serves as reference. It is clearly seen that all the measured samples, as well the ones with “l”(= synthesized via layering method) as the one with “s”(= synthesized under stirring conditions) show a good accordance to (12)-Dy simu. However, the synthesis under stirring condition was only successful in the case of Dy, in all other ten cases the PXRD patterns did not agree to the simulated pattern. For this reason, these patterns are not shown in Figure 5.46.

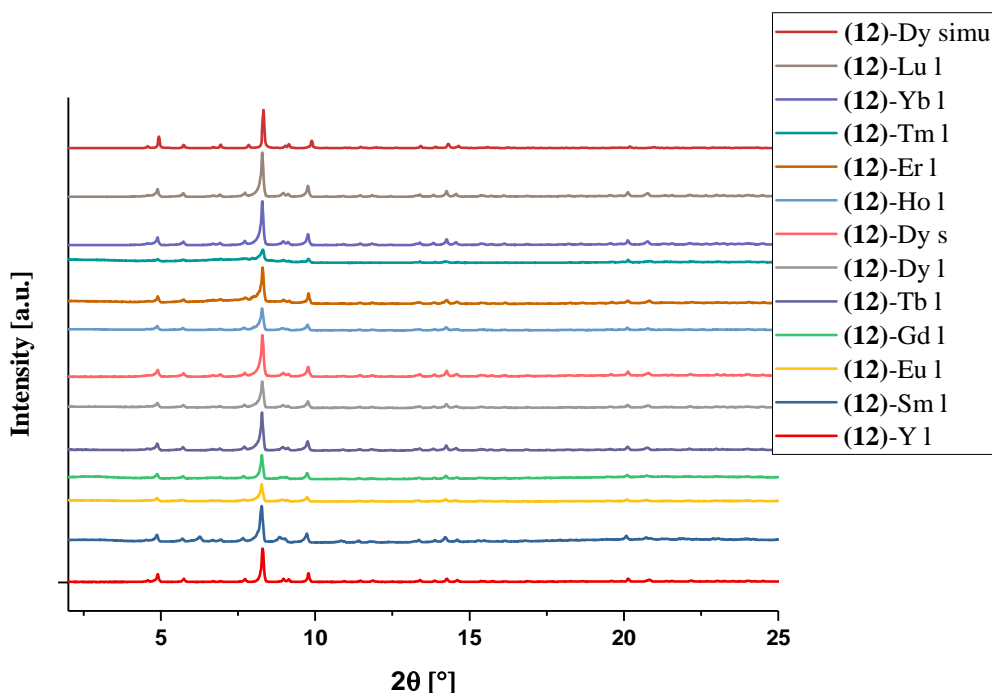


Figure 5.46: PXRD-patterns of the (12)-RE series (with RE = Y, Sm - Lu), simu is abbreviation for simulation, “s”. is abbreviation for stirring method, “l” is abbreviation for layering method.

For further characterization and properties compound (12)-Dy was chosen as a representative for this RE-series.

5.3.1.2.4 Solid state UV-vis studies

The UV-vis spectrum of compound (12)-Dy is shown in Figure 5.47. This spectrum shows one absorption band at $\lambda = 530$ nm, which can be denoted to a d-d electron transfer from the t_{2g} orbital to the e_g^* orbital within one Mn^{3+} ion. The maximum absorption at $\lambda = 276$ nm can be allocated to a LMCT. The change of absorbance at $\lambda = 350$ nm was caused by the change of the lamp during the record of the spectrum. The bandgap of 2.46 eV was found using the Tauc method.

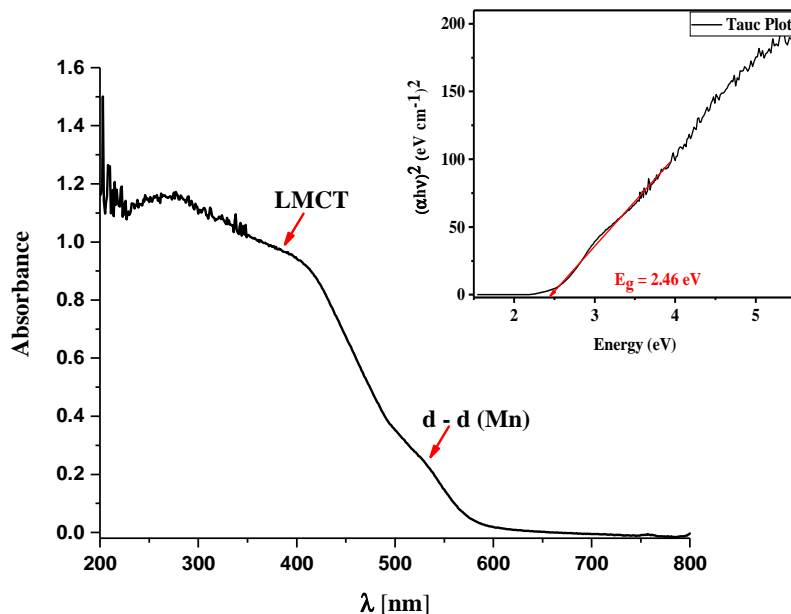


Figure 5.47: Solid state UV-vis spectrum of compound (12)-Dy.

5.3.1.2.5 Catalytic Studies

Catalysis of the reaction of furfural with morpholine

According to the catalytic properties of (11)-Ce, which can catalyze a domino condensation/ring-opening/electrocyclization process of the transformation of biomass furfural to *trans*-4,5-dimorpholinocyclopent-2-en-1-one, an alternative hard Lewis acid rare earth metal ion is required. Considering the series of rare earth metals La-Lu, there is a decrease in both the atomic radii and in the radii of the RE³⁺ ions, caused by the lanthanide contraction.¹⁶⁴ According to the HSAB principle, the Lewis acidity increases with decreasing of the ionic radii. Therefore, (12)-Dy was chosen as alternative catalyst.

Figure 5.48 and Figure 5.49 show the time-dependent studies of the conversion of furfural to (19) using ¹H-NMR for loadings of 0.5 and 1 mol% of (12)-Dy, respectively. The results show similarities to the investigations of (11)-Ce with an

5. Results and Discussion

increase of efficiency related to the conversion of furfural of 7 % at a loading of 1 mol% after 30 min.

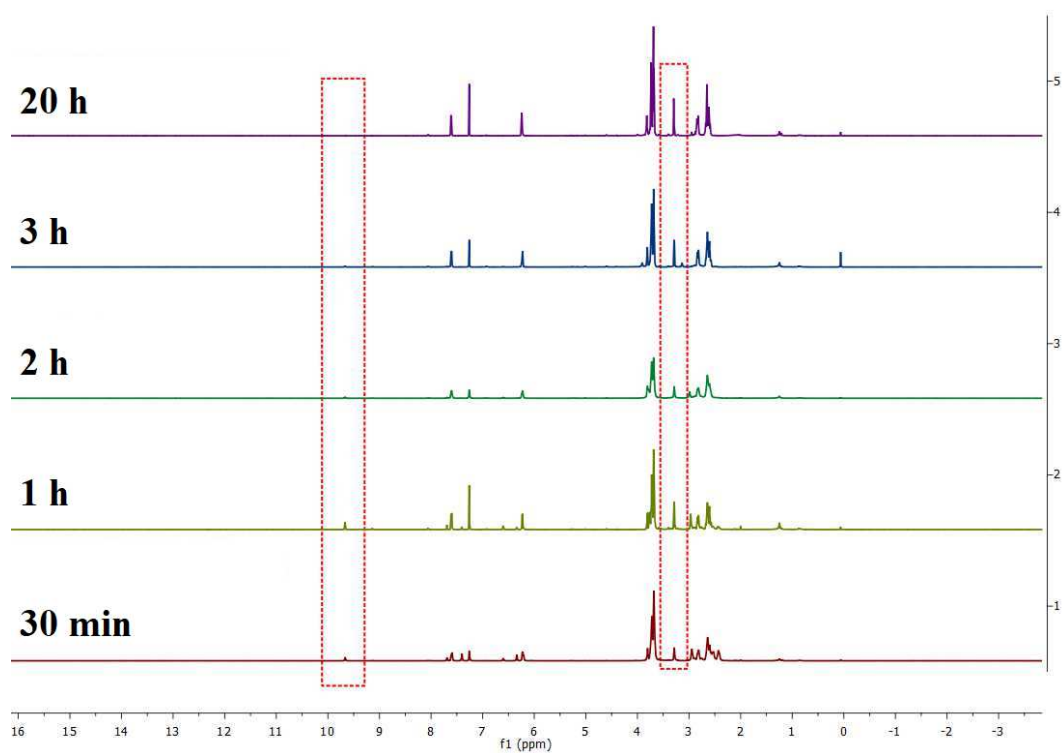


Figure 5.48: Time-dependent studies of conversion using $^1\text{H-NMR}$ for loading of 0.5 mol%.

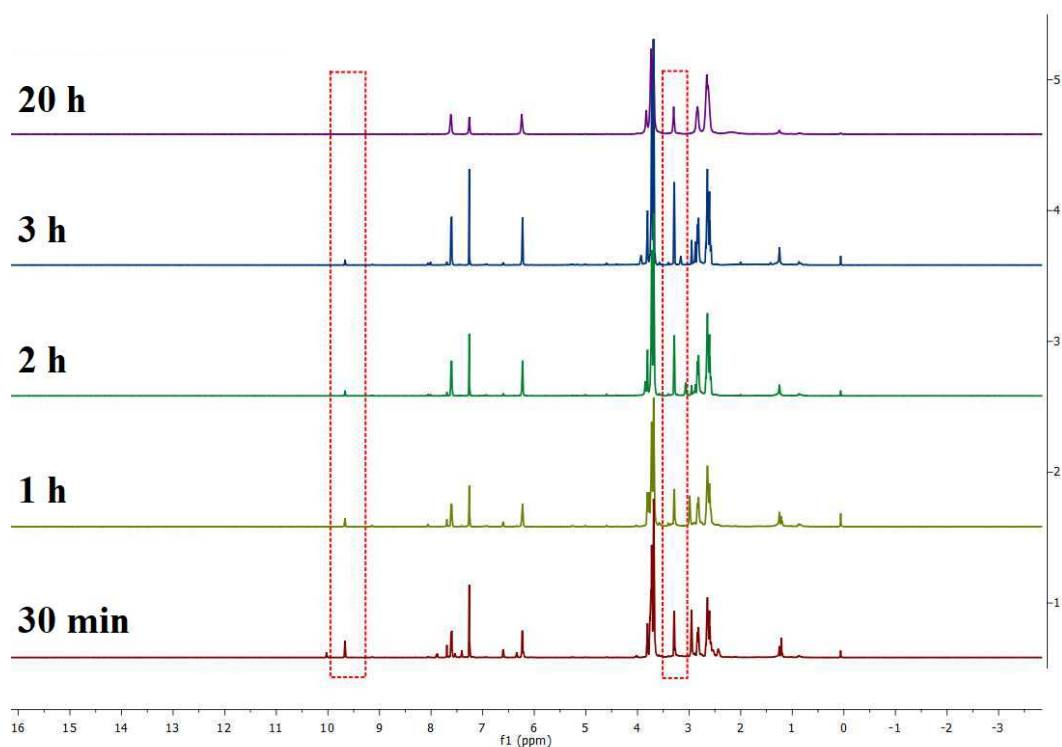


Figure 5.49: Time-dependent studies of conversion using $^1\text{H-NMR}$ for loading of 1 mol%

In summary, Figure 5.50 shows the results from the $^1\text{H-NMR}$ studies of Figure 5.48 and Figure 5.49. The catalyst (**12**)-Dy is highly efficient for the reaction of furfural with morpholine to form *trans*-4,5-dimorpholinocyclopent-2-en-1-one. Considering the 0.5 mol% loading of (**12**)-Dy, a conversion of 85 % is achieved after 30 minutes and a plateau is reached after three hours, indicating the completion of conversion (red line). In the case of the loading of 1 mol% a conversion of 83 % is achieved after 30 min, but the plateau, indicating the completion of the conversion (blue line), was also reached after three hours.

These results are a proof that a 0.5 mol% loading of (**12**)-Dy is adequate, where the completion of the reaction is reached after three hours.

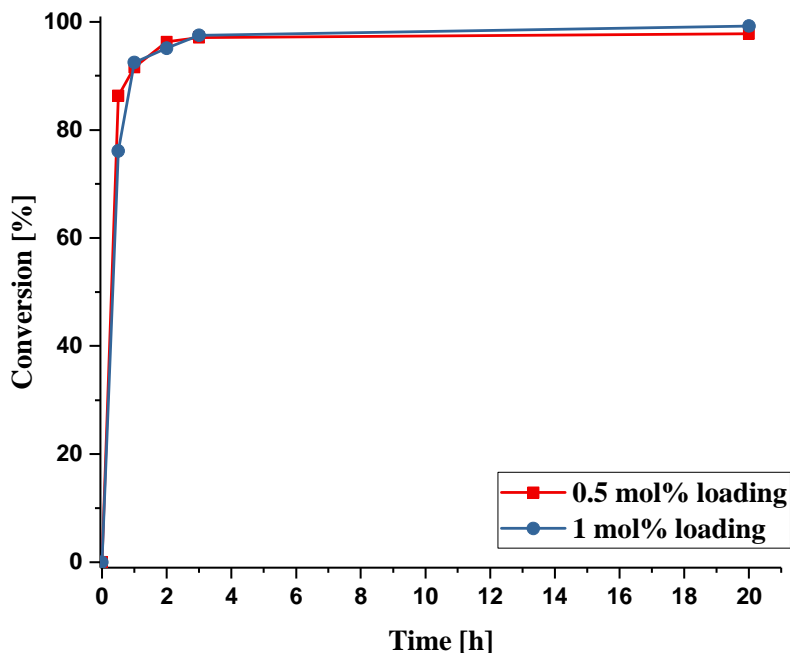


Figure 5.50: Conversion of furfural as a function of time in the reaction of furfural with morpholine with 0.5 mol% and 1 mol% loadings of the catalyst (12)-Dy, respectively. The conversion was determined by ^1H NMR spectroscopy.

Photo-electrocatalytic studies

Compound (12)-Dy has also been studied as a photo catalyst for photo-electrochemical catalysis of water splitting. Therefore, the preparation of the working electrode and the catalytic studies were performed under the same conditions of (5) (see section 5.2.1.4).

The photo-electrocatalytic studies of compound (12)-Dy are shown in Figure 5.51 and Figure 5.52 and exhibit photo-electrocatalytic properties of this compound for water splitting.

Using an artificial sunlight while a run of a linear sweep voltammetry (see Figure 5.51 (a)), the current begins to develop at a potential of -0.15 V vs. Ag/AgCl with

5. Results and Discussion

a maximum value of $4.04 \cdot 10^{-1} \text{ mA/cm}^2$ at 1.4 V vs. Ag/AgCl. Recording three runs of linear sweep voltammetry, the stability of compound (12)-Dy was confirmed under these conditions where the values did not change significantly.

Additionally, measurements utilizing a filter with a UV-cutoff (<420 nm) were performed three times in order to approve the stability of (12)-Dy under these conditions (see Figure 5.51 (b)).

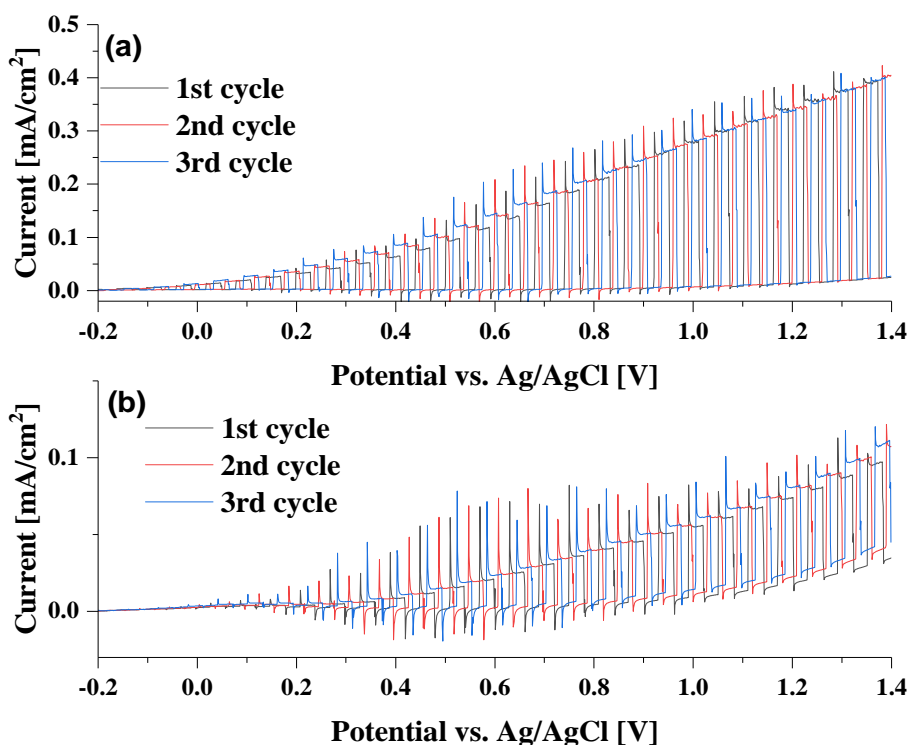


Figure 5.51: Photo-electrocatalytic results of compound (12)-Dy recorded in 0.5 M Na_2SO_4 (pH = 8.6) over the range -0.2 V to 1.4 V at a scan rate of 0.01 V/s and sunlight simulation without any filter (a) and with filtering the radiation below 420 nm (b).

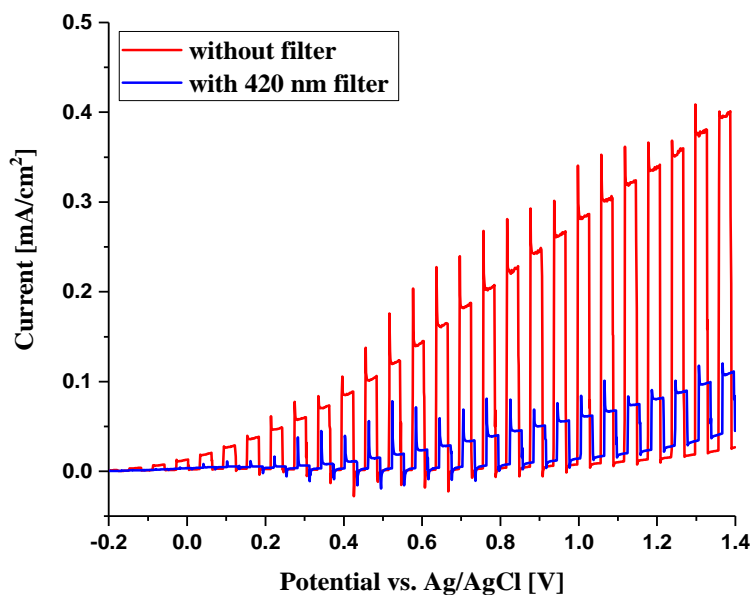


Figure 5.52: Comparison of photocatalytic studies of compound (12)-Dy in 0.5 M Na₂SO₄ (pH = 8.6) over the range -0.2 V to 1.4 V at a scan rate of 0.01 V/s: Studies with and without filter (< 420 nm), for comparison in each case the final 3rd cycle was chosen.

The direct comparison of catalytic studies with and without filter are shown in Figure 5.52. It is clearly seen that a development of the current for filtered sample occurs at a potential of 0.1 V vs. Ag/AgCl, which corresponds to a shift of +0.25 V compared to measurement without filter (anodic shift). With progress of the scan the current increases to reach a maximum of $1.10 \cdot 10^{-1}$ mA/cm² at 1.4 V vs. Ag/AgCl. This demonstrates that filtering radiation below 420 nm reduces the catalytic activity of the system by 73 %.

In addition, a mere electrochemical process occurs, indicated by an onset at a potential of +0.8 V, which is light-independent, since this behavior is observable in phases both with and without irradiating light on the photo-electrode and under filtered and unfiltered light conditions.

This behavior appears to be more pronounced at **(12)**-Dy than at **(11)**-Ce, resulting in the performance of subsequently electrocatalytic studies.

Electrocatalytic studies

The electrocatalytic studies on **(12)**-Dy were performed by the group of Prof. P. De Oliveira from Laboratoire de Chimie Physique, UMR8000 - Université Paris-Sud Bâtiment 349 - Campus d'Orsay 15, avenue Jean Perrin 91405 Orsay, FRANCE).

Compound **(12)**-Dy, which may be regarded as a representative of series **(11)** and **(12)**, was studied in three different media: 0.2 M Na₂SO₄ + H₂SO₄, pH = 3, 0.4 M CH₃COONa + CH₃COOH, pH = 5 and 0.4 M NaH₂PO₄ + NaOH; pH = 7.

At pH = 3, the cyclic voltammogram (CV) of the compound rapidly evolves, as shown in Figure 5.53, with the progressive fading of the reduction wave at 0.08 V vs. SCE, and the increase of the current of the reduction wave peaking at -0.7 V vs. SCE.

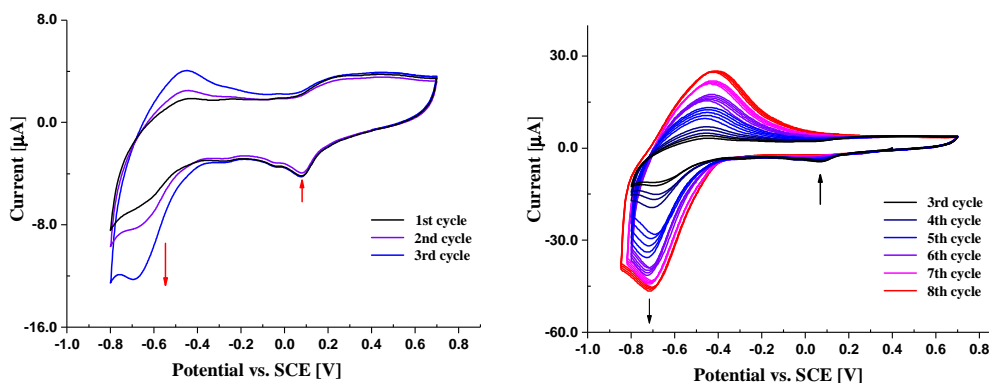


Figure 5.53: Evolution of the CVs of **(12)**-Dy recorded in 0.2 M Na₂SO₄ + H₂SO₄, pH = 3 as a function of time upon successive scanning over the range 0.70 V to -0.95 V. Scan rate: 100 mV/s. Working electrode: glassy carbon; counter electrode: platinum; reference electrode: SCE.

5. Results and Discussion

After a few tens of cycles, a stable CV is obtained which is characterised by a reduction wave peaking at $E_{pc} = -0.7$ V vs. SCE (see Figure 5.54 (a)) and an oxidation wave at $E_{pa} = 1.16$ V vs. SCE (see Figure 5.54 (b)). The evolution of the peak currents reveals that the electron transfer phenomena are diffusion-controlled and that there is no formation of deposits on the surface of the working electrode (see Figure 5.55).

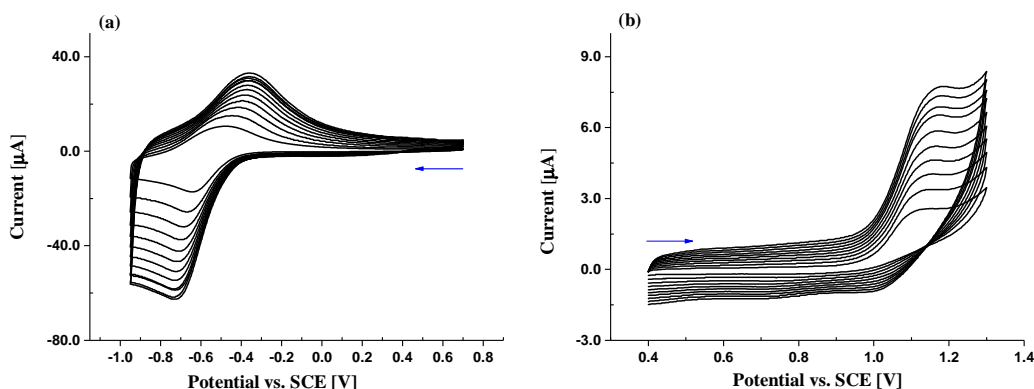


Figure 5.54: CVs of (12)-Dy recorded in 0.2 M $\text{Na}_2\text{SO}_4 + \text{H}_2\text{SO}_4$, pH = 3 at different scan rates, ranging from 10 to 100 mV/s. The slowest scan rate is the central one. (a) Potential range 0.7 V to -0.95 V. (b) Potential range 0.4 V to 1.3 V. Working electrode: glassy carbon; counter electrode: platinum; reference electrode: SCE.

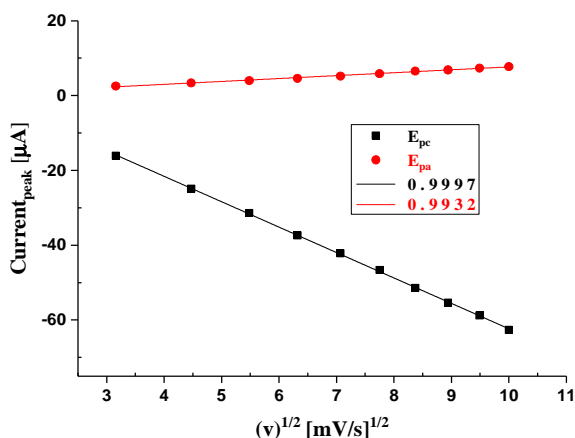


Figure 5.55: Evolution of the reduction (black) and the oxidation (red) peak currents as a function of the scan rate, between 10 and 100 mV/s. The values were taken from CVs of (12)-Dy recorded in 0.2 M $\text{Na}_2\text{SO}_4 + \text{H}_2\text{SO}_4$, pH = 3. Working electrode: glassy carbon; counter electrode: platinum; reference electrode: SCE.

A pH 3 medium is not the most convenient one for the study of the electro-catalytic oxidation of water. Therefore, the study was carried on in two other media having higher pH values: 0.4 M $\text{CH}_3\text{COONa} + \text{CH}_3\text{COOH}$, pH = 5 and 0.4 M $\text{NaH}_2\text{PO}_4 + \text{NaOH}$, pH = 7. The redox behaviour of (**12**)-Dy in these two media is very similar, but quite distinct from the response observed at pH = 3. The CV was reproducible upon successive scanning. There is a reduction wave peaking at -0.06 V vs. SCE, which corresponds to that one observed at 0.08 V vs. SCE at pH = 3, but the latter disappears fast. This wave is stable at pH = 5 and the electron transfer associated with it is diffusion-controlled. At pH = 7, it shifts to more negative potentials, as expected, peaking at -0.14 V vs. SCE (see Figure 5.56 (a)). However, the oxidation wave observed in the CVs seems to be pH-independent between pH = 5 and pH = 7. In fact, it peaks at 1.08 V vs. SCE in both media (see Figure 5.56 (a)). When the potential range was extended up to 1.6 V vs. SCE in order to explore the electro-catalytic properties of this compound towards the oxidation of water, it is observed that the process is more efficient at pH = 7 than at pH = 5, even if the redox behaviour is similar in the two media (see Figure 5.56 (b)).

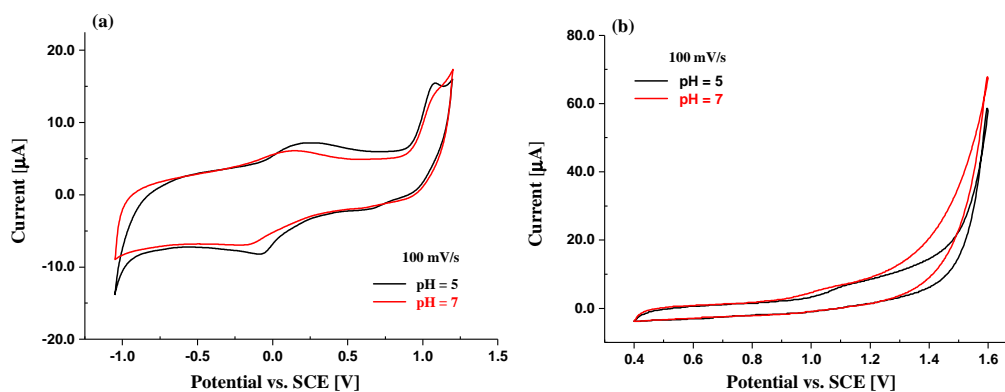


Figure 5.56: CVs of (**12**)-Dy recorded in 0.4 M $\text{CH}_3\text{COONa} + \text{CH}_3\text{COOH}$, pH = 5 (black) and in 0.4 M $\text{NaH}_2\text{PO}_4 + \text{NaOH}$, pH = 7 (red). (a) Potential range 1.2 V to -1.05 V. (b) Potential range 0.4 V to 1.6 V. Scan rate: 100 mV/s. Working electrode: glassy carbon; counter electrode: platinum; reference electrode: SCE.

5. Results and Discussion

The CVs of **(12)**-Dy at pH = 5 and pH = 7 with the scan rates from 10 to 100 mV/s over the range 1.2 V to -1.05 V and 0.4 V to 1.6 V, respectively, are shown in Figure 5.57 and Figure 5.58.

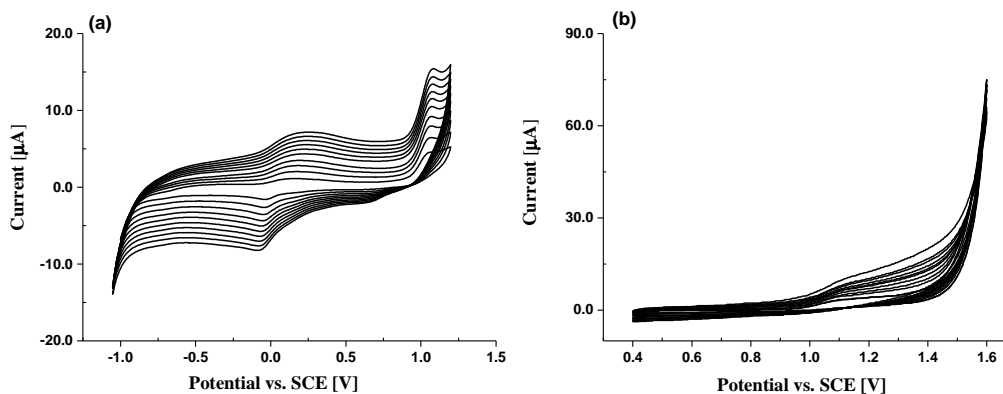


Figure 5.57: CVs of **(12)**-Dy recorded in 0.4 M $\text{CH}_3\text{COONa} + \text{CH}_3\text{COOH}$, pH = 5 at different scan rates ranging from 10 to 100 mV/s. The slowest scan rate is the central one. (a) Potential range 1.2 V to -1.05 V. (b) Potential range 0.4 V to 1.6 V. Working electrode: glassy carbon; counter electrode: platinum; reference electrode: SCE.

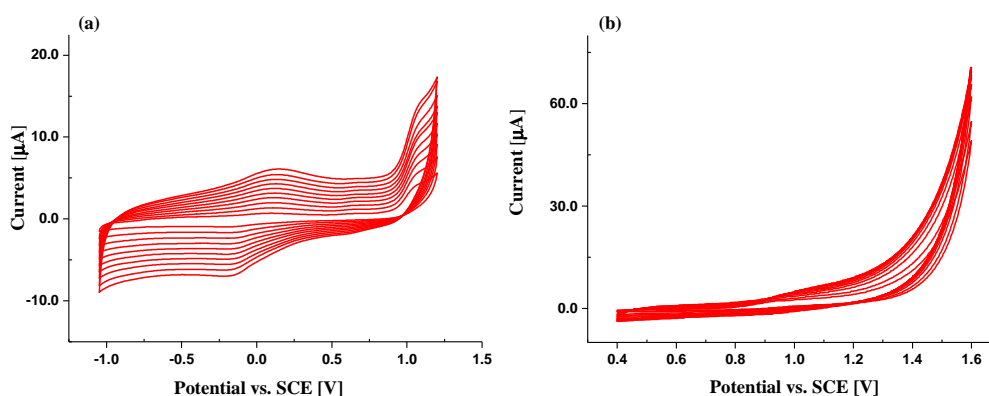


Figure 5.58: CVs of **(12)**-Dy recorded in 0.4 M $\text{NaH}_2\text{PO}_4 + \text{NaOH}$, pH = 7 at different scan rates ranging from 10 to 100 mV/s. The slowest scan rate is the central one. (a) Potential range 1.2 V to -1.05 V. (b) Potential range 0.4 V to 1.6 V. Working electrode: glassy carbon; counter electrode: platinum; reference electrode: SCE.

In order to assess the catalytic efficiency of **(12)**-Dy, both qualitatively and quantitatively, it is necessary to carry out a CV study at a small scan rate (2 mV/s) in the absence (just the electrolyte) and in the presence of the compound (see Figure 5.59). At a potential of 1.6 V vs. SCE, the normalised catalytic current, calculated

with the formula $I_{CAT} = [(I_{(12)\text{-Dy}} - I_0) / I_0] \times 100$, where $I_{(12)\text{-Dy}}$ and I_0 are the currents in the presence and in the absence of compound (12)-Dy, respectively, equals 183 %.

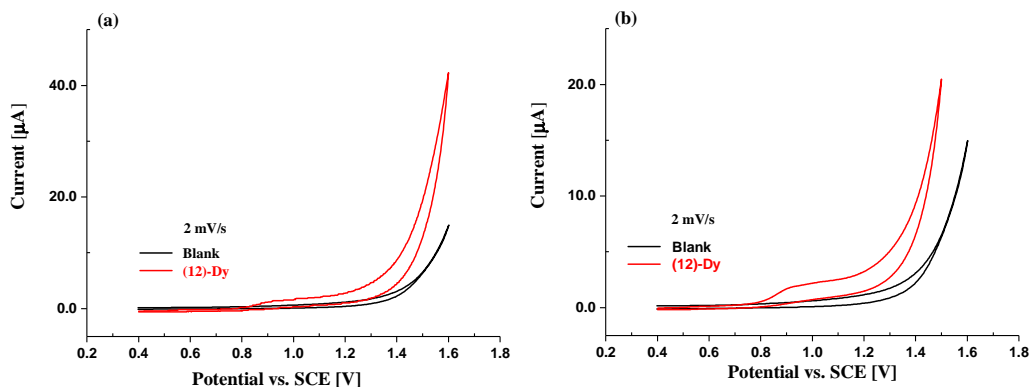


Figure 5.59: CVs recorded in 0.4 M $\text{NaH}_2\text{PO}_4 + \text{NaOH}$, $\text{pH} = 7$: electrolyte alone (black); (12)-Dy (red). (a) Potential range 0.4 V to 1.6 V. (b) Potential range 0.4 V to 1.5 V. Scan rate: 2 mV/s. Working electrode: glassy carbon; counter electrode: platinum; reference electrode: SCE.

5.3.1.2.6 Conclusion

The series of (12), containing the rare earth metals Y and Sm to Lu, was successfully synthesized and isolated in the form of crystals.

Due to the lanthanide contraction, the radii of the earlier rare earth metal ions (La – Nd) are bigger, thus the closely isostructural 3D networks of the series (11) are crystalizing in the space group $P2_1$, whereas the 3D structures of the series of (12) have the space group $P2_1/c$.

The results of the powder X-ray diffractograms of series (12) reveal that all the utilized rare earth metal ions show similar PXRD patterns. These results further demonstrate that the Dy containing structure was the only one, which could be also obtained under stirring conditions of the reactant (5) with the Dy salt.

Additionally, the whole series was characterized by FT-IR spectroscopy.

For this reason, the Dy comprising compound was chosen as a representative for the series (12) and characterizations such as SCXRD, UV-vis spectroscopy and in addition, catalytic properties were investigated.

The catalytic studies on (12)-Dy for the implementation of furfural and morpholine to form *trans*-4,5-dimorpholinocyclopent-2-en-1-one show an increase of the efficiency related to the conversion compared to the catalyst (11)-Ce. As aforementioned for (11)-Ce, also for (12)-Dy the variation of amine derivatives should be investigated for this kind of reaction.

In addition, preliminary photo-electrocatalytic studies reveal that compound (12)-Dy shows catalytic properties for the application of water splitting. However, these studies require further investigation, as well as the process of coating of (12)-Dy onto the substrate has to be optimized.

Compound (12)-Dy was chosen as a representative for both series (11) and (12) for electrocatalytic studies and reveals promising results.

Further investigation of this compound as electro-catalyst requires O₂ evolution experiments.

5.3.2 Transition metal containing polyoxometalate-based metal organic frameworks (TM-POMOFs)

5.3.2.1 [N(*n*-C₄H₉)₄]₅[CuCl(DMF){MnMo₆O₁₈((OCH₂)₃CN=CH(4-C₅H₄N))₂]₂·3DMF (13)

The reaction was carried out by stirring a mixture of [N(*n*-C₄H₉)₄]₃[MnMo₆O₁₈{(OCH₂)₃CNH₂]₂ (3), CuCl₂·2H₂O, 4-pyridinecarboxaldehyde and DMF for 20 h at 85 °C. Afterwards, compound (13) was isolated as crystalline material by exposure to ether vapour.

5.3.2.1.1 Single crystal structure

The crystallographic data of compound (**13**) are given in Table 8.10.

The single crystal X-ray diffraction analysis reveals that compound (**13**) crystallizes in the monoclinic space group $I2/a$ with the unit cell parameters: $a = 27.9207(12) \text{ \AA}$, $b = 27.5317(11) \text{ \AA}$, $c = 27.9543(13) \text{ \AA}$, $\beta = 99.258(4)^\circ$ and $V = 21208.7(16) \text{ \AA}^3$. The structure of compound (**13**), shown in Figure 5.60, is built from $\{\text{MnMo}_6\text{O}_{18}\{(\text{OCH}_2)_3\text{CN}=\text{CH}(4\text{-C}_5\text{H}_4\text{N})\}_2\}^{3-}$ units coordinating via the pyridyl groups (Npy) of the organic ligands to $\{\text{CuCl}(\text{DMF})\}^{1+}$ moieties, forming 2D sheets, which lie parallel to each other with an A-B alternation (see Figure 5.61).

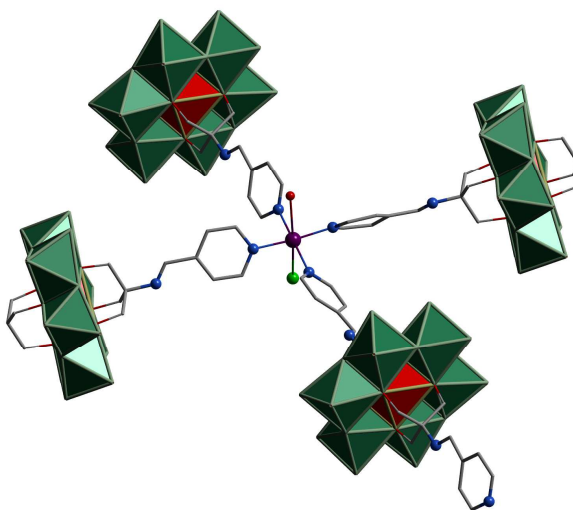


Figure 5.60: Structure of (**13**) Colour code: Anderson-Evans polyanions: green ring with red polyhedral models, Cu: violet, O: red, C: grey wire/stick, N: blue, Cl: green. TBA counterions, DMF molecules and H atoms are omitted for clarity.

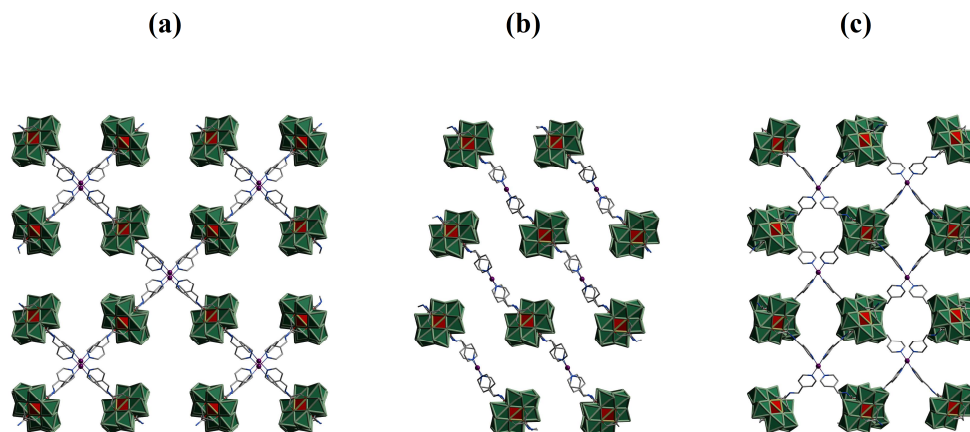


Figure 5.61: View along the *a*-axis (a), *b*-axis (b) and *c*-axis (c). Colour code: Anderson-Evans polyanions: green ring with red polyhedral models, Cu: violet, O: red, C: grey wire/stick, N: blue wire/stick. DMF molecules, Cl atoms, TBA counterions and H atoms are omitted for clarity.

Forgan *et al.* reported a compound containing $[\text{MnMo}_6\text{O}_{18}\{(\text{OCH}_2)_3\text{CC}_5\text{H}_4\text{N}\}_2]^{3-}$ polyanions, which coordinate to Cu^{2+} ions via pyridyl groups forming 2D square grids, similar to compound **(13)**.⁴⁶ In the following, the bond lengths and angles within the crystal structure of **(13)** will be compared to the ones of Forgan *et al.*, where these values are in parentheses after the parameters of **(13)**. The $\text{N}_{\text{py}}\text{-Cu-N}_{\text{py}}$ angle within one sheet is in the range 86.9° to 174.0° (90.9° to 178.7°). The $\text{N}_{\text{py}}\text{-N}_{\text{py}}$ distance within one POM hybrid is 18.8 \AA (14.6 \AA), which is the length of hybrid **(4)** without coordination to any metal atom. As shown in Figure 5.62, the shortest Mn-Cu and Cu-Cu distances within one sheet are 11.4 \AA (9.3 \AA) and 22.7 \AA (18.7 \AA), respectively. The Mn-Mn distance between two *cis* coordinating hybrids is 13.8 \AA (13.1 \AA), whereas the Mn-Mn distance between two *trans* coordinating hybrids is 22.7 \AA (18.6 \AA). The distances between two Cu atoms opposite to each other within one rhombus are 27.5 \AA (26.2 \AA) and 36.2 \AA (26.4 \AA). The shortest Cu-Cu distance between two sheets is 14.0 \AA (13.6 \AA).

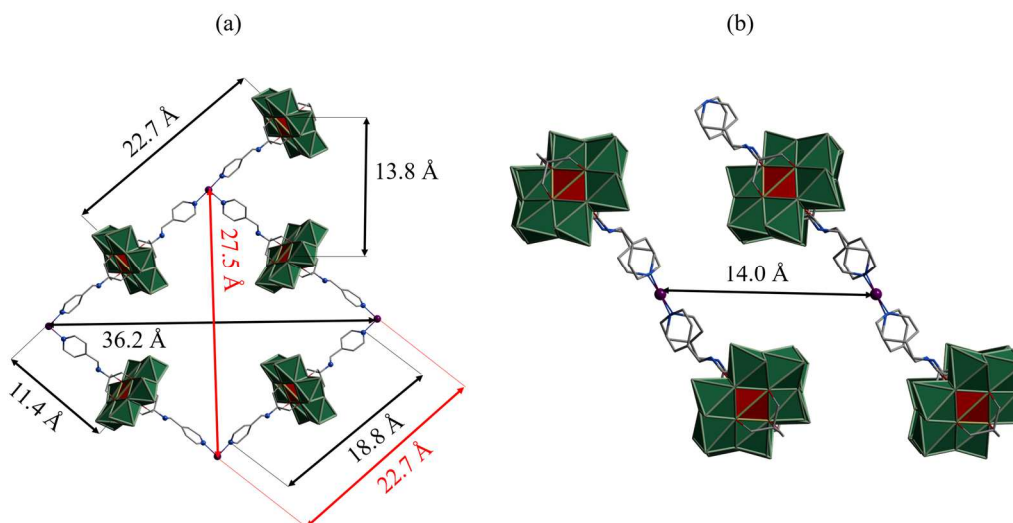


Figure 5.62: View on top of one 2D layer (a) and parallel to 2D layers (b). Colour code: Anderson-Evans polyanions : green ring with red polyhedral models, Cu: violet, O: red, C: grey stick/wire, N: blue stick/wire. DMF molecules, Cl atoms, counterions and H atoms are omitted for clarity.

The comparison of the two structures reveals that due to the difference of the length of the hybrid linkers, the parameters of rhombs of the square lattice in **(13)** are bigger than in the structure of Forgan and co-workers.

In compound **(13)**, the Cl, DMF and two out of four N_{py} groups coordinating to the Cu centre are disordered (kink at N disorder, see section 5.2.3.1). Nevertheless, the twofold disorder could be modelled for all the ligands.

The charge is balanced by tetrabutylammonium ($[N(n-C_4H_9)_4]^+$) cations in the lattice. Considering the asymmetric unit, which contains two $\{MnMo_6O_{18}\{(OCH_2)_3CN=CH(4-C_5H_4N)_2\}^{3-}$ units and one $\{CuCl(DMF)\}^{1+}$ moiety, five $[N(n-C_4H_9)_4]^+$ ions balance the charge. One of the TBA ion is presumably disordered over an inversion centre. Electron density resulting from three DMF molecules was also observed, but could also not be modelled. The contribution of half of the cation and three DMF molecules were therefore calculated using the SQUEEZE function within PLATON.¹⁵⁹

Considering the $\{\text{CuCl}(\text{DMF})(\text{N}_{\text{py}})_4\}$ unit, the analysis with the computer program SHAPE¹⁵⁶ reveals that the geometry of the six-coordinated Cu atom in this moiety (shown in Figure 5.63) is distorted from the idealized octahedron (OC) geometry by 2.976. The continuous shape measurements (CShM's) are listed in Table 8.17 in section 8.2.4.

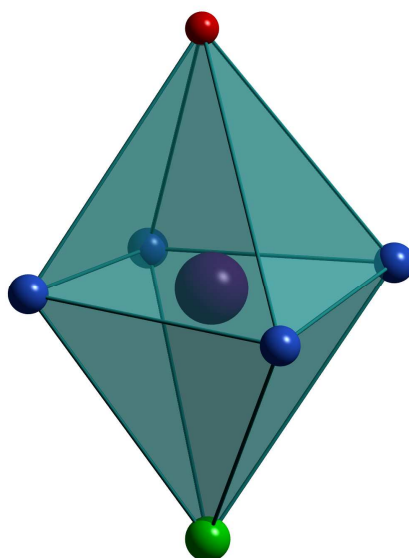


Figure 5.63: The environment of the $\{\text{CuCl}(\text{DMF})(\text{N}_{\text{py}})_4\}$. The DMF molecule and N_{py} groups are represented as O and N atoms, respectively. Colour code: Cu: violet, O: red, N: blue, Cl: green.

5.3.2.1.2 Topological analysis

Figure 5.64 shows an extract of the topological analysis of **(13)**.

Considering the $\{\text{MnMo}_6\text{O}_{18}\{(\text{OCH}_2)_3\text{CN}=\text{CH}(4\text{-C}_5\text{H}_4\text{N})\}_2\}$ unit (marked as green stick) as a linear linker, which connects two Cu centres (marked as magenta sphere), 2D sheets with an A-B-A alternation are formed. The topology can be identified as a 4-coordinated, unidonal net with point symbol $\{4^4.6^2\}$ and the topological type square lattice (sql).

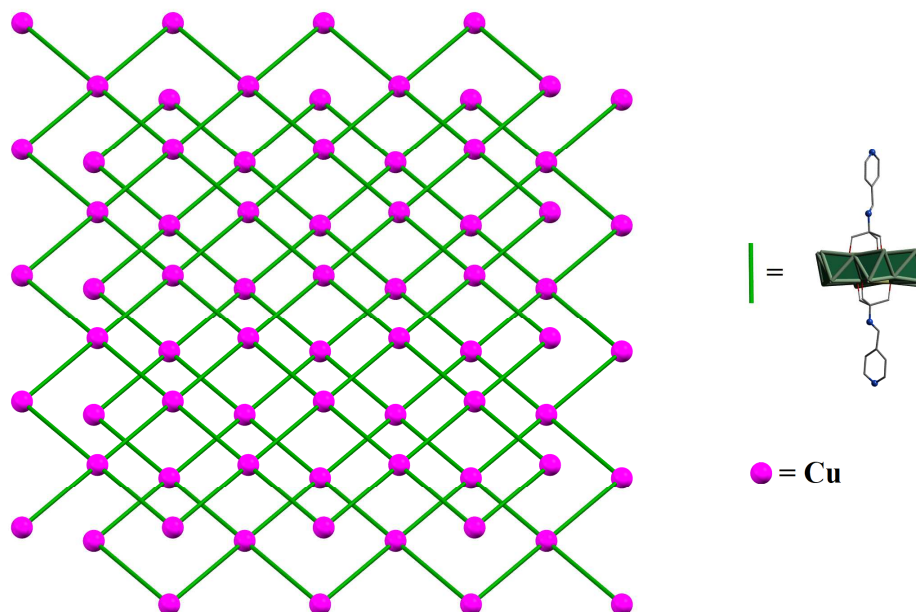


Figure 5.64: Topological extract of (13). Colour code: Cu: magenta sphere, hybrid (4): green stick.

5.3.2.1.3 Powder X-ray diffraction

Figure 5.65 shows the simulated (simu) and experimental (exp) PXRD-patterns of (13). The simulated pattern serves as reference. The experimental pattern shows a good accordance to (13)-simu.

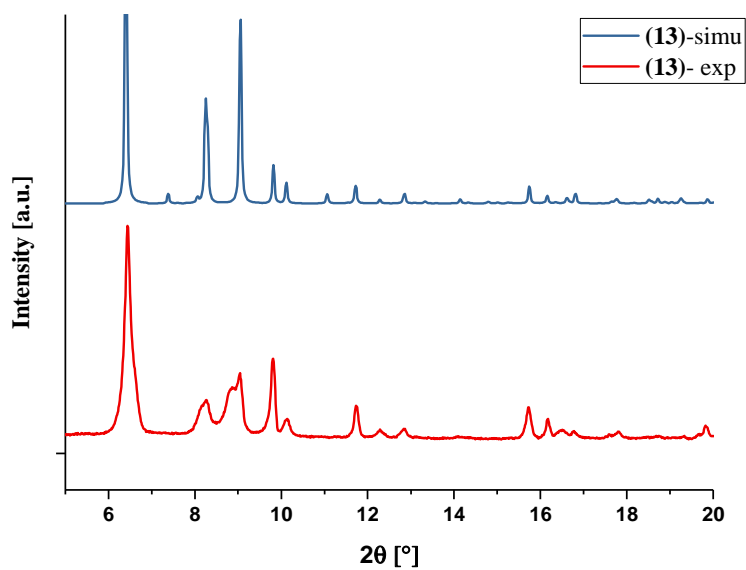


Figure 5.65: Simulated (*simu*) and experimental (*exp*) PXRD-patterns of (**13**).

5.3.2.1.4 Solid state UV-vis studies

Figure 5.66 shows the solid state UV-vis spectrum of compound (**13**). The spectrum shows one absorption band at $\lambda = 659$ nm, which can be assigned to a d-d electron transfer from the t_{2g} orbital to the e_g^* orbital within one Cu^{2+} ion.

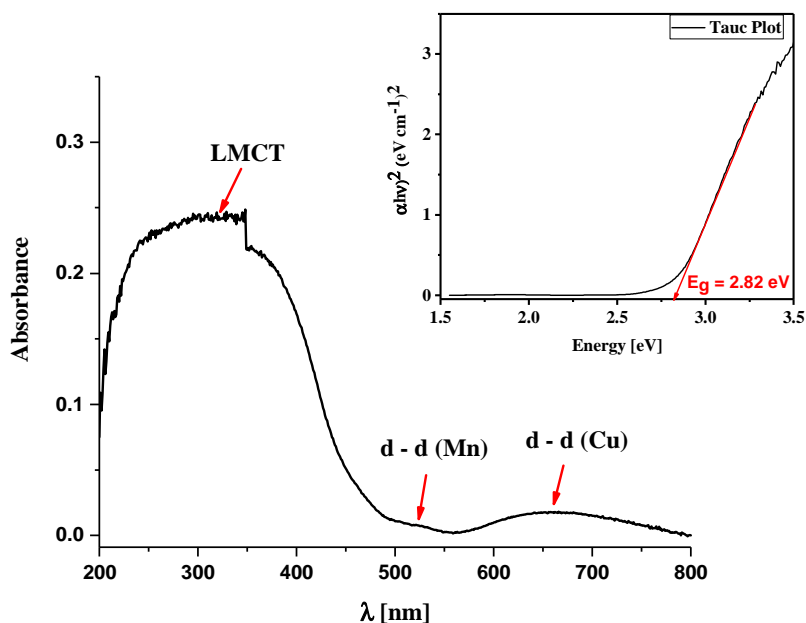


Figure 5.66: Solid state UV-vis spectrum of compound (**13**).

Additionally, an absorption band at $\lambda = 524$ nm observable, which can be denoted to a d-d electron transfer from the t_{2g} orbital to the e_g^* orbital within one Mn^{3+} ion. The maximum absorption at $\lambda = 321$ nm can be allocated to a LMCT. The change of absorbance at $\lambda = 350$ nm was caused by the change of the lamp during the record of the spectrum. The bandgap of 2.82 eV was found using the Tauc method.

5.3.2.2 Catalytic studies

A³-Coupling

$Cu^{1+/2+}$ and Ag^{1+} containing compounds are well known as catalysts for three-component coupling of an aldehyde, an amine and an alkyne (A³-Coupling, a scheme for this reaction is shown in Figure 5.67), which has been figured out as a powerful method in order to synthesize propargylic amines.^{131,132} Therefore, the catalytic performance of compound (**13**) was investigated for this kind of reaction.

5. Results and Discussion

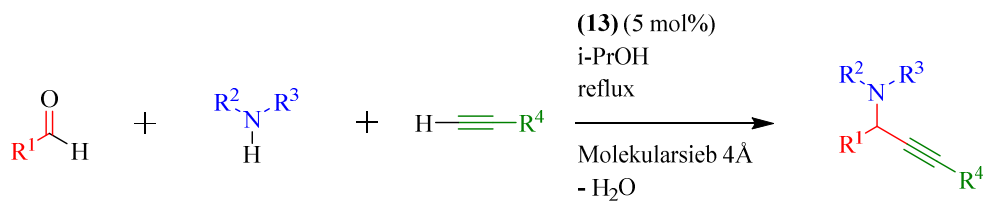


Figure 5.67: A³-Coupling of an aldehyde, an amine and an alkyne in order to form propargylic amines.

Table 5.2 shows the summary of A³-Coupling reactions using the general procedure described in section 4.6.1.

Table 5.2: Summary of A³-Coupling reactions.

Aldehyde	Amine	Alkyne	Desired Product	Yield [%]
				52
				49
				93
				N.R.

N.R. = no reaction.

5.3.2.2.1 Conclusion

Compound **(13)** was successfully synthesized by stirring a mixture of $[N(n\text{-C}_4\text{H}_9)_4]_3[\text{MnMo}_6\text{O}_{18}\{(\text{OCH}_2)_3\text{CNH}_2\}_2]$ (**3**), $\text{CuCl}_2 \cdot 2\text{H}_2\text{O}$, 4-pyridinecarboxaldehyde and DMF for 20 h at 85 °C and was isolated in the form of crystals, whereby a crystal structure could be determined. Furthermore, this compound was also characterized by PXRD, EA, UV-vis and FT-IR spectroscopy. Additionally, compound **(13)** shows catalytic properties for a series of A^3 -Coupling reactions with moderate to high yields.

Furthermore, electrochemical studies were performed, however, the decomposition of **(13)** in water was observed, and therefore further studies were not continued.

5.3.2.3 $[\text{Zn}(\text{DMF})_4][\text{Zn}(\text{DMF})_2\text{MnMo}_6\text{O}_{18}\{(\text{OCH}_2)_3\text{CN}=\text{CH}(4\text{-C}_5\text{H}_4\text{N})\}_2] \cdot 10\text{DMF}$ (**14A**) and $[(\text{Zn}(\text{DMF})_3)_2(\text{Zn}(\text{DMF})_4\text{MnMo}_6\text{O}_{18}\{(\text{OCH}_2)_3\text{CN}=\text{CH}(4\text{-C}_5\text{H}_4\text{N})\}_2)] \cdot 9\text{DMF}$ (**14B**)

Compounds **(14A)** and **(14B)** were obtained by over-layering a buffer solution of DMF/MeCN (1:1/v:v) on top of a solution of $[N(n\text{-C}_4\text{H}_9)_4]_3[\text{MnMo}_6\text{O}_{18}\{(\text{OCH}_2)_3\text{CN}=\text{CH}(4\text{-C}_5\text{H}_4\text{N})\}_2] \cdot 3\text{DMF}$ (**4**) in DMF. Afterwards, a solution of the ZnCl_2 in MeCN was layered on top of the buffer layer. Due to the diffusion of the reactants through the layers crystals of **(14A)** and **(14B)** were formed.

5.3.2.3.1 Single crystal structure of $[\text{Zn}(\text{DMF})_4][\text{Zn}(\text{DMF})_2\text{MnMo}_6\text{O}_{18}\{(\text{OCH}_2)_3\text{CN}=\text{CH}(\text{4-C}_5\text{H}_4\text{N})\}_2] \cdot 10\text{DMF}$ (**14A**)

The crystallographic data of compound (**14A**) are given in Table 8.11.

The single crystal X-ray diffraction analysis reveals that compound (**14A**) crystallizes in the cubic space group $I432$ with unit cell parameters $a = 36.7518(7) \text{ \AA}$, $V = 49640(3) \text{ \AA}^3$. The framework structure, shown in Figure 5.68, is built from $\{\text{MnMo}_6\text{O}_{18}\{(\text{OCH}_2)_3\text{CN}=\text{C}(\text{4-C}_5\text{H}_4\text{N})\}_2\}^{3-}$ (**4**) units linking to $\{\text{Zn}(\text{DMF})_2\}^{2+}$ (Zn1) moieties, form a 3D network (see Figure 5.68 (c)). The coordination sphere of the Zn1 ion in the framework is filled by two DMF molecules, two terminal oxygen (O_t) atoms of two POMs (**4**) and two N_{py} groups of two other hybrids (**4**) (see Figure 5.68 (a)). The two DMF molecules, as well as the two N_{py} are *cis* to one another, whereas the O_t s are *trans* to each other. In addition, every POM hybrid (**4**) coordinates to two Zn1 ions via two pyridyl groups and to another two Zn1 centres via two terminal oxygens (see Figure 5.68 (b)).

The charge of the framework is balanced by $\{\text{Zn}(\text{DMF})_4\}^{2+}$ (Zn2) units, which are located in the lattice (see Figure 5.68 (a)), thus leading to the chemical ratio of POM (**4**): $\{\text{Zn}^{2+}\}$ of 2:3.

The DMF molecules coordinating to the metal centres Zn1 and Zn2 are twofold disordered. Furthermore, there are ten DMF molecules in the lattice, which were identified via the SQUEEZE function within PLATON.¹⁵⁹

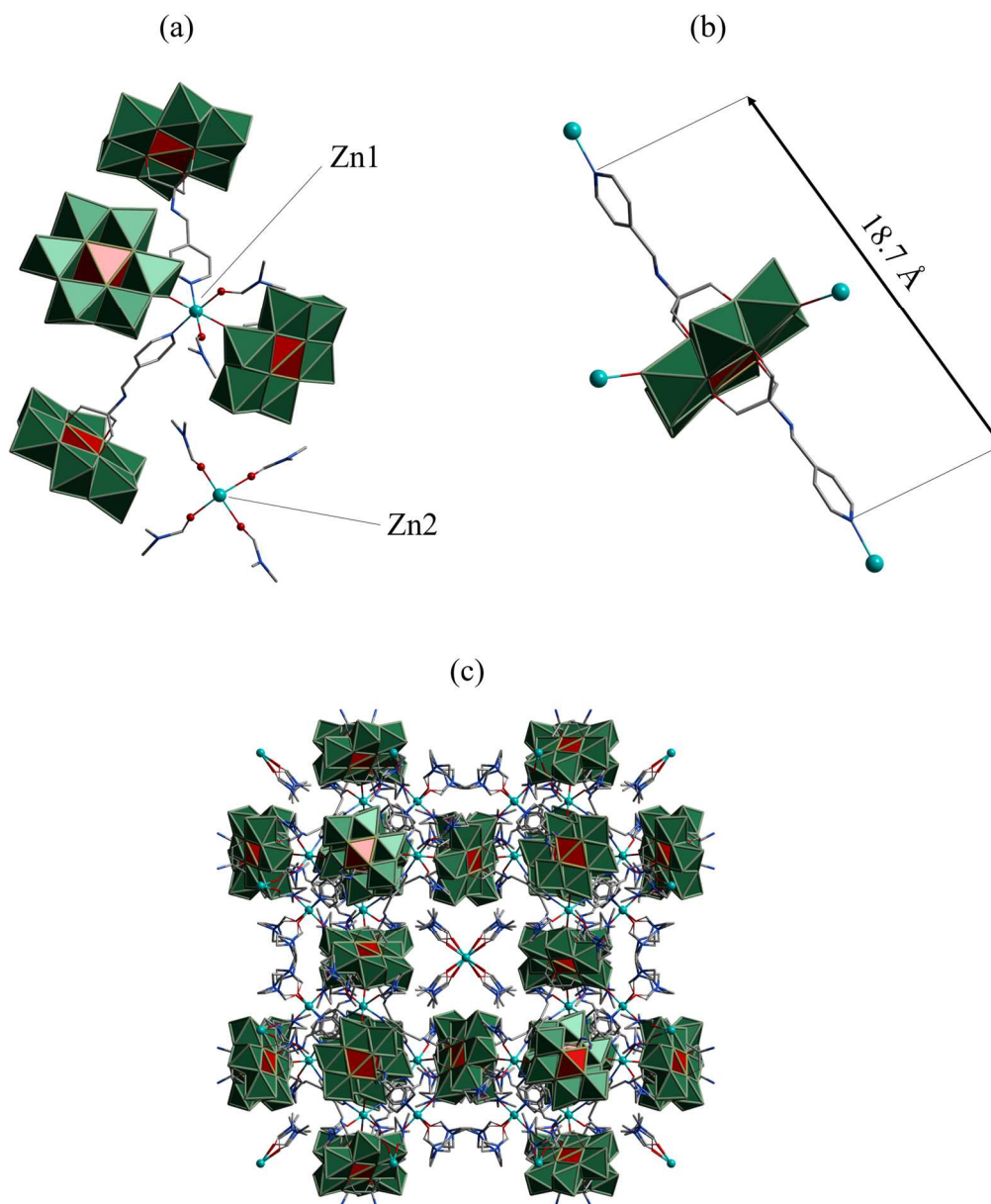


Figure 5.68: (a) The environment of the Zn^{2+} ions, (b) environment of the Anderson-Evans hybrid and (c) the 3D framework of compound (**14A**). Colour code: C: grey wire/stick, N: blue wire/stick, Zn (light blue), O (red), Anderson-Evans polyanions (greens ring with red polyhedral models). Solvent molecules in lattice and H atoms are omitted for clarity.

In Figure 5.69, some selected distances are noted within the structure of **(14A)**. In **(14A)** the length of the hybrid from N_{py} to N_{py} amounts to 18.7 Å. In comparison to the “naked” hybrid **(4)** (in which the N_{py} - N_{py} distance is 18.8 Å) the POM-unit in compound **(14A)** is compressed by 0.1 Å. The distance between two Zn atoms coordinated by the pyridyl groups of one hybrid is 22.9 Å, whereas the distance between two Mn centres of two POMs linked via a Zn atom by a terminal oxygen is 13.4 Å. The distance between two Zn atoms coordinated by two terminal oxygen atoms of one polyanion is 11.1 Å. Furthermore the diameter of a channel in the POMOF system is 9.8 Å.

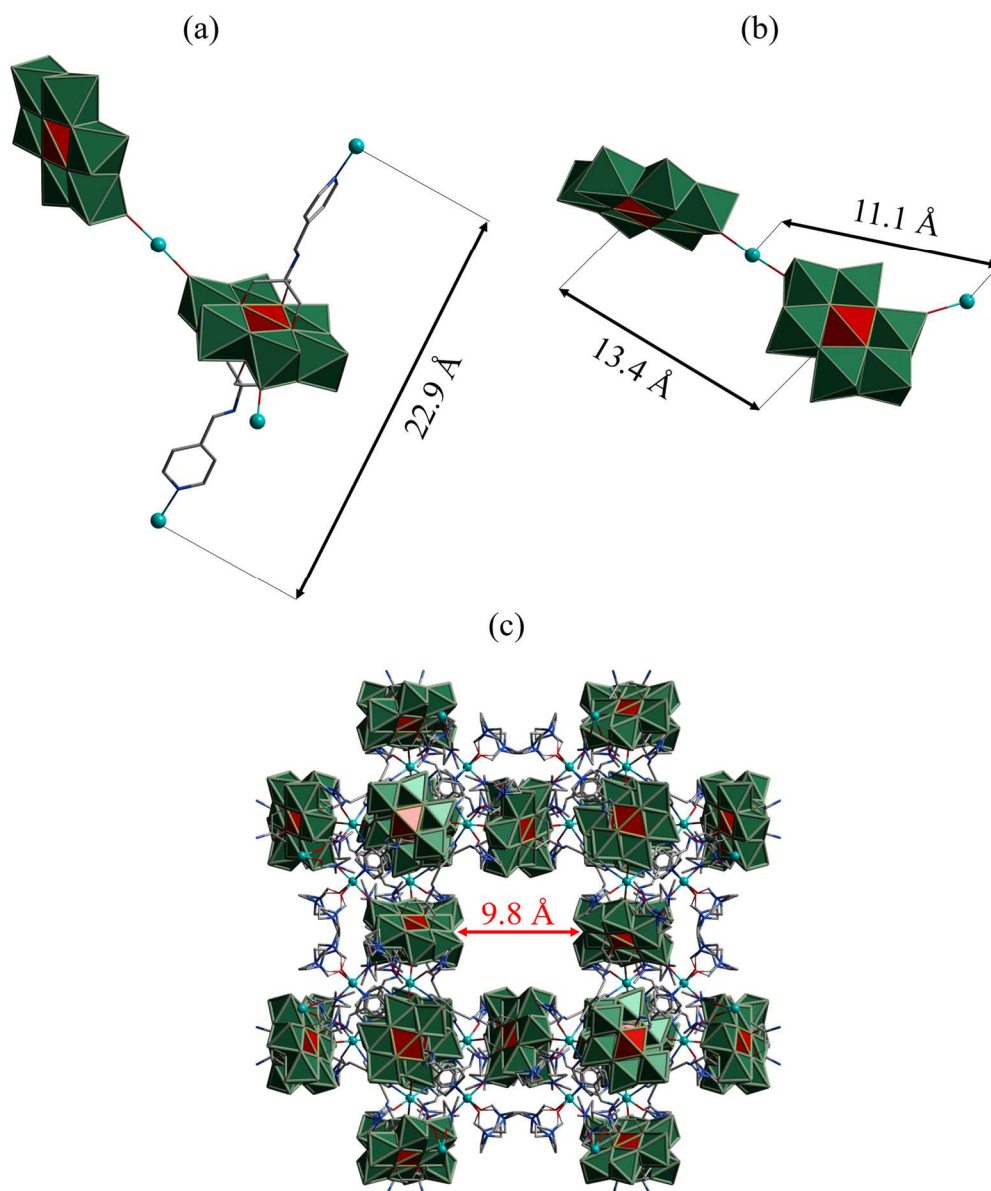


Figure 5.69: Distances noted in some extracts of (**14A**). Colour code: C: grey wire/stick, N: blue wire/stick, Zn (light blue), O (red), Anderson-Evans polyanions (greens ring with red polyhedral models).

The analysis with the computer program SHAPE¹⁵⁶ reveals that the geometries of the six-coordinated Zn1 atom in the $\{\text{Zn}(\text{DMF})_2(\text{O}_t)_2(\text{N}_{\text{py}})_2\}$ unit and the four-

coordinated Zn²⁺ ion in the {Zn(DMF)₄} (Figure 5.70) are distorted from the idealized octahedron (OC) geometry by 0.114. The continuous shape measurements (CShM's) are listed in Table 8.18 in section 8.2.5.8.2.2

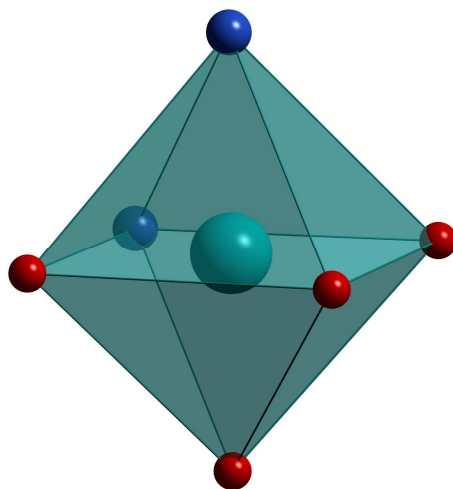


Figure 5.70: Environment of six-coordinated Zn1 in the {Zn(DMF)₂(O_i)₂(N_{py})₂}. Colour code: Zn: light blue, O: red, N: blue.

5.3.2.3.2 Topological analysis of [Zn(DMF)₄][Zn(DMF)₂MnMo₆O₁₈{(OCH₂)₃CN=CH(4-C₅H₄N)}₂]₂·10DMF (14A)

Figure 5.71 shows an extract of the topological analysis of (14A). A 3D network results from the fourfold connection through {MnMo₆O₁₈{(OCH₂)₃CN=CH(4-C₅H₄N)}₂} linkers (purple spheres) between the Zn1 nodes (light blue spheres).

Considering the {MnMo₆O₁₈{(OCH₂)₃CN=CH(4-C₅H₄N)}₂} unit as a fourfold coordinating linker with its Mn core (purple spheres) and the Zn metals (light blue spheres) as nodes connecting the linkers, thus forming a 3D network. The topology can be identified as a (4,4) binodal net with point symbol {4².8³.10}{4².6⁴}. The stoichiometry of the nodes is 1 : 1 and the topology of this network has never been reported before, therefore this topology has been assigned as “mpm1”.

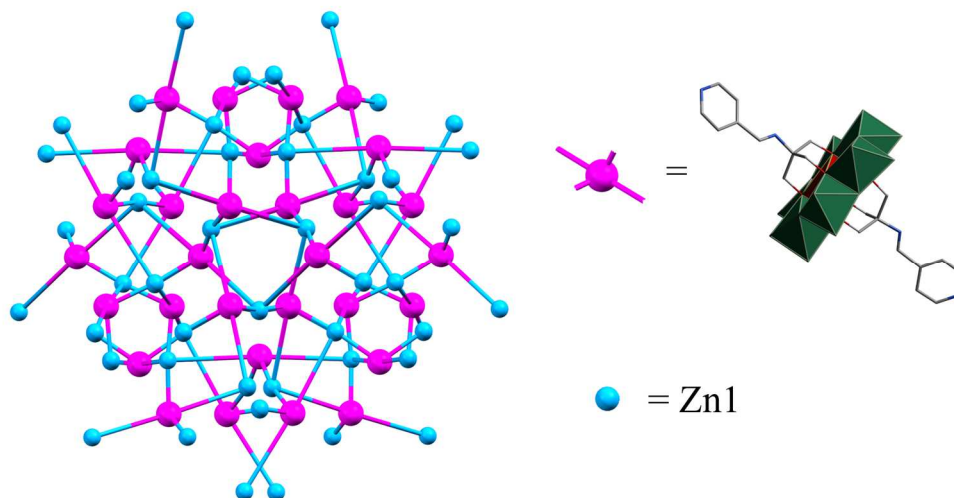


Figure 5.71: Topological extract of (14A). Colour code: hybrid (4): purple sphere, Zn: light blue sphere.

5.3.2.3.3 Single crystal structure of $[(\text{Zn}(\text{DMF})_3)_2(\text{Zn}(\text{DMF})_4\text{MnMo}_6\text{O}_{18}\{(\text{OCH}_2)_3\text{CN}=\text{CH}(4\text{-C}_5\text{H}_4\text{N})_2\})_2]\cdot 9\text{DMF}$ (14B)

The crystallographic data of compound (14B) are given in Table 8.12.

Compound $[(\text{Zn}(\text{DMF})_3)_2(\text{Zn}(\text{DMF})_4\text{MnMo}_6\text{O}_{18}\{(\text{OCH}_2)_3\text{CN}=\text{CH}(4\text{-C}_5\text{H}_4\text{N})_2\})_2]\cdot 9\text{DMF}$ (14B) crystallizes in the monoclinic space group $C2/c$ with unit cell parameters $a = 44.0133(6) \text{ \AA}$, $b = 12.9451(2) \text{ \AA}$, $c = 28.3784(4) \text{ \AA}$, $\beta = 102.002(1)^\circ$, $V = 15815.3(4) \text{ \AA}^3$. As in the structure (14A), units of $\{\text{MnMo}_6\text{O}_{18}\{(\text{OCH}_2)_3\text{CN}=\text{CH}(4\text{-C}_5\text{H}_4\text{N})_2\}_2\}$ (4) also coordinate to Zn atoms via pyridyl groups and terminal oxygen (O_t) atoms in structure (14B), resulting in a 3D network. In contrast to compound (14A), compound (14B) contains two different octahedral coordination spheres of the $\{\text{Zn}\}^{2+}$ cations within the framework. Zn1 is coordinated by three DMF molecules, two N_{py} groups of two hybrids (4) and one O_t atom of one POM (4). The two N_{py} groups are *trans* to each other, whereas the terminal oxo group and the three DMF molecules lie in the square plane (see Figure 5.72 (a)). Zn2 is coordinated by four DMF molecules in the square plane and two

terminal oxygen atoms of two POM hybrids (**4**), which are *trans* to each other (see Figure 5.72 (b)). This combination of these Zn-nodes results in the 3D-structure shown in Figure 5.72 (c) and (d).

In the structure, every second pyridyl group of the organic ligand is disordered by the kink at N disorder, mentioned in section 5.2.3.1. Nevertheless, the twofold disorder could be satisfactory modelled. Additionally, in the lattice one DMF molecule could be refined, whereas further eight DMF molecules were identified via the SQUEEZE function within PLATON.¹⁵⁹ As in the case of compound (**14A**) the ratio of POM (**4**): {Zn²⁺} is 2:3, giving the chemical formula, [Zn(DMF₃)₂Zn(DMF)₄POM(**4**)]₂·9DMF.

The following distances within the structure (**14B**) are shown in Figure 5.72. The distance between the Mn core of a POM to a Zn₂ atom, connected through a terminal oxygen of the polyanion is 6.5 Å, whereas the space between a Mn core and a Zn₁ centre, which are also linked via a O_t is about 0.1 Å longer. The distance between one Mn centre of a POM coordinating to one Zn₁ atom via a N_{py} group is 11.5 Å. The space between two neighboring Zn₁ and Zn₂ nodes bridged by a POM via terminal oxygen atoms is 11.2 Å. The parameters of a rhombus, forming 1D channels in the network, are 11.4 Å and 22.9 Å, respectively. Additionally, the length from N_{py} to N_{py} of one hybrid (**4**) in compound (**14B**) amounts to 18.8 Å, which corresponds to the length of the non-coordinating starting material.

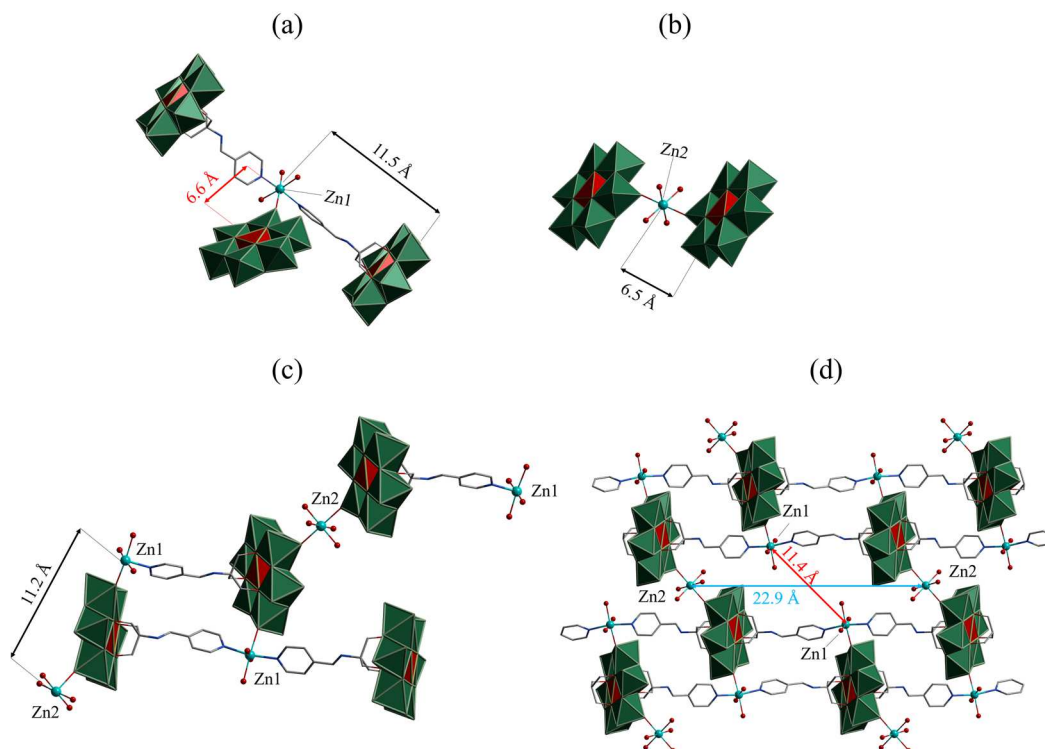


Figure 5.72: Compound (**14B**): (a) The environment of the Zn1. (b) The environment of the Zn2. (c)+(d) the 3D framework of compound (**14B**). Colour code: C: grey wire/stick, N: blue wire/stick, Zn: light blue, O: red, Anderson-Evans polyanions: green ring with red polyhedral models. Solvent molecules in the lattice and H atoms are omitted for clarity. DMF molecules coordinating to Zn atoms are represented by their O atom.

The analysis with the computer program SHAPE¹⁵⁶ reveals that the geometries of the six-coordinated Zn1 and Zn2 atoms in the $\{\text{Zn}(\text{DMF})_3(\text{O}_t)(\text{N}_{\text{py}})_2\}$ and $\{\text{Zn}(\text{DMF})_4(\text{O}_t)_2\}$ units, respectively, (shown in Figure 5.73) are distorted from the ideal shape. The deviation value of Zn1 and Zn2 from the idealized octahedron (OC) geometries are 0.477 and 0.130, respectively.

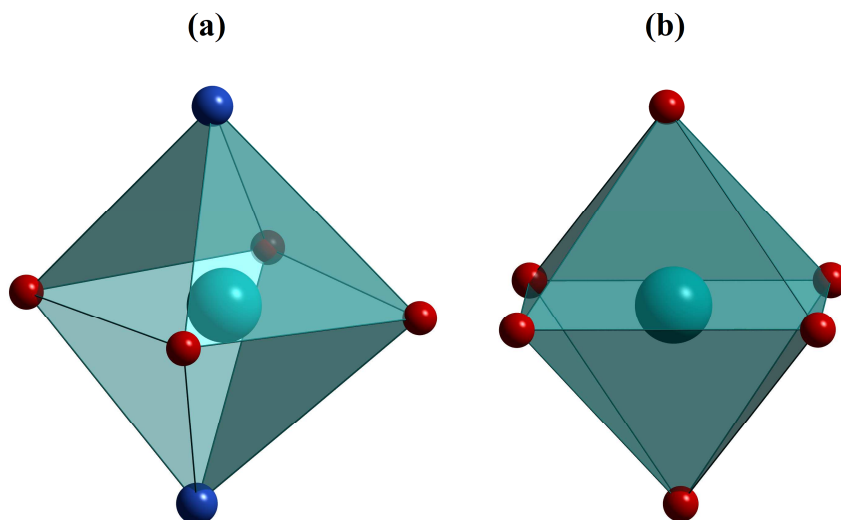


Figure 5.73: Coordination octahedra of Zn1 in $\{Zn(DMF)_3(O_t)(N_{py})_2\}$ (a) and Zn2 in $\{Zn(DMF)_4(O_t)_2\}$ (b).

The continuous shape measurements (CShM's) are listed in Table 8.19 in section 8.2.6.

5.3.2.3.4 Topological analysis of $[(Zn(DMF)_3)_2(Zn(DMF)_4MnMo_6O_{18}((OCH_2)_3CN=CH(4-C_5H_4N))_2)] \cdot 9DMF$ (**14B**)

Figure 5.74 shows an extract of the topological analysis of (**14B**). As in compound (**14A**), also in structure (**14B**) the $\{MnMo_6O_{18}((OCH_2)_3CN=CH(4-C_5H_4N))_2\}$ unit is considered as a fourfold coordinating linker with its Mn core (purple spheres) linking to the Zn metal centres (light blue spheres). Zn1 coordinates to two N atoms belonging to two different $\{MnMo_6O_{18}((OCH_2)_3CN=CH(4-C_5H_4N))_2\}$ units and to one terminal O atom of the inorganic $\{MnMo_6O_{18}\}$ moiety belonging to a third $\{MnMo_6O_{18}((OCH_2)_3CN=CH(4-C_5H_4N))_2\}$ unit, thus forming a three connected T shaped node (Figure 5.74: light blue colour). Zn2 connects via an O_t to two $\{MnMo_6O_{18}\}$ units forming a 2-connected node, however according to the topological regulations (two connected nodes do not contribute in the overall

topology, therefore these should be omitted) it can not be considered as node, but as an extension of the linker that links two adjacent $\{\text{MnMo}_6\text{O}_{18}\}$ units. Therefore, each $\{\text{MnMo}_6\text{O}_{18}\{(\text{OCH}_2)_3\text{CN}=\text{CH}(4\text{-C}_5\text{H}_4\text{N})\}_2\}$ linker connects to three Zn1 centres (two from the pyridyl groups and one via an O_t atom) and to one $\{\text{MnMo}_6\text{O}_{18}\{(\text{OCH}_2)_3\text{CN}=\text{CH}(4\text{-C}_5\text{H}_4\text{N})\}_2\}$ linker via a Zn2 node (Figure 5.74: pink colour). Thus, the topology can be identified as a (3,4) binodal net with point symbol $\{4.6^2.8\}\{4.6^2.8.10^2\}$ and labeling **fsx-3,4-C2/c-2**. As shown in Figure 5.74 the resulting topology is completely different from that found for **(14A)**. This illustrates the value of the topological analysis approach.

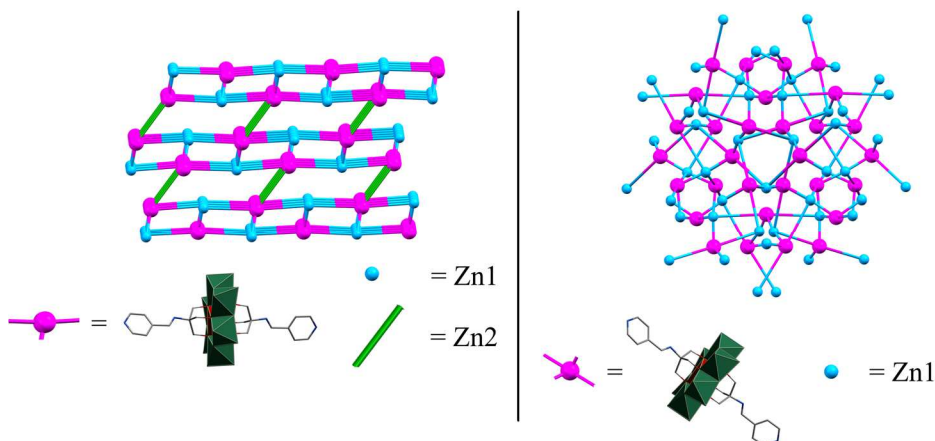


Figure 5.74: Topological extract of **(14B)**. Colour code: hybrid (**4**): purple sphere, Zn: light blue sphere. The topological analysis for **(14A)** is shown on the right for comparison.

5.3.2.3.5 Solid state UV-vis studies

Figure 5.75 shows the solid state UV-vis spectrum of compound **(14B)**. The spectrum reveals one absorption band at $\lambda = 524$ nm, which can be allocated to a d-d electron transfer from the t_{2g} orbital to the e_g^* orbital within one Mn^{3+} ion. Furthermore, the maximum absorption at $\lambda = 296$ nm can be allocated to a LMCT. The change of absorbance at $\lambda = 350$ nm was caused by the change of the lamp

during the record of the spectrum. The bandgap of 2.89 eV was found using the Tauc method.

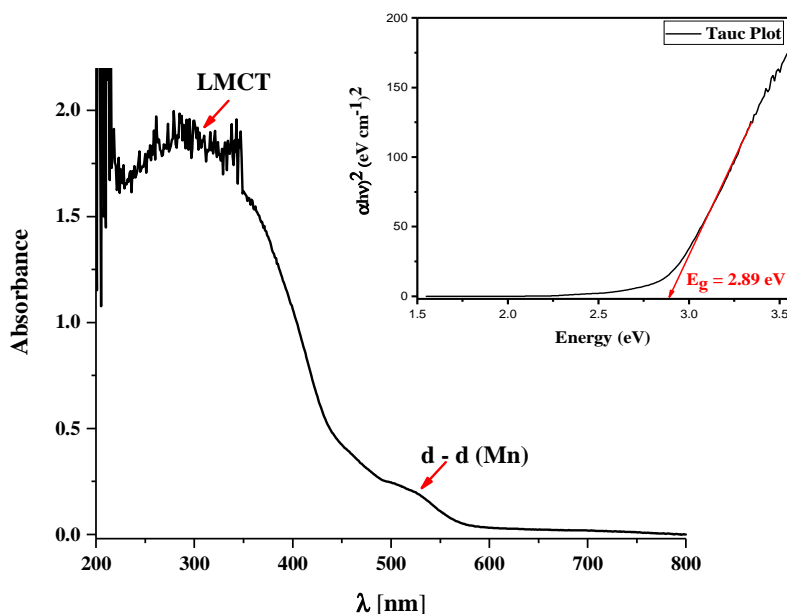


Figure 5.75: Solid state UV-vis spectrum of the mixture of (14A) and (14B).

5.3.2.3.6 Catalytic studies

Photo-electrocatalytic studies

The preparation of the working electrode and photo-electrocatalytic studies of the mixture of (14A) and (14B) were performed under the same conditions of (5) (see section 5.2.1.4). The results of the photocatalytic studies, shown in Figure 5.76 and Figure 5.77, demonstrate photo-electrocatalytic properties of these compounds for water splitting.

Utilizing linear sweep voltammetry from -0.8 V to 1.4 V under irradiation of artificial sunlight (see Figure 5.76 (a)), the current starts to develop at a potential of -0.14 V vs. Ag/AgCl with a maximum value of $4.74 \cdot 10^{-1}$ mA/cm² at a potential of 1.4 V vs. Ag/AgCl. The stability of the mixture of (14A) and (14B) under these

conditions was confirmed by measuring three runs of linear sweep voltammetry where the values did not change significant.

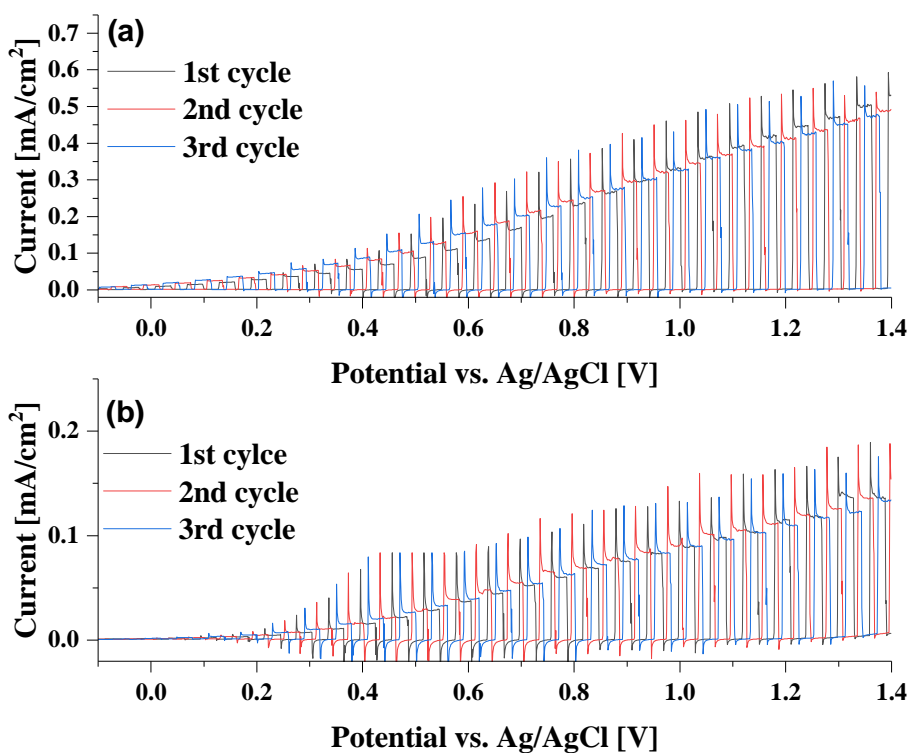


Figure 5.76: Photo-electrocatalytic results of the mixture of (14A) and (14B) recorded in 0.5M Na₂SO₄ (pH = 8.6) over the range -0.1 V to 1.4 V at a scan rate of 0.01 V/s and sunlight simulation without any filter (a) and filtering the radiation below 420 nm (b).

The measurements with a UV-cutoff (< 420 nm) were also performed three times, revealing the stability of the mixture under these conditions (see Figure 5.76 (b)).

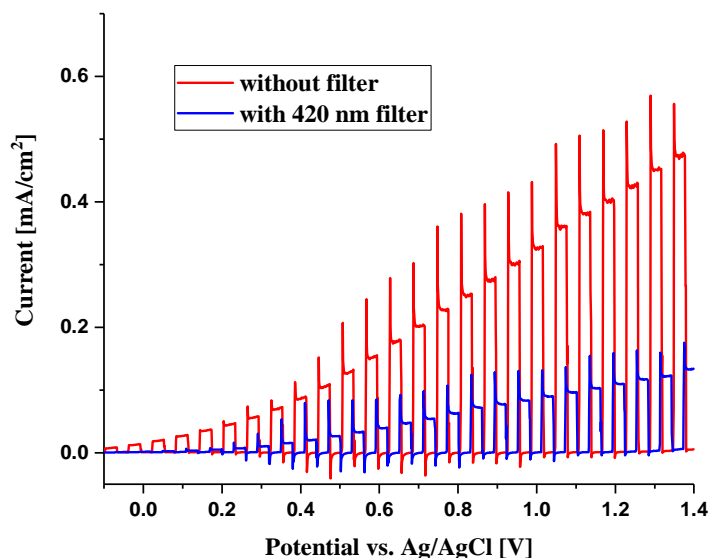


Figure 5.77: Comparison of photocatalytic studies of the mixture of **(14A)** and **(14B)** in $0.5M Na_2SO_4$ ($pH = 8.6$) over the range $-0.1 V$ to $1.4 V$ at a scan rate of $0.01 V/s$: Studies with and without filter ($< 420 nm$), for comparison in each case the final 3rd cycle was chosen.

The direct comparison of catalytic studies with and without filter are shown in Figure 5.77.

For the filtered sample the onset of current begins at a potential of $0.07 V$ vs. $Ag/AgCl$, which corresponds to a shift of $+0.21 V$ compared to measurement without filter. With progress of the scan the current increases to reach a maximum of $1.33 \cdot 10^{-1} mA/cm^2$ at $1.4 V$ vs. $Ag/AgCl$. This reveals that filtering radiation below $420 nm$ also reduces the catalytic activity of the system by 72% .

5.3.2.3.7 Conclusion

The reaction of compound **(4)** with $ZnCl_2$ results in two POMOF structures in the form of crystals, which could not be isolated separately in spite of many trials. Additionally, the mixture of **(14A)** and **(14B)** shows photo-electrocatalytic

properties for water splitting. Furthermore, the topological analysis reveals that **(14A)** exhibits a new topology in 3D framework structures.

5.3.2.4 [Cd(DMF)₂][Cd][N(*n*-C₄H₉)₄]₂[MnMo₆O₁₈{(OCH₂)₃CN=CH(4-C₅H₄N)}₂]₂·2DMF (**15**)

Compound **(15)** was obtained by over-layering a buffer solution of DMF/MeCN (1:1/v:v) on top of a solution of [N(*n*-C₄H₉)₄]₃[MnMo₆O₁₈{(OCH₂)₃CN=CH(4-C₅H₄N)}₂]₃·3DMF (**4**) in DMF. Afterwards, a solution of the Cd(NO₃)₂·4H₂O in MeCN was layered on top of the buffer layer. Crystals of **(15)** were formed due to the diffusion of the reactants through the layers.

5.3.2.4.1 Single crystal structure

The crystallographic data of compound **(15)** are given in Table 8.13.

The single crystal X-ray diffraction analysis reveals that compound **(15)** crystallizes in the triclinic space group *P*-1 with the unit cell parameters $a = 11.9141(5) \text{ \AA}$, $b = 13.4714(6) \text{ \AA}$, $c = 22.9561(9) \text{ \AA}$, $\alpha = 96.999(3)^\circ$, $\beta = 101.332(3)^\circ$, $\gamma = 113.688(3)^\circ$ and $V = 3224.5(2) \text{ \AA}^3$. The network structure of compound **(15)** is shown in Figure 5.78 and consist of two {MnMo₆O₁₈{(OCH₂)₃CN=CH(4-C₅H₄N)}₂}⁻³, one {Cd(DMF)₂}²⁺, one {Cd}²⁺ and two [N(*n*-C₄H₉)₄]⁺ units. Furthermore, there are two DMF molecule in the lattice.

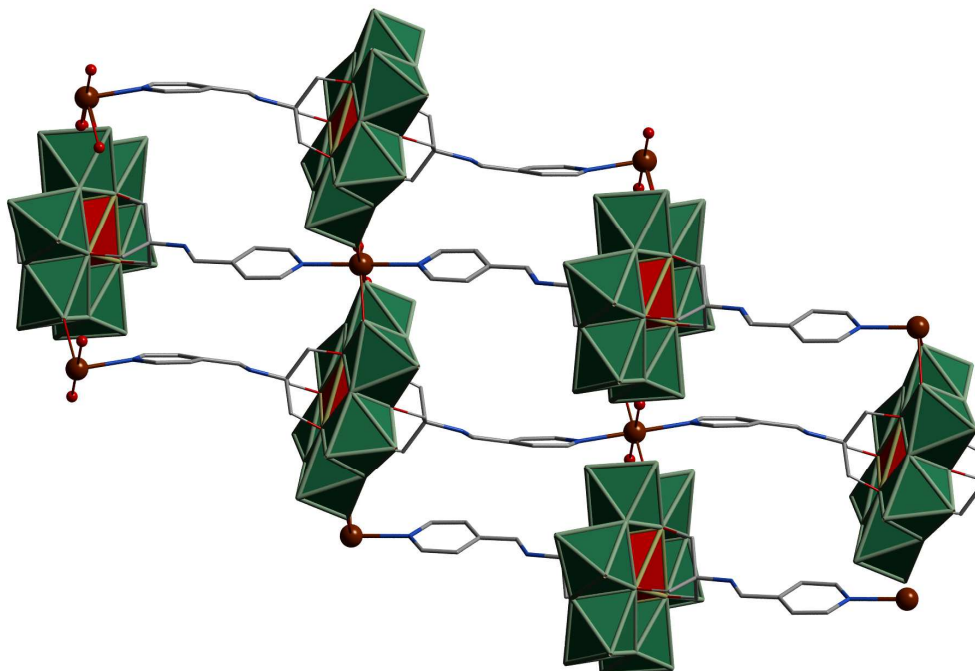


Figure 5.78: Structure of (**15**). Colour code: Anderson-Evans polyanions :green ring with red polyhedral models, Cd: brown, O: red, C: grey wire/stick, N: blue wire/stick. TBA counterions and DMF molecules in the lattice are omitted for clarity. DMF molecules coordinating to Cd ions are represented by their O atom.

The Anderson-Evans hybrids coordinate to the Cd centres in two ways: On the one hand via the pyridyl groups of the organic ligand, which is attached to the inorganic $\{\text{MnMo}_6\text{O}_{18}\}$ part by means via a tris residue, and on the other hand via one (Figure 5.79 (a)) or two (Figure 5.79 (b)) terminal oxygen atoms of the inorganic part of the hybrid. Figure 5.79 (a) and (b) also show the environments of the two octahedrally coordinated Cd cations ($\{\text{Cd}\}^{2+}$ (Cd1) and $\{\text{Cd}(\text{DMF})_2\}^{2+}$ (Cd2)).

In order to describe the structure of the network in a simple way, the inorganic parts of the Anderson-Evans POM hybrids with different connectivities are shown in different colours (see Figure 5.79). The $\{\text{Cd}\}^{2+}$ (Cd1) is coordinated by two N_{py} ligands from two different hybrids (coloured in red), which are *trans* to each other,

and by two terminal oxygen atoms of two different $\{\text{MnMo}_6\text{O}_{18}\}$ units (shown in green) (see Figure 5.79 (a)).

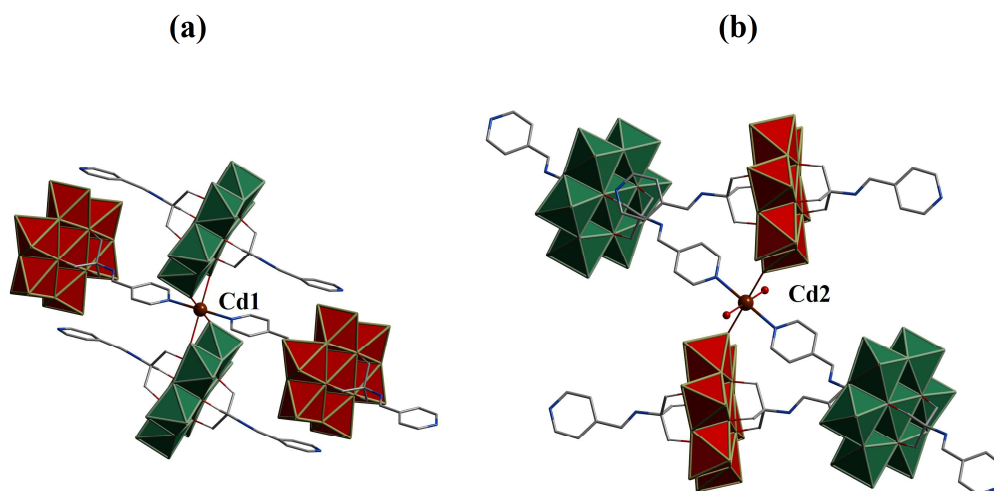


Figure 5.79: The coordination environments of the Cd ions of (15): $\{\text{Cd}\}^{+2}$ and $\{\text{Cd}(\text{DMF})_2\}^{+2}$. Colour code: Anderson-Evans polyanions : green and red polyhedral models, Cd: brown, O: red, C: grey wire /stick, N: blue wire/stick. TBA counterions and DMF molecules in the lattice are omitted for clarity. DMF molecules coordinating to Cd ions are represented by their O atom.

The $\{\text{Cd}(\text{DMF})_2\}^{2+}$ (Cd2) centre is coordinated by two DMF molecules, two terminal oxygen atoms of two different POMs (shown in red) and two N_{py} from another two different hybrids (shown in green). The DMF, terminal oxygen and pyridyl ligands are trans to each other (Figure 5.79 (b)).

Considering the connection between the $\{\text{Cd}(\text{DMF})_2\}^{2+}$ and $\{\text{Cd}\}^{2+}$ moieties via the red and green marked Anderson-Evans hybrids a 3D structure is constructed. An extract of this framework is shown in Figure 5.80. This figure also reveals that the red and green Anderson-Evans polyanions are arranged in an alternating A-B-A sequence.

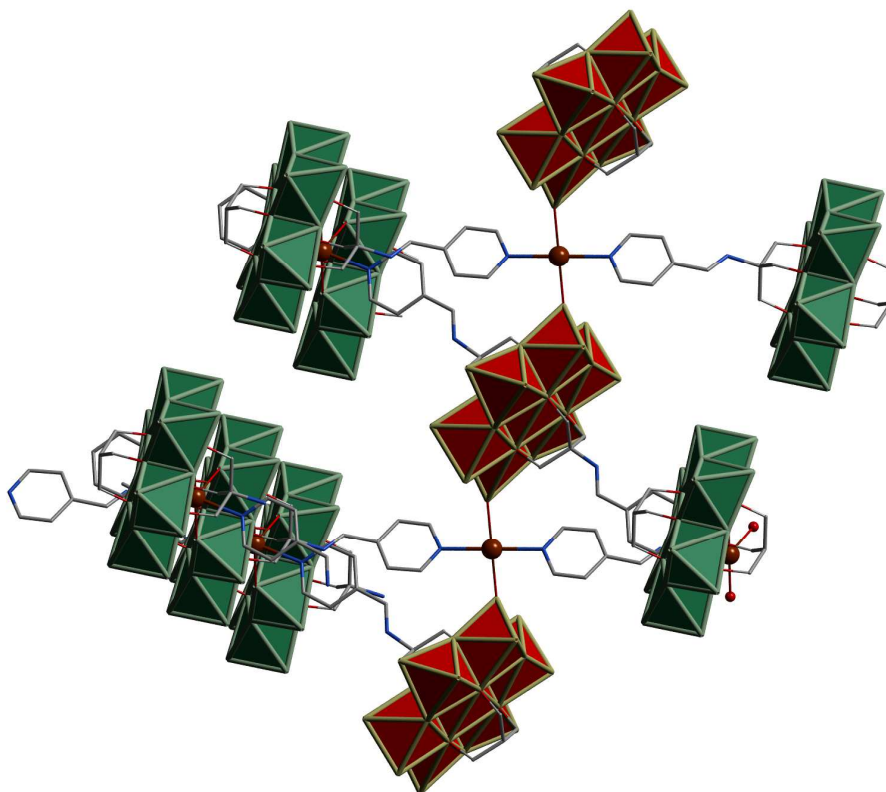


Figure 5.80: Extract of the 3D structure of **(15)**. Colour code: Anderson-Evans polyanions: green, red, Cd: brown, O: red, C: grey wire/stick, N: blue wire/stick. DMF molecules, H atoms and TBA counterions are omitted for clarity.

In the following, some parameters within the structure of **(15)** will be described and the values are also given in Figure 5.81. The Cd2-Cd2' distance of two Cd2 ions coordinated by each one terminal oxygen atom of one POM is 13.5 Å, whereas the Cd1-Cd1' distance coordinated by each two terminal oxygen atoms of one polyanion is 11.9 Å. The N_{py} to N_{py} distance within one L – POM – L coordinating to two Cd1 ions is 18.8 Å and 18.6 Å for the coordination to two Cd2 ions. In comparison to the non-coordinating hybrid **(4)** (in which the N_{py}-N_{py} distance is 18.8 Å) the POM-unit in compound **(15)** is compressed by 0.1 Å. The distance between two Cd1 ions coordinated on both pyridyl groups amounts to 23.2 Å, in comparison, the distance of two Cd2 coordinated by two N_{py} groups of one

polyanion is 23.0 Å. The diagonal of one 1D channel from one Cd1 to a Cd2 centre is 11.9 Å.

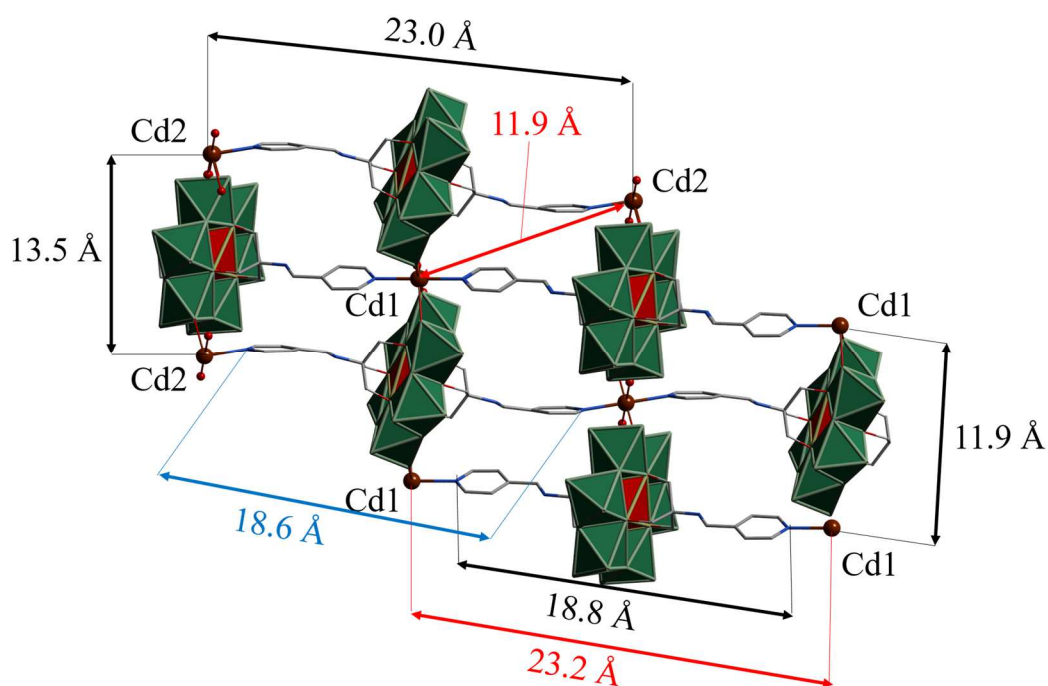


Figure 5.81: Distances noted in some extracts of (15). Colour code: Anderson-Evans polyanions: green ring with red polyhedral models, Cd: brown, O: red, C: grey wire/stick, N: blue wire/stick.

The analysis with the computer program SHAPE¹⁵⁶ reveals that the geometries of the six-coordinated Cd1 and Cd2 atoms in the $\{\text{Cd}(\text{DMF})_2(\text{O}_t)_2(\text{N}_{\text{py}})_2\}$ and $\{\text{Cd}(\text{N}_{\text{py}})_2(\text{O}_t)_4\}$ units, respectively, (shown in Figure 5.82) are distorted from idealized octahedral geometry (OC) by 0.185 and 0.044, respectively.

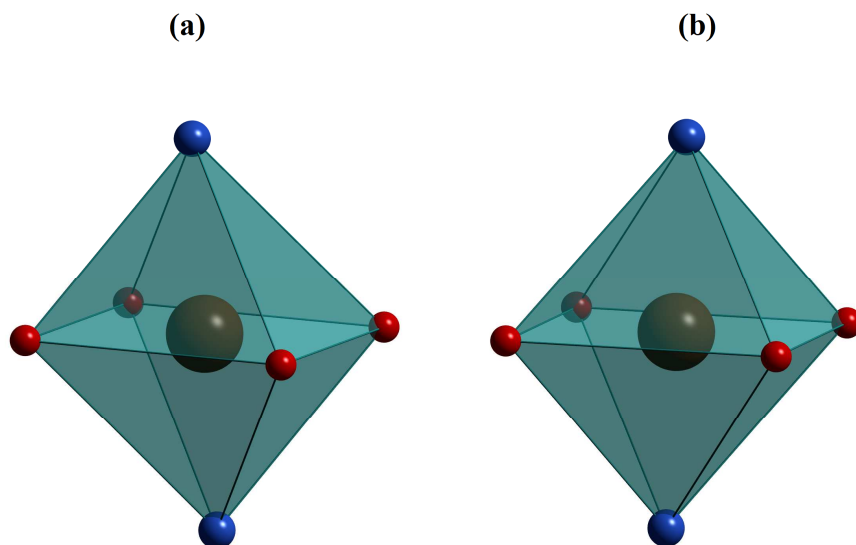


Figure 5.82: Coordination octahedra of Cd1 in $\{Cd(DMF)_2(O_t)_2(N_{py})_2\}$ (a) and Cd2 in $\{Cd(N_{py})_2(O_t)_4\}$ (b).

The continuous shape measurements (CSM's) are listed in Table 8.20 in section 8.2.7.

5.3.2.4.2 Topological analysis

An extract of the topological analysis of **(15)** is shown in Figure 5.83. From the topological point of view, the $\{MnMo_6O_{18}\{(OCH_2)_3CN=CH(4-C_5H_4N)\}_2\}$ unit can be considered as a fourfold linker with its Mn centre connecting to Cd metal nodes. In terms of coordination, the Anderson-Evans POM hybrid, which links to Cd1 ions via terminal oxygen atoms, is a sixfold linker binding via four terminal oxygens and two N_{py} groups to Cd metals. Due to the fact that this POM only binds to one Cd1 ion via two O_t groups, it is a fourfold linker in topological terms. Cd1 (light brown sphere) is coordinated by two N atoms belonging to two different $\{MnMo_6O_{18}\{(OCH_2)_3CN=CH(4-C_5H_4N)\}_2\}$ units (red sphere) and by two O_t atoms of the inorganic $\{MnMo_6O_{24}\}$ moiety (green sphere) belonging to two other $\{MnMo_6O_{18}\{(OCH_2)_3CN=CH(4-C_5H_4N)\}_2\}$ units, thus forming a four connected

cross shaped node (see Figure 5.83 (a)). Cd2 (dark brown sphere) connects via two terminal O atoms to two $\{\text{MnMo}_6\text{O}_{24}\}$ units (red sphere) and two N atoms belonging to two different $\{\text{MnMo}_6\text{O}_{18}\{(\text{OCH}_2)_3\text{CN}=\text{CH}(4\text{-C}_5\text{H}_4\text{N})\}_2\}$ units (green sphere) forming a four-connected node (see Figure 5.83 (a)). Figure 5.83 (b) shows the topological network without any regard to the type of Cd atom (blue sphere) and the POM hybrids (magenta sphere). This is a valid approach since the Cd ions are topologically equivalent to each other, which is also the case for the L – POM – Ls. Thus, the topology can be identified as a 4-coordinated uninodal net with point symbol $\{4^2.8^4\}$ and labelled **lvt**; **4/4/t1**.

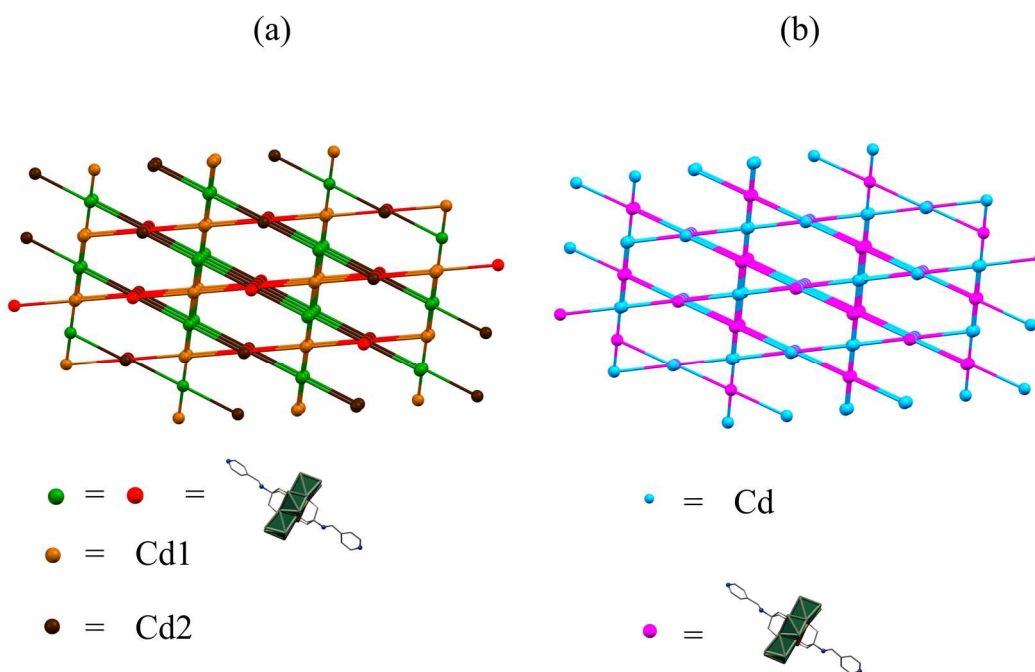


Figure 5.83: Topological extract of (15). Colour code: (a) $\{\text{MnMo}_6\text{O}_{18}\{(\text{OCH}_2)_3\text{CN}=\text{CH}(4\text{-C}_5\text{H}_4\text{N})\}_2\}$ unit: red and green sphere, Cd1: light brown sphere, Cd2: dark brown sphere, (b) $\{\text{MnMo}_6\text{O}_{18}\{(\text{OCH}_2)_3\text{CN}=\text{CH}(4\text{-C}_5\text{H}_4\text{N})\}_2\}$ unit: magenta sphere, Cd: blue sphere.

5.3.2.4.3 Powder X-ray diffraction

Figure 5.84 shows the PXRD patterns of **(15)** simulated (simu) and recorded PXRD-patterns of **(15)**. The simulated (simu) pattern serves as reference. From all PXRD patterns of **(15)**, it is clearly seen that the samples contain the desired products.

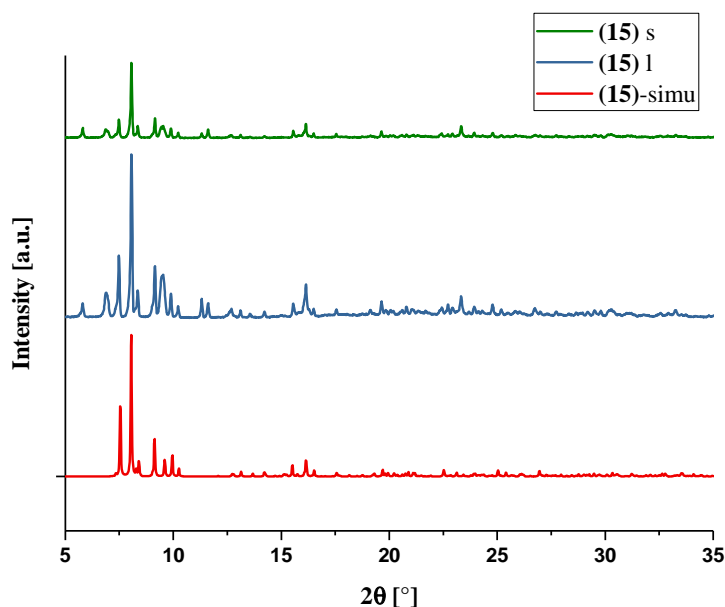


Figure 5.84: Simulated (simu) and experimental PXRD-patterns of **(15)**. Hereby, *a. r.* is abbreviation for alternative route, means stirring, *l. m.* is abbreviation for layering method.

However, the patterns with the labelling “l” (= synthesized by layering method) and “s” (= stirring method) show some extra reflections at e.g. 5.8° in 2θ , 6.9° in 2θ , 11.3° in 2θ and 11.6° in 2θ , respectively. This reveals that during the reactions at least one other unknown compound was formed.

5.3.2.4.4 Solid state UV-vis studies

Figure 5.85 shows the solid state UV-vis spectrum of compound (15).

The absorption band at $\lambda = 526$ nm can be denoted to a d-d electron transfer from the t_{2g} orbital to the e_g^* orbital within one Mn^{3+} ion. Additionally, the maximum absorption at $\lambda = 292$ nm can be assigned to a LMCT. The change of absorbance at $\lambda = 350$ nm was caused by the change of the lamp during the record of the spectrum. The bandgap of 2.89 eV was found using the Tauc method.

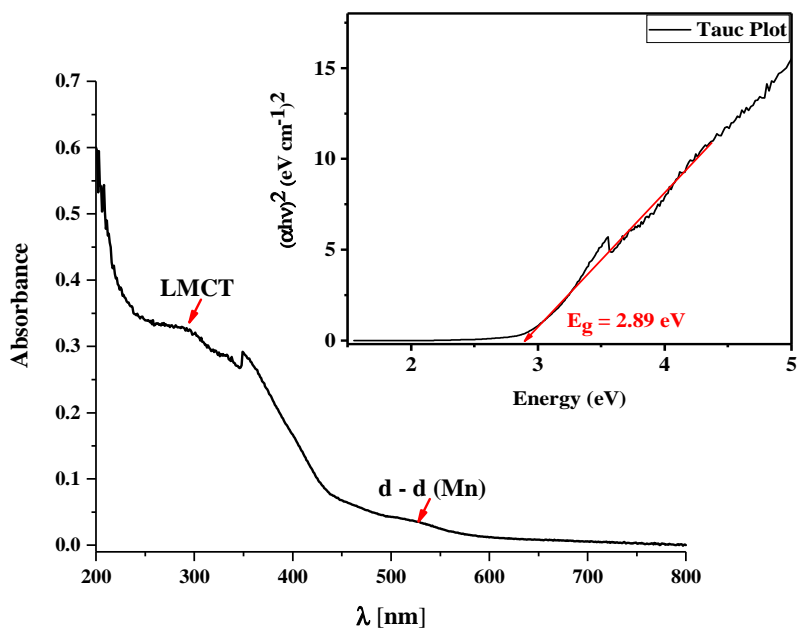


Figure 5.85: Solid state UV-vis spectrum of compound (15).

The maximum absorption is in the range 440 nm to 220 nm. The change of absorbance at 350 nm was caused by the change of the lamp during recording of the spectrum.

5.3.2.4.5 Catalytic studies

Photo-electrocatalytic studies

The preparation of the working electrode and the photo-electrocatalytic studies were performed under the same condition of (5) (see section 5.2.1.4).

Figure 5.86 and Figure 5.87 show the results of the photo-electrocatalytic studies of compound (15) and reveal photo-electrocatalytic properties for water splitting.

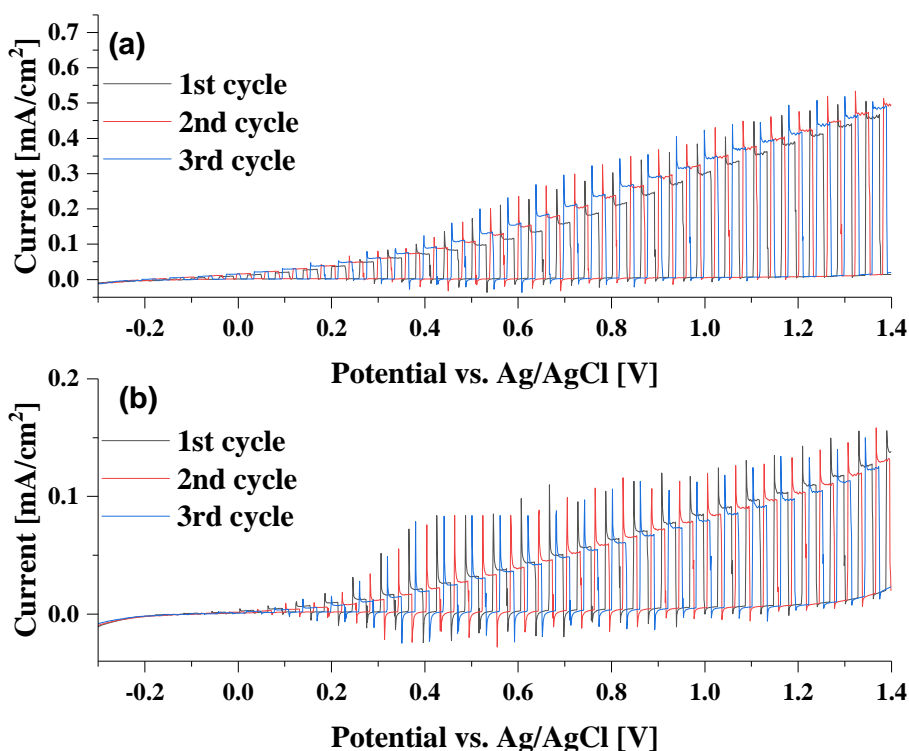


Figure 5.86: Photo-electrocatalytic results of compound (15) recorded in 0.5M Na₂SO₄ (pH = 8.6) over the range -0.3 V to 1.4 V at a scan rate of 0.01 V/s and sunlight simulation without any filter (a) and with filtering the radiation below 420 nm (b).

Performing linear sweep voltammetry combined with artificial sunlight irradiating the working electrode, an onset at a potential of -0.2 V vs. Ag/AgCl with a

maximum photocurrent of $4.92 \cdot 10^{-1} \text{ mA/cm}^2$ at a potential of 1.4 V vs. Ag/AgCl are observable (see Figure 5.86 (a)). The stability of compound (**15**) was confirmed by repeating the experiment another two times where the values did not change considerably. The three runs of linear sweep voltammetry filtering light below 420 nm are shown in Figure 5.86 (b). It is clearly seen that under these conditions the LSV shows a stable behavior.

The direct comparison of catalytic studies with and without filter are shown in Figure 5.87. A development of a current for the filtered sample occurs at a potential of 0.14 V vs. Ag/AgCl, thus having a shift of +0.34 V compared to measurement without filter. At a potential of 1.4 vs. Ag/AgCl, the voltammogram shows a maximum of $1.24 \cdot 10^{-1} \text{ mA/cm}^2$, revealing that filtering radiation below 420 nm also reduces the catalytic activity of the system by 75 %.

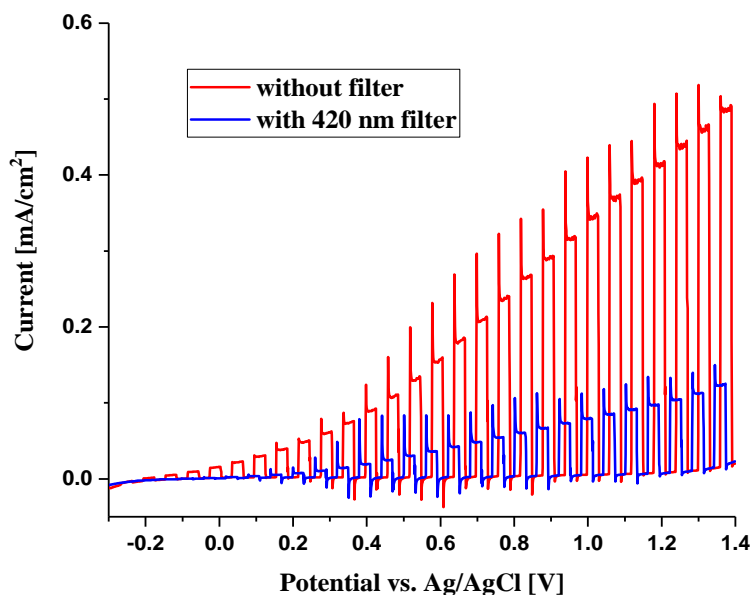


Figure 5.87: Comparison of photocatalytic studies of compound (**15**) in 0.5M Na₂SO₄ (pH = 8.6) over the range -0.3 V to 1.4 V at a scan rate of 0.01 V/s: Studies with and without filter (< 420 nm), for comparison in each case the final 3rd cycle was chosen.

Additionally, starting at a potential of +1.3 V the current slightly increases at phases, when the light of the Xe lamp is switched off. Since this process is light-independent, this behavior occurs both under filtered and unfiltered light conditions indicating mere electrochemical processes.

5.3.2.4.6 Conclusion

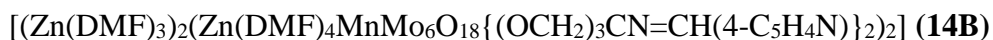
Compound (**15**) was successfully synthesized and isolated in the form of crystals, whereby a crystal structure could be determined. Furthermore, this compound was also characterized by PXRD, EA, UV-vis and FT-IR spectroscopy. Initial photoelectrocatalytic studies reveal that compound (**15**) shows catalytic properties for the application of water splitting. These studies, however, need further investigation and the process of coating of (**15**) onto the substrate needs to be optimized. This is the first Cd based POMOF in which the POM is part of the linker.

6 CONCLUSION AND OUTLOOK

POMOFs can be regarded in general terms as frameworks containing POMs. Here, we can identify three distinct categories: (a) POMs occupying the cavities of a MOF structure (POM@MOF), (b) POMs used as SBUs in the network and (c) POMs as part of the linker of the framework. The work presented in this thesis concentrated on developing approach (c) since very few examples of this type of network exist in the literature. During the course of this doctoral research, several organic-inorganic Anderson-Evans POM hybrid linkers, designated L – POM – Ls, $[\text{MnMo}_6\text{O}_{18}\{(\text{OCH}_2)_3\text{CN}=\text{CH}(4\text{-C}_5\text{H}_4\text{N})\}_2]^{3-}$ (**4**), $[\text{MnMo}_6\text{O}_{18}((\text{OCH}_2)_3\text{CNHCH}_2(\text{C}_6\text{H}_4)\text{COOH})((\text{OCH}_2)_3\text{CNHCH}_2(\text{C}_6\text{H}_4)\text{COO})]^{4-}$ (**5**), $[\text{AlMo}_6\text{O}_{18}((\text{OCH}_2)_3\text{CH}_2\text{COCH}_2\text{C}(\text{CH}_2\text{OH})_3)_2]^{3-}$ (**6**), $[\text{MnMo}_6\text{O}_{18}((\text{OCH}_2)_3\text{CNH}(\text{C}_6\text{H}_4)\text{C}\equiv\text{N}_2)]^{3-}$ (**7**), $[\text{MnMo}_6\text{O}_{18}\{(\text{OCH}_2)_3\text{CNHC}=\text{O}(\text{C}_6\text{H}_4\text{NO}_2)\}_2]^{3-}$ (**8**) and $[\text{MnMo}_6\text{O}_{18}((\text{OCH}_2)_3\text{CNH}(\text{C}_6\text{H}_5))_2]^{3-}$ (**9**) were synthesized and structurally characterized using single crystal X-ray diffraction. These should be used as linking units within POMOFs, i.e. multifunctional POM based frameworks. In this work only (**4**) and (**5**) proofed to provide single crystals of the desired POMOFs with TM (TM = Cu, Zn, Cd) or RE (RE = Y, La - Lu), respectively.

Given that Cu^{2+} , Zn^{2+} and Cd^{2+} have a strong affinity to coordinate to pyridyl groups, it was decided that hybrid (**4**) is particularly suitable for synthesizing TM based POMOF frameworks. The inclusion of these metal centres, not only plays a role in forming these networks, but can also tune the physical and chemical properties of the resultant materials. The presence of POM moiety, organic linker and metal ions within the same framework suggests a plethora of possible applications. For example $[\text{CuCl}(\text{DMF})\{\text{MnMo}_6\text{O}_{18}((\text{OCH}_2)_3\text{CN}=\text{CH}(4\text{-C}_5\text{H}_4\text{N}))_2\}_2]$ (**13**) showed catalytic activity for A^3 coupling reactions and

6. Conclusion and Outlook



and $[\text{Cd}(\text{DMF})_2][\text{Cd}][\text{N}(n\text{-C}_4\text{H}_9)_4]_2[\text{MnMo}_6\text{O}_{18}\{(\text{OCH}_2)_3\text{CN}=\text{CH}(4\text{-C}_5\text{H}_4\text{N})\}_2]_2$ **(15)** were used as photo-electrocatalyst for water splitting. This work also demonstrates that small changes in reaction parameters and variation of the transition metals affect the overall structure and thus the properties. Using a Zn salt, two framework structures with different topologies were obtained and the topology of this **(14A)** has never been reported before, therefore this topology has been assigned as “mpm1”.

The L – POM – L **(5)** unit was chosen to explore incorporation of rare earth metal ions since carboxylate groups should suite these oxophilic ions. The interaction of RE ions with **(5)** result in two series of compounds $\text{RE}(\text{DMF})_6\text{RE}(\text{DMF})_5\text{RE}_3(\text{DMF})_{10}[(\text{MnMo}_6\text{O}_{18})((\text{OCH}_2)_3\text{CNHCH}_2(\text{C}_6\text{H}_4)\text{COO})_2]_3$ (RE = La - Nd) **(11)** and $[\text{RE}(\text{DMF})_4(\text{H}_2\text{O})]_2[\text{RE}_3(\text{DMF})_6][(\text{MnMo}_6\text{O}_{18})((\text{OCH}_2)_3\text{CNHCH}_2(\text{C}_6\text{H}_4)\text{COO})_2]_3$ (RE = Y, Sm - Lu) **(12)**. The formation of these two families reflects the change in ionic radius of the RE cations. The factors affecting the crystallization process were explored and it was found for family **(11)** a stirring method was required, whereas for family **(12)** layering method proofed most fruitful. The preliminary investigation of **(11)**-Ce and **(12)**-Dy as catalysts for the reaction of furfural and morpholine to form *trans*-4,5-dimorpholinocyclopent-2-en-1-one was performed and showed an increase in efficiency using the more Lewis acidic metal ion Dy^{3+} . Additionally, these two compounds were also selected to investigate their photo-electrocatalytic activities for water splitting.

In photocatalysis three characteristic values of the compound are decisive for the catalytic activity: a low bandgap, a low onset potential and a high maximum of the photocurrent at a low potential. Table 6.1 summarizes these values for the compounds investigated in this work on photocatalytic properties.

Table 6.1: Summary of the values for the compounds investigated in this work on photocatalytic properties.

Compound	Bandgap [eV]	onset potential [V]	maximum of Photocurrent [A/cm²]
(5)	2.85	-0.2	$5.81 \cdot 10^{-4}$
(11)-Ce	2.76	-0.3	$3.47 \cdot 10^{-4}$
(12)-Dy	2.46	-0.15	$4.04 \cdot 10^{-4}$
(14A) + (14B)	2.89	-0.14	$4.74 \cdot 10^{-4}$
(15)	2.89	-0.2	$4.92 \cdot 10^{-4}$

Amongst all the photo-electrocatalytic studies in this doctoral research, **(12)-Dy** has the smallest bandgap, **(11)-Ce** showed the lowest onset of activity and compound **(5)** revealed the highest photocurrent at a potential of 1.4 V vs Ag/AgCl.

During the course of this research work, a novel and unique self-assemble POM system $[\text{Mn}_2\text{Mo}_4\text{O}_{14}((\text{OCHCH}_2)_2\text{NCH}_2\text{CH}_2\text{OH})_2]$ (**10**) was also synthesized and characterized. This hybrid with different inorganic core and backbone might be an interesting potential building block for the engineering of functional new nanoscale architectures.

All the above mentioned compounds were characterized by Single Crystal X-ray Diffraction (SCXRD), Powder X-ray Diffraction (PXRD), Elemental Analysis (EA), UV-vis and Fourier Transform Infrared (FT-IR) Spectroscopy.

In conclusion POMOFs of type (c) offer a promising means to provide multifunctional materials sometimes with completely new topologies.

7 REFERENCES

- (1) Berzelius, J. J. *Ann. d. Phys.* **1826**, B82, 369.
- (2) Keggin, J. F. *Nature* **1933**, 351.
- (3) Long, D. L.; Tsunashima, R.; Cronin, L. *Angew. Chem. Int. Ed.* **2010**, 49, 1736.
- (4) Huheey, J.; Keiter, E.; Keiter, R. *Anorganische Chemie*, 5th ed.; De Gruyter: Berlin, 2014.
- (5) Gouzerh, P.; Che, M. *Actual. Chim.* **2006**, 298, 9.
- (6) Pope, M. T.; Müller, A. *Anal. Chim. Acta* **2007**, 587, 124.
- (7) Sadakane, M.; Steckhan, E. *Chem. Rev.* **1998**, 98, 219.
- (8) Hoffmann, N. *Angew. Chem. Int. Ed.* **2013**, 52, 11456.
- (9) Pope, M. T.; Müller, A. *Angew. Chem. Int. Ed.* **1991**, 30, 34.
- (10) Song, Y.-F.; Tsunashima, R. *Chem. Soc. Rev.* **2012**, 41, 7384.
- (11) Ilyes, E.; Florea, M.; Madalan, A. M.; Haiduc, I.; Parvulescu, V. I.; Andruh, M. *Inorg. Chem.* **2012**, 51, 7954.
- (12) Yang, H.; Song, T.; Liu, L.; Devadoss, A.; Xia, F.; Han, H.; Park, H.; Sigmund, W.; Kwon, K.; Paik, U. *J. Phys. Chem. C* **2013**, 117, 17376.
- (13) Constable, E. C.; Housecroft, C. E. *Chem. Soc. Rev.* **2013**, 42, 1429.
- (14) Janiak, C. *J. Chem. Soc., Dalt. Trans.* **2003**, 2781.
- (15) Hoskins, B. F.; Robson, R. *J. Am. Chem. Soc.* **1990**, 112, 1546.
- (16) Rowsell, J. L. C.; Yaghi, O. M. *Microporous Mesoporous Mater.* **2004**, 73, 3.
- (17) Bauer, S.; Stock, N. *Chem. Unserer Zeit* **2008**, 42, 12.
- (18) Ma, S.; Wang, X. S.; Yuan, D.; Zhou, H. C. *Angew. Chem. Int. Ed.* **2008**, 47,

7. References

- 4130.
- (19) Eddaoudi, M.; Kim, J.; Rosi, N.; Vodak, D.; Wachter, J.; Keeffe, M. O.; Yaghi, O. M.; Eddaoudi, M.; Kimrn, J.; Rosi, N.; Yaghil, O. M. *Science* **2002**, 295, 469.
- (20) Bhadra, B. N.; Jhung, S. H. *ACS Appl. Mater. Interfaces* **2016**, 8, 6770.
- (21) Brown, K.; Zolezzi, S.; Aguirre, P.; Venegas-Yazigi, D.; Paredes-Garcia, V.; Baggio, R.; Novak, M. A.; Spodine, E. *Dalt. Trans.* **2009**, 1422.
- (22) Mingabudinova, L. R.; Vinogradov, V. V.; Milichko, V. A.; Hey-Hawkins, E.; Vinogradov, A. V. *Chem. Soc. Rev.* **2016**, 45, 5408.
- (23) Shimizu, G. K. H.; Taylor, J. M.; Kim, S. *Science* **2013**, 341, 354.
- (24) Long, J. R.; Yaghi, O. M.; Zhou, H.-C. *Chem. Rev.* **2012**, 112, 673.
- (25) Huxford, R. C.; Della Rocca, J.; Lin, W. *Curr. Opin. Chem. Biol.* **2010**, 14, 262.
- (26) Hagrman, D.; Zubieta, C.; Rose, D. J. *Angew. Chem.* **1997**, 1, 904.
- (27) Rowsell, J. L. C.; Eckert, J.; Yaghi, O. M. *J. Am. Chem. Soc.* **2005**, 127, 14904.
- (28) Siegelman, R. L.; McDonald, T. M.; Gonzalez, M. I.; Martell, J. D.; Milner, P. J.; Mason, J. A.; Berger, A. H.; Bhown, A. S.; Long, J. R. *J. Am. Chem. Soc.* **2017**, 139, 10526.
- (29) Lennartson, A.; Christine, J. M. *J. Coord. Chem.* **2012**, 65, 4194.
- (30) Bendi, R.; Kumar, V.; Bhavanasi, V.; Parida, K.; Lee, P. S. *Adv. Energy Mater.* **2016**, 6, 1.
- (31) Liu, J.; Lukose, B.; Shekhah, O.; Arslan, H. K.; Weidler, P.; Gliemann, H.; Bräse, S.; Grosjean, S.; Godt, A.; Feng, X.; Müllen, K.; Magdau, I. B.; Heine, T.; Wöll, C. *Sci. Rep.* **2012**, 2, 1.
- (32) Song, G.; Wang, Z.; Wang, L.; Li, G.; Huang, M.; Yin, F. *Chin. J. Catal.*

7. References

- 2014**, *35*, 185.
- (33) Maeng, H. J.; Kim, D. H.; Kim, N. W.; Ruh, H.; Lee, D. K.; Yu, H. *Curr. Appl. Phys.* **2018**, *18*, S21.
- (34) Okamura, T.; Wu, B.; Iguchi, H.; Breedlove, B. K.; Yamashita, M.; Kosaka, W.; Miyasaka, H.; Takaishi, S. *Chem. Commun.* **2017**, *53*, 6512.
- (35) Schenck, H.; Frohberg, M. G.; Hoffmann, K. *Arch. für das Eisenhüttenwes.* **1962**, *33*, 369.
- (36) Rodriguez-Albelo, L. M.; Ruiz-Salvador, A. R.; Sampieri, A.; Lewis, D. W.; Gómez, A.; Nohra, B.; Mialane, P.; Marrot, J.; Sécheresse, F.; Mellot-Draznieks, C.; Biboum, R. N.; Keita, B.; Nadjo, L.; Dolbecq, A. *J. Am. Chem. Soc.* **2009**, *131*, 16078.
- (37) Nohra, B.; El Moll, H.; Rodriguez Albelo, L. M.; Mialane, P.; Marrot, J.; Mellot-Draznieks, C.; O’Keeffe, M.; Ngo Biboum, R.; Lemaire, J.; Keita, B.; Nadjo, L.; Dolbecq, A. *J. Am. Chem. Soc.* **2011**, *133*, 13363.
- (38) Zheng, S. T.; Zhang, J.; Yang, G. Y. *Angew. Chem. Int. Ed.* **2008**, *47*, 3909.
- (39) Sha, J.; Huang, L.; Peng, J.; Pang, H.; Tian, A.; Zhang, P.; Chen, Y.; Zhu, M. *Solid State Sci.* **2009**, *11*, 417.
- (40) Shi-Zhou; Kong, Z. G.; Wang, Q. W.; Li, C. B. *Inorg. Chem. Commun.* **2012**, *20*, 131.
- (41) Yang, H.; Li, J.; Zhang, H.; Lv, Y.; Gao, S. *Micropor. Mesopor. Mat.* **2014**, *195*, 87.
- (42) Song, J.; Luo, Z.; Britt, D. K.; Furukawa, H.; Yaghi, O. M.; Hardcastle, K. I.; Hill, C. L. *J. Am. Chem. Soc.* **2011**, *133*, 16839.
- (43) Li, S.; Ma, H.; Pang, H.; Zhang, L.; Zhang, Z.; Lin, H. *Inorg. Chem. Commun.* **2014**, *44*, 15.
- (44) Qin, J. S.; Du, D. Y.; Guan, W.; Bo, X. J.; Li, Y. F.; Guo, L. P.; Su, Z. M.; Wang, Y. Y.; Lan, Y. Q.; Zhou, H. C. *J. Am. Chem. Soc.* **2015**, *137*, 7169.

7. References

- (45) Zhu, P. P.; Sun, L. J.; Sheng, N.; Sha, J. Q.; Liu, G. D.; Yu, L.; Qiu, H. Bin; Li, S. X. *Cryst. Growth Des.* **2016**, *16*, 3215.
- (46) Yazigi, F.-J.; Wilson, C.; Long, D.-L.; Forgan, R. S. *Cryst. Growth Des.* **2017**, *17*, 4739.
- (47) Li, X. X.; Wang, Y. X.; Wang, R. H.; Cui, C. Y.; Tian, C. Bin; Yang, G. Y. *Angew. Chem. Int. Ed.* **2016**, *55*, 1.
- (48) Sun, C.; Liu, S.; Liang, D.; Shao, K.; Ren, Y. *J. Am. Chem. Soc.* **2009**, *131*, 1883.
- (49) Wang, X.; Chang, Z.; Lin, H.; Tian, A.; Liu, G.; Zhang, J. *Dalt. Trans.* **2014**, *43*, 12272.
- (50) Wei, M.; Wang, X.; Duan, X. *Chem. Eur. J.* **2013**, *19*, 1607.
- (51) Wei, M.; Wang, X.; Sun, J.; Duan, X. *J. Solid State Chem.* **2013**, *202*, 200.
- (52) Bridgeman, A. J. *J. Phys. Chem. A* **2002**, *106*, 12151.
- (53) Pope, M. T. *Polyoxometalate Chemistry From Topology via Self-Assembly to Applications*; Springer-Verlag, 2002.
- (54) T., P. M. *Heteropoly and Isopoly Oxometalates*; Springer-Verlag: Berlin, 1983.
- (55) Himeno, S.; Murata, S.; Eda, K. *Dalt. Trans.* **2009**, 6114.
- (56) Pope, M. T. *Heteropoly and Isopoly Oxometalates*; Springer-Verlag: New York, 1983; Vol. 8.
- (57) Lis, S. *Acta Phys. Pol. A* **1996**, *A90*, 275.
- (58) Hao, J. *Self-Assembled Structures: Properties and Applications in Solution and on Surfaces*; Taylor & Francis Group: New York, 2010.
- (59) Sanchez, C.; Livage, J.; Launay, J. P.; Fournier, M.; Jeannin, Y. *J. Am. Chem. Soc.* **1982**, *104*, 3194.
- (60) Contant, R.; Teze, A. *Inorg. Chem* **1985**, *24*, 4610.

7. References

- (61) Zhang, J.; Liu, Z.; Huang, Y.; Zhang, J.; Hao, J.; Wei, Y. *Chem. Commun.* **2015**, *51*, 9097.
- (62) Su, X.-F.; Zhu, B.; Wu, C.-X.; Yan, L.-K.; Su, Z.-M. *J. Theor. Comput. Chem.* **2017**, *16*, 1750054.
- (63) Nagano, O.; Sasaki, Y. *Acta Cryst.* **1979**, *B35*, 2387.
- (64) Yan, L.; López, X.; Carbó, J. J.; Sniatynsky, R.; Duncan, D. C.; Poblet, J. M. *J. Am. Chem. Soc.* **2008**, *130*, 8223.
- (65) Klemperer, W. G., Ginsberg, A. P., E. *Inorganic Syntheses*; John Wiley & Sons, 1990; Vol. 27.
- (66) Marcoux, P. R.; Hasenknopf, B.; Vaissermann, J.; Gouzerh, P. *Eur. J. Chem.* **2003**, 2406.
- (67) Schmidt, K. J.; Schrobilgen, G. J.; Sawyer, J. F. *Acta Cryst. Sect. C* **1986**, *42*, 1115.
- (68) Kondo, H.; Kobayashi, A.; Sasaki, Y. *Acta Cryst.* **1980**, *B36*, 661.
- (69) Shivaiah, V.; Das, S. K. *J. Chem. Sci.* **2005**, *117*, 227.
- (70) Perloff, A. *Inorg. Chem.* **1970**, *9*, 2228.
- (71) Wu, C.; Lin, X.; Yu, R.; Yang, W.; Lu, C.; Zhuang, H. *Sci. China, Ser. B Chem.* **2001**, *44*, 49.
- (72) Blazevic, A.; Rompel, A. *Coord. Chem. Rev.* **2016**, *307*, 42.
- (73) Lee, B. Y. U. K.; Kobayashi, A.; Sasaki, Y. *Acta Cryst. Sect. C* **1983**, 817.
- (74) Nolan, A. L.; Burns, R. C.; Lawrance, G. A.; Craig, D. C. *Acta Cryst. Sect. C* **2000**, *56*, 729.
- (75) Naruke, H.; Yamase, T. *Acta Cryst. Sect. C* **1992**, *48*, 597.
- (76) Allen, C. C.; Burns, R. C.; Lawrance, G. A.; Turner, P.; Hambley, T. W. *Acta Cryst. Sect. C* **1997**, *53*, 7.
- (77) Ito, F.; Ozeki, T.; Ichida, H.; Miyamae, H.; Sasaki, Y. *Acta Cryst. Sect. C*

7. References

- 1989**, *45*, 946.
- (78) Liu, F. X.; Marchal-Roch, C.; Dambournet, D.; Acker, A.; Marrot, J.; Sécheresse, F. *Eur. J. Chem.* **2008**, 2191.
- (79) Lee, U.; Joo, H. C. *Acta Cryst.* **2010**, *E62*, i231.
- (80) Lee, U.; Joo, H.-C.; Kwon, J.-S.; Cho, M.-A. *Acta Cryst. Sect. E* **2001**, *57*, i112.
- (81) Ozawa, Y.; Hayashi, Y.; Isobe, K. *Acta Cryst. Sect. C* **1991**, *47*, 637.
- (82) Mensinger, Z. L.; Zakharov, L. N.; Johnson, D. W. *Acta Cryst.* **2008**, *E64*, i8.
- (83) Evans, H. T. *J. Am. Chem. Soc.* **1948**, *70*, 1291.
- (84) Lindqvist, I. *Acta Cryst.* **1950**, *3*, 159.
- (85) Bridgeman, A. J.; Cavigliasso, G. *J. Chem. Soc., Dalt. Trans.* **2002**, 2244.
- (86) Wang, W.; Liu, W.; Chang, I.-Y.; Wills, L. A.; Zakharov, L. N.; Boettcher, S. W.; Cheong, P. H.-Y.; Fang, C.; Keszler, D. A. *PNAS* **2013**, *110*, 18397.
- (87) Allain, C.; Favette, S.; Chamoreau, L. M.; Vaissermann, J.; Ruhlmann, L.; Hasenknopf, B. *Eur. J. Chem.* **2008**, 3433.
- (88) Contant, R.; Thouvenot, R. *Inorg. Chim. Acta* **1993**, *212*, 41.
- (89) Baker, L. C. W.; Figgis, J. S. *J. Am. Chem. Soc.* **1970**, *92*, 3794.
- (90) López, X.; Poblet, J. M. *Inorg. Chem.* **2004**, *43*, 6863.
- (91) Weinstock, I. A.; Cowan, J. J.; Barbuzzi, E. M. G.; Zeng, H.; Hill, C. L. *J. Am. Chem. Soc.* **1999**, *121*, 4608.
- (92) Hervé, G.; Tézé, A. *Inorg. Chem.* **1977**, *16*, 2115.
- (93) Canny, J.; Tézé, A.; Thouvenot, R.; Hervé, G. *Inorg. Chem.* **1986**, *25*, 2114.
- (94) Contant, R.; Ciabrini, J. P. *J. Inorg. Nucl. Chem.* **1981**, *43*, 1525.
- (95) Dey, C.; Kundu, T.; Biswal, B. P.; Mallick, A.; Banerjee, R. *Acta Cryst.*

7. References

- 2014**, *B70*, 3.
- (96) Shimizu, G. K. H.; Vaidhyanathan, R.; Taylor, J. M. *Chem. Soc. Rev.* **2009**, 38, 1430.
- (97) Wise, D. L. *Electrical and Optical Polymer Systems: Fundamentals: Methods, and Applications*; 1998.
- (98) Seki, K.; Takamizawa, S.; Mori, W. *Chem. Lett.* **2001**, 30, 332.
- (99) Sakata, Y.; Furukawa, S.; Kondo, M.; Hirai, K.; Horike, N.; Takashima, Y.; Uehara, H.; Louvain, N.; Meilikhov, M.; Tsuruoka, T.; Isoda, S.; Kosaka, W.; Sakata, O.; Kitagawa, S. *Science* **2013**, 339, 193.
- (100) Yaghi, O. M.; O'Keeffe, M.; Eddaoudi, M.; Li, H. *Nature* **1999**, 402, 276.
- (101) Chui, S. S. Y.; Lo, S. M. F.; Charmant, J. P. H.; Orpen, A. G.; Williams, I. D. *Science* **1999**, 283, 1148.
- (102) Lo, S. M. F.; Chui, S. S. Y.; Shek, L. Y.; Lin, Z.; Zhang, X. X.; Wen, G. H.; Williams, I. D. *J. Am. Chem. Soc.* **2000**, 122, 6293.
- (103) Férey, G.; Mellot-Draznieks, C.; Serre, C.; Millange, F.; Dutour, J.; Surblé, S.; Margiolaki, I. *Science* **2005**, 309, 2040.
- (104) Carson, C. G.; Hardcastle, K.; Schwartz, J.; Liu, X.; Hoffmann, C.; Gerhardt, R. A.; Tannenbaum, R. *Eur. J. Chem.* **2009**, 2338.
- (105) Rosi, N. L.; Eckert, J.; Eddaoudi, M.; Vodak, T.; Kim, J.; Keffe, M. O.; Yaghi, O. M. *Science* **2003**, 300, 1127.
- (106) Jiang, H. L.; Makal, T. A.; Zhou, H. C. *Coord. Chem. Rev.* **2013**, 257, 2232.
- (107) Han, S. S.; Mendoza-Cortés, J. L.; Goddard, W. A. *Chem. Soc. Rev.* **2009**, 38, 1460.
- (108) Batten, S. R. *CrystEngComm* **2001**, 18, 1.
- (109) Gao, Y.; Cao, J.; Song, Y.; Zhang, G.; Wang, Y.; Liu, Z. *Cryst. Eng. Comm.* **2013**, 15, 8522.

7. References

- (110) Vittal, J. J. *Coord. Chem. Rev.* **2007**, *251*, 1781.
- (111) Hu, C.; Englert, U. *Angew. Chem. Int. Ed.* **2005**, *44*, 2281.
- (112) Kondo, M.; Shimamura, M.; Noro, S. I.; Kimura, Y.; Uemura, K.; Kitagawa, S. *J. Solid State Chem.* **2000**, *152*, 113.
- (113) Wu, C. De; Lin, W. *Angew. Chem. Int. Ed.* **2005**, *44*, 1958.
- (114) Zhang, J. P.; Lin, Y. Y.; Zhang, W. X.; Chen, X. M. *J. Am. Chem. Soc.* **2005**, *127*, 14162.
- (115) Suh, M. P.; Ko, J. W.; Choi, H. J. *J. Am. Chem. Soc.* **2002**, *124*, 10976.
- (116) Zeng, M.-H.; Feng, X.-L.; Chen, X.-M. *Dalt. Trans.* **2004**, 2217.
- (117) Chem, A.; Ed, I.; Biradha, K.; Hongo, Y.; Fujita, M. *Angew. Chem. Int. Ed.* **2002**, *41*, 3395.
- (118) Biradha, K.; Fujita, M. *Angew. Chem. Int. Ed.* **2002**, *41*, 3392.
- (119) Maji, T. K.; Uemura, K.; Chang, H.; Matsuda, R.; Kitagawa, S. *Angew. Chem. Int. Ed.* **2004**, *43*, 3269.
- (120) Chen, C. L.; Goforth, A. M.; Smith, M. D.; Su, C. Y.; Zur Loye, H. C. *Angew. Chem. Int. Ed.* **2005**, *44*, 6673.
- (121) Kurmoo, M.; Kumagai, H.; Chapman, K. W.; Kepert, C. J. *Chem. Commun.* **2005**, 3012.
- (122) Wong, K. L.; Law, G. L.; Yang, Y. Y.; Wong, W. T. *Adv. Mater.* **2006**, *18*, 1051.
- (123) Macgillivray, L. R.; Papaefstathiou, G. S.; Friscic, T.; Hamilton, T. D.; Bucar, D.-K.; Chu, Q.; Varshney, D. B.; Georgiev, I. G. *Acc. Chem. Res.* **2008**, *41*, 280.
- (124) Wei, M.; Wang, X.; Sun, J.; Duan, X. *J. Solid State Chem.* **2013**, *202*, 200.
- (125) Sha, J.-Q.; Sun, J.-W.; Wang, C.; Li, G.-M.; Yan, P.-F.; Li, M.-T.; Liu, M.-Y. *Cryst. Eng. Comm.* **2012**, *14*, 5053.

7. References

- (126) Jong, W. H.; Hill, C. L. *J. Am. Chem. Soc.* **2007**, *129*, 15094.
- (127) Zheng, S.-T.; Zhang, J.; Yang, G.-Y. *Angew. Chem. Int. Ed.* **2008**, *120*, 3973.
- (128) Gan, X.; Hu, X.; Shi, Z.; Yin, Y. *J. Coord. Chem.* **2013**, *66*, 2930.
- (129) Sha, J. Q.; Sun, J. W.; Wang, C.; Li, G. M.; Yan, P. F.; Li, M. T. *Cryst. Growth Des.* **2012**, *12*, 2242.
- (130) Fan, W.; Yuan, W.; Ma, S. *Nat. Commun.* **2014**, *5*, 1.
- (131) Loukopoulos, E.; Kallitsakis, M.; Tsoureas, N.; Abdul-Sada, A.; Chilton, N. F.; Lykakis, I. N.; Kostakis, G. E. *Inorg. Chem.* **2017**, *56*, 4898.
- (132) Zhao, C.; Seidel, D. *J. Am. Chem. Soc.* **2015**, *137*, 4650.
- (133) Duspara, P. A.; Batey, R. A. *Angew. Chem. Int. Ed.* **2013**, *52*, 1.
- (134) Nunes, J. P. M.; Afonso, C. A. M.; Caddick, S. *RSC Adv.* **2013**, *3*, 14975.
- (135) Menjo, Y.; Hamajima, A.; Sasaki, N.; Hamada, Y. *Org. Lett.* **2011**, *13*, 5744.
- (136) Li, S. W.; Batey, R. A. *Chem. Commun.* **2007**, *8*, 3759.
- (137) Mattock, J. D.; Kumar, P.; Coles, S. J.; Griffiths, K.; Kostakis, G. E.; Vargas, A.; Pitak, M. B.; Abdul-Sada, A.; Navarro, O. *Inorg. Chem.* **2016**, *55*, 6988.
- (138) Goberna-Ferrón, S.; Vígara, L.; Soriano-López, J.; Galán-Mascarós, J. R. *Inorg. Chem.* **2012**, *51*, 11707.
- (139) Govindaraju, G. V.; Wheeler, G. P.; Lee, D.; Choi, K. S. *Chem. Mater.* **2017**, *29*, 355.
- (140) Speiser, B. *Chem. Unserer Zeit* **1981**, *15*, 21.
- (141) Neghmouche, N. S. *Anal. Electrochem.* **2007**, *2*, 2.
- (142) Speiser, B. *Chem. Unserer Zeit* **1981**, *15*, 62.
- (143) Ebel, H. F.; Bliefert, C.; Greulich, W. *Schreiben und Publizieren in den Naturwissenschaften*, 5th ed.; WILEY-VCH Verlag GmbH & Co. KGaA: Weinheim, 2006.

7. References

- (144) Riedel, E. *Anorganische Chemie*, 6th ed.; de Gruyter GmbH & Co.KG: Berlin, 2004.
- (145) Srikant, V.; Clarke, D. R. *J. Appl. Phys.* **1998**, *83*, 5447.
- (146) Dette, C.; Pérez-Osorio, M. A.; Kley, C. S.; Punke, P.; Patrick, C. E.; Jacobson, P.; Giustino, F.; Jung, S. J.; Kern, K. *Nano Lett.* **2014**, *14*, 6533.
- (147) Muuronen, M.; Parker, S. M.; Berardo, E.; Le, A.; Zwijnenburg, M. A.; Furche, F. *Chem. Sci.* **2017**, *8*, 2179.
- (148) Ando, Y.; Ishizuka, S.; Wang, S.; Chen, J.; Islam, M. M.; Shibata, H.; Akimoto, K.; Sakurai, T. *Jpn. J. Appl. Phys.* **2018**, *57*, 08RC08.
- (149) Sheldrick, G. M. *SHELXTL 6.12*; Bruker AXS, 2003.
- (150) Dolomanov, O. V.; Bourhis, L. J.; Gildea, R. J.; Howard, J. A. K.; Puschmann, H. *J. Appl. Cryst.* **2009**, *42*, 339.
- (151) Putz, H.; Brandenburg, K. *Diam. 4, Cryst. IMPACT GbR*; Bonn, Deutschland, 2014.
- (152) *Stoe WinXPow V2.25*; STOE & Cie GmbH, Darmstadt, 2005.
- (153) Kraus, W.; Nolze, G. *Appl. Crystallogr.* **1996**, *29*, 301.
- (154) Blatov, V. A.; Shevchenko, A. P.; Proserpio, D. M. *Cryst. Growth Des.* **2014**, *14*, 3576.
- (155) Macrae, C. F.; Bruno, I. J.; Chisholm, J. A.; Edgington, P. R.; McCabe, P.; Pidcock, E.; Rodriguez-monge, L.; Taylor, R.; Streek, J. Van De; Wood, P. A. *Appl. Crystallogr.* **2008**, *41*, 466.
- (156) Llunell, M.; Casanova, D.; Cirera, J.; Alvarez, S.; Alemany, P. SHAPE: Program for the Stereochemical Analysis of Molecular Fragments by Means of Continuous Shape Measures and Associated Tools, version 2.1: Universitat de Barcelona: Barcelona 2013,.
- (157) Manikumari, S.; Shivaiah, V.; Das, S. K. *Inorg. Chem. Commun.* **2002**, *41*,

7. References

6953.

- (158) Liu, S.; Ma, L.; McGowty, D.; Zubieta, J. *Polyhedron* **1990**, *9*, 1541.
- (159) Spek, A. L. *Acta Cryst. Sect. C* **2015**, *71*, 9.
- (160) Legon, A. C.; Millen, D. J. *Chem. Soc. Rev.* **1987**, *16*, 467.
- (161) Walwil, A. M. *J. Lab. Chem. Educ.* **2016**, *4*, 4.
- (162) Procopio, A.; Costanzo, P.; Curini, M.; Nardi, M.; Oliverio, M.; Sindona, G. *ACS Sustain. Chem. Eng.* **2013**, *1*, 541.
- (163) Guzei, I. A. *Notes on OLEX2*; 2013.
- (164) Cotton, S. *Lanthanide and Actinide Chemistry*; John Wiley & Sons: Uppingham, 2006.

8 APPENDIX

8.1 Crystallographic data

Table 8.1: Crystal data of compound (4).

Compound	(4)
Empirical formula	C ₇₇ H ₁₅₁ MnMo ₆ N ₁₀ O ₂₇
Formula weight [g/mol]	2279.65
Temperature [K]	180.15
Crystal system	triclinic
Space group	<i>P</i> -1
a [Å]	16.3464(12)
b [Å]	17.0199(12)
c [Å]	20.0780(14)
α [°]	83.675(6)
β [°]	71.790(5)
γ [°]	67.634(5)
Volume [Å ³]	4906.8(6)
Z	2
ρ _{calc} [cm ³]	1.543
μ [mm ⁻¹]	0.94
F(000)	2352
Crystal size [mm ³]	0.38 × 0.24 × 0.07
Radiation	MoKα (λ = 0.71073)
2θ range for data collection [°]	2.82 to 54.916
Index ranges	-21 ≤ h ≤ 20, -21 ≤ k ≤ 22, -25 ≤ l ≤ 25
Reflections collected	41247
Independent reflections	21451 [R _{int} = 0.0224, R _{sigma} = 0.0210]
Data/restraints/parameters	21451/44/1057
Goodness-of-fit on F ²	1.04
Final R indexes [I > 2σ (I)]	R ₁ = 0.0268, wR ₂ = 0.0739
Final R indexes [all data]	R ₁ = 0.0323, wR ₂ = 0.0762
Largest diff. peak/hole [e Å ⁻³]	0.83/-0.46

Table 8.2: Crystal data of compound (5).

Compound	(5)
Empirical formula	C ₉₇ H ₁₉₀ MnMo ₆ N ₉ O ₃₁
Formula weight [g/mol]	2609.15
Temperature [K]	180.15
Crystal system	monoclinic
Space group	<i>P</i> 2 ₁ / <i>c</i>
a [Å]	22.3589(8)
b [Å]	17.1768(9)
c [Å]	32.5454(12)
α [°]	90
β [°]	100.346(3)
γ [°]	90
Volume [Å ³]	12296.0(9)
Z	4
ρ _{calc} [cm ³]	1.409
μ [mm ⁻¹]	0.762
F(000)	5440
Crystal size [mm ³]	0.45 × 0.21 × 0.12
Radiation	MoKα (λ = 0.71073)
2θ range for data collection [°]	2.866 to 51.364
Index ranges	-23 ≤ h ≤ 27, -20 ≤ k ≤ 20, -39 ≤ l ≤ 39
Reflections collected	89648
Independent reflections	23307 [R _{int} = 0.0845, R _{sigma} = 0.0605]
Data/restraints/parameters	23307/3/1256
Goodness-of-fit on F ²	0.875
Final R indexes [I > 2σ (I)]	R ₁ = 0.0467, wR ₂ = 0.1166
Final R indexes [all data]	R ₁ = 0.0739, wR ₂ = 0.1278
Largest diff. peak/hole [e Å ⁻³]	0.83/-0.51

Table 8.3: Crystal data of compound (6).

Compound	(6)
Empirical formula	$C_{68}H_{150}AlMo_6N_3O_{34}$
Formula weight [g/mol]	2156.52
Temperature [K]	180(2)
Crystal system	monoclinic
Space group	$P2_1/n$
a [Å]	13.9305(11)
b [Å]	23.8385(13)
c [Å]	15.3355(12)
α [°]	90
β [°]	113.593(7)
γ [°]	90
Volume [Å ³]	4667.0(6)
Z	2
ρ_{calc} [cm ³]	1.535
μ [mm ⁻¹]	0.869
F(000)	2232
Crystal size [mm ³]	0.44 × 0.32 × 0.23
Radiation	MoK α ($\lambda = 0.71073$)
2 θ range for data collection [°]	3.344 to 50.7
Index ranges	-16 ≤ h ≤ 16, -26 ≤ k ≤ 28, -18 ≤ l ≤ 18
Reflections collected	23421
Independent reflections	8465 [$R_{\text{int}} = 0.0332$, $R_{\text{sigma}} = 0.0417$]
Data/restraints/parameters	8465/157/494
Goodness-of-fit on F ²	0.905
Final R indexes [$I > 2\sigma(I)$]	$R_1 = 0.0476$, $wR_2 = 0.1284$
Final R indexes [all data]	$R_1 = 0.0775$, $wR_2 = 0.1419$
Largest diff. peak/hole [e Å ⁻³]	0.82/-0.38

Table 8.4: Crystal data of compound (7).

Compound	(7)
Empirical formula	C ₈₄ H ₁₇₀ MnMo ₆ N ₁₃ O ₂₄
Formula weight [g/mol]	2376.9
Temperature [K]	180.15
Crystal system	triclinic
Space group	<i>P</i> -1
a [Å]	20.3358(3)
b [Å]	28.4667(5)
c [Å]	30.2411(5)
α [°]	67.3340(10)
β [°]	70.1380(10)
γ [°]	76.5140(10)
Volume [Å ³]	15087.5(5)
Z	6
ρ _{calc} [cm ³]	1.57
μ [mm ⁻¹]	0.92
F(000)	7404
Crystal size [mm ³]	0.52 × 0.43 × 0.33
Radiation	MoKα (λ = 0.71073)
2θ range for data collection [°]	3.554 to 54.206
Index ranges	-26 ≤ h ≤ 15, -36 ≤ k ≤ 33, -38 ≤ l ≤ 35
Reflections collected	136907
Independent reflections	65534 [R _{int} = 0.0314, R _{sigma} = 0.0372]
Data/restraints/parameters	65534/2574/2855
Goodness-of-fit on F ²	1.017
Final R indexes [I >= 2σ (I)]	R ₁ = 0.0682, wR ₂ = 0.1860
Final R indexes [all data]	R ₁ = 0.1010, wR ₂ = 0.2187
Largest diff. peak/hole [e Å ⁻³]	2.78/-1.83

Table 8.5: Crystal data of compound (8).

Compound	(8)
Empirical formula	C ₈₂ H ₁₅₈ MnMo ₆ N ₁₁ O ₃₄
Formula weight [g/mol]	2472.76
Temperature [K]	293(2)
Crystal system	orthorhombic
Space group	<i>Pbcn</i>
a [Å]	63.585(4)
b [Å]	18.1926(12)
c [Å]	26.6998(12)
α [°]	90
β [°]	90
γ [°]	90
Volume [Å ³]	30886(3)
Z	12
ρ_{calc} [cm ³]	1.595
μ [mm ⁻¹]	7.456
F(000)	15312
Crystal size [mm ³]	0.52 × 0.47 × 0.42
Radiation	CuK α ($\lambda = 1.54186$)
2 θ range for data collection [°]	6.402 to 125.266
Index ranges	-72 ≤ h ≤ 51, -20 ≤ k ≤ 20, -28 ≤ l ≤ 30
Reflections collected	68817
Independent reflections	23944 [$R_{\text{int}} = 0.0307$, $R_{\text{sigma}} = 0.0233$]
Data/restraints/parameters	23944/102/1678
Goodness-of-fit on F ²	1.049
Final R indexes [$I \geq 2\sigma(I)$]	$R_1 = 0.0436$, $wR_2 = 0.1299$
Final R indexes [all data]	$R_1 = 0.0549$, $wR_2 = 0.1367$
Largest diff. peak/hole [e Å ⁻³]	1.02/-0.86

Table 8.6: Crystal data of compound (9).

Compound	(9)
Empirical formula	C ₇₀ H ₁₃₇ MnMo ₆ N ₆ O ₂₅
Formula weight [g/mol]	2093.43
Temperature [K]	180.15
Crystal system	triclinic
Space group	<i>P</i> -1
a [Å]	13.9550(10)
b [Å]	17.1438(14)
c [Å]	19.1438(16)
α [°]	81.478(7)
β [°]	78.320(6)
γ [°]	83.957(6)
Volume [Å ³]	4422.2(6)
Z	2
ρ _{calc} [cm ³]	1.572
μ [mm ⁻¹]	1.033
F(000)	2152
Crystal size [mm ³]	0.52 × 0.46 × 0.39
Radiation	MoKα (λ = 0.71073)
2θ range for data collection [°]	2.99 to 50.696
Index ranges	-16 ≤ h ≤ 16, -20 ≤ k ≤ 20, -23 ≤ l ≤ 23
Reflections collected	25690
Independent reflections	15123 [R _{int} = 0.0500, R _{sigma} = 0.0922]
Data/restraints/parameters	15123/2/1001
Goodness-of-fit on F ²	0.846
Final R indexes [I >= 2σ (I)]	R ₁ = 0.0370, wR ₂ = 0.0634
Final R indexes [all data]	R ₁ = 0.0824, wR ₂ = 0.0724
Largest diff. peak/hole [e Å ⁻³]	0.62/-0.56

Table 8.7: Crystal data of compound (10).

Compound	(10)
Empirical formula	C ₄₄ H ₉₈ Mn ₂ Mo ₄ N ₄ O ₂₀
Formula weight [g/mol]	1496.9
Temperature [K]	180.15
Crystal system	monoclinic
Space group	<i>P2₁/n</i>
a [Å]	9.9770(11)
b [Å]	16.1440(18)
c [Å]	18.730(2)
α [°]	90
β [°]	95.186(9)
γ [°]	90
Volume [Å ³]	3004.5(6)
Z	2
ρ _{calc} [cm ³]	1.655
μ [mm ⁻¹]	1.287
F(000)	1536
Crystal size [mm ³]	0.76 × 0.21 × 0.19
Radiation	MoKα (λ = 0.71073)
2θ range for data collection [°]	3.336 to 54.936
Index ranges	-12 ≤ h ≤ 12, -20 ≤ k ≤ 20, -24 ≤ l ≤ 24
Reflections collected	25730
Independent reflections	6788 [R _{int} = 0.0699, R _{sigma} = 0.0487]
Data/restraints/parameters	6788/12/344
Goodness-of-fit on F ²	0.985
Final R indexes [I >= 2σ (I)]	R ₁ = 0.0334, wR ₂ = 0.0794
Final R indexes [all data]	R ₁ = 0.0498, wR ₂ = 0.0848
Largest diff. peak/hole [e Å ⁻³]	1.02/-0.95

Table 8.8: Crystal data of compound (II)-Ce

Compound	(II)-Ce
Empirical formula	C ₁₇₄ H ₃₁₆ Ce ₅ Mn ₃ Mo ₁₈ N ₄₂ O ₁₁₈
Formula weight [g/mol]	7477.01
Temperature [K]	180.15
Crystal system	monoclinic
Space group	<i>P</i> 2 ₁
a [Å]	19.2936(2)
b [Å]	25.6462(2)
c [Å]	26.1388(3)
α [°]	90
β [°]	90.1440(10)
γ [°]	90
Volume [Å ³]	12933.6(2)
Z	2
ρ _{calc} [cm ³]	1.92
μ [mm ⁻¹]	10.266
F(000)	7438
Crystal size [mm ³]	0.22 × 0.11 × 0.06
Radiation	GaKα (λ = 1.34143)
2θ range for data collection [°]	4.2 to 123.246
Index ranges	-21 ≤ h ≤ 25, -26 ≤ k ≤ 33, -29 ≤ l ≤ 34
Reflections collected	181817
Independent reflections	51909 [R _{int} = 0.0416, R _{sigma} = 0.0399]
Data/restraints/parameters	51909/940/2355
Goodness-of-fit on F ²	1.031
Final R indexes [I > 2σ (I)]	R ₁ = 0.0568, wR ₂ = 0.1595
Final R indexes [all data]	R ₁ = 0.0677, wR ₂ = 0.1646
Largest diff. peak/hole [e Å ⁻³]	1.95/-1.42
Flack χ parameter	0.126(4)

Table 8.9: Crystal data of compound (12)-Dy

Compound	(12)-Dy
Empirical formula	C ₁₂₇ H ₂₀₇ Dy ₅ Mn ₃ Mo ₁₈ N ₂₄ O ₁₀₄
Formula weight [g/mol]	6438.39
Temperature [K]	150.15
Crystal system	monoclinic
Space group	<i>P</i> 2 ₁ / <i>c</i>
a [Å]	19.5819(7)
b [Å]	25.2560(10)
c [Å]	25.3233(9)
α [°]	90
β [°]	90.306(3)
γ [°]	90
Volume [Å ³]	12523.7(8)
Z	2
ρ _{calc} [cm ³]	1.707
μ [mm ⁻¹]	13.69
F(000)	6260
Crystal size [mm ³]	0.25 × 0.21 × 0.16
Radiation	GaKα (λ = 1.34143)
2θ range for data collection [°]	4.3 to 120.076
Index ranges	-25 ≤ h ≤ 25, -23 ≤ k ≤ 32, -32 ≤ l ≤ 30
Reflections collected	87057
Independent reflections	26547 [R _{int} = 0.0512, R _{sigma} = 0.0442]
Data/restraints/parameters	26547/331/1073
Goodness-of-fit on F ²	0.98
Final R indexes [I > 2σ (I)]	R ₁ = 0.0789, wR ₂ = 0.2304
Final R indexes [all data]	R ₁ = 0.1165, wR ₂ = 0.2605
Largest diff. peak/hole [e Å ⁻³]	2.74/-1.34

Table 8.10: Crystal data of compound (13).

Compound	(13)
Empirical formula	C ₁₃₂ H ₂₃₃ ClCuMn ₂ Mo ₁₂ N ₁₇ O ₅₂
Formula weight [g/mol]	4250.49
Temperature [K]	180(2)
Crystal system	monoclinic
Space group	<i>I</i> 2/ <i>a</i>
a [Å]	27.9207(12)
b [Å]	27.5317(11)
c [Å]	27.9543(13)
α [°]	90
β [°]	99.258(4)
γ [°]	90
Volume [Å ³]	21208.7(16)
Z	4
ρ _{calc} [cm ³]	1.331
μ [mm ⁻¹]	0.973
F(000)	8640
Crystal size [mm ³]	0.45 × 0.39 × 0.23
Radiation	MoKα (λ = 0.71073)
2θ range for data collection [°]	3.418 to 55.056
Index ranges	-36 ≤ h ≤ 32, -35 ≤ k ≤ 35, -36 ≤ l ≤ 36
Reflections collected	91425
Independent reflections	23884 [R _{int} = 0.1141, R _{sigma} = 0.0718]
Data/restraints/parameters	23884/272/808
Goodness-of-fit on F ²	1.475
Final R indexes [I > 2σ (I)]	R ₁ = 0.1223, wR ₂ = 0.3448
Final R indexes [all data]	R ₁ = 0.1403, wR ₂ = 0.3786
Largest diff. peak/hole [e Å ⁻³]	0.94/-3.34

Table 8.11: Crystal data of compound (14A).

Compound	(14A)
Empirical formula	$C_{94}H_{168}Mn_2Mo_{12}N_{26}O_{66}Zn_3$
Formula weight [g/mol]	4175.8
Temperature [K]	180.15
Crystal system	cubic
Space group	<i>I</i> 432
a [Å]	36.7518(7)
b [Å]	36.7518(7)
c [Å]	36.7518(7)
α [°]	90
β [°]	90
γ [°]	90
Volume [Å ³]	49640(3)
Z	12
ρ_{calc} [cm ³]	1.676
μ [mm ⁻¹]	1.534
F(000)	25032
Crystal size [mm ³]	0.13 × 0.11 × 0.07
Radiation	MoK α ($\lambda = 0.71073$)
2 θ range for data collection [°]	2.216 to 51.354
Index ranges	-44 ≤ h ≤ 43, -44 ≤ k ≤ 43, -44 ≤ l ≤ 44
Reflections collected	135893
Independent reflections	7899 [$R_{\text{int}} = 0.0501$, $R_{\text{sigma}} = 0.0179$]
Data/restraints/parameters	7899/81/340
Goodness-of-fit on F ²	0.943
Final R indexes [$I > 2\sigma(I)$]	$R_1 = 0.0458$, $wR_2 = 0.1329$
Final R indexes [all data]	$R_1 = 0.0551$, $wR_2 = 0.1402$
Largest diff. peak/hole [e Å ⁻³]	0.51/-0.45
Flack χ parameter	0.11(3)

Table 8.12: Crystal data of compound (**14B**).

Compound	(14B)
Empirical formula	C ₉₇ H ₁₇₅ Mn ₂ Mo ₁₂ N ₂₇ O ₆₇ Zn ₃
Formula weight [g/mol]	4248.9
Temperature [K]	100.15
Crystal system	monoclinic
Space group	C2/c
a [Å]	44.0133(6)
b [Å]	12.9451(2)
c [Å]	28.3784(4)
α [°]	90
β [°]	102.002(1)
γ [°]	90
Volume [Å ³]	15815.3(4)
Z	4
ρ _{calc} [cm ³]	1.784
μ [mm ⁻¹]	1.607
F(000)	8504
Crystal size [mm ³]	0.48 × 0.28 × 0.12
Radiation	MoKα (λ = 0.71073)
2θ range for data collection [°]	3.516 to 62.244
Index ranges	-61 ≤ h ≤ 61, -18 ≤ k ≤ 16, -39 ≤ l ≤ 40
Reflections collected	178407
Independent reflections	22059 [R _{int} = 0.0616, R _{sigma} = 0.0363]
Data/restraints/parameters	22059/43/825
Goodness-of-fit on F ²	1.054
Final R indexes [I > 2σ (I)]	22059/43/825
Final R indexes [all data]	1.054
Largest diff. peak/hole [e Å ⁻³]	R ₁ = 0.0445, wR ₂ = 0.1105
Flack χ parameter	R ₁ = 0.0593, wR ₂ = 0.1164

Table 8.13: Crystal data of compound (15).

Compound	(15)
Empirical formula	C ₄₂ H ₇₂ CdMnMo ₆ N ₇ O ₂₆
Formula weight [g/mol]	1834.04
Temperature [K]	180(2)
Crystal system	triclinic
Space group	<i>P</i> -1
a [Å]	11.9141(5)
b [Å]	13.4714(6)
c [Å]	22.9561(9)
α [°]	96.999(3)
β [°]	101.332(3)
γ [°]	113.688(3)
Volume [Å ³]	3224.5(2)
Z	2
ρ _{calc} [cm ³]	1.889
μ [mm ⁻¹]	9.348
F(000)	1812
Crystal size [mm ³]	0.34 × 0.21 × 0.19
Radiation	GaKα (λ = 1.34143)
2θ range for data collection [°]	6.396 to 123.89
Index ranges	-15 ≤ h ≤ 9, -13 ≤ k ≤ 17, -30 ≤ l ≤ 30
Reflections collected	39959
Independent reflections	14922 [R _{int} = 0.0699, R _{sigma} = 0.0469]
Data/restraints/parameters	14922/26/760
Goodness-of-fit on F ²	1.767
Final R indexes [I >= 2σ (I)]	R ₁ = 0.1049, wR ₂ = 0.2581
Final R indexes [all data]	R ₁ = 0.1178, wR ₂ = 0.2633
Largest diff. peak/hole [e Å ⁻³]	5.59/-1.74

8.2 SHAPE analysis results for coordination polyhedra

8.2.1 SHAPE analysis for compound (10)

Table 8.14: Continuous shape measurements (CShM's) of compound (10).

{MoO₅}						
Ideal	structures	ML5				
PP-5	1	D _{5h}	Pentagon			
OC-5	2	C _{4v}	Vacant	octahedron		
TBPY-5	3	D _{3h}	Trigonal	bipyramid		
SPY-5	4	C _{4v}	Spherical	square	pyramid	
JTBPY-5	5	D_{3h}	Johnson	trigonal	bipyramid	J12
Structure	1	[Mo]				
	Mo	2.744	11.7564	9.272		
	O	1.5853	10.6499	10.1803		
	O	3.8998	10.9484	8.1014		
	O	3.5336	12.864	10.3112		
	O	1.703	12.6965	8.2995		
	O	4.0644	10.0557	10.5742		
	PP-5	Ideal	structure	CShM	=	33.61759
	Mo	M	2.9217	11.4951	9.4564	
	O	L1	1.6629	10.7566	9.982	
	O	L3	4.446	11.3546	9.206	
	O	L4	3.434	12.8307	8.8565	
	O	L5	1.714	12.4611	9.336	
	O	L2	3.3514	10.0727	9.9016	
	vOC-5	Ideal	structure	CShM	=	6.27707
	Mo	M	2.8083	11.2517	9.2967	
	O	L2	1.4198	11.0798	10.5444	
	O	L4	4.1968	11.4236	8.049	
	O	L1	3.4885	12.7123	10.2549	
	O	L3	1.7483	12.4142	8.2772	

8. Appendix

	O	L5	3.8683	10.0892	10.3162	
	TBPY-5	Ideal	structure	CShM	=	2.2299
	Mo	M	2.9217	11.4951	9.4564	
	O	L2	1.3854	10.596	10.069	
	O	L3	3.8036	10.9007	7.9031	
	O	L4	3.576	12.9887	10.3971	
	O	L1	1.8417	12.6275	8.4099	
	O	L5	4.0017	10.3628	10.5029	
	SPY-5	Ideal	structure	CShM	=	5.14319
	Mo	M	2.9217	11.4951	9.4564	
	O	L2	1.4283	10.9664	10.42	
	O	L4	4.0863	11.2921	8.0279	
	O	L1	3.5791	12.9585	10.3862	
	O	L3	1.7317	12.2197	8.2328	
	O	L5	3.7829	10.0388	10.2151	
	JTBPY-5	Ideal	structure	CShM	=	1.90296
	Mo	M	2.9217	11.4951	9.4564	
	O	L1	1.6178	10.7375	9.9718	
	O	L2	3.6654	10.9949	8.1387	
	O	L3	3.4818	12.753	10.2588	
	O	L4	1.6345	12.8629	8.2107	
	O	L5	4.2089	10.1274	10.7022	
{MoO ₆ }						
Ideal	structures	ML6				
HP-6	1	D6h	Hexagon			
PPY-6	2	C5v	Pentagonal	pyramid		
OC-6	3	Oh	Octahedron			
TPR-6	4	D3h	Trigonal	prism		
JPPY-6	5	C5v	Johnson	pentagonal	pyramid	J2
Structure	1	[Mo]				
	O	1.5853	10.6499	10.1803		

8. Appendix

	O	4.0644	10.0557	10.5742		
	Mo	2.115	9.0576	11.2775		
	O	3.1589	7.5156	11.4606		
	O	0.5439	8.4093	11.2944		
	O	2.3057	9.7927	12.8029		
	O	2.7181	8.3423	9.1517		
	HP-6	Ideal	structure	CShM	=	47.65353
	O	M	2.3559	9.1176	10.9631	
	O	L1	3.4539	9.9444	10.6368	
	Mo	L3	1.4714	9.4938	11.9984	
	O	L5	2.1424	7.9145	10.254	
	O	L4	1.2579	8.2907	11.2894	
	O	L2	2.5694	10.3207	11.6721	
	O	L6	3.2404	8.7413	9.9277	
	PPY-6	Ideal	structure	CShM	=	30.34489
	O	M	2.2505	9.3142	10.8872	
	O	L2	3.715	9.9254	10.4375	
	Mo	L4	1.1705	9.2152	12.1299	
	O	L1	2.9881	7.938	11.4186	
	O	L5	0.961	8.4241	10.3721	
	O	L3	2.8726	10.1431	12.1703	
	O	L6	2.5335	8.8631	9.3261	
	OC-6	Ideal	structure	CShM	=	31.35478
	O	M	2.3559	9.1176	10.9631	
	O	L1	3.7662	9.875	10.7293	
	Mo	L2	1.5637	10.4485	10.496	
	O	L4	3.1481	7.7866	11.4302	
	O	L6	0.9456	8.3602	11.1969	
	O	L3	2.3295	9.6392	12.4942	
	O	L5	2.3822	8.5959	9.4319	
	TPR-6	Ideal	structure	CShM	=	37.32128

8. Appendix

	O	M	2.3559	9.1176	10.9631	
	O	L1	3.5906	9.9702	10.5912	
	Mo	L5	1.885	8.344	12.2159	
	O	L2	3.4056	7.9833	10.9298	
	O	L6	0.8318	9.2189	10.7252	
	O	L4	2.0699	10.3309	11.8773	
	O	L3	2.3525	8.8582	9.4391	
	JPPY-6	Ideal	structure	CShM	=	34.24333
	O	M	2.2893	9.2408	10.9141	
	O	L1	3.7805	9.8648	10.4555	
	Mo	L3	1.1857	9.146	12.1778	
	O	L6	2.7555	8.3783	11.2567	
	O	L4	0.9799	8.3258	10.3926	
	O	L2	2.9166	10.0972	12.2167	
	O	L5	2.5836	8.77	9.3282	
{MnMosN}						
Ideal	structures	ML6				
HP-6	1	D6h	Hexagon			
PPY-6	2	C5v	Pentagonal	pyramid		
OC-6	3	Oh	Octahedron			
TPR-6	4	D3h	Trigonal	prism		
JPPY-6	5	C5v	Johnson	pentagonal	pyramid	J2
Structure	1	[Mn]				
	Mn	3.5478	6.7145	9.822		
	O	4.3838	5.1962	10.5515		
	O	3.1589	7.5157	11.4601		
	N	1.639	5.8337	8.9235		
	O	4.2191	6.0889	8.0787		
	O	2.7181	8.3424	9.1512		
	O	5.5654	7.8024	9.5018		
	HP-6	Ideal	structure	CShM	=	30.53039
	Mn	M	3.6046	6.7848	9.6412	

8. Appendix

	O	L1	4.9765	5.7807	9.5999	
	O	L3	3.5862	8.1585	10.6437	
	N	L5	2.2511	6.4153	8.6802	
	O	L6	3.623	5.4111	8.6388	
	O	L4	2.2326	7.789	9.6826	
	O	L2	4.9581	7.1544	10.6023	
	PPY-6	Ideal	structure	CShM	=	21.65502
	Mn	M	3.4057	6.6369	9.7234	
	O	L2	4.569	5.6067	10.6859	
	O	L3	3.555	7.364	11.3938	
	N	L5	2.5944	6.8243	8.0961	
	O	L6	3.9753	5.2731	8.6478	
	O	L4	2.3346	8.1166	9.7933	
	O	L1	4.7982	7.6721	9.1483	
	OC-6	Ideal	structure	CShM	=	2.97663
	Mn	M	3.6046	6.7848	9.6412	
	O	L1	4.3867	5.1275	10.4666	
	O	L2	3.0516	7.4307	11.4623	
	N	L3	1.8377	5.8491	9.4366	
	O	L4	4.1575	6.1389	7.8202	
	O	L6	2.8225	8.4421	8.8159	
	O	L5	5.3715	7.7206	9.8459	
	TPR-6	Ideal	structure	CShM	=	10.85932
	Mn	M	3.6046	6.7848	9.6412	
	O	L1	3.5641	5.1059	10.585	
	O	L4	3.8884	7.4631	11.4219	
	N	L2	2.1353	5.9731	8.6959	
	O	L3	4.6278	5.7396	8.3875	
	O	L5	2.4597	8.3303	9.5328	
	O	L6	4.9522	8.0969	9.2244	
	JPPY-6	Ideal	structure	CShM	=	25.6229

8. Appendix

	Mn	M	3.595	6.9152	9.5407	
	O	L6	3.6622	6.0027	10.2442	
	O	L1	3.8782	8.0552	10.9925	
	N	L3	2.2827	6.0447	8.5369	
	O	L4	4.4489	5.9411	8.1956	
	O	L2	1.93	7.3513	10.2655	
	O	L5	5.435	7.1837	9.7132	

8.2.2 SHAPE analysis for compound (11)-Ce

Table 8.15: Continuous shape measurements (CShM's) of compound (11)-Ce.

{Ce(DMF)₅(O_t)₃} (Ce₂)							
Ideal	structures	ML8					
OP-8	1	D8h	Octagon				
HPY-8	2	C7v	Heptagonal	pyramid			
HBPY-8	3	D6h	Hexagonal	bipyramidal			
CU-8	4	Oh	Cube				
SAPR-8	5	D4d	Square	antiprism			
TDD-8	6	D2d	Triangular	dodecahedron			
JGBF-8	7	D2d	Johnson	gyrobifastigium	J26		
JETBPY-8	8	D3h	Johnson	elongated	triangular	bipyramidal	J14
JBTPR-8	9	C2v	Biaugmented	trigonal	prism	J50	
Structure	1	[Ce]					
	Ce	15.2367	14.8435	21.1209			
	O	13.2844	16.1981	21.9748			
	O	14.017	15.7493	19.11			
	O	16.767	12.9872	21.9095			
	O	17.1394	14.7748	19.604			
	O	15.9513	17.1727	20.9842			
	O	13.8082	13.3463	22.3564			
	O	14.6952	13.0001	19.4943			
	O	16.0533	15.5262	23.3968			

8. Appendix

	OP-8	Ideal	structure	CShM	=	29.54764	
	Ce	M	15.2169	14.8443	21.1057		
	O	L1	14.5405	16.469	22.2278		
	O	L3	15.3287	16.06	19.4127		
	O	L6	15.6162	12.8357	21.5093		
	O	L4	15.7743	14.5551	19.1151		
	O	L2	14.8176	16.8528	20.702		
	O	L7	15.1052	13.6285	22.7986		
	O	L5	15.8934	13.2195	19.9835		
	O	L8	14.6595	15.1334	23.0962		
	HPY-8	Ideal	structure	CShM	=	22.3995	
	Ce	M	15.3626	14.9938	20.9772		
	O	L2	13.7834	16.534	20.9791		
	O	L3	13.746	15.308	19.5095		
	O	L6	17.1362	13.9646	21.7906		
	O	L5	16.4347	13.2475	20.1603		
	O	L8	15.01	16.6002	22.4473		
	O	L1	14.0515	13.648	22.1332		
	O	L4	14.926	13.8453	19.1451		
	O	L7	16.5021	15.4567	22.8085		
	HBPY-8	Ideal	structure	CShM	=	16.0159	
	Ce	M	15.2169	14.8443	21.1057		
	O	L1	13.3524	15.4599	22.2623		
	O	L2	14.4596	15.9794	19.2805		
	O	L5	15.9743	13.7091	22.9308		
	O	L8	17.0815	14.2286	19.949		
	O	L3	15.7642	17.038	20.8202		
	O	L6	14.6697	12.6505	21.3911		
	O	L7	13.9123	13.7857	19.5659		
	O	L4	16.5216	15.9028	22.6454		
	CU-8	Ideal	structure	CShM	=	9.02514	

8. Appendix

	Ce	M	15.2169	14.8443	21.1057		
	O	L1	13.2881	15.5014	22.3196		
	O	L2	13.8277	16.1781	19.7212		
	O	L8	16.6061	13.5104	22.4901		
	O	L7	17.1457	14.1871	19.8917		
	O	L3	16.4101	16.7734	20.4125		
	O	L5	14.0238	12.9151	21.7988		
	O	L6	14.5634	13.5918	19.2004		
	O	L4	15.8705	16.0967	23.0109		
	SAPR-8	Ideal	structure	CShM	=	0.51714	
	Ce	M	15.2169	14.8443	21.1057		
	O	L1	13.3305	16.2245	21.9352		
	O	L2	14.1837	15.8184	19.0721		
	O	L8	16.7864	13.0638	21.8259		
	O	L7	17.0155	14.8362	19.3977		
	O	L6	16.0381	17.1831	21.0186		
	O	L4	13.8596	13.3118	22.506		
	O	L3	14.7128	12.9056	19.643		
	O	L5	15.809	15.4106	23.4467		
	TDD-8	Ideal	structure	CShM	=	1.33558	
	Ce	M	15.2169	14.8443	21.1057		
	O	L1	13.4892	16.2193	22.2127		
	O	L2	13.7593	15.7062	19.3075		
	O	L8	16.5361	12.9509	21.9869		
	O	L7	17.3126	14.7915	19.7993		
	O	L3	15.8724	17.1992	20.7505		
	O	L5	13.5914	13.2616	22.0823		
	O	L6	14.9701	13.0076	19.4725		
	O	L4	16.2044	15.6177	23.2335		
	JGBF-8	Ideal	structure	CShM	=	16.01082	
	Ce	M	15.2169	14.8443	21.1057		
	O	L1	13.3208	16.6198	21.5265		
	O	L3	13.9025	14.7266	19.7938		

8. Appendix

	O	L8	15.9016	12.4492	21.9541		
	O	L6	16.4283	15.4637	19.8363		
	O	L2	15.8467	17.357	21.569		
	O	L4	14.0055	14.2248	22.375		
	O	L7	15.7986	12.951	19.3729		
	O	L5	16.5314	14.9619	22.4175		
	JETBPY-8	Ideal	structure	CShM	=	28.75513	
	Ce	M	15.2169	14.8443	21.1057		
	O	L1	14.0191	15.9258	21.6945		
	O	L2	14.1022	14.7073	19.8057		
	O	L4	15.3264	13.1466	20.8664		
	O	L6	16.3469	14.8511	19.8117		
	O	L5	16.2638	16.0696	21.7005		
	O	L3	15.2433	14.3651	22.7552		
	O	L8	15.3264	13.2401	18.619		
	O	L7	15.1075	16.4484	23.5923		
	JBTPR-8	Ideal	structure	CShM	=	2.36964	
	Ce	M	14.9044	14.7707	21.0224		
	O	L3	13.3969	16.2248	21.9479		
	O	L4	14.2485	15.829	19.1006		
	O	L8	16.77	12.6039	21.8816		
	O	L2	16.9612	14.9568	20.0332		
	O	L7	15.8518	17.5997	20.9125		
	O	L5	13.9293	13.3283	22.5098		
	O	L6	14.7809	12.9325	19.6624		
	O	L1	16.1096	15.3526	22.8805		
{Ce(DMF)₆(O)₃} (Ce1)							
Ideal	structures	ML9					
EP-9	1	D9h	Enneagon				
OPY-9	2	C8v	Octagonal	pyramid			
HBPY-9	3	D7h	Heptagonal	bipyramid			
JTC-9	4	C3v	Johnson	triangular	cupola	J3	
JCCU-9	5	C4v	Capped	cube	J8		
CCU-9	6	C4v	Spherical-relaxed	capped	cube		
JCSAPR-9	7	C4v	Capped	square	antiprism	J10	
CSAPR-9	8	C4v	Spherical	capped	square	antiprism	

8. Appendix

JTCTPR-9	9	D3h	Tricapped	trigonal	prism	J51
Structure	1	[Ce]				
	Ce	3.5762	17.6656	17.8512		
	O	2.0312	19.4783	17.0372		
	O	5.7743	16.6085	16.9928		
	O	5.169	17.2163	19.8524		
	O	1.2509	16.7726	17.3822		
	O	3.3416	17.1547	15.3905		
	O	3.4594	15.2774	18.3834		
	O	2.1878	17.6754	19.9883		
	O	4.0652	19.7681	19.178		
	O	5.0653	19.3552	16.6111		
	EP-9	Ideal	structure	CShM	=	37.34954
	Ce	M	3.5921	17.6972	17.8667	
	O	L1	2.2698	17.5635	16.3581	
	O	L4	5.3778	18.57	17.5639	
	O	L6	4.3906	17.5046	19.7018	
	O	L9	1.7445	16.9966	17.4957	
	O	L2	3.4138	18.1929	15.9264	
	O	L8	2.0837	16.7575	18.8069	
	O	L7	3.1287	16.9582	19.6782	
	O	L5	5.2788	18.1412	18.8668	
	O	L3	4.6413	18.5905	16.4026	
	OPY-9	Ideal	structure	CShM	=	22.23111
	Ce	M	3.5646	17.508	17.7477	
	O	L2	1.9252	18.494	16.5584	
	O	L5	5.7988	17.3209	17.5296	
	O	L6	5.2041	16.522	18.9369	
	O	L9	1.3304	17.695	17.9657	
	O	L3	3.4803	18.7153	15.8478	
	O	L7	3.6489	16.3006	19.6475	
	O	L8	2.0444	16.7865	19.2452	
	O	L1	3.8392	19.4005	18.9381	
	O	L4	5.0849	18.2294	16.2501	

8. Appendix

	HBPY-9	Ideal	structure	CShM	=	20.55709
	Ce	M	3.5921	17.6972	17.8667	
	O	L2	2.99	19.1891	16.2737	
	O	L1	5.3187	17.012	16.5724	
	O	L5	4.7138	17.0295	19.7165	
	O	L7	2.4246	15.8453	17.2896	
	O	L8	2.1729	17.4085	16.1265	
	O	L6	3.5554	15.6766	18.8874	
	O	L9	1.8655	18.3824	19.161	
	O	L4	5.0276	18.8852	19.1527	
	O	L3	4.2604	19.8463	17.6205	
	JTC-9	Ideal	structure	CShM	=	16.69696
	Ce	M	3.5731	18.0145	17.3723	
	O	L1	1.5072	19.0045	18.0869	
	O	L4	5.639	17.0245	16.6576	
	O	L8	5.0211	16.9701	18.9758	
	O	L6	1.4849	16.9846	16.7914	
	O	L5	3.5508	15.9946	16.0768	
	O	L9	2.9328	15.9402	18.395	
	O	L7	2.9552	17.9601	19.6904	
	O	L2	3.5954	20.0345	18.6677	
	O	L3	5.6614	19.0444	17.9531	
	JCCU-9	Ideal	structure	CShM	=	10.77286
	Ce	M	3.8865	17.8107	17.9274	
	O	L1	2.2947	18.8636	16.6342	
	O	L4	5.7619	17.3967	16.652	
	O	L6	5.4784	16.7578	19.2207	
	O	L9	0.9422	16.6757	17.3201	
	O	L3	3.3227	16.4565	16.1489	
	O	L5	3.0392	15.8175	18.7176	
	O	L7	2.0112	18.2247	19.2029	
	O	L8	4.4503	19.165	19.706	
	O	L2	4.7339	19.8039	17.1373	
	CCU-9	Ideal	structure	CShM	=	9.57161
	Ce	M	3.6114	17.7047	17.8707	
	O	L1	2.2215	19.1546	16.5287	
	O	L6	5.6731	17.4468	16.6386	

8. Appendix

	O	L8	5.4321	16.7404	19.1318	
	O	L9	1.3986	16.85	17.4146	
	O	L2	3.4313	16.3791	15.8593	
	O	L4	3.1442	15.5375	18.8299	
	O	L3	1.9343	18.313	19.4993	
	O	L7	4.4167	19.0698	19.6936	
	O	L5	4.6577	19.7762	17.2004	
	JCSAPR-9	Ideal	structure	CShM	=	1.34752
	Ce	M	3.897	17.8157	17.9302	
	O	L2	2.1118	19.3014	17.2112	
	O	L5	5.8735	16.6699	17.0981	
	O	L7	5.1114	17.119	19.9181	
	O	L9	0.8477	16.6312	17.2949	
	O	L4	3.2988	17.0564	15.6993	
	O	L6	3.4082	15.4466	18.1755	
	O	L8	2.2211	17.6916	19.6874	
	O	L1	4.1947	19.8448	19.2362	
	O	L3	4.9568	19.3956	16.4162	
	CSAPR-9	Ideal	structure	CShM	=	0.30743
	Ce	M	3.5943	17.6981	17.8672	
	O	L2	2.0204	19.5513	17.1454	
	O	L7	5.8169	16.7207	17.1341	
	O	L8	5.0832	17.1542	19.847	
	O	L1	1.274	16.7953	17.3839	
	O	L3	3.3647	17.011	15.4366	
	O	L4	3.4889	15.1915	18.2392	
	O	L5	2.1446	17.7318	19.9479	
	O	L9	4.2001	19.7759	19.1893	
	O	L6	4.9338	19.3424	16.4764	
	JTCTPR-9	Ideal	structure	CShM	=	2.31999
	Ce	M	3.5921	17.6972	17.8667	
	O	L1	2.1594	19.3224	17.2213	
	O	L8	5.9674	16.285	16.8418	
	O	L4	5.2106	17.4998	19.4326	
	O	L7	0.8963	16.6468	17.3041	

8. Appendix

	O	L5	3.3508	17.0758	15.7066	
	O	L6	3.4618	15.4631	18.186	
	O	L3	2.2704	17.7096	19.7006	
	O	L9	3.9125	20.1597	19.4542	
	O	L2	5.0996	19.1126	16.9532	
{Ce(DMF)₄(O₂,Coo)(O_{Coo})₂} (Ce3)						
Ideal	structure	ML8				
OP-8	1	D8h	Octagon			
HPY-8	2	C7v	Heptagonal	pyramid		
HBPY-8	3	D6h	Hexagonal	bipyramid		
CU-8	4	Oh	Cube			
SAPR-8	5	D4d	Square	antiprism		
TDD-8	6	D2d	Triangular	dodecahedron		
JGBF-8	7	D2d	Johnson	gyrobifastigium	J26	
JETBPY-8	8	D3h	Johnson	elongated	triangular	bipyramid
JBTPR-8	9	C2v	Biaugmented	trigonal	prism	J50
Structure	1	[Ce]				
	Ce	7.1106	16.1407	3.1568		
	O	7.1226	15.6314	5.5937		
	O	7.8013	18.2191	4.2554		
	O	9.5501	15.321	3.9234		
	O	8.5623	14.1875	2.3969		
	O	8.8328	16.9675	1.4585		
	O	6.1768	15.5416	1.1527		
	O	4.8407	16.9214	3.845		
	O	5.82	14.0387	3.4137		
	OP-8	Ideal	structure	CShM	=	28.09844
	Ce	M	7.313	15.8854	3.244	
	O	L1	6.6179	16.7482	5.0276	
	O	L2	8.1618	17.0895	4.7402	
	O	L3	9.2085	16.7255	3.5764	

8. Appendix

	O	L5	8.0082	15.0226	1.4604		
	O	L4	9.1449	15.8693	2.2179		
	O	L6	6.4643	14.6813	1.7478		
	O	L8	5.4812	15.9015	4.2702		
	O	L7	5.4176	15.0454	2.9116		
	HPY-8	Ideal	structure	CShM	=	22.97104	
	Ce	M	7.1859	15.7654	3.4131		
	O	L2	8.4308	16.6533	4.9789		
	O	L3	6.8754	17.6355	4.5068		
	O	L8	9.0487	15.0025	4.272		
	O	L7	8.264	13.9262	2.9183		
	O	L1	8.3298	16.8453	1.8915		
	O	L5	5.4613	15.6961	2.0674		
	O	L4	5.5539	17.2095	3.211		
	O	L6	6.6675	14.2349	1.9371		
	HBPY-8	Ideal	structure	CShM	=	17.06649	
	Ce	M	7.313	15.8854	3.244		
	O	L1	7.8373	15.8156	5.4362		
	O	L2	6.8563	18.0865	3.4233		
	O	L4	9.3992	15.2055	2.7235		
	O	L5	7.7697	13.6844	3.0647		
	O	L3	8.9425	17.4065	2.9028		
	O	L8	6.7888	15.9552	1.0519		
	O	L7	5.2269	16.5654	3.7646		
	O	L6	5.6836	14.3643	3.5853		
	CU-8	Ideal	structure	CShM	=	11.77258	
	Ce	M	7.313	15.8854	3.244		
	O	L1	7.8523	15.7917	5.5046		
	O	L2	7.0535	17.9939	4.1911		
	O	L4	9.5202	15.193	3.4865		
	O	L8	7.5726	13.777	2.297		
	O	L3	8.7214	17.3952	2.1729		
	O	L7	6.7737	15.9792	0.9834		
	O	L6	5.1059	16.5779	3.0016		
	O	L5	5.9047	14.3757	4.3151		

8. Appendix

	SAPR-8	Ideal	structure	CShM	=	1.5379	
	Ce	M	7.313	15.8854	3.244		
	O	L1	7.0056	15.6706	5.6724		
	O	L5	7.7967	18.1168	4.152		
	O	L4	9.5846	15.7244	4.1668		
	O	L3	8.3704	14.0315	2.0265		
	O	L8	8.7617	16.9578	1.574		
	O	L7	6.0795	15.7228	1.1252		
	O	L6	5.1144	16.8818	3.7033		
	O	L2	5.7914	13.9778	3.5321		
	TDD-8	Ideal	structure	CShM	=	3.84316	
	Ce	M	7.313	15.8854	3.244		
	O	L2	7.3793	15.3636	5.6145		
	O	L1	7.7231	17.9849	4.3931		
	O	L3	9.6582	15.8711	3.8737		
	O	L7	8.2197	13.778	2.4486		
	O	L4	8.4548	17.3215	1.6534		
	O	L8	6.2799	15.4699	1.0862		
	O	L5	5.1983	17.0786	3.2596		
	O	L6	5.591	14.2159	3.6231		
	JGBF-8	Ideal	structure	CShM	=	15.44464	
	Ce	M	7.313	15.8854	3.244		
	O	L3	7.6929	15.9287	5.0635		
	O	L4	6.9283	17.704	3.2811		
	O	L7	9.8739	15.4681	3.6692		
	O	L6	7.6977	14.0669	3.2069		
	O	L8	9.1094	17.2435	1.8869		
	O	L5	6.9332	15.8422	1.4246		
	O	L1	5.132	16.3459	4.6383		
	O	L2	5.1369	14.4842	2.7817		
	JETBPY-8	Ideal	structure	CShM	=	25.40841	
	Ce	M	7.313	15.8854	3.244		
	O	L1	7.0376	15.8416	4.9721		

8. Appendix

Structure	1	[Ce]				
	Ce	9.8491	15.6637	6.3522		
	O	7.1226	15.6314	5.5937		
	O	8.0962	14.0028	6.6863		
	O	8.3937	16.647	8.0638		
	O	10.6807	14.9107	8.5343		
	O	9.4536	17.8087	5.497		
	O	11.8607	17.2625	7.3084		
	O	12.0987	16.1007	5.5074		
	O	9.5501	15.321	3.9234		
	O	10.9863	13.4899	5.9335		
	EP-9	Ideal	structure	CShM	=	35.17421
	Ce	M	9.8092	15.6838	6.34	
	O	L1	7.7955	15.8227	6.1192	
	O	L2	8.2699	14.6991	5.4548	
	O	L9	8.2634	16.8813	6.887	
	O	L6	11.6996	16.1339	6.9285	
	O	L8	9.4545	17.3796	7.3989	
	O	L7	10.8116	17.0844	7.4152	
	O	L5	11.7031	14.9727	6.1664	
	O	L3	9.4645	14.0363	5.2045	
	O	L4	10.8203	14.1443	5.4855	
	OPY-9	Ideal	structure	CShM	=	20.19585
	Ce	M	9.7149	15.885	6.3844	
	O	L2	7.8159	15.226	5.3395	
	O	L3	7.8074	14.8484	7.0317	
	O	L4	8.9162	15.078	8.3448	
	O	L5	10.493	15.7803	8.5095	
	O	L8	10.5136	16.692	4.424	
	O	L6	11.6139	16.5439	7.4293	
	O	L7	11.6225	16.9216	5.7371	
	O	L9	8.9369	15.9897	4.2593	
	O	L1	10.6574	13.8733	5.9402	

8. Appendix

	HBPY-9	Ideal	structure	CShM	=	15.64955
	Ce	M	9.8092	15.6838	6.34	
	O	L2	7.581	15.1216	6.6294	
	O	L3	8.8159	13.5965	6.195	
	O	L8	8.024	17.07	6.8458	
	O	L1	10.1878	15.3467	8.6	
	O	L7	9.8112	17.9746	6.6814	
	O	L6	11.5969	17.1542	6.2599	
	O	L5	12.0364	15.2266	5.8987	
	O	L9	9.4306	16.021	4.08	
	O	L4	10.7987	13.6432	5.8698	
	JTC-9	Ideal	structure	CShM	=	16.96995
	Ce	M	9.7896	15.1509	6.1054	
	O	L1	7.6657	15.6469	5.1562	
	O	L6	7.8028	14.6858	7.3276	
	O	L9	9.2383	16.4519	8.0187	
	O	L5	9.9266	14.1898	8.2768	
	O	L7	9.1012	17.413	5.8473	
	O	L8	11.2251	16.9171	6.7965	
	O	L3	11.7764	15.616	4.8831	
	O	L2	9.6525	16.112	3.9339	
	O	L4	11.9134	14.6549	7.0545	
	JCCU-9	Ideal	structure	CShM	=	7.91605
	Ce	M	10.1129	15.6274	6.438	
	O	L9	7.0756	16.1916	5.458	
	O	L1	8.5179	13.993	6.0007	
	O	L3	8.2845	15.9335	7.8414	
	O	L4	10.8006	15.4661	8.6533	
	O	L5	9.1917	17.7292	6.0635	
	O	L6	11.7079	17.2618	6.8753	
	O	L8	11.9413	15.3213	5.0346	
	O	L7	9.4251	15.7887	4.2227	
	O	L2	11.0341	13.5256	6.8125	
	CCU-9	Ideal	structure	CShM	=	7.74404
	Ce	M	9.8289	15.68	6.3465	

8. Appendix

	O	L9	7.5647	16.1213	5.6075	
	O	L1	8.4524	13.7083	6.0547	
	O	L2	8.2241	16.0123	8.1302	
	O	L6	10.7463	15.5176	8.5825	
	O	L4	9.3051	18.0221	6.0181	
	O	L8	11.6536	17.2044	6.8098	
	O	L7	11.8452	15.2706	5.0678	
	O	L3	9.5334	15.718	3.9425	
	O	L5	10.9379	13.5838	6.8405	
	JCSAPR-9	Ideal	structure	CShM	=	2.669
	Ce	M	10.1177	15.6258	6.437	
	O	L9	7.032	16.2058	5.4669	
	O	L2	8.4057	13.9757	6.7451	
	O	L4	8.5344	16.6368	7.9269	
	O	L3	10.5655	14.6518	8.5817	
	O	L6	9.5284	17.7085	5.4054	
	O	L5	11.3593	17.2912	7.6343	
	O	L7	11.9713	16.1674	5.0158	
	O	L8	9.3998	15.0474	4.2237	
	O	L1	11.1774	13.5279	5.9631	
	CSAPR-9	Ideal	structure	CShM	=	2.54209
	Ce	M	9.8114	15.6834	6.3407	
	O	L1	7.4783	16.1393	5.6013	
	O	L2	8.3222	13.7445	6.8108	
	O	L3	8.4774	16.7312	8.1629	
	O	L6	10.5511	14.6712	8.4916	
	O	L4	9.612	17.9523	5.3355	
	O	L7	11.3267	17.2016	7.6044	
	O	L8	11.9157	16.1398	5.0911	
	O	L5	9.4568	14.9655	3.9834	
	O	L9	11.1401	13.6094	5.9783	
	JTCTPR-9	Ideal	structure	CShM	=	3.51066
	Ce	M	9.8092	15.6838	6.34	
	O	L7	7.0775	16.2078	5.4907	
	O	L1	8.4482	13.9704	6.7733	

8. Appendix

	O	L5	8.5949	16.6401	7.9484	
	O	L2	10.8973	14.8496	8.0994	
	O	L6	9.5863	17.701	5.4143	
	O	L8	11.3015	17.7241	7.778	
	O	L4	11.8886	15.9105	5.5654	
	O	L3	9.4396	15.0313	4.2392	
	O	L9	11.0485	13.1196	5.7512	
{Ce(DMF)(O₂,Coo)(O_{Coo})₆} (Ce5)						
Ideal	structures	ML9				
EP-9	1	D9h	Enneagon			
OPY-9	2	C8v	Octagonal	pyramid		
HBPY-9	3	D7h	Heptagonal	bipyramid		
JTC-9	4	C3v	Johnson	triangular	cupola	J3
JCCU-9	5	C4v	Capped	cube	J8	
CCU-9	6	C4v	Spherical-relaxed	capped	cube	
JCSAPR-9	7	C4v	Capped	square	antiprism	J10
CSAPR-9	8	C4v	Spherical	capped	square	antiprism
JTCTPR-9	9	D3h	Tricapped	trigonal	prism	J51
Structure	1	[Ce]				
	Ce	11.8851	16.9857	9.8232		
	O	9.6771	17.7626	9.4308		
	O	12.5609	14.544	9.6635		
	O	10.6807	14.9107	8.5343		
	O	11.8607	17.2625	7.3084		
	O	10.4516	15.698	11.4069		
	O	13.3969	16.588	11.7284		
	O	14.1946	17.1317	9.0858		
	O	10.9388	18.555	11.7807		
	O	12.7289	19.3834	9.6217		
	EP-9	Ideal	structure	CShM	=	34.75233
	Ce	M	11.8375	16.8821	9.8384	
	O	L1	10.0523	15.9382	10.1566	
	O	L3	11.7474	15.718	8.1602	
	O	L2	10.6134	15.5062	8.9508	
	O	L4	12.9235	16.4746	8.1549	
	O	L9	10.3265	16.8119	11.2136	
	O	L7	12.5368	18.2337	11.2036	

8. Appendix

	O	L5	13.5915	17.4218	8.9373	
	O	L8	11.3077	17.7184	11.6271	
	O	L6	13.4388	18.1165	10.1413	
	OPY-9	Ideal	structure	CShM	=	23.25619
	Ce	M	11.8481	16.8129	10.0501	
	O	L2	9.7671	17.5369	10.3907	
	O	L5	12.7588	14.8925	9.3765	
	O	L4	11.0549	14.821	9.4382	
	O	L1	11.7424	17.5052	7.9333	
	O	L3	9.8157	15.9164	9.8583	
	O	L7	13.8805	17.7094	10.2418	
	O	L6	13.9292	16.0889	9.7094	
	O	L9	10.9374	18.7334	10.7236	
	O	L8	12.6413	18.8048	10.6619	
	HBPY-9	Ideal	structure	CShM	=	17.97736
	Ce	M	11.8375	16.8821	9.8384	
	O	L2	9.8643	17.6706	10.6977	
	O	L5	13.2191	15.2628	8.9881	
	O	L4	11.3861	14.6642	9.4763	
	O	L1	11.1124	17.3754	7.7206	
	O	L3	9.8931	15.7358	10.2372	
	O	L9	12.5627	16.3889	11.9561	
	O	L6	14.0117	17.0807	9.1402	
	O	L8	11.3213	19.0117	10.5112	
	O	L7	13.1671	18.7492	9.818	
	JTC-9	Ideal	structure	CShM	=	14.30631
	Ce	M	11.6864	17.3042	9.4486	
	O	L1	9.3465	16.9633	9.9871	
	O	L9	12.0985	14.9319	9.7381	
	O	L6	10.3788	15.6854	8.2032	
	O	L5	12.7187	16.0262	7.6647	
	O	L7	11.0662	16.2099	11.522	
	O	L8	13.4061	16.5507	10.9835	
	O	L4	14.0263	17.645	8.9101	
	O	L2	10.6541	18.5821	11.2325	

8. Appendix

	O	L3	12.9939	18.9229	10.694	
	JCCU-9	Ideal	structure	CShM	=	10.42417
	Ce	M	11.9454	16.7035	9.5947	
	O	L1	10.3664	18.3693	9.4243	
	O	L6	13.5243	15.0377	9.7651	
	O	L4	11.0317	14.7069	8.9048	
	O	L2	11.2595	16.8894	7.4056	
	O	L3	10.1385	16.1868	10.9235	
	O	L5	12.6312	16.5176	11.7838	
	O	L8	13.7522	17.2202	8.2659	
	O	L9	10.8672	18.4899	12.0315	
	O	L7	12.859	18.7001	10.2846	
	CCU-9	Ideal	structure	CShM	=	9.59238
	Ce	M	11.8446	16.8705	9.8224	
	O	L1	10.1358	18.4619	9.2401	
	O	L8	13.5162	15.14	9.769	
	O	L6	11.076	14.7494	8.9846	
	O	L5	11.2137	16.8706	7.5	
	O	L2	9.9717	15.9345	11.009	
	O	L4	12.8792	16.4	11.9436	
	O	L7	13.6538	17.2612	8.2844	
	O	L9	11.0413	18.206	11.6561	
	O	L3	13.0432	18.9273	10.1747	
	JCSAPR-9	Ideal	structure	CShM	=	1.99385
	Ce	M	11.9504	16.695	9.5898	
	O	L2	9.8386	17.8507	9.4036	
	O	L5	12.8789	14.5071	10.0156	
	O	L3	10.4877	15.1548	8.4416	
	O	L1	11.864	17.4875	7.3106	
	O	L4	10.5563	15.7433	11.3163	
	O	L6	13.2203	16.9348	11.6295	
	O	L7	14.2552	16.8398	8.8846	
	O	L9	10.8214	18.5662	12.0752	
	O	L8	12.5026	19.0422	9.7168	

8. Appendix

	CSAPR-9	Ideal	structure	CShM	=	1.28931
	Ce	M	11.8384	16.8808	9.8366	
	O	L2	9.6195	17.9183	9.2681	
	O	L7	12.844	14.5805	9.9787	
	O	L6	10.5463	15.2105	8.4714	
	O	L9	11.8714	17.4506	7.3877	
	O	L3	10.4282	15.532	11.4225	
	O	L4	13.4404	16.8707	11.7746	
	O	L8	14.1692	16.8206	8.8949	
	O	L1	10.9862	18.3004	11.729	
	O	L5	12.6318	19.2571	9.6203	
	JTCTPR-9	Ideal	structure	CShM	=	2.59962
	Ce	M	11.8375	16.8822	9.8384	
	O	L1	9.8417	17.8045	9.3642	
	O	L4	12.7938	14.8711	9.522	
	O	L9	10.0446	15.0045	8.475	
	O	L2	12.0502	16.9758	7.6012	
	O	L3	10.5853	15.6998	11.285	
	O	L6	13.2489	16.9185	11.5893	
	O	L8	14.6385	17.1063	8.9997	
	O	L7	10.8295	18.5357	12.0404	
	O	L5	12.5053	19.0232	9.6685	

8.2.3 SHAPE analysis for compound (12)-Dy

Table 8.16: Continuous shape measurements (CShM's) of compound (12)-Dy.

{Dy(DMF)₄(H₂O)(O_t)₃}						
Ideal	structures	ML8				
OP-8	1	D8h	Octagon			
HPY-8	2	C7v	Heptagonal	pyramid		
HBPY-8	3	D6h	Hexagonal	bipyramid		
CU-8	4	Oh	Cube			
SAPR-8	5	D4d	Square	antiprism		
TDD-8	6	D2d	Triangular	dodecahedron		

8. Appendix

JGBF-8	7	D2d	Johnson	gyrobifastigium	J26		
JETBPY-8	8	D3h	Johnson	elongated	triangular	bipyramidal	J14
JBTPR-8	9	C2v	Biaugmented	trigonal	prism	J50	
Structure	1	[Dy]					
	Dy	15.5218	13.741	14.0089			
	O	17.2359	15.3001	14.6605			
	O	14.1824	13.0171	12.1613			
	O	13.548	12.7874	15.0253			
	O	15.326	15.5128	12.4287			
	O	17.2782	13.2853	12.5662			
	O	16.2432	13.199	16.1412			
	O	15.841	11.3831	14.0067			
	O	14.3199	15.4881	15.0701			
	OP-8	Ideal	structure	CShM	=	29.78418	
	Dy	M	15.4996	13.746	14.0077		
	O	L1	16.1663	15.6044	14.2443		
	O	L4	15.4187	12.4638	12.4899		
	O	L6	14.6376	12.4	15.1907		
	O	L2	16.3616	15.092	12.8246		
	O	L3	16.0519	13.7911	12.0979		
	O	L7	14.9473	13.7009	15.9174		
	O	L5	14.8329	11.8876	13.771		
	O	L8	15.5805	15.0282	15.5254		
	HPY-8	Ideal	structure	CShM	=	23.74608	
	Dy	M	15.6976	13.8303	13.9214		
	O	L2	16.0347	14.8624	15.7035		
	O	L5	14.9462	13.6153	11.9865		
	O	L1	13.9155	13.0716	14.6979		
	O	L4	14.6165	15.2068	12.785		
	O	L6	15.8417	12.1857	12.645		

8. Appendix

	O	L8	16.7146	13.1858	15.6258		
	O	L7	16.6288	11.9946	14.2646		
	O	L3	15.1009	15.7618	14.4392		
	HBPY-8	Ideal	structure	CShM	=	16.81916	
	Dy	M	15.4996	13.746	14.0077		
	O	L2	16.4337	14.7991	15.6517		
	O	L5	14.5655	12.693	12.3636		
	O	L1	13.6922	13.523	15.1773		
	O	L4	14.3931	14.8456	12.5074		
	O	L8	17.307	13.969	12.838		
	O	L7	16.6061	12.6464	15.5079		
	O	L6	15.6721	11.5934	13.8638		
	O	L3	15.3271	15.8987	14.1515		
	CU-8	Ideal	structure	CShM	=	9.83811	
	Dy	M	15.4996	13.746	14.0077		
	O	L1	17.0402	14.8576	15.2195		
	O	L7	13.9591	12.6345	12.7958		
	O	L3	13.6158	13.5107	15.2216		
	O	L6	15.043	14.904	12.1293		
	O	L5	17.3834	13.9813	12.7937		
	O	L4	15.9562	12.588	15.886		
	O	L8	16.2994	11.7118	13.4602		
	O	L2	14.6998	15.7803	14.5551		
	SAPR-8	Ideal	structure	CShM	=	0.64638	
	Dy	M	15.4996	13.746	14.0077		
	O	L1	17.2673	15.2178	14.5592		
	O	L7	14.3363	12.8612	12.1478		
	O	L8	13.5262	12.8006	14.906		
	O	L6	15.2989	15.549	12.4897		
	O	L2	17.1595	13.3602	12.3672		
	O	L4	16.0138	13.2744	16.2678		
	O	L3	15.906	11.4168	14.0758		
	O	L5	14.4888	15.4883	15.2478		

8. Appendix

	TDD-8	Ideal	structure	CShM	=	1.03082	
	Dy	M	15.4996	13.746	14.0077		
	O	L1	17.0566	15.375	14.7118		
	O	L7	13.9547	13.0514	12.3632		
	O	L6	13.6782	12.7937	15.1693		
	O	L3	15.5211	15.4099	12.3329		
	O	L4	17.4572	13.3841	12.7387		
	O	L5	16.3524	12.9969	16.0776		
	O	L8	15.7425	11.4055	13.8165		
	O	L2	14.2341	15.5517	14.851		
	JGBF-8	Ideal	structure	CShM	=	14.84722	
	Dy	M	15.4996	13.746	14.0077		
	O	L1	17.4792	15.319	14.0387		
	O	L5	14.8673	13.5584	12.3457		
	O	L7	14.1524	12.3606	15.6385		
	O	L2	15.3506	15.9888	12.8493		
	O	L4	16.9958	12.8886	13.5352		
	O	L3	16.1319	13.9336	15.6696		
	O	L8	15.0162	11.3156	13.5041		
	O	L6	14.0034	14.6034	14.4802		
	JETBPY-8	Ideal	structure	CShM	=	29.31234	
	Dy	M	15.4996	13.746	14.0077		
	O	L1	16.6329	14.8418	14.4338		
	O	L4	15.4933	12.3318	13.1911		
	O	L6	14.2061	13.0632	14.7338		
	O	L7	15.9382	16.3822	13.1238		
	O	L3	15.8264	14.3342	12.5197		
	O	L2	16.2997	12.8394	15.1052		
	O	L8	15.061	11.1098	14.8916		
	O	L5	14.5392	15.0656	14.0624		
	JBTPR-8	Ideal	structure	CShM	=	2.14194	

8. Appendix

	Dy	M	15.2147	13.8586	13.9264		
	O	L7	17.3238	15.6604	14.5909		
	O	L5	14.3964	12.8469	12.1676		
	O	L6	13.5873	12.781	14.9147		
	O	L3	15.3554	15.5238	12.5144		
	O	L1	17.106	13.3041	12.9767		
	O	L2	16.2969	13.2381	15.7238		
	O	L8	15.6698	11.0435	13.9929		
	O	L4	14.5463	15.4578	15.2614		

8.2.4 SHAPE analysis for compound (13)

Table 8.17: Continuous shape measurements (CShM's) of compound (13).

{CuCl(DMF)(N_{py})₄}						
Ideal	structures	ML6				
HP-6	1	D6h	Hexagon			
PPY-6	2	C5v	Pentagonal	pyramid		
OC-6	3	Oh	Octahedron			
TPR-6	4	D3h	Trigonal	prism		
JPPY-6	5	C5v	Johnson	pentagonal	pyramid	J2
Structure	1	[Cu]				
	Cu	18.6919	13.3661	13.7951		
	Cl	20.9558	13.7025	12.3935		
	O	16.5611	12.783	15.4422		
	N	17.8911	11.9488	12.5756		
	N	19.4927	11.9488	15.0146		
	N	19.3324	14.7295	15.1415		
	N	18.0514	14.7295	12.4487		
	HP-6	Ideal	structure	CShM	=	28.22389
	Cu	M	18.7109	13.3154	13.8302	
	Cl	L1	20.0516	14.417	12.9804	
	O	L4	17.3702	12.2139	14.6799	
	N	L3	17.1696	12.723	12.827	
	N	L5	18.9115	12.8063	15.6831	

8. Appendix

	N	L6	20.2522	13.9079	14.8334	
	N	L2	18.5103	13.8245	11.9772	
	PPY-6	Ideal	structure	CShM	=	24.63874
	Cu	M	18.7163	13.0777	13.6708	
	Cl	L2	20.6135	13.4661	13.1562	
	O	L4	17.5597	12.1484	15.0174	
	N	L5	16.8032	13.3787	13.1567	
	N	L3	19.9146	12.2023	15.0172	
	N	L1	18.6783	14.7417	14.7865	
	N	L6	18.6906	14.1931	12.0064	
	OC-6	Ideal	structure	CShM	=	2.9755
	Cu	M	18.7109	13.3154	13.8302	
	Cl	L1	20.5988	13.5372	12.6332	
	O	L6	16.823	13.0937	15.0271	
	N	L2	17.9954	11.7305	12.4081	
	N	L3	19.6958	11.7391	15.0916	
	N	L4	19.4263	14.9004	15.2522	
	N	L5	17.726	14.8918	12.5688	
	TPR-6	Ideal	structure	CShM	=	14.98026
	Cu	M	18.7109	13.3154	13.8302	
	Cl	L1	20.7312	13.7852	13.4845	
	O	L5	17.5468	12.8386	15.5151	
	N	L6	17.2558	12.1417	12.8675	
	N	L4	19.5332	11.4235	14.2378	
	N	L2	18.7447	15.2003	14.7618	
	N	L3	18.4537	14.5034	12.1142	
	JPPY-6	Ideal	structure	CShM	=	26.94002
	Cu	M	18.723	13.1616	13.7325	
	Cl	L1	20.6786	13.6258	13.243	
	O	L3	17.5291	12.1904	15.1149	
	N	L4	16.7526	13.3816	13.1421	
	N	L2	19.9555	12.3413	15.1773	
	N	L6	18.6384	14.2386	14.4161	

	N	L5	18.699	14.2687	11.9852	
--	---	----	--------	---------	---------	--

8.2.5 SHAPE analysis for compound (14A)

Table 8.18: Continuous shape measurements (CShM's) of compound (14A).

{Zn(DMF)₂(Ot)₂(Npy)₂}						
Ideal	structures	ML6				
HP-6	1	D6h	Hexagon			
PPY-6	2	C5v	Pentagonal	pyramid		
OC-6	3	Oh	Octahedron			
TPR-6	4	D3h	Trigonal	prism		
JPPY-6	5	C5v	Johnson	pentagonal	pyramid	J2
Structure	1	[Zn]				
	Zn	32.4195	14.0436	27.5638		
	O	33.991	12.5419	27.7138		
	O	30.9178	15.6151	27.4139		
	O	33.4074	15.1932	28.9898		
	O	33.5691	15.0315	26.1379		
	N	31.3566	13.0506	29.1184		
	N	31.4265	12.9807	26.0093		
	HP-6	Ideal	structure	CShM	=	33.10628
	Zn	M	32.4411	14.0652	27.5639	
	O	L1	33.4105	13.0959	28.6385	
	O	L4	31.4718	15.0346	26.4892	
	O	L2	33.9925	14.6472	28.1012	
	O	L3	33.0231	15.6166	27.0265	
	N	L6	31.8591	12.5139	28.1012	
	N	L5	30.8898	13.4832	27.0265	
	PPY-6	Ideal	structure	CShM	=	29.22293
	Zn	M	32.4958	14.1883	27.3426	

8. Appendix

	O	L2	33.3296	12.7024	26.7218	
	O	L4	30.9018	15.0489	27.4275	
	O	L5	32.7407	15.7321	28.262	
	O	L6	34.2412	14.2819	27.8258	
	N	L1	32.1131	13.3266	28.8916	
	N	L3	31.2657	13.1764	26.4757	
	OC-6	Ideal	structure	CShM	=	0.11361
	Zn	M	32.4411	14.0652	27.5639	
	O	L1	33.9433	12.563	27.6957	
	O	L6	30.9389	15.5674	27.432	
	O	L2	33.4395	15.1954	29.0661	
	O	L3	33.5713	15.0636	26.0616	
	N	L5	31.3109	13.0669	29.0661	
	N	L4	31.4428	12.935	26.0616	
	TPR-6	Ideal	structure	CShM	=	15.91117
	Zn	M	32.4411	14.0652	27.5639	
	O	L1	33.1912	12.2713	27.3813	
	O	L5	30.6472	14.8153	27.7464	
	O	L6	32.9136	15.6806	28.5546	
	O	L3	34.0565	14.5377	26.5731	
	N	L4	32.0483	13.4142	29.3627	
	N	L2	31.7901	13.6724	25.765	
	JPPY-6	Ideal	structure	CShM	=	32.52913
	Zn	M	32.3791	13.929	27.4971	
	O	L1	33.7916	12.9453	28.1929	
	O	L3	30.661	14.5415	27.8431	
	O	L6	32.8132	14.8828	27.9643	
	O	L5	33.7466	13.9216	26.2415	
	N	L2	31.8846	13.3285	29.1828	
	N	L4	31.8118	14.908	26.0253	

8.2.6 SHAPE analysis for compound (14B)

Table 8.19: Continuous shape measurements (CShM's) of compound (14B).

Zn1						
Ideal	structures	ML6				
HP-6	1	D6h	Hexagon			
PPY-6	2	C5v	Pentagonal	pyramid		
OC-6	3	Oh	Octahedron			
TPR-6	4	D3h	Trigonal	prism		
JPPY-6	5	C5v	Johnson	pentagonal	pyramid	J2
Structure	1	[Zn]				
	Zn	34.5966	2.5906	24.0923		
	O	34.0802	1.9634	22.1075		
	O	35.0398	4.5786	23.5577		
	O	34.9767	2.9463	26.0787		
	O	34.3132	0.5862	24.6251		
	N	36.5769	2.0131	23.6187		
	N	32.5607	3.1635	24.1625		
	HP-6	Ideal	structure	CShM	=	31.43096
	Zn	M	34.592	2.5488	24.0346	
	O	L1	33.4864	1.7339	22.9631	
	O	L3	34.3355	4.223	24.4422	
	O	L4	35.6976	3.3637	25.1062	
	O	L6	34.8485	0.8746	23.6271	
	N	L5	35.9541	1.6895	24.6987	
	N	L2	33.2299	3.4081	23.3706	
	PPY-6	Ideal	structure	CShM	=	25.63649
	Zn	M	34.3602	2.5605	24.1568	
	O	L2	33.6427	1.4252	22.9047	
	O	L4	34.6626	4.3258	24.5613	
	O	L5	35.2187	2.6321	25.7784	
	O	L6	34.5883	0.8394	24.7545	

8. Appendix

	N	L1	35.9828	2.4785	23.3014	
	N	L3	33.6886	3.58	22.7853	
	OC-6	Ideal	structure	CShM	=	0.47665
	Zn	M	34.592	2.5488	24.0346	
	O	L1	34.1648	2.0708	22.0362	
	O	L2	35.014	4.5261	23.4715	
	O	L6	35.0191	3.0268	26.0331	
	O	L4	34.17	0.5716	24.5977	
	N	L3	36.603	2.0324	23.7283	
	N	L5	32.581	3.0652	24.341	
	TPR-6	Ideal	structure	CShM	=	12.70222
	Zn	M	34.592	2.5488	24.0346	
	O	L1	33.7842	1.4966	22.5841	
	O	L5	35.3843	4.3404	24.1964	
	O	L6	34.1904	2.8631	25.9329	
	O	L3	35.0247	0.7557	24.7138	
	N	L2	36.2186	2.233	22.9773	
	N	L4	32.9498	3.604	23.8033	
	JPPY-6	Ideal	structure	CShM	=	29.19342
	Zn	M	34.4485	2.551	24.1178	
	O	L1	33.6948	1.39	22.8476	
	O	L3	34.7258	4.3582	24.5493	
	O	L4	35.3907	2.6222	25.7416	
	O	L5	34.7535	0.7877	24.6898	
	N	L6	35.453	2.5358	23.5356	
	N	L2	33.6777	3.5967	22.7607	
Zn2						
Ideal	structures	ML6				
HP-6	1	D6h	Hexagon			
PPY-6	2	C5v	Pentagonal	pyramid		
OC-6	3	Oh	Octahedron			
TPR-6	4	D3h	Trigonal	prism		
JPPY-6	5	C5v	Johnson	pentagonal	pyramid	J2

8. Appendix

Structure	1	[Zn]				
	Zn	30.0594	3.2363	13.879		
	O	28.7152	3.8329	12.338		
	O	31.4015	2.6399	15.4215		
	O	31.1843	4.9035	13.5494		
	O	28.9324	1.5693	14.2102		
	O	28.8349	4.2588	15.1487		
	O	31.2818	2.214	12.6108		
	HP-6	Ideal	structure	CShM	=	31.40875
	Zn	M	30.0585	3.2364	13.8797	
	O	L1	29.1739	4.5151	13.159	
	O	L4	30.943	1.9577	14.6004	
	O	L2	30.7974	4.2266	12.692	
	O	L5	29.3196	2.2462	15.0673	
	O	L6	28.435	3.5249	14.3466	
	O	L3	31.682	2.9478	13.4127	
	PPY-6	Ideal	structure	CShM	=	29.2775
	Zn	M	30.1193	3.0828	13.6899	
	O	L2	28.6887	3.6072	12.8066	
	O	L4	30.7272	1.8988	14.8435	
	O	L6	30.5664	4.474	12.7068	
	O	L3	28.7881	2.0156	14.1271	
	O	L1	29.6934	4.1582	15.0181	
	O	L5	31.8262	3.4182	13.9657	
	OC-6	Ideal	structure	CShM	=	0.13033
	Zn	M	30.0585	3.2364	13.8797	
	O	L1	28.7943	3.7824	12.337	
	O	L6	31.3227	2.6903	15.4224	
	O	L2	31.1865	4.9395	13.5582	
	O	L4	28.9305	1.5333	14.2012	
	O	L3	28.8729	4.2744	15.2187	
	O	L5	31.2441	2.1983	12.5407	

8. Appendix

	TPR-6	Ideal	structure	CShM	=	16.22145
	Zn	M	30.0585	3.2364	13.8797	
	O	L1	28.7846	2.9588	12.5058	
	O	L5	31.3574	2.1719	14.7555	
	O	L6	31.2723	4.6153	14.3406	
	O	L2	28.8798	2.0982	14.8296	
	O	L3	28.7946	4.5416	14.4148	
	O	L4	31.2622	3.0325	12.4317	
	JPPY-6	Ideal	structure	CShM	=	32.55151
	Zn	M	30.0877	3.1377	13.7582	
	O	L1	28.6039	3.7289	12.9207	
	O	L3	30.7179	1.9037	14.9127	
	O	L5	30.5519	4.5431	12.7277	
	O	L2	28.7065	2.0976	14.2711	
	O	L6	29.8831	3.8287	14.6085	
	O	L4	31.8584	3.4151	13.9588	

8.2.7 SHAPE analysis for compound (15)

Table 8.20: Continuous shape measurements (CShM's) of compound (15).

{Cd(DMF)₂(O)₂(Npy)₂} (Cd1)						
Ideal	structures	ML6				
HP-6	1	D6h	Hexagon			
PPY-6	2	C5v	Pentagonal	pyramid		
OC-6	3	Oh	Octahedron			
TPR-6	4	D3h	Trigonal	prism		
JPPY-6	5	C5v	Johnson	pentagonal	pyramid	J2
Structure	1	[Cd]				
	Cd	0.4507	-8.685	10.9693		
	O	-1.2182	-7.1235	11.1855		
	O	2.1203	-10.2466	10.7517		

8. Appendix

	O	-1.1859	-10.3187	11.1413		
	O	2.088	-7.0514	10.7959		
	N	0.2732	-8.8586	8.6829		
	N	0.6289	-8.5115	13.2543		
	HP-6	Ideal	structure	CShM	=	29.71132
	Cd	M	0.451	-8.685	10.9687	
	O	L1	-1.1467	-8.1461	11.9124	
	O	L4	2.0488	-9.224	10.025	
	O	L2	-1.2773	-9.3215	10.3842	
	O	L5	2.1794	-8.0486	11.5532	
	N	L3	0.3204	-9.8604	9.4406	
	N	L6	0.5816	-7.5096	12.4968	
	PPY-6	Ideal	structure	CShM	=	28.65501
	Cd	M	0.3051	-8.4541	10.901	
	O	L2	-0.9779	-8.8411	12.3454	
	O	L1	1.3267	-10.0708	11.3752	
	O	L3	-1.13	-9.5797	10.1553	
	O	L5	1.9849	-7.5193	10.469	
	N	L4	0.7011	-8.7627	8.9956	
	N	L6	0.9472	-7.5677	12.5393	
	OC-6	Ideal	structure	CShM	=	0.18448
	Cd	M	0.451	-8.685	10.9687	
	O	L1	-1.2017	-7.0854	11.0794	
	O	L6	2.1037	-10.2846	10.858	
	O	L2	-1.1366	-10.3398	11.1776	
	O	L4	2.0386	-7.0303	10.7599	
	N	L3	0.2264	-8.7586	8.6782	
	N	L5	0.6757	-8.6115	13.2592	
	TPR-6	Ideal	structure	CShM	=	16.23943
	Cd	M	0.451	-8.685	10.9687	
	O	L1	-0.6216	-7.0804	11.8195	
	O	L5	2.4122	-9.4435	11.1362	
	O	L3	-1.4826	-9.5201	10.8529	

8. Appendix

	O	L4	1.4685	-7.1028	10.0144	
	N	L6	0.6076	-9.5425	9.0479	
	N	L2	0.322	-9.421	12.9413	
	JPPY-6	Ideal	structure	CShM	=	31.91414
	Cd	M	0.3659	-8.5372	10.9173	
	O	L1	-1.0123	-8.8276	12.3628	
	O	L6	0.9617	-9.5722	11.2773	
	O	L2	-1.1211	-9.6619	10.1444	
	O	L4	2.1367	-7.6626	10.5016	
	N	L3	0.8251	-8.9418	8.994	
	N	L5	1.0011	-7.592	12.5836	
{Cd(N_{py})₂(O)₄} (Cd1)						
Ideal	structures	ML6				
HP-6	1	D6h	Hexagon			
PPY-6	2	C5v	Pentagonal	pyramid		
OC-6	3	Oh	Octahedron			
TPR-6	4	D3h	Trigonal	prism		
JPPY-6	5	C5v	Johnson	pentagonal	pyramid	J2
Structure	1	[Cd]				
	Cd	-1.2598	1.1346	21.9385		
	O	0.611	2.3732	22.1053		
	O	-3.13	-0.1041	21.7705		
	N	-1.4135	1.7813	19.7526		
	N	-1.1055	0.4879	24.1232		
	O	-0.0769	-0.723	21.3407		
	O	-2.442	2.9921	22.5351		
	HP-6	Ideal	structure	CShM	=	32.23241
	Cd	M	-1.2595	1.1346	21.938	
	O	L1	-0.4655	2.7758	21.5215	
	O	L4	-2.0536	-0.5067	22.3544	
	N	L2	-0.341	1.3459	20.3226	
	N	L5	-2.178	0.9233	23.5533	
	O	L3	-1.1351	-0.2954	20.7391	
	O	L6	-1.384	2.5645	23.1369	

8. Appendix

	PPY-6	Ideal	structure	CShM	=	29.72591
	Cd	M	-1.5187	1.0728	21.8685	
	O	L1	0.2956	1.5054	22.3548	
	O	L2	-1.3262	-0.6595	22.6917	
	N	L4	-1.309	2.0473	20.2187	
	N	L6	-2.0506	1.2282	23.7147	
	O	L3	-0.8679	-0.1533	20.5311	
	O	L5	-2.0399	2.9011	22.1863	
	OC-6	Ideal	structure	CShM	=	0.04433
	Cd	M	-1.2595	1.1346	21.938	
	O	L1	0.6544	2.343	22.1271	
	O	L6	-3.1734	-0.0738	21.7488	
	N	L2	-1.4308	1.7472	19.7575	
	N	L4	-1.0882	0.522	24.1184	
	O	L3	-0.0484	-0.6885	21.3307	
	O	L5	-2.4706	2.9576	22.5453	
	TPR-6	Ideal	structure	CShM	=	16.23487
	Cd	M	-1.2595	1.1346	21.938	
	O	L1	0.4529	2.0955	21.2542	
	O	L5	-2.4631	-0.4184	21.2575	
	N	L2	-2.0967	2.1035	20.2998	
	N	L6	-1.9516	0.4656	23.7811	
	O	L4	0.0865	-0.4264	22.2119	
	O	L3	-1.5851	2.9875	22.8233	
	JPPY-6	Ideal	structure	CShM	=	33.11181
	Cd	M	-1.4242	1.1048	21.8899	
	O	L6	-0.2717	1.3135	22.2267	
	O	L1	-1.3363	-0.6902	22.7014	
	N	L3	-1.1219	2.1201	20.2267	
	N	L5	-2.0011	1.2569	23.7693	
	O	L2	-0.793	-0.1567	20.512	
	O	L4	-1.8685	2.9937	22.2398	

8.3 Publications

- Schmidt, S. F. M., Merkel, M. P., Kostakis, G. E., Buth, G., Anson, C. E. and Powell, A. K., SMM Behaviour and Magnetocaloric Effect in Heterometallic 3d-4f Coordination Clusters with High Azide: Metal Ratios. *Dalt. Trans.* **2017**, 46, 15661-15665.
- Peewasan, K.; Merkel, M. P.; Zarschler, K.; Stephan, H.; Anson, C. E.; Powell, A. K., Tetranuclear Cu(II)-chiral complexes: synthesis, characterization and biological activity. *RSC Adv.* **2019**, 9, 24087.
- Peewasan, K.; Merkel, M. P.; Fuhr, O., Powell, A. K., A designed and potentially decadentate ligand for use in lanthanide(III) catalysed biomass transformations: targeting diastereoselective trans-4,5-diaminocyclopentenone derivatives. *Dalt. Trans.* **2020**, DOI: 10.1039/D0DT00183J.

8.4 Conferences

- 2016** FMOCS IV @ PoCheMoN, Newcastle upon Tyne, UK, poster presentation.
- 2018** 3MET, Karlsruhe, DE, participation.
- 2019** Spin begins at 60, Karlsruhe, DE, flash presentation.

8.5 Work shops

- "Olex2 für Könner" from 7. to 8. March 2018
- Sommerschule Kristallographie“, Hardehausen 17. – 21. September 2018 „Grundlagen der Einkristallstrukturbestimmung“

8.6 Stay Abroad

- Short-term stay at the University of Sussex (Dr. George E. Kostakis) from January 14. To February 24, 2019

8.7 Collaborations

- Prof. Dr. Pedro De Oliveira and Dr. Mbomekalle Israël (electrocatalytic studies) (Laboratoire de Chimie Physique, UMR8000 - Université Paris-Sud Bâtiment 349 - Campus d'Orsay 15, avenue Jean Perrin 91405 Orsay, FRANCE)
- Dr. George E. Kostakis (Topology) (University of Sussex, Chichester 3 3R 3R507, Brighton, BN1 9RH, United Kingdom)
- Dr. Ying-Chu (photocatalytic studies) (Prof. Dr. Claus Feldmann) from the Institut für Anorganische Chemie, Karlsruher Institut für Technologie (KIT), Engesserstr, 15 Geb, 30.45.

8.8 Teaching assistant

WS2015/16	Anorganisch-chemisches Praktikum für Fortgeschrittene
SS2016	Anorganisch-chemisches Praktikum für Fortgeschrittene Anorganisch-chemisches Praktikum für studierende der Physik
WS2016/17	Anorganisch-chemisches Praktikum für Fortgeschrittene Betreuung der Bachelorarbeit von Johannes Wenz Betreuung der Bachelorarbeit von Jonas Morgenstern
SS2017	Anorganisch-chemisches Praktikum für Fortgeschrittene
WS2017/18	Anorganisch-chemisches Praktikum für Fortgeschrittene

8. Appendix

SS2018	Anorganisch-chemisches Praktikum für Fortgeschrittene
WS2018/19	Anorganisch-chemisches Praktikum für Fortgeschrittene Betreuung der Bachelorarbeit von Fatih Ulusoy

9 EIDESSTATTLICHE ERKLÄRUNG

Ich versichere hiermit wahrheitsgemäß, die Arbeit bis auf die dem Aufgabensteller bereits bekannten Hilfsmittel selbständig angefertigt, alle benutzten Hilfsmittel vollständig und genau angegeben und alles kenntlich gemacht zu haben, was aus Arbeiten anderer unverändert oder mit Abänderungen übernommen wurde.

Karlsruhe, den

Datum und Unterschrift